

The author of the doctoral	dissertation: Patryk Błaszczak	
Scientific discipline: Mater	ials Engineering	
DOCTORAL DISSER	TATION	
Title of doctoral dissertation	on: Nanostructural ceramic-bimetallic materials fo	r efficient energy
conversion	m. Nanostructural ceramic-bimetaliic materials to	i emclent energy
Conversion		
Title of doctoral dissertation	on (in Polish): Nanostrukturalne materiały ceramicz	no-himetaliczne dla
wydajnej konwersji energii		ino-bimetaliczne dia
wydajnej konwersji energii		
•		
	Supervisor	
	dr hab. inż. Beata Bochentyn	



STATEMENT

The author of the doctoral dissertation: Patryk Błaszczak

I, the undersigned, declare that I am aware that in accordance with the provisions of A (2) of the Act of 4th February 1994 on Copyright and Related Rights (Journal of Laws 1062), the university may use my doctoral dissertation entitled: 'Nanostructural ceramic-bimetallic materials for efficient energy conversion' for scienti purposes. ¹	of 2021, item
Gdańsk,	
signature of the P	hD student
Aware of criminal liability for violations of the Act of 4th February 1994 on Copyright Rights and disciplinary actions set out in the Law on Higher Education and Science (Jo 2021, item 478), as well as civil liability, I declare, that the submitted doctoral dissertat work.	ournal of Laws
I declare, that the submitted doctoral dissertation is my own work performed cooperation with the supervision of dr hab. inż. Beata Bochentyn.	under and in
This submitted doctoral dissertation has never before been the basis of an offic associated with the awarding of a PhD degree.	ial procedure
All the information contained in the above thesis which is derived from written and elect is documented in a list of relevant literature in accordance with Art. 34 of the Copyrigh Rights Act.	
I confirm that this doctoral dissertation is identical to the attached electronic version.	
Gdańsk,	
signature of the P	
I, the undersigned, agree to include an electronic version of the above doctoral disservation, institutional, digital repository of Gdańsk University of Technology.	ertation in the
Gdańsk,signature of the P	

¹ Art 27. 1. Educational institutions and entities referred to in art. 7 sec. 1 points 1, 2 and 4-8 of the Act of 20 July 2018 – Law on Higher Education and Science, may use the disseminated works in the original and in translation for the purposes of illustrating the content provided for didactic purposes or in order to conduct research activities, and to reproduce for this purpose disseminated minor works or fragments of larger works.

^{2.} If the works are made available to the public in such a way that everyone can have access to them at the place and time selected by them, as referred to in para. 1, is allowed only for a limited group of people learning, teaching or conducting research, identified by the entities listed in paragraph 1.



DESCRIPTION OF DOCTORAL DISSERTATION

The Author of the doctoral dissertation: Patryk Błaszczak

Title of doctoral dissertation: Nanostructural ceramic-bimetallic materials for efficient energy

conversion

Title of doctoral dissertation in Polish: Nanostrukturalne materiały ceramiczno-bimetaliczne dla

wydajnej konwersji energii

Language of doctoral dissertation: English

Supervisor: Beata Bochentyn

Date of doctoral defense:

Keywords of doctoral dissertation in Polish: ogniwo tlenkowe, elektrochemia, katalizator,

mikrostruktura, aktywność katalityczna

 $\textbf{Keywords of doctoral dissertation in English}: \ solid \ oxide \ cell, \ electrochemistry, \ catalyst,$

microstructure, catalytic activity

Summary of doctoral dissertation in Polish:

Niniejsza praca doktorska przedstawia nowe podejście do zwiększania wydajności i trwałości ogniw tlenkowych (SOC). Badania koncentrują się na zaawansowanych materiałach katalitycznych oraz modyfikacji architektury elektrod, mających na celu zmniejszenie degradacji i zwiększenie żywotności SOC.

Kluczową innowacją jest przedstawienie metody impregnacji na mokro wspomaganej β-cyklodekstryną (βCD) do syntezy nanocząstek metali przejściowych (Ni, Co, Cu, Fe, Mn) na tlenku ceru. Podejście to pozwoliło uzyskać małe cząstki o dobrej dyspersji oraz silnych oddziaływaniach z podłożem. Katalizator βCD-Ni/CeO₂ osiągnął wysoką wydajność w warunkach pracy SOC, zachowując doskonałą stabilność termiczną w 700 °C.

Praca opisuje także proces modyfikacji elektrody Ni-YSZ nanocząstkami Co, które zwiększają wydajność koelektrolizy CO₂/H₂O i metanizacji. Optymalne stężenie Co (3,6% mas.) doprowadziło do powstania fazy spinelu zbliżonej do NiCo₂O₄ oraz stabilnej struktury typu rdzeń-powłoka, co ponad dwukrotnie zwiększyło produkcję CH₄.

Dodatkowo opracowano nową metodę wytwarzania nanokompozytów Ni-YSZ oraz YSZ z użyciem systemu CTAB/Pluronic P123 i NaCl. Powstałe struktury typu wormhole wykazały znakomitą dyspersję niklu, stabilność redoks oraz długotrwałą wydajność przez ponad 160 godzin.

Praca ta stanowi preludium do rozwoju wydajnych i trwałych ogniw SOC dla zeroemisyjnych zastosowań energetycznych.

Summary of doctoral dissertation in English:

This dissertation presents novel strategies to enhance the performance and durability of solid oxide cells (SOCs). The research focuses on advanced catalytic materials and electrode architectures to overcome limitations such as degradation and short lifespan.

A key innovation is the β -cyclodextrin (β CD)-assisted wet impregnation method for synthesizing transition metal (Ni, Co, Cu, Fe, Mn) nanoparticles on ceria support. This approach yielded small, well-dispersed particles with strong metal-oxide interactions. The catalyst β CD-Ni/CeO₂ achieved outstanding efficiency under SOC operational conditions, maintaining excellent thermal stability at 700 °C.

The study also describes Ni-YSZ electrodes with Co nanoparticles, enhancing CO_2/H_2O coelectrolysis and methanation processes. An optimal Co loading (3.6 wt.%) led to the formation of a $NiCo_2O_4$ -like spinel phase and a stable Ni-Co core-shell structure, more than doubling CH_4 production.

Additionally, a novel templating method using CTAB/Pluronic P123 and NaCl was developed to synthesize highly porous 8YSZ and NiO-YSZ nanocomposites. These wormhole-like structures exhibited excellent Ni dispersion, redox stability, and sustained performance for over 160 hours.

Overall, this work provides a solid foundation for developing efficient, durable SOC systems for future carbon-neutral energy applications.



Table of contents

Abstract	6
Streszczenie	8
List of important abbreviations and mathematical symbols	10
1. INTRODUCTION	13
1.1 Motivation of the study	13
1.2 Scientific problem and research gap	15
1.3 Hypotheses and objectives of the thesis	20
2. THEORY OF THE CHEMISTRY AND ELECTROCHEMISTRY IN SOLID OXIDE	
2.1 Introduction to Solid Oxide Cell (SOC) technology	22
2.2 Thermodynamic principles of SOC operation	25
2.3 Efficiency and thermal balance of SOC	28
2.4 Catalysts and various processes in SOC	31
2.4.1 Coelectrolysis in SOEC	32
2.4.2 Methane reforming and synthesis	34
2.5 Materials used for construction of SOC	36
2.5.1 Electrolyte	36
2.5.2 Hydrogen (fuel) electrode	38
2.5.3 Oxygen electrode	41
2.6 Degradation in SOC	43
3.EXPERIMENTAL METHODS	48
3.1 Basic material characterization methods	48
3.1.1 Scanning Electron (SEM) and Transmission Electron (TEM) Microscopy	48
3.1.2 X-ray Diffractometry (XRD)	48
3.1.3 X-ray Photoelectron Spectroscopy (XPS)	48
3.1.4 Temperature Programmed Reduction (TPR) and Oxidation (TPO)	48
3.1.5 Dilatometry	49

3.1.6 Thermogravimetry (TG) and Differential Scanning Calorimetry (DSC)	49
3.1.7 Archimedes principle density measurement and Mercury Intrusion Porosimetry .	49
3.1.8 Nitrogen sorption measurement	50
3.2 Electrical measurement methods	50
3.2.1 Conductivity measurement using Van der Pauw method (VdP)	50
3.2.2 Electrochemical Impedance Spectroscopy (EIS)	51
3.2.3 Distribution of Relaxation Times technique (DRT)	51
3.3 Synchrotron radiation-based measurement methods	52
3.3.1 X-ray Absorption Fine Structure Spectroscopy (XAFS)	52
3.3.2 Scanning Transmission X-ray Microscopy (STXM)	53
3.3.3 Near Ambient Pressure X-ray Photoelectron Spectroscopy (NAP-XPS)	53
3.4 Chemical equilibrium simulations	54
3.5 Non-equilibrium thermodynamic analysis of the reaction state	54
3.6 SOC testing system construction	55
3.7. SOC testing cells and selected measurement procedure	58
3.8 Packed-bed reactor and measurement procedures	60
3.9 Synthesis of materials	61
3.9.1 Wet impregnation method	62
3.9.2 Co-precipitation method for NiO-YSZ and YSZ scaffold synthesis	62
3.9.3 Preparation of the specimens for conductivity measurements	63
4. RESULTS AND DISCUSSION	65
4.1 Influence of nanometric catalysts on methanation and methane reforming	65
4.1.1 Phase composition	65
4.1.2 Reducibility and integration of metal with the support	67
4.1.3 Microstructure	74
4.1.4 Catalytic efficiency	76
4.1.5 Analysis of reaction quotients of methanation	80
Summary of the section	81
4.2 Modification of SOEC with nanoparticles performing coelectrolysis and methanation	83

Abstract

The growing awareness of climate change has contributed to a global trend towards the development of more sustainable energy systems. An example of this is the rapidly growing renewable energy sector. Unfortunately, due to the intermittent nature of renewable energy sources and their dependence on climatic conditions, significant challenges arise e.g., related to the stability of energy grids or the development of advanced electricity production methods. As a potential solution to these challenges, the concept of smart grids and hydrogen-based technologies are increasingly being discussed. Within this trend, the use of Solid Oxide Cells (SOCs) plays an important role, as they can assist in the integration of renewable energy with existing infrastructure. The main advantage of Solid Oxide Cells is their ability to both generate and store energy, depending on the operating mode. However, technology also has its drawbacks, such as relatively high starting material costs and limited durability, which effectively hinders its widespread implementation in the market.

This dissertation investigates novel approaches for the design and synthesis of catalytic materials and functional electrodes to enhance SOC performance. A particular focus was put on wide characterization of the materials, their electrochemical and chemical activity, long-term stability, and description of the mechanisms causing the enhancements of SOCs.

A ground innovation in this work was the use of β -cyclodextrin (β CD)-assisted wet impregnation to fabricate transition metal nanoparticles (Ni, Co, Cu, Fe, Mn) for ceria-supported catalysts used in direct CO methanation under SOC working conditions. Structural characterization using XRD and TEM confirmed the formation of smaller, well-dispersed nanoparticles with strong metal–support interactions. β CD facilitated improved dispersion and the development of intermixed metal-oxide layers that prevented nanoparticle agglomeration. Temperature-programmed reduction (H₂-TPR) analyses revealed improved reducibility and better metallic particle anchoring. Ni-based and Co-based catalysts demonstrated enhanced activity and stability, with β CD–Ni/CeO₂ achieving 98.5% CO conversion and 79.9% CH₄ yield. Stability tests at 700 °C indicated minimal degradation, highlighting the potential of β CD-assisted route of modification in SOC catalyst design.

In addition, the study explored modifications of Ni–YSZ fuel electrodes by the usage to the aforementioned methodology. Cobalt nanoparticles were incorporated to enhance CO₂/H₂O coelectrolysis and methanation processes in SOECs. Optimal Co loading (3.6 wt.%) resulted in the formation of NiCo₂O₄-like spinel phase and improved electrochemical performance, supported by increased surface basicity and formation of active redox couples. These modifications more than doubled methane production and enhanced CO₂ conversion beyond thermodynamic limits, indicating strong synergistic catalytic-electrochemical effects.

Spectroscopic and microscopic analyses revealed the development of a stable Ni-Co core-shell structure.

Furthermore, a novel soft–hard templating method using CTAB/Pluronic P123 and crystallizing NaCl was developed to synthesize highly porous (~50%) 8YSZ and NiO–YSZ nanocomposites without external pore formers. The resulting wormhole-like porous structures exhibited high thermal stability, optimized porosity, and excellent Ni dispersion. Redox cycling and conductivity tests confirmed improved electrode integrity and performance over extended operation timespan (160 hours).

Overall, this work provides a set of novel strategies for improving catalytic activity and stability of the materials and electrodes in SOCs. The insights gained into materials' behavior, redox mechanisms, and catalyst–support interactions can give a strong foundation for the development of high-performance and durable SOC systems for carbon-neutral energy applications.

Streszczenie

Rosnąca świadomość zmian klimatycznych przyczyniła się do globalnego trendu ku rozwojowi bardziej zrównoważonych systemów energetycznych. Jako przykład posłużyć może chociażby gwałtownie rozwijający się sektor energii odnawialnych. Niestety, ze względu na to, że OZE (odnawialne źródła energii) mają charakter nieciągły i zależą od warunków klimatycznych, pojawiają się istotne wyzwania, między innymi dotyczące stabilności sieci energetycznych czy też rozwoju nowoczesnych metod generowania prądu. Jako potencjalne rozwiązanie powyższych wyzwań, coraz częściej pojawia się koncept systemów inteligentnych sieci elektroenergetycznych (z ang. *smart grids*) czy technologie oparte na wytwarzaniu oraz wykorzystaniu wodoru. W ten trend wpisuje się wykorzystanie ogniw tlenkowych (z ang. *Solid Oxide Cells, SOCs*), które mogą wspomóc integrację odnawialnych źródeł energii z istniejącą infrastrukturą energetyczną. Główną zaletą ogniw tlenkowych jest ich zdolność do zarówno produkowania energii, jak i jej magazynowania w zależności od trybu pracy. Niestety, technologia ogniw tlenkowych posiada także wady, jak relatywnie wysokie koszty materiałowe czy ograniczona trwałość, co skutecznie ogranicza ich wdrożenie na szeroki rynek.

Niniejsza rozprawa poświęcona jest badaniu nowych sposobów projektowania i syntezy materiałów katalitycznych oraz elektrod w celu poprawy wydajności ogniw tlenkowych bez użycia metali szlachetnych. Szczególny nacisk położono na kompleksową charakterystykę materiałów, ocenę ich aktywności elektrochemicznej i chemicznej, stabilności długoterminowej oraz analizę mechanizmów odpowiedzialnych za obserwowaną poprawę parametrów pracy SOC.

Kluczową innowacją przedstawioną w pracy było zastosowanie metody impregnacji na mokro wspomaganej β-cyklodekstryną (βCD) w celu wytworzenia nanocząstek metali przejściowych (Ni, Co, Cu, Fe, Mn) na nośniku z tlenku ceru (IV). Tak wytworzone materiały mogą zostać zastosowane jako katalizatory do bezpośredniej metanizacji CO luz CO₂ w warunkach pracy SOC. Badania strukturalne m.in. SEM oraz TEM potwierdziły uzyskanie drobnych, równomiernie rozproszonych nanocząstek o silnych interakcjach metal–podłoże. Zastosowanie βCD poprawiło dyspersję metali i sprzyjało tworzeniu się warstw przejściowych, zapobiegając aglomeracji nanocząstek. Badania za pomocą temperaturowo programowanej redukcji (H₂-TPR) wykazały lepszą podatność na redukcję i silniejsze zakotwiczenie cząstek metalicznych. Katalizatory zawierające nikiel i kobalt wykazały podwyższoną aktywność i stabilność. Katalizator βCD–Ni/CeO₂ osiągnął konwersję CO na poziomie 98,5% oraz wydajność uzysku metanu wynoszącą 79,9%. Testy stabilności prowadzone w temperaturze 700 °C wykazały minimalną degradację, co potwierdza potencjał tej metody modyfikacji w syntezie katalizatorów do SOC.

Ponadto, przedstawiona metoda syntezy została wykorzystana do modyfikacji elektrody paliwowej ogniw tlenkowych. Nanocząstki kobaltu zostały wprowadzone do cermetowej

elektrody Ni–YSZ w celu poprawy procesu koelektrolizy CO₂/H₂O oraz metanizacji w trybie pracy SOEC (z ang. Solid Oxide Electrolysis Cell). Optymalna zawartość kobaltu (3,6% mas.) spowodowała częściowe wytworzenie fazy typu spinel NiCo₂O₄. Przypuszcza się, że właśnie ta faza odpowiadała za poprawę parametrów elektrochemicznych, dzięki wzrostowi zasadowości powierzchniowej elektrody i powstanie aktywnych par redoks. Wszystkie te zmiany pozwoliły na ponad dwukrotny wzrost produkcji metanu oraz przekroczenie termodynamicznych limitów konwersji CO₂. Wskazało to na silny synergizm pomiędzy aktywnością chemiczną i elektrochemiczną. Analizy spektroskopowe i mikroskopowe potwierdziły także uformowanie się stabilnej struktury typu rdzeń–powłoka pomiędzy niklem oraz osadzonym na powierzchni jego ziaren kobaltem.

Dodatkowo, opracowano nową metodę syntezy wykorzystującą układ organiczny CTAB/Pluronic P123 oraz krystalizującą sół NaCl, umożliwiającą syntezę wysoko porowatego (~50%) 8YSZ oraz kompozytu NiO–YSZ bez konieczności stosowania zewnętrznych środków porotwórczych. Otrzymane struktury o morfologii przypominającej sieć połączonych mikrokanałów cechowały się wysoką stabilnością termiczną, zoptymalizowaną porowatością oraz jednorodną dyspersją Ni. Cykliczny test redukcji-utleniania nanokompozytu i pomiary przewodnictwa potwierdziły poprawę integralności niklu i 8YSZ w elektrodzie oraz zwiększoną stabilność struktury w czasie 160 godzin testowania.

Podsumowując, niniejsza praca przedstawia zestaw nowatorskich rozwiązań materiałowych mających na celu poprawę aktywności katalitycznej i stabilności materiałów stosowanych w ogniwach tlenkowych. Uzyskane wyniki pogłębiają wiedzę na temat ich zachowania w warunkach pracy, mechanizmów redoks obecnych podczas działania oraz wpływu interakcji metal—nośnik. Stanowi to solidną podstawę do dalszego rozwoju wysokowydajnych i trwałych systemów SOC, wspierających transformację energetyczną w kierunku neutralności klimatycznej.

List of important abbreviations and mathematical symbols

AFL anode-functional layer

BET Brunauer–Emmett–Teller

βCD β-cyclodextrine

CHP ombined heat and power

CMC critical micelle (micellar) concentration

CTAB cetyltrimethylammonium bromide

DC4W Direct Current four Wire conductivity

DI deionized water

DRT Distribution of Relaxation Times

DSC Differential Scanning Calorimetry

EDX Energy Dispersive X-ray Spectroscopy

EI Electron Ionization

EIS Electrochemical Impedance Spectroscopy

EV electric vehicle

F-T Fischer-Tropsch

FIB-SEM Focused Ion Beam Scanning Electron Microscope

FTIR Fourier Transform Infrared spectroscopy

GCMS Gas Chromatography Mass Spectrometry

GDC (CGO) gadolinia doped ceria (cerium-gadolinium oxide)

GHSV gas hourly space velocity

GOF goodness of fit

HHV high heating value

iV current-potential curve

LHV low heating value

LSC lanthanum strontium cobaltite

LSCF lanthanum strontium cobalt ferrite

LSGM lanthanum strontium magnesium gallate

LSM lanthanum strontium manganite

MICP Mercury Injection Capillary Pressure (porosimetry)

MIEC mixed ion electron conductor

NAP-XPS Near Ambient Pressure X-ray Photoelectron Spectroscopy

NPs nanoparticles

OCV Open Circuit Voltage

OER oxygen evolution reaction

ORR oxygen reduction reaction

P2H power-to-hydrogen (hydrocarbon)

PFY partial fluorescence yield

PMMA poly(methyl methacrylate)

PV photovoltaic cell

RE renewable energy

rSOC reversible Solid Oxide Cell

RWGS Reverse Water Gas Shift reaction

SEM Scanning Electron Microscopy

SOC Solid Oxide Cell

SOEC Solid Oxide Electrolysis Cell

SOFC Solid Oxide Fuel Cell

SSA specific surface area

STXM Scanning Transmission X-Ray Microscopy

TCD thermal conductivity detector

TEC thermal expansion coefficient

TEM Transmission Electron Microscopy

TEY total electron yield

TG Thermogravimetry

ToS Time-On-Stream

TPB triple phase boundary

TPO Temperature Programmed Oxidation

TPR Temperature Programmed Reduction

TrMe transition metal

VdP Van der Pauw

WGS Water-Gas Shift reaction

XAFS X-ray Absorption Fine Structure

XPS X-Ray Photoelectron Spectroscopy

XRD X-ray Diffraction

YSZ yttria stabilized zirconia

Mathematical symbols (as appearing in the text)

△H enthalpy change

△S entropy change

 ΔG Gibbs free energy change

 E_{ThN} thermoneutral voltage

F Faraday constant

 E^{θ} standard potential

 a_x activity of component x

 p_x partial pressure of component x

 K_p equilibrium constant

 V_{rev} reversible potential

UF utilization factor

X conversion

Y yield

S selectivity

σ apparent conductivity

1. INTRODUCTION

1.1 Motivation of the study

The awareness in society about the problems and risks associated with the constantly changing climate provides the response to a transition from the use of fossil fuels to renewable sources of energy. At the same time, there is an ongoing increase in the energy demand for everyday life. The growing number of various electrical appliances used for cooling, heating and transportation poses a challenge to electricity production and distribution systems. The important issue of eliminating excessive greenhouse gas emissions entails a growing sense of urgency within both citizens and governments. The switch to more environmentally friendly energy sources is observed when considering the harvesting of electricity and heat from renewable sources such as photovoltaic solar cells (PV) and wind turbines.

According to the report by R. Puertas *et al.* [1], the mean consumption of renewable energy (RE) in Europe has shown an increasing trend over the last decade. It is mostly connected to the harsh policies of the European Union that drive the changes. In numbers, the share of RE in electricity increased from 25.5% in 2010 to 37.4% in 2019, while the use of RE in heating and cooling increased from 23.4% to 31% during the same time period. Across Europe, the most common sources of sustainable energy are hydrological and wind power plants, followed by solar

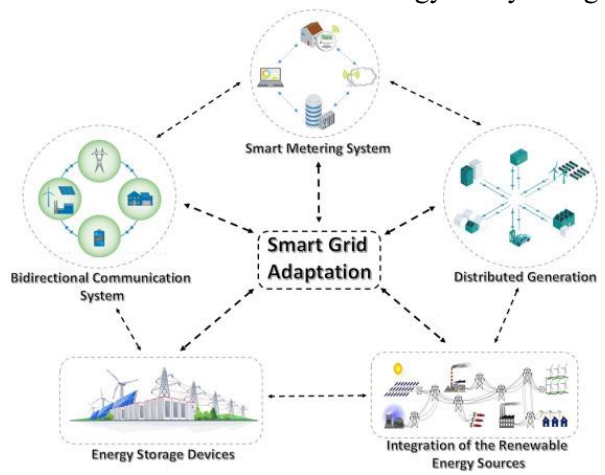


Figure 1. Conceptual view on smart grids [1].

panels and biofules (both liquid and solid). Another proof that the energy transition progresses is undeniably an increase in the capacity of renewable sources in the time range 2010-2021. Within these few years, the capacity increased from 1200 MW to 3100 MW with photovoltaics and wind energy being the main responsible for this increase [2].

Unfortunately, the intermittent nature of renewables generally causes the

existence of overproduction and periods of energy shortage. Renewable energy sources are still considered not capable to be an instantaneous supply of energy [3,4]. For example, heating systems and electric vehicles (EVs) can in certain situations generate a high demand peak. Unfortunately, conventional renewables are not able to momentarily adjust the output rates. The most challenging is finding a way to fill up power shortages and to effectively handle surplus energy to maintain balanced network at all times [5]. The concept is often referred to the evolution of smart grids (Fig. 1) that can be defined as a self-sufficient system, which can react instantly to

momentary energy needs and maintain the undisturbed energy flow. Decentralized energy provision and storage on a smaller scale is still a big challenge in designing fully independent and self-regulating smart grids [6–8]. Success may depend on the development of well-planned and demand-responsive mechanisms that involve reversible conversion. For this purpose, the solution should consider a fully autonomous way of producing and storing energy on demand.

The recently introduced 'Fit for 55' European climate law states that EU countries are required to reduce their emissions by at least 55% by 2030 to further make Europe climate neutral by 2050 [9]. The new law includes a series of rules that will help shift countries towards greater use of renewable and low-carbon gases. Hydrogen in energy systems is among most discussed fuels, leading to very promising predictions on achieving EU decarbonization. It is called the ultimate energy of the 21st century and will surely play an important role in smart grids, as it can be used as an energy vector – both a way to store energy and as an emission-free fuel. Integration of H₂ into smart grids will minimize the impact on the environment and provide sustainability [10]. Hydrogen is a 'silver lining' solution in the development of a global energy transformation looking for lower carbon emission [11,12]. Hydrogen in smart grid systems is now becoming more and more frequent but must be coupled with the development of electrolytic, so called 'green hydrogen' and fuel cell systems [13]. In the future, eventually, RE will generate most of the electricity, but the randomness of energy accessibility would pose a challenge to the optimal operation of smart grids. The coupling between the generation and long-term storage of energy could be achieved through the operational flexibility of Solid Oxide Cells (SOCs). Owing to the ability to respond reasonably fast, introduction of SOCs could provide real-time support to maintain the undisturbed flow of energy in smart grids [14]. Following this idea, the excess energy from RE in smart grids can be converted into chemical fuel (e.g., hydrogen or methane) using power-to-hydrogen (P2H) systems. If an event of energy inaccessibility occurs, fuel cells can be used to maintain the recovery of the smart grid, acting as a support power source that consumes stored hydrogen [15,16].

Searching for a proper way to enclose the energy flow loop brought a lot of research that focused on finding solutions to eradicate the use of fossil fuels and achieve carbon neutrality. The concept of hydrogen-assisted smart grid resilience is a new opportunity to further increase the viability of the development of renewable energy sources and lead Europe towards lower emissions.

1.2 Scientific problem and research gap

Fuel cells offer much higher efficiency and much reduced emissions compared to conventional technologies. The modular construction of the SOC systems makes that technology a major choice for a wide range of applications such as combined heat and power (CHP) production or distributed power generation and hydrogen supply station. This multifunctionality reduces reliance on import of fossil fuels, primary energy carriers and strengthen local production [17]. What is more, the theoretical efficiency of the SOCs is much higher than combustion engines, reaching around 60%. For combined systems harvesting electricity and heat the conversion can reach up to 70-90% [18]. Fig. 2 represents comparison in efficiency of various energy sources including Solid Oxide Fuel Cell as power producing unit. It is quite apparent that SOFCs exhibit higher efficiency than all other energy sources.

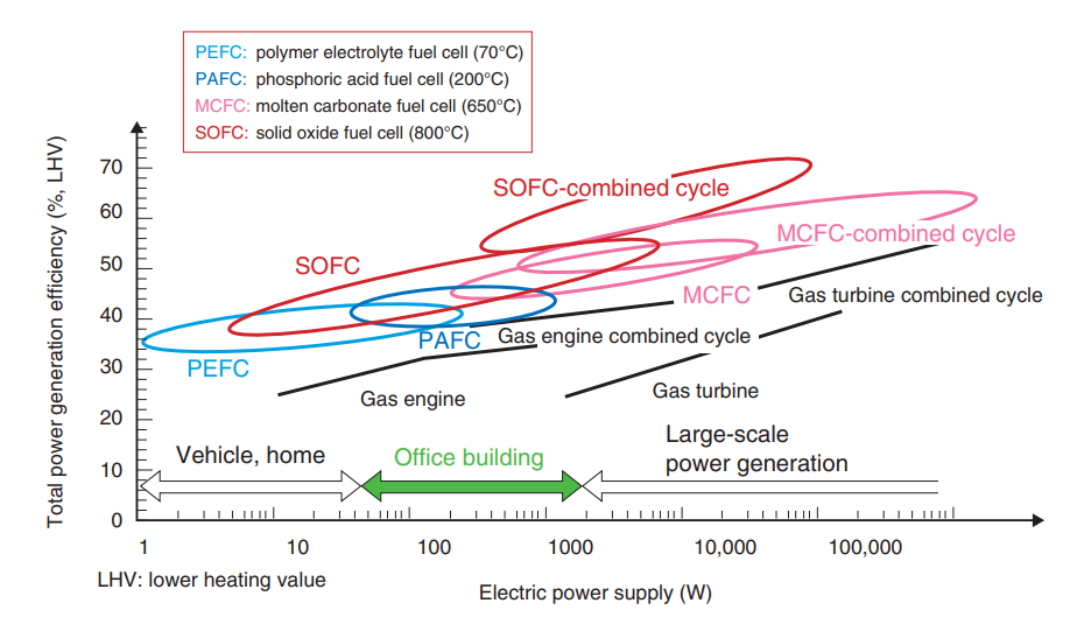


Figure 2. Comparison of the efficiency of SOFC and other energy generators [19].

The Solid Oxide Fuel Cells utilizing H₂ as a feedstock material are quite well developed and 10 kW stacks can be easily purchased from commercial companies e.g. Elcogen (www.elcogen.com). The switch to other operation modes like solid oxide electrolysis (SOEC) or utilization of carbon containing fuels is still very challenging. SOCs may suffer from various degradation issues, which in the end create technical barriers and limit commercialization. Despite their high efficiency and various modes of operation the factors such as relatively high cost, ohmic losses, sluggish catalytic activity for specific processes, high operation temperature, issues of safety and insufficient life span cause concerns around SOC technology [20].

The cells, on shell level, are composed nearly fully of ceramic or ceramic-metallic materials in the form of either dense or porous layers. Monolithic construction is considered a positive aspect of this technology, but the structural complexity may be also a source of problems.

To better visualize the issues in SOCs, the causes of ceramic electrode failures were analyzed using an Ishikawa 'cause and effect' diagram (Fig. 3). Contributing factors of the degradation were categorized and included under the names 'Operation', 'Material', 'Environment', and 'Fuel'. 'Operation' encompasses failures occurring during the SOFC's operational phase, while 'Environment' covers failures during storage or non-operational periods. The 'Fuel' category addresses degradation due to fuel impurities, and the 'Material' category focuses on purely material degradation.

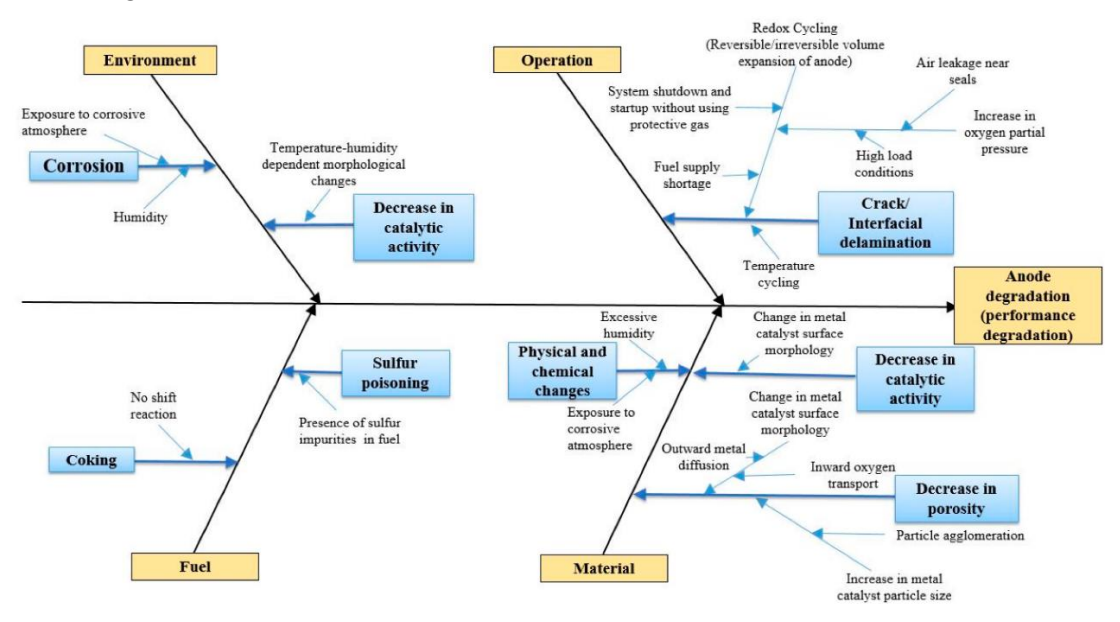


Figure 3. Ishikawa diagram describing degradation issues in SOCs [21].

The 'Material' category identifies the degradation mechanisms that compromise the electrode structure and functioning that lead to SOC failure. Alterations in constituent materials' properties directly affect performance. The primary causes of degradation are a decrease in electrode porosity and a reduction in the catalytic activity of the metal in the hydrogen electrode. Metal catalyst surface morphology can be altered by thermal metal diffusion and oxygen activity changes across the electrode. Moreover, morphological and phase changes within the material itself are critical failure factors. They often result from exposure to excessive humidity or corrosive environments (e.g., fuel volatile impurities). These physical and chemical changes severely undermine the electrode's structural integrity, consequently impairing performance.

A wide range of studies, research, development, and demonstrations have been undertaken in recent years to improve the performance of SOCs. These efforts have led to the implementation of different SOC designs, often involving the use of new materials replacing the old solutions. To address the issues limiting the wide usage of SOCs, a new line of functional materials has to be introduced, or the microstructure of the conventional components needs to be redesigned. It is a known fact that even a small change in the microstructure, composition and behavior of the inter-material interface is of crucial importance to the stability of the SOCs.

Unprecedented progress in science and technology enabled the convergence of advanced innovations and nanoscale research, marking the beginning of the nanotechnology era. Consequently, the development in nanoscience and nanotechnology have stimulated the growth of new fields, including nanocatalysis [22,23]. Nanocatalysts bring together homogeneous and heterogeneous catalysis and offer advantages in terms of selectivity, activity, efficiency, recycling, and overcome many disadvantages or limitations seen in conventional catalysts. The upsides and downsides of different catalysis approaches are summarized and presented in Table 1. The comparison corresponds only to the general characteristics of the catalysts' groups even though certain improvements were made in each field.

Table 1. Comparison of the nanocatalysis with homo- and heterogeneous catalysis. Advantages and disadvantages.

Homogeneous catalysis	Nanocatalysis	Heterogeneous catalysis
	Advantages	
High selectivity	High selectivity	High stability
High activity	High activity	Excellent accessibility
Short reaction time	High stability	Easy to separate
High efficiency	Easily recyclable	Low price
	Eco-friendly synthesis	
	Energy efficient	
	Economically viable	
	Disadvantages	
Difficult to recover	Nanotoxic	High reaction times
Product contamination	Higher production costs	Lower activity per gram catalyst
Lower recyclability		Lower selectivity

The excellent activity of nanocatalysts lies in the large surface area to volume ratio. Enormous specific surface area of nanoparticles has a straightforward beneficial influence on the reaction rates. At the same time the intrinsic properties of the nanoparticles affect the activity and selectivity. A proper control over the size, bond lengths, crystal lattice orientation and surface termination is crucial in obtaining useful nanocatalyst [23,24].

For decades noble metals were widely used for the preparation of the catalysts due to their high activity and outstanding stability. However, the price of noble metals is one of the main factors that may prevent usage on an industrial scale. Therefore, cheaper compounds with a beneficial role are implemented in the catalyst studies. Transition metals are a great alternative to noble metals for the catalysis of various reactions. High activity and much lower price are the main driving forces towards the fast development of their high-scale usage. Although there are many advantages, transition metals are usually less active and not so resistive to deactivation compared to e.g., Pt, Ru or Pd [25,26]. One of the solution to the mentioned problem may be the

addition of promoter oxides or active support oxides such as VO_x, CeO₂, MgO and La₂O₃, which affect the electron mobility, crystal texture, metal dispersion, and thermal stability of the catalysts [27]. As a result, they can provide some anti-sintering [28] and anti-coking [29] properties, as well as increased sulfur poisoning resistance [30] of the material.

Beyond stabilization, support may enhance the activity of the metallic nanoparticles by synergistically interacting with their surfaces and actively taking part in the reaction. This behavior is analogous to the synergistic effects observed in alloys formed between intermixed transition metal atoms, where the addition of other metal highly increased the usability of the catalyst. Thus, catalytic powders are not only limited to the monometallic nanoparticles supported on the oxides, but they extend towards binary or even ternary systems. The complexification of the nanocatalysts brings superior properties unfamiliar to the singular elements themselves [31]. These are, so called, synergistic effects.

Despite the positive aspects described above, nickel is still the most widely used metal in industrial catalysis due to its low price and good activity. Unfortunately, as a non-selectively active catalyst, it suffers from e.g. carbon deposition and formation of volatile carbonyl compounds in the presence of CO. What is more problematic, the high tendency towards agglomeration and sintering results in low stability. These issues were previously solved to some extent by e.g. addition of Co into nickel catalyst and formation of Ni–Co alloys. The binary system came out as less susceptible for coking [32,33]. It can be clearly assumed that properties of different individual metals are able to merge and influence the final catalytic activity and stability. The study of the dependencies between the metals concerning their synergistic effects gave a strong background for further studies over mono- and bimetallic catalysts.

According to the literature findings [34,35], specific modification can influence greatly the characteristic parameters of operating catalyst. The reported effect of adding second metal to fabricate bimetallic particles could be classified into 3 groups:

- (i) modifying catalyst selectivity,
- (ii) increasing catalyst activity or
- (iii) improving catalyst stability.

The alloys of catalytic metals very often increase the activity by inducing hydrogen spill-over process, where one metal is helping the second one to reduce it more easily. Another mechanisms were ascribed to metal-metal interactions, which were divided into 5 different phenomena [25,36]:

- 1. Geometric effect second metal alters the geometry of active sites distributes on primary metal,
- 2. Electronic effect promoter metal is changing the electron properties of the active sites comprised of active metal by electron transfer,
- 3. Stabilization effect the addition of promoter metal improves the stability of active metal by e.g., reducing the sinterability or suppressing coke deposition,
- 4. Synergistic effect two metal components are taking active part in bonding reaction intermediates,
- 5. Bi-functional effect each metal takes care of different process in the same overall reaction mechanism (increasing the rate of slow processes that monometallic catalyst would suffer from).

The representation of metal-metal effects in Ni-Fe catalysts used in methane steam reforming was schematically presented in Fig. 4.



Figure 4. Schematic presentation of steam reforming over Ni-Fe catalytic alloys. Synergistic effect in (b) Ni-rich Ni-Fe alloy [37].

According to these interactions, bimetallic particles have triggered an interest in the field of catalysis. Starting from noble alloys such as Pt-Pd, Pd-Ru or Pt-Ru [38,39], through mixed alloys of noble metals and transition metals (e.g. Pt-Ni, Ru-Ni [40]) development is being oriented more and more strongly towards fully non-noble metals. The highly active Ni–Co/YSZ catalyst for bioethanol reforming has been prepared by C. Resini *et al.* [41], which was characterized by 65% yield of H₂ at low temperature of 670 K. The addition of Co into Ni resulted in the inhibition of the dehydration reaction as well as of methane production. Promising results were also presented by G. Garbarino *et al.* [42], whose group prepared Ni_{0.25}Co_{0.75} NPs for direct EtOH steam reforming resulting in 100% conversion of ethanol and the yield of H₂ equal to 87%. Their study revealed that activity strictly depends on the composition of the bimetallic nanoparticles. The group of M. Wang *et al.* [43], as one of the few, tested Ni exsolved from La_{0.8}Ce_{0.2}Mn_{0.6}Ni_{0.4}O₃ impregnated after with CuO and reached around 90% conversion of ethanol followed by increased chemical stability and limited carbon deposition. The results presented by K. M. Kim *et al.* [44] concerning Ni-Fe/Al₂O₃ catalysts for propane steam reforming revealed that using Ni_{0.8}Fe_{0.2} alloy

allowed to obtain 86% H₂ selectivity at 700 °C. The addition of Fe also suppressed the carbon formation.

It is obvious that nanostructuring of the electrodes, a selection of the proper support oxides, and harnessing the positive aspects of the synergistic effects between various metals is a key to improving chemical and electrochemical activity of the materials used in SOCs. Despite some research already done in this field, many promising bimetal compositions were poorly or not studied up to date. Even though some high activity and good selectivity catalysts were presented, the mechanisms of enhancement, technological aspects, and long-term stability should be more intensively studied. Looking at available scientific reports it is clearly visible that the subject of catalysts and nanocatalysts is cutting-edge, but there is still a lack of systematic research. Due to this fact, the subject of the presented thesis can generate a huge scientific impact on the field of material science as it will provide a wide spectrum of experimental data describing new groups of nanostructured materials introduced into SOC technology. The state-of-the-art research is following a trend towards finding new, eco-friendly, and cheap substitutes for noble metals and their mixtures. Transition metals, even though they are less stable and active, are characterized by the way lower prices and limited impact on the environment. Finding the best way to utilize the potential of nanostructuring will ensure the transition metal-based catalysts to increase the technological value of SOC technology for wider use.

1.3 Hypotheses and objectives of the thesis

The research presented in this thesis focuses on the design of the fabrication routes of the nanostructured catalysts to be utilized in Solid Oxide Cells (SOCs) working mostly under the electrolysis of CO₂-H₂O mixture with subsequent production of syngas or hydrocarbons such as methane. The study investigated the influence of the preparation routes on the chemical activity of the nanocatalysts with a focus on the constructive and strong integration of metallic particles with oxide support. The synergistic effects of the transition metal were utilized to influence the rates of the reactions in SOCs omitting the usage of noble metals. The work aimed to visualize the positive aspects of introducing nanoobjects and support the claims about the possibility of increasing stability via nanostructuring.

Main hypotheses on which the research was conducted in the topic were as follows:

- 1. It is possible to fabricate nanoparticles strongly bound to the substrate through easy, scalable wet chemistry methods.
- 2. It is possible to increase the efficiency of SOCs thanks to synergistic effects of two transition metals coexisting in fuel electrode.
- Nanostructuring of the fuel electrode increases metal-oxide interactions and increases its lifespan.

Main aim of the work was to introduce nanostructured materials into Solid Oxide Cells without the usage of noble metals to increase the chemical and electrochemical efficiency of these devices along maintained stability. To reach the main aim a series of secondary milestones had to be accomplished:

- Novel route of fabrication of the nanometric metal-oxide catalysts is formulated through the utilization of the wet chemical synthesis methodology
- New materials are tested in simulated conditions before the application in SOCs
- Most promising catalytic materials are introduced into SOCs via commercially viable technological processes
- The influence of the composition and fabrication technique on the efficiency and stability of SOCs are determined
- Mechanisms of increased efficiency are properly described

By these means, the results presented in this thesis are cutting-edge and can influence the research field by giving out a wide spectrum of fundamental data in the field of materials engineering on the topics dealing with the SOCs technologies involving new materials or efficiency boosters. The findings described in this thesis illustrate the methodology of the preparation of the novel catalytic materials via easy and scalable techniques giving out outstanding increase in performance of the SOCs. This enhancement is also deeply explained in terms of the mechanistic view on the catalytic processes occurring inside the cells.

This dissertation was divided into two major parts: theoretical and experimental. In the theoretical section (Chapter 2) the author described the fundamental information about the chemistry and electrochemistry in Solid Oxide Cells (SOCs) emphasizing various modes of operation, materials used for construction and degradation issues. In the experimental section (Chapter 3) the methodology was described in detail and the results of the research were introduced and deeply analyzed in Chapter 4. Chapter 5 contains the summary and remarks of the study. Additionally, the dissertation contains the list of mathematical symbols and abbreviations, literature, scientific achievements of the author, followed by the lists of figures and tables.

2. THEORY OF THE CHEMISTRY AND ELECTROCHEMISTRY IN SOLID OXIDE CELLS

2.1 Introduction to Solid Oxide Cell (SOC) technology

A fuel cell is a device that converts fuel, usually hydrogen, into electricity and heat via direct electrochemical reaction. Its working principles are in opposition to e.g. thermal generators, which involve first the combustion of the fuel, then the heat is transformed into mechanical energy and finally into electrical energy [45]. In contrast to thermal engines, fuel cells enable direct energy conversion, typically resulting in higher efficiency. When operating on hydrogen, fuel cells produce no greenhouse gases such as CO₂, nor pollutants like CO, NO_x, or SO_x, the only byproduct is water. They also offer excellent scalability, from kilowatt (kW) to megawatt (MW) ranges, simply by adjusting system size, and maintain high efficiency even under partial load conditions [46]. Moreover, unlike batteries, their operating time is not limited, as it depends on the size of the fuel reservoir, which can be also rapidly restocked. Solid Oxide Cells (SOCs) are generally composed of three fundamental components: a dense ceramic electrolyte, a fuel (hydrogen) electrode, and an air (oxygen) electrode. SOCs can operate either in fuel cell mode (Solid Oxide Fuel Cell), when generating electricity and heat, or in electrolysis mode (Solid Oxide Electrolysis Cell), where the excess energy can be transformed into chemical fuel. The role of the electrodes is determined by the direction of operation. Specifically, the air electrode acts as the cathode during SOFC operation and as the anode during SOEC operation, while the fuel electrode serves as the anode in SOFC mode and the cathode in SOEC mode [47].

SOCs are further classified based on the type of charge carriers transported through the impermeable electrolyte, that separates two electrodes. Oxygen-ion-conducting SOCs (O-SOCs) utilize electrolytes that facilitate O²⁻ movement, while proton-conducting SOCs (H-SOCs) employ proton-conducting ceramic electrolytes that enable the transport of H⁺ ions across the cell. A schematic diagram of the working principle of SOCs in fuel cell and electrolysis mode are depicted in Fig. 5.

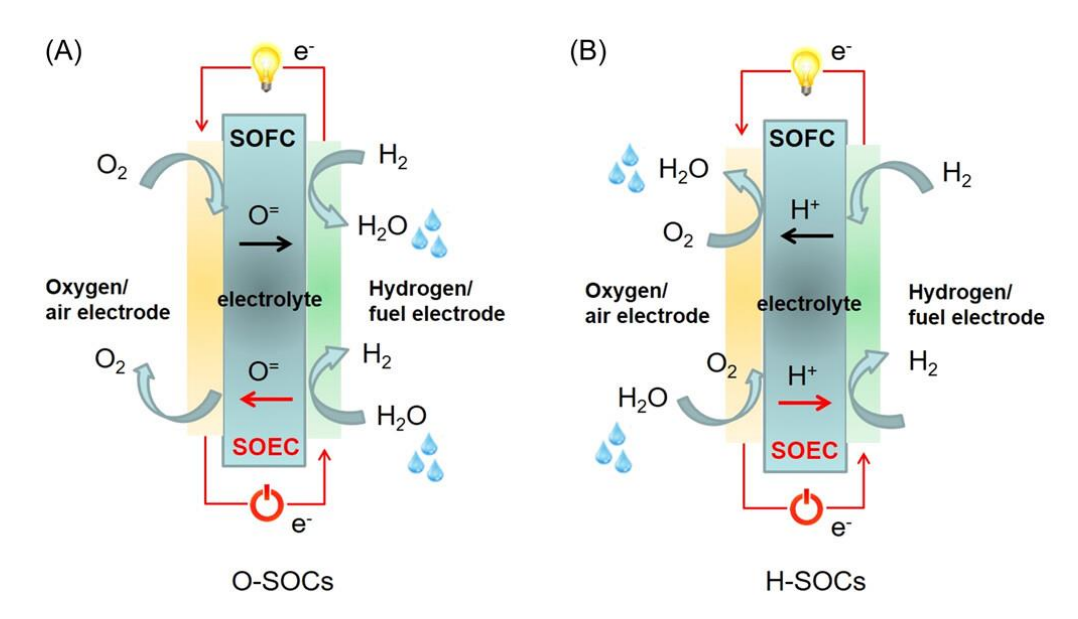


Figure 5. Schematic representation of the working principle in (A) O-SOC and (B) H-SOC [48].

In oxygen ion-conducting SOCs operating in fuel cell (SOFC) mode, hydrogen (or other fuel) is oxidized at the fuel electrode, releasing two electrons and forming hydrogen ions (H^+). Simultaneously, oxygen is adsorbed, dissociated, and reduced to oxygen ions (O^{2-}) at the air electrode. The electrons for the reduction come from the fuel electrode via the external circuit. Supplying hydrogen to the fuel side and oxygen to the air side of the cell generates a chemical potential between these regions. This oxygen partial pressure (pO_2) gradient drives the ions through the electrolyte to the fuel electrode, where they react with H^+ ions to form water. This flow of charge carriers generates electricity and power in the external load. The driving force of this process is strictly connected to lower Gibbs free energy of the water molecules compared to both H_2 and O_2 supplied to the cell.

In SOEC mode, an external power source pumps electrons to the fuel electrode, electrochemically splitting steam into H_2 and oxygen ions. The O^{2-} are then transferred through the electrolyte to the oxygen/air electrode, undergo oxidation, and oxygen is released. This mode of operation is also known as high-temperature steam electrolysis.

The reactions that take place at the air and fuel electrodes in SOFC and SOEC modes of O-SOC are as follows:

1) For SOFC

O₂ reduction at air electrode
$$\frac{1}{2}O_2 + 2e^- \rightarrow O^{2-} \tag{1}$$

$$H_2$$
 oxidation at fuel electrode $H_2 + O^{2-} \rightarrow H_2O + 2e^-$ (2)

Overall reaction in SOFC
$$H_2 + \frac{1}{2}O_2 \rightarrow H_2O$$
 (3)

2) For SOEC

O₂ evolution at air electrode
$$O^{2-} \rightarrow \frac{1}{2}O_2 + 2e^-$$
 (4)

$$H_2O$$
 reduction at fuel electrode $H_2O + 2e^- \rightarrow H_2 + O^{2-}$ (5)

Overall reaction in SOEC
$$H_2O \rightarrow H_2 + \frac{1}{2}O_2$$
 (6)

The processes in the H-SOCs are similar, the only difference lies within the type of charge carriers transported through the electrolyte, which are H⁺ ions instead of oxygen ions for protonic cells. This type of cells is also widely studied and is emerging as a promising alternative to O-SOCs for intermediate temperature range operation (550-700 °C) [49] but will not be covered in this dissertation.

Among various types of electrochemical energy devices, SOCs are one of the most promising solutions for future use as a green power system from both material point of view and thanks to the features that make them unique, such as:

- high conversion rates and high efficiency of electricity generation, regarding the ratio of energy output to fuel input,
- good fuel flexibility,
- simple design,
- fully solid construction with no moving parts susceptible to wear and failure,
- low noise levels during operation,
- possibility to cogenerate heat and high purity steam,
- emission of no harmful byproducts,
- eliminated usage of precious metals,
- low CO₂ emission,
- operation without the use of liquid and corrosive electrolytes,
- reasonable manufacturing costs.

The basic SOC is the electrolyte sandwiched between the porous electrodes. This construct is conventionally assembled via sintering into a layered structure. SOCs are typically classified into four main designs depending on the fuel and air supply methods: planar, tubular, flat tubular, and monoblock-layer build-type (MOLB-type). The listed design types are presented in Fig. 6.

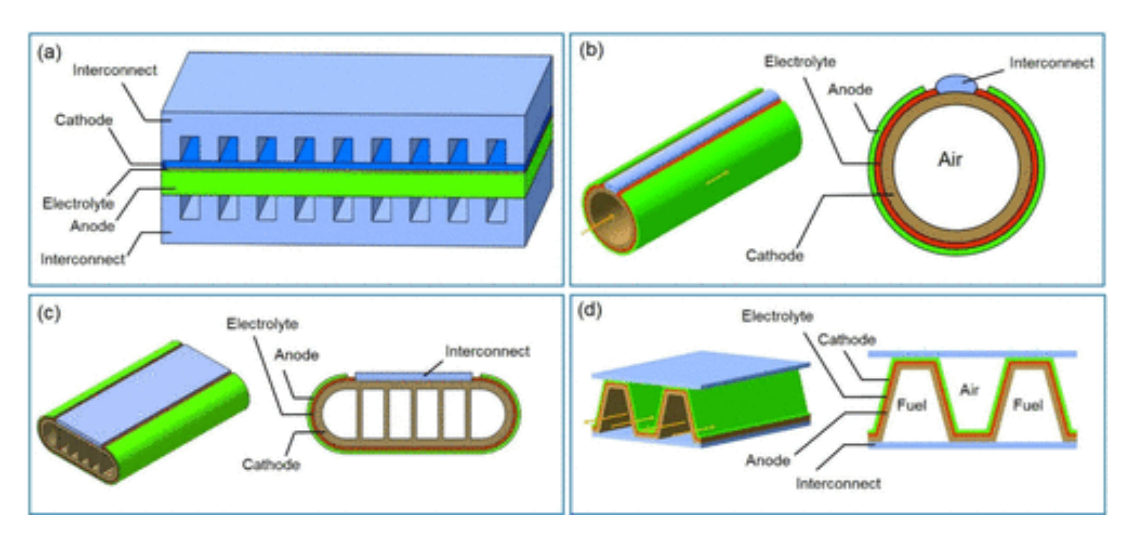


Figure 6. Representation of different SOFC structures. (a) planar structure; (b) tubular structure; (c) flat tubular structure; (d) MOLB-type structure [50].

Planar SOCs offer advantages such as straightforward fabrication, low production cost, and high-power density. As a downside, they require good sealing, which may pose an engineering challenge [51]. Despite that, planar configurations currently dominate stationary power generation applications. In contrast, tubular SOCs structure provides high mechanical strength and simple gas sealing but the cells suffer from lower performance due to high ohmic losses. The tubular SOCs are also associated with relatively high manufacturing costs [52]. To combine the advantages of both designs, a novel flat-tubular SOFC architecture was introduced. It is still under research but achieving quite high power densities under elevated operating temperatures [53]. Inspired by the planar configuration and 3D modelling, MOLB-type SOFCs have also emerged. These cells feature the structure of wavy planar cells, which increases the effective active area of the working electrodes, minimizes internal stress and resistance, increases volumetric power density, and eliminates the usage of glass and high temperature sealing materials that may contaminate the cell. Unfortunately, the complexity of their fabrication process remains a significant downside and lowers the commercial viability [50,54].

2.2 Thermodynamic principles of SOC operation

The overall chemical reaction involved in a SOC is given below in Eq. 7:

$$H_2O \leftrightarrow H_2 + \frac{1}{2}O_2 \tag{7}$$

From left to right it describes the SOEC mode and from right to left the SOFC operation. Knowing the reaction, it is possible to calculate the theoretical voltage of electrochemical cells. This reversible voltage is taken from the change of enthalpy, Gibbs free energy and entropy of the progressing reaction. These parameters are linked together as shown in Eq. 8:

$$\Delta H = \Delta G + T \Delta S \tag{8}$$

This is why:

$$\Delta G = \Delta H - T \Delta S \tag{9}$$

where ΔH is the change of enthalpy during the reaction (J·mol⁻¹), ΔG is the change of Gibbs free energy (J·mol⁻¹), T is the temperature (K) and ΔS is the change of entropy (J·mol⁻¹K⁻¹). Gibbs free energy stands for reversible work delivered by the SOFC or demanded for the electrolysis in SOEC and T ΔS is the heat that is released to the environment in fuel cell mode or utilized for the electrolysis. The values of those parameters in standard state can be computed or retrieved from the databases for produced water in both liquid and gas phase [55]. The values are listed in Tab. 2 and Tab. 3.

Table 2. Reaction enthalpy, reaction entropy and Gibbs free energy for H₂ oxidation reaction (water in liquid phase, minus sign for SOFC, plus sign for SOEC) [55].

$H_2O_{(l)}$	$\Delta H^0_{25^oC} \ (J \cdot mol^{-1})$	$\Delta S_{25^{\circ}C}^{0} \ (J \cdot mol^{-1}K^{-1})$	$\Delta G_{25^{o}C}^{0} \ (J \cdot mol^{-1})$
SOFC/SOEC	±285800	±160	±237100

Table 3. Reaction enthalpy, reaction entropy and Gibbs free energy for H₂ oxidation reaction (water in gas phase, minus sign for SOFC, plus sign for SOEC) [55].

$H_2O_{(g)}$	$\Delta H^0_{25^oC} \ (J \cdot mol^{-1})$	$\Delta S_{25^{\circ}C}^{0} \ (J \cdot mol^{-1}K^{-1})$	$\Delta G_{25^{o}C}^{0} \ (J \cdot mol^{-1})$
SOFC/SOEC	±241800	±44	±228600

A negative value of ΔH° at 25 °C in SOFC mode indicates that the reaction is exothermic, meaning it releases heat, similarly to all fuel oxidation reactions in conventional power devices. On the other hand, in electrolysis mode, the reaction is endothermic and absorbs heat from the surroundings [55]. The enthalpy change for the hydrogen oxidation reaction, when water forms in the liquid state, represents the higher heating value (HHV) of hydrogen. It reflects the total energy yield, including the heat from steam condensation. If water remains in the gaseous phase, the corresponding enthalpy change is known as the lower heating value (LHV), which is lower since it excludes the latent heat of condensation [55,56].

For Gibbs free energy, a negative value signifies that the reaction is spontaneous. Regarding standard conditions, the redox potential is negative in fuel cell mode and positive in electrolysis mode, yet both correspond to the same absolute potential value according to Eq. 10:

$$E_{25^{\circ}C}^{0} = \mp \frac{\Delta G_{25^{\circ}C}^{0}}{2F} = 1.23V \tag{10}$$

Where, number 2 comes from the number of electrons involved in the reaction per 1 molecule of H₂ and F is the Faraday constant (96485 C·mol⁻¹).

However, SOCs operate at temperatures higher than room temperature, and thus, according to the Eq. 9. Gibbs free energy decreases when the temperature rises. Furthermore,

enthalpy and entropy are also lowered at higher temperatures. This is why the standard state potential as a function of the temperature is expressed using Eq. 11:

$$E_T^0 = \mp \frac{\Delta H_T^0 - T\Delta S_T^0}{2F} \tag{11}$$

At 700 °C, which is quite a common temperature where SOC operates, the standard state potential is given by:

$$E_{700^{\circ}C}^{0} = -\frac{-247543 J \cdot mol^{-1} + 973.15 K \cdot 54.7 J \cdot mol^{-1} \cdot K^{-1}}{2 \cdot 96485 C \cdot mol^{-1}} = 1.01V \quad (12)$$

The lowering of potential due to high operating temperature is overcome by increased electrode activity, which enhances efficiency and allows for greater fuel flexibility. Additionally, the lower potential in electrolysis mode means that less electrical energy is required [57]. Furthermore, in both fuel cell and electrolysis modes, integration into a combined heat and power (CHP) system is feasible [58].

Along the thermodynamic parameters the concentration of the species in SOC is important. To take them into account, the Nernst potential is used to calculate the reversible potential at steady state according to Eq. 13:

$$E_T^{Nernst} = E_T^0 + \frac{RT}{2F} \ln \left(\frac{a_{H_2} \cdot a_{O_2}^{\frac{1}{2}}}{a_{H_2O}} \right)$$
 (13)

Here, R is the ideal gas constant (8.31 J·mol⁻¹K⁻¹), and a_j^i represents the chemical activity of component j raised to the power of i, its chemical reaction stoichiometric coefficient. For gases, the activity is defined as the partial pressure p_j divided by the standard pressure p_0 . The partial pressure can also be expressed in terms of the molar fraction x_j following Eq. 14:

$$a_j = \frac{p_j}{p_0} = \frac{x_j \cdot p_{total}}{p_0} \tag{14}$$

where p_{total} is the pressure of the mixture. In case of working SOC there are two different mixtures denoted as p_{fe} and p_{ae} , where first one corresponds to fuel electrode chamber and the second one to air electrode atmosphere, respectively. Thus, the Nernst potential can be expressed using Eq. 15:

$$E_T^{Nernst} = E_T^0 + \frac{RT}{2F} \ln \left[\frac{x_{H_2} \frac{p_{fe}}{p_0} \cdot x_{O_2}^{\frac{1}{2}} (\frac{p_{ae}}{p_0})^{\frac{1}{2}}}{x_{H_2O} \cdot \frac{p_{fe}}{p_0}} \right] = E_T^0 + \frac{RT}{2F} \ln \left[(\frac{x_{H_2} \cdot x_{O_2}^{\frac{1}{2}}}{x_{H_2O}}) \cdot (\frac{p_{ae}}{p_0})^{\frac{1}{2}} \right]$$
(15)

As steam is not present in the gases fed to the fuel electrode the resultant Nernst potential is infinite. If the assumption is made that the feeding stream contains 1% of H_2O , air $(21\% O_2)$ is delivered to the air electrode and the pressure at the air electrode is atmospheric equal to 1 bar

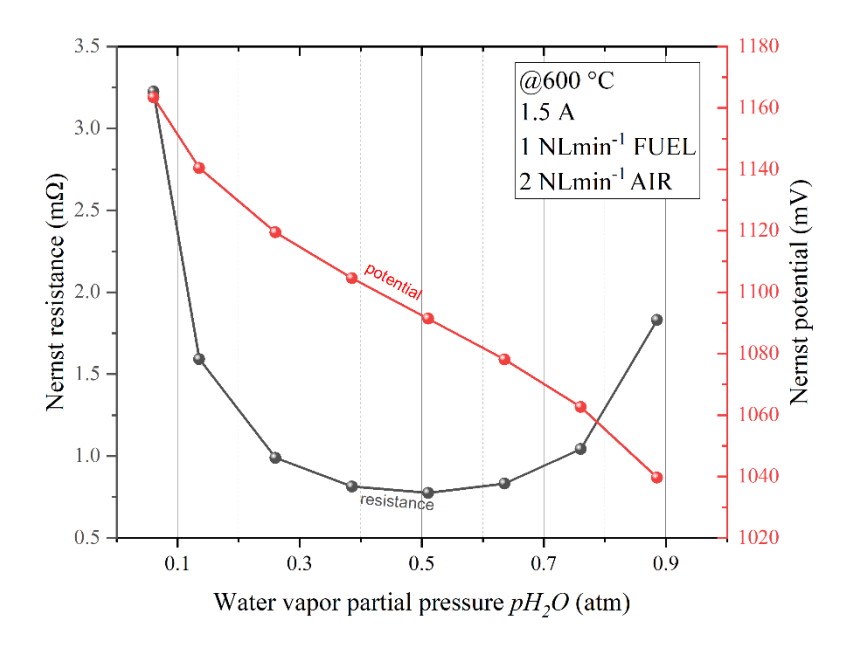


Figure 7. Representation of the Nernst resistance and the potential changes vs. water partial pressure in fuel feed stream [59].

then the voltage will be 1.17 V. This indicates an increase in potential by 0.16 V. In case of low amounts of steam high present and concentration of at the air oxygen electrode the Nernst potential will be higher. When the concentration of the gases drops, the voltage will decrease, what is observed

during the operation of the cells. It is visible in the calculations made using MATLAB environment while studying the large-scale cells working at 600 °C (Fig. 7.) and described in the publication [59] **Blaszczak P.**, Mäkinen P., Mroziński A., Ducka A., Jasiński G., Himanen O., Jasiński P., *Uncovering the electrochemical processes and understanding the causes of the degradation via EIS-DRT in large-scale Solid Oxide Fuel Cell*. Appl Energy 2025;393. 10.1016/j.apenergy.2025.125983.

2.3 Efficiency and thermal balance of SOC

In reality, the voltage values calculated using previously described equations consider ideal Solid Oxide Cell operating at high temperatures. In SOFC mode, during practical operation under load conditions, the measured terminal voltage is invariably lower than the OCV. This discrepancy arises from kinetic limitations associated with a variety of electrochemical and mass transport processes occurring at the air electrode, fuel electrode, and electrolyte interfaces. The aggregate effect of these phenomena is commonly referred to as polarization or overpotential, which fundamentally lead the deviation of the cell voltage from its theoretical maximum.

Losses in SOCs, including fuel cells and electrolysis cells, can be divided into three major groups. The first one considers ohmic losses (η_{ohm}) caused by electrical current flowing through the cell that is characterized by nonnegligible electrical resistance. This includes the resistance of the electrode material, the electrolyte, and interconnecting elements (current collectors).

Secondly, there are polarization losses (η_{act}), coming from electrochemical reactions and/or mass transfer limitations at both electrodes. And lastly, the concentration overpotential (η_{con}), which arises when the concentration of reactants changes strongly along the length of the cell during operation. The resulting overpotential in fuel cell mode is due to a lower hydrogen concentration in the middle of the cell compared to the inlet due to the oxidation to steam in an active layer close to the electrolyte. Conversely, in electrolysis mode, the increasing hydrogen concentration along the cell causes a rise in voltage. These losses are particularly significant near the cell outlet (where the fuel composition is hardly different from the inlet) or under high current densities, where reactant concentrations are generally lower. Both issues should be addressed and minimized to obtain the highest power from the cell. The representative view on the exemplary iV curve of the SOFC and SOEC are presented in Fig. 8.

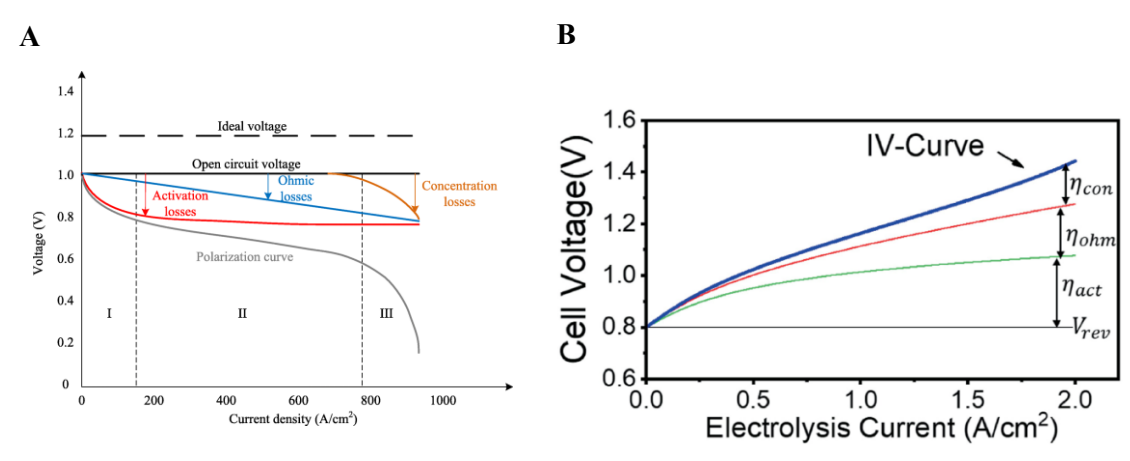


Figure 8. Voltage losses on polarization curves of an operating SOC in (A) SOFC mode [60] and (B) SOEC mode [61]. V_{rev} – reversible potential

The effects of the existence of those three overpotentials are easy to distinguish in polarization curve of SOFC. Activation, ohmic, and concentration losses predominate in the zones I, II, III, respectively.

The actual voltage of the cell in SOFC mode can be defined as [55]:

$$U_{SOFC} = E_T^{Nernst} - \eta_{act} - \eta_{ohm} - \eta_{con}$$
 (16)

And in SOEC mode:

$$U_{SOEC} = E_T^{Nernst} + \eta_{act} + \eta_{ohm} + \eta_{con}$$
 (17)

In that sense the efficiency of the fuel cell in galvanic mode is given as [55]:

$$\eta_{SOFC} = \frac{P_{electrical}}{P_{chemical}} = \frac{U_{SOFC} \cdot I}{\Delta H_{25^{\circ}C}^{0} \cdot \dot{N}_{H_{2}}^{in}}$$
(18)

And in electrolysis:

$$\eta_{SOEC} = \frac{P_{chemical}}{P_{electrical}} = \frac{\Delta H_{25^{o}C}^{0} \cdot N_{H_{2}}^{\dot{o}ut}}{U_{SOEC} \cdot I}$$
(19)

where I – the current (A), $N_{H_2}^{in}$ – the inlet molar flow rate of hydrogen, and $N_{H_2}^{out}$ – the molar flow rate of produced hydrogen. These two values of molar flows are proportional to the current flowing through the cell as in Eq. 20

$$N_{H_2}^{burned} \text{ or } N_{H_2}^{in} = \frac{I}{2F}$$
 (20)

where $N_{H_2}^{in} = N_{H_2}^{burned}$ in the even of 100% fuel utilization. Considering Eq. 18-19 and Eq. 20 the efficiencies (for 100% utilization situation) can be expressed as follows:

$$\eta_{SOFC} = \frac{U_{SOFC}}{\frac{\Delta H_{25^{\circ}C}^{0}}{2F}} \tag{21}$$

and

$$\eta_{SOEC} = \frac{\frac{\Delta H_{25^{o}C}^{0}}{2F}}{U_{SOEC}} \tag{22}$$

when $N_{H_2}^{out} = \frac{I}{2F}$

The term $\frac{\Delta H_{25}^0 o_C}{2F}$ is known as the thermoneutral voltage – denoted hereafter as E_{ThN} . It carries a negative sign in SOFC mode and a positive sign in SOEC mode, though in both cases it results in a positive value. While this term does not represent a physically meaningful voltage in fuel cell operation, it is a relevant parameter in electrolysis mode. In both modes, however, it helps describe the system's thermal behavior. The power balance in SOFC mode, with positive values indicating inputs to the system, can be expressed as follows [55]:

$$P_{chemical} = P_{electrical} + P_{heat}$$
 (23)

while the heat produced by the fuel cell can be written as:

$$P_{heat} = P_{chemical} - P_{electrical} = \left(\frac{\Delta H_T^0}{2F} - U_{SOFC}\right) \cdot I = (E_{ThN} - U_{SOFC}) \cdot I$$
 (24)

Similarly, for SOEC mode

$$P_{electrical} = P_{chemical} + P_{heat}$$
 (25)

and

$$P_{heat} = P_{electrical} - P_{chemical} = \left(U_{SOEC} - \frac{\Delta H_T^0}{2F}\right) \cdot I = \left(U_{SOEC} - E_{ThN}\right) \cdot I \quad (26)$$

This equation highlights a key aspect of electrolysis operation: when the cell voltage is lower than the thermoneutral voltage, thus $P_{heat} < 0$, it indicates that the process absorbs heat (endothermic

process). Otherwise, when the cell voltage U_{SOEC} exceeds E_{ThN} , the system releases heat, exhibiting exothermic behavior. In the case of SOFC operation is always within exothermic range. Fig. 9 represents the exemplary polarization curve of SOC with the regions of different thermal balance pointed out.

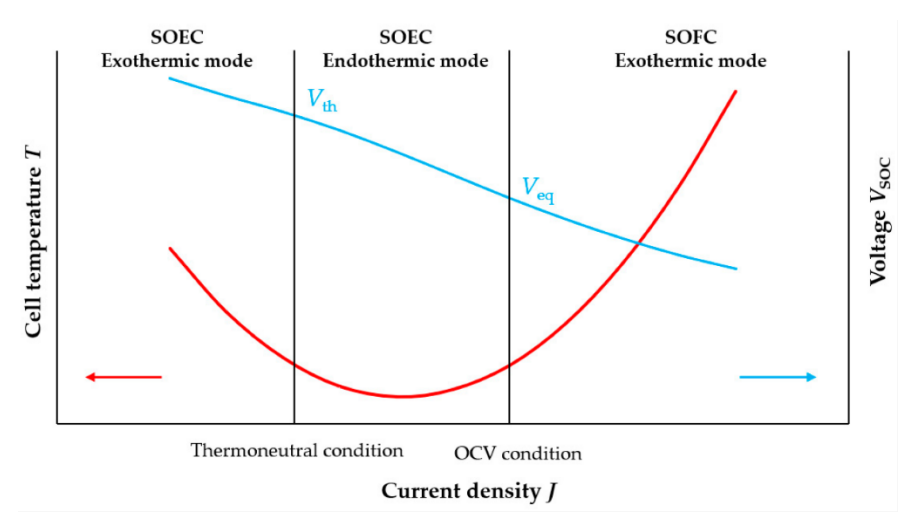


Figure 9. Thermal balance regions in SOC (adiabatic conditions). V_{th} – thermoneutral voltage, V_{eq} – steady state voltage. Image adopted from [62].

As SOCs can operate in both electrolysis and fuel cell mode it is quite interesting to introduce this technology as both energy-producing device and energy storage unit. This concept of combining both modes is called reversible Solid Oxide Cell (rSOC). Its main advantage is the ability to easily switch between both modes of operation in response to the momentary demand [63]. Even though, looking at Fig. 9, it is obvious that proper thermal management with the cell is crucial to maintain stable performance and limit the degradation connected to the thermal stresses and mechanical failure [64].

2.4 Catalysts and various processes in SOC

As shown in previous sections, Solid Oxide Cells (SOCs) may stand out as promising energy devices thanks to their high energy efficiency and robustness. Despite this, the economic competitiveness of SOC technology is currently a barrier to wider market adoption. A key strategy to improve economic feasibility is to lower the operating temperature from the high-temperature range (800–1000 °C) to intermediate temperatures (600–800 °C). Lowering the temperature offers several additional advantages: it limits strongly the degradation, simplifies sealing, and improves the response to faster start-up and reversible operation. In addition, introducing new modes of operation may increase the value of this technology. Due to the high temperature of work, it is possible to supply SOCs with fuel other than pure hydrogen. The H₂ is directly produced at the fuel electrode through e.g., catalytic cracking or steam reforming. Furthermore, the cell were tested for performing catalytic processes such as methanation [65], syngas

production [66] or direct gasification of carbon [67]. The key to success is to define proper components, designs, and structures in SOC technology. In the past 15 years, a lot of effort has been put into the development of new materials with various approaches to enhance the performance of the SOCs, especially regarding the catalytic activity improvement and the fight against instability.

2.4.1 Coelectrolysis in SOEC

The ongoing technical development and global industrialization have resulted in a growing demand for fossil fuels. At the same time, burning carbon-based fuels releases an enormous amount of carbon dioxide, which is one of the most infamous greenhouse gases. An increasing environmental awareness in society and exhaustibility of natural resources have led to the transition from conventional fuels to renewable energy sources. The reduction of carbon dioxide concentration in the atmosphere and the development of renewable energy sources are the most urgent concerns that governments and society are facing nowadays. One of the most promising methods to utilize CO₂ from burning fossil fuels is the conversion of carbon dioxide into valuable chemicals that can be subsequently used as a fuel [68–70].

An additional significant advantage of this method is providing energy storage, when the electricity supply does not match the current demand. Electrochemical reduction of CO₂ and H₂O, called coelectrolysis, is believed to be one of the most promising conversion strategies. Coelectrolysis of CO₂-H₂O could consume excess energy to efficiently produce syngas (CO + H₂), which can be further utilized by the Fischer-Tropsch process to produce synthetic fuel [70,71]. The CO₂/H₂O electrolysis may be environmentally neutral if the amount of CO₂ produced by oxidation of synthetic fuels is equal to the carbon dioxide consumed during the coelectrolysis [70,72]. The CO₂ and H₂O splitting reactions can be written as:

$$CO_{2(g)} \xrightarrow{electricity + \Delta T} CO_{(g)} + \frac{1}{2}O_{2(g)}$$
 (27)

$$H_2 O_{(g)} \xrightarrow{electricity + \Delta T} H_{2(g)} + \frac{1}{2} O_{2(g)}$$
 (28)

The splitting of CO₂ and H₂O requires energy due to the endothermic properties of the aforementioned reactions [73], which can be delivered as electrical or thermal energy. The total energy demand of both processes at standard pressure is depicted in Fig. 10. As one can see, the total energy input can be separated into electricity demand and heat demand. With increasing temperature, the need for electrical energy decreases, which is the driving force behind the use of SOEC technology in CO₂ electrolysis.

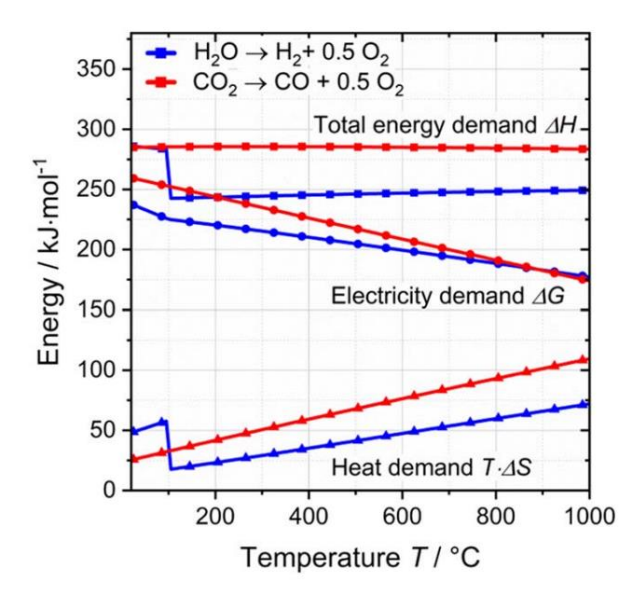


Figure 10. Energy demand of the H₂O and CO₂ electrolysis reactions depicting the total energy needed with an indication of the electricity demand and the heat demand [73].

Furthermore, wet CO₂ electrolysis has a lower activation energy than dry, in lower resulting polarization resistance and overpotential compared to dry carbon dioxide electrolysis [70,74].Another significant disadvantage of dry electrolysis of CO₂ is the high risk of carbon deposition on the cell, leading to degradation. material Despite reactions (27) and (28), a Reverse Water-Gas Shift (RWGS) reaction occurs, in which carbon dioxide is converted into carbon monoxide, according to the reaction:

$$CO_{2(g)} + H_{2(g)} \leftrightarrow CO_{(g)} + H_2O_{(g)}$$
 (29)

As one can already see, the coelectrolysis of CO₂/H₂O is a complicated process, mostly due to the involvement of multiple gases [68,70]. To determine the overall syngas production, both the electrolysis processes and the RWGS must be properly quantified. The contribution of the RWGS reaction to the total amount of CO was found to depend on the temperature, the voltage applied, and the composition of the inlet gases [70]. Ni *et al.* [75] has proven that at high cell voltages carbon (II) oxide may be consumed by the RWGS reaction, while at low voltage it is produced significantly. However, the total contribution of RWGS in CO production is still questionable [71]. Some studies show that CO production mostly relies on the electrolysis process and RWGS has a small contribution [71,76,77]. At the same time, other studies show that a significant amount of carbon monoxide is produced via RWGS [78–80].

The CO₂/H₂O electrolysis might be performed in the Solid Oxide Electrolysis Cells (SOEC), which have been intensely developed within the last decade [81]. The schematic view on the utilization of the SOEC to perform the coelectrolysis process is depicted in Fig. 11.

Despite the usage of state-of-the-art materials for SOECs, many studies focused on the different materials with respect to their influence on the outcome of the coelectrolysis and RWGS processes. Ebbesen *et al.* [77] analyzed the Ni/YSZ electrode and stated that CO production occurs

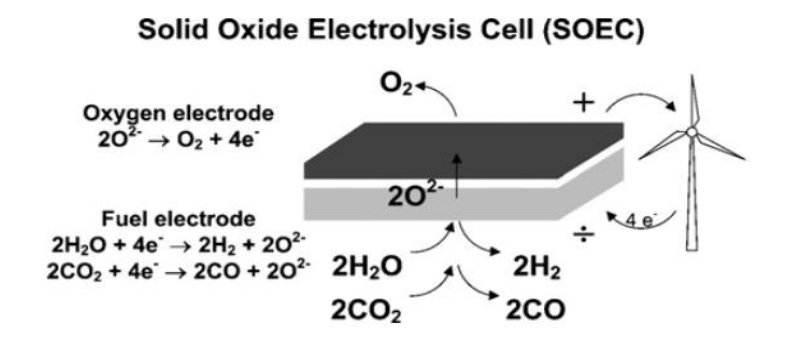


Figure 11. The design and working principles of Solid Oxide Electrolysis

Cell (SOEC) [82]

predominantly through the RWGS process. Research of Ioannidou *et al.* [71] focused on the modifications of Ni/CGO with Au/Mo/Fe. It has been proved that Fe/Mo modification enhances CO production, while Au works as an inhibitor of RWGS. In general, coelectrolysis and RWGS reactions may be affected by the structural characteristics of the electrodes (specific surface area, porosity, particle size, conductivity) or by operating conditions such as gas composition, temperature, or applied voltage [71].

2.4.2 Methane reforming and synthesis

Sustainable production of energy is a significant challenge for our society. Food, fuel and chemical industries need to follow the increasing demands of a fast-growing population. Despite

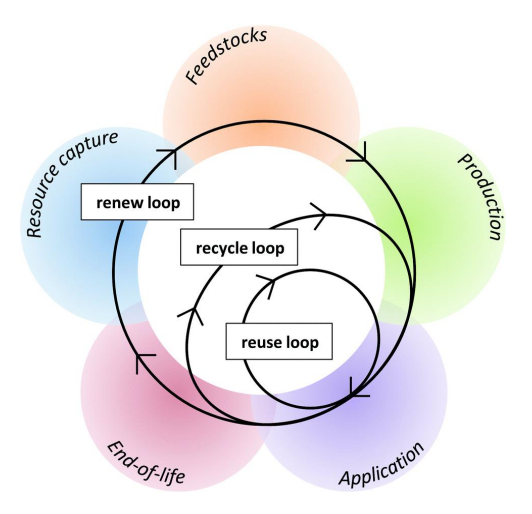


Figure 12. Schematic view of the circular economy concept [83].

this, a lot of pollutants are being released every day into the atmosphere and water, what can finally cause serious human health issues and irreversible environmental destruction. One of the solutions to the problems mentioned is the idea of circular economy (Fig. 12.) [84]. This strategy puts away the most common "direct" economy, which relay on transformation of feedstock material followed by discarding by-products. It describes the system that can utilize the waste generated from other processes and greatly limit our dependency on natural

resources. Those changes in feedstock to be used raise the need to develop new catalytic materials and introduce new technologies able to suit them [36]. One of the systems able to provide the circulation of the chemical energy and support the smart grid concept are Solid Oxide Cells performing coelectrolysis with possibility to produce methane from the syngas obtained during the process within one reaction chamber.

Nanoparticulate, mostly ceramic and cermet-like, catalysts have gained the attention of researchers all around the globe and became a huge group of heterogenous catalysts. Those can be used in speeding up and increasing selectivity of various chemical processes. Methane reforming and synthesis (methanation) are two opposite reactions that can be involved in ecofriendly energy provision, hydrogen generation and excess energy storage. To produce heat, electricity, and hydrogen stream methane-rich natural gas can be easily burned. It is also a very good feedstock for production of, so called, syngas (CO-H₂ mixture) by undergoing steam reforming as follows [85]:

$$CH_4 + H_2O \rightarrow CO + 3H_2$$
 $\Delta H_{298} = 206.3 \text{ kJ} \cdot \text{mol}^{-1}$ (30)

$$CH_4 + 2H_2O \rightarrow CO_2 + 4H_2$$
 $\Delta H_{298} = 165.3 \text{ kJ} \cdot mol^{-1}$ (31)

Even though the reforming of methane is a long-known process, the exact description of all the reactions and intermediates is still missing. What is sure, parallel to production of syngas, other reactions can take place such as Water Gas Shift (WGS), which is considered a fast-equilibrated reaction [85]:

$$CO + H_2O \rightarrow CO_2 + H_2$$
 $\Delta H_{298} = -41.2 \text{ kJ} \cdot \text{mol}^{-1}$ (32)

From the practical point of view, the reactor set-up and catalyst composition can define the product of reforming reactions according to actual needs.

The exhaust gases produced mostly by industry, instead of being thrown into the atmosphere, can be further recycled into methane. By using catalytic or electrocatalytic (involving CO₂/H₂O coelectrolysis in SOEC) methanation reactions, one can use up CO₂-CO-H₂O-H₂ mixtures to convert the waste by-products back into CH₄. Liquefied methane is again a good source of energy as well as being safely stored and transported. The methanation (known as Sabatier process) can be described generally by the following two overall reactions [85]:

$$CO_2 + 4H_2 \rightarrow CH_4 + 2H_2O$$
 $\Delta H_{298} = -165 \, kJ \cdot mol^{-1}$ (33)

$$CO + 3H_2 \rightarrow CH_4 + H_2O$$
 $\Delta H_{298} = -206 \, kJ \cdot mol^{-1}$ (34)

Each of the mentioned processes, which are taking part in circulating energy conversion, are mostly catalyzed nowadays by the metallic particles supported on the oxide-based material [34].

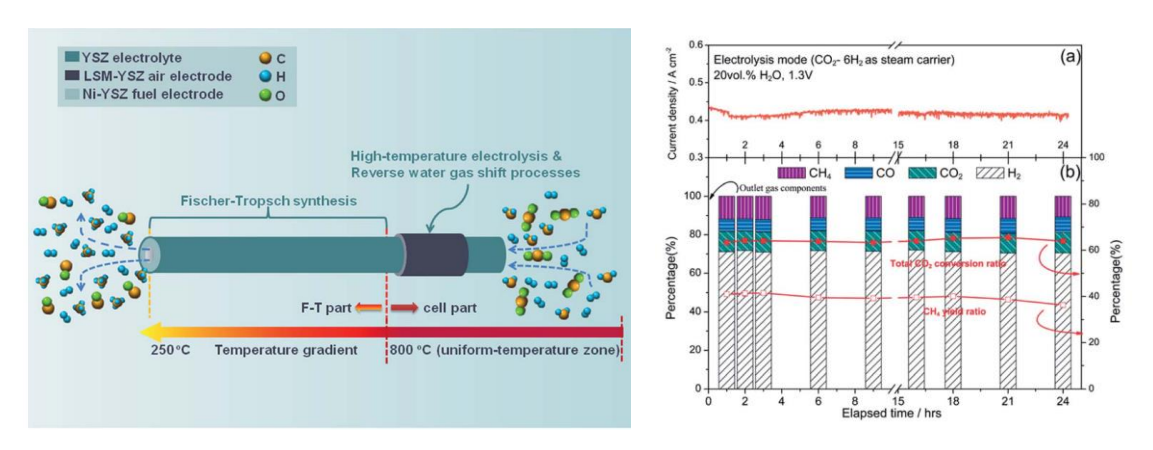


Figure 13. A) Illustration of the setup for direct methane synthesis from coelectrolysis in a tubular cell and B) electrical and chemical performance of the unit operated at 1.3 V [86]

As an example, in the work of Chen *et al.* [86], a novel design was introduced for the direct synthesis of methane from CO₂–H₂O coelectrolysis, utilizing a tubular system that enabled spatial temperature control. One section was maintained at high temperature for SOEC performing electroreduction of H₂O-CO₂ and another part was kept at a lower temperature suitable for the Fischer–Tropsch (F–T) process, which is a direct process of converting syngas into hydrocarbons [87]. This idea came from the technical problem with integrating the SOEC and F–T processes. SOECs typically require high operating temperatures (600–1000 °C) to achieve favorable thermodynamic and kinetics. In contrast, the methanation process is typically carried out at lower temperatures (200-300 °C) as the CO_x hydrogenation is an exothermic process. The system was constructed using a long tubular cell composed of porous Ni–YSZ substrate coated with a dense YSZ electrolyte layer. The idea along with the performance results are presented in Fig. 13.

The electrochemical cell operated at $800\,^{\circ}\text{C}$, where the syngas was produced via coelectrolysis and later it was directly converted to methane in the Fischer–Tropsch (F–T) section maintained at temperatures as low as $250\,^{\circ}\text{C}$. This bifunctional design significantly enhanced the CH₄ yield, reaching 11.84 %, while maintaining short-term stable performance over 24 hours. This finding marked a notable advancement in the direct conversion of CO_2 and H_2O into hydrocarbons.

2.5 Materials used for construction of SOC

2.5.1 Electrolyte

The main task of the electrolyte is to selectively transport O^{2-} ions formed at one electrode through its volume to the reaction area. Due to this, the compound forming the electrolyte should be as dense as possible, blocking for electrons, impermeable to gases, and stable (for SOC) within a range of different oxygen partial pressures (pO_2): from approximately 1 bar in the air side to approximately 10^{-22} bar on the hydrogen side [88].

The process of O²⁻ ionic transport in electrolyte materials, e.g. YSZ, occurs due to the existence of lattice defects, the socalled oxygen vacancies $(V_O^{\bullet \bullet})$, which allow the formation and movement of oxygen ions across the crystal lattice. Defining the of the materials structure containing the defects is a very complex issue, and the Kröger-Vink notation is most often used. In this notation, each defect is assigned with an appropriate symbol with specific upper and

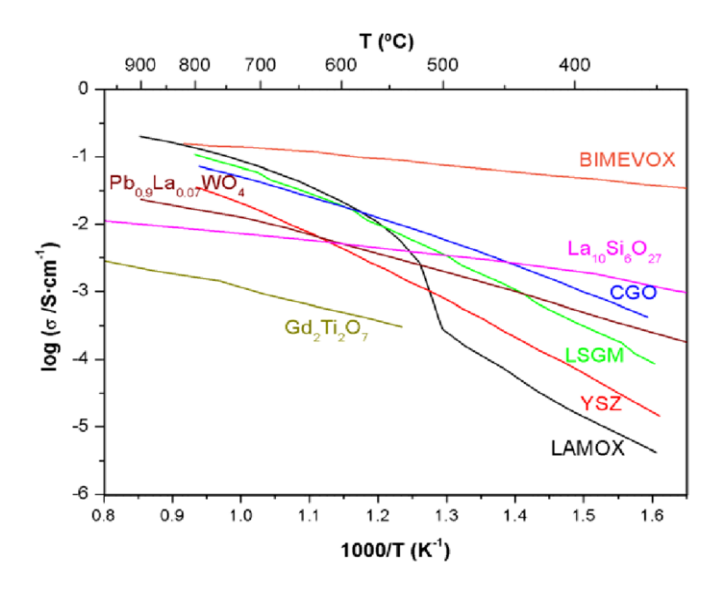


Figure 14. Comparison of various electrolyte materials used in SOC [89]. BIMEVOX - $Bi_4V_2O_{11}$, CGO - $Ce_{1-x}Gd_xO_{2-\delta}$, LSGM - $La_{0.9}Sr_{0.1}Ga_{0.8}Mg_{0.2}O_{3-\delta}$, LAMOX - $La_2Mo_2O_9$, YSZ - $Zr_{1-x}Y_xO_2$

lower indices. Thus, V denotes a vacancy, the element symbol indicates the corresponding ion in the structure, the lower index specifies the position occupied by the defect, and the upper index defines the electrical charge of the defect with respect to the ideal lattice [90]. The formation of vacancies ('empty spaces' in the structure) is related to the stoichiometry of the compound and the type of dopants used. A parameter that strongly influences the concentration of defects is temperature, due to the thermally driven nature of the formation and excitation of vacancy movement. Due to the varied activation energy of the ion conduction process for different materials used as electrolytes, it directly defines the operating temperature of the entire cell. The dependence of the ionic conductivity (σ_{ion}) on temperature for several selected compounds is presented in Fig. 14.

With increasing temperature, the conductivity value for each oxide material increases as it is a thermally activated process. Among the materials used to produce fuel cell electrolytes, compounds with a perovskite (ABO₃) or fluorite (AO₂, where A is a tetravalent cation) structure are most often selected. High ionic conductivity has been also reported for BIMEVOX-type compounds, i.e., doped Bi₄V₂O₁₁. Unfortunately, these materials are not used on a large scale due to instability in a reducing atmosphere [91]. Widely used YSZ, i.e., a mixed oxide consisting of Y₂O₃ and ZrO₂, is characterized by minorly lower σ_{ion} values. Despite lower conductivity, this material, due to its high chemical and mechanical stability at high temperatures, has found exceptional recognition as an electrolyte in SOC. Zirconium oxide stabilized with yttrium oxide with the general formula Zr_{1-x}Y_xO₂ is produced by doping and stabilizing the ZrO₂ cubic lattice with Y³⁺ ions. A cationic dopant with a lower oxidation state causes the formation of oxygen

vacancies to maintain the electrical neutrality of the lattice according to the reaction presented in Eq. 35.

$$Y_2O_3(ZrO_2) \to 2Y'_{Zr} + 3O_0^x + V_0^{\bullet \bullet}$$
 (35)

Along with the increasing amount of yttrium, ionic conductivity goes up until 8-11 mol.% of Y_2O_3 is present, then declines [92]. This composition is generally considered optimal for SOC applications. The theoretical density of 8YSZ ceramics is around 5.959 g·cm⁻³, while the coefficient of thermal expansion equals $10.3 \cdot 10^{-6} \text{ K}^{-1}$ [93].

Another material widely recognized as an electrolyte in SOC is gadolinium-doped cerium oxide (GDC, CGO) with the general formula Ce_{1-x}Gd_xO_{2-δ}. It is characterized by a higher ionic conductivity than YSZ, however, at elevated temperatures and low oxygen partial pressures, it exhibits increased electronic conductivity. This consequently leads to a decrease in cell efficiency [94]. This compound is mostly used as a barrier layer between YSZ electrolyte and the cathode. Its purpose is to limit the diffusion of the elements (especially Sr) from the cathode and formation of the parasitic phases [95].

Due to strict requirements, only a limited number of ion-conducting oxides have been successfully developed as electrolytes for SOCs. These electrolytes must exhibit several critical properties: high enough oxygen conductivity (~0.1 S·cm⁻¹ at operating temperatures), suppressed electronic conductivity (with an electronic transference number <10⁻³), good chemical and thermodynamic stability across a broad range of temperatures and oxygen partial pressures, negligible volatilization, thermal expansion coefficients (TEC) matching with other components of the cell, adequate mechanical strength, and minimal interaction with electrode materials during fabrication and operation [45].

2.5.2 Hydrogen (fuel) electrode

As a key component, the hydrogen electrode plays a crucial role in both Solid Oxide Fuel Cells (SOFCs) and Solid Oxide Electrolysis Cells (SOECs). In SOFC, it oxidizes the fuel, while during the electrolysis, it reduces H₂O and CO₂. Consequently, the choice of materials for this electrode is critical, significantly impacting the performance of SOCs regardless of operating mode. The electrochemical or chemical processes generally occur near the electrolyte and at preferential surfaces and triple-phase boundaries (TPBs), which are described as the sites where the electron-conductive phase, the electrolyte material (ionic conductor), and the gas phase meet.

The major requirements for the SOC electrode material during the operation are as follows: excellent catalytic activity for the oxidation of the fuel or electrosplitting, high enough electronic conductivity (min. 1 S·cm⁻¹) to transport electrons between the reaction sites and the interconnect, well distributed and developed porosity to allow the gases and byproducts to easily diffuse through the electrode, long-term chemical and thermal stability, matching thermal

expansion coefficient with other components, sufficient ionic conductivity, tolerance to poisoning and deposition of the carbonaceous species. It should not be susceptible to re-oxidation. From the economical point of view, it must have low cost of raw materials and should be easy of fabricate at large scale [96].

Because of its exceptional catalytic activity, electrical conductivity, and accessibility, nickel oxide is without any doubt the most widely employed hydrogen electrode material for SOCs [96] even though there was a lot of other research concerning the use of alternative materials based on e.g. perovskites, double perovskites, or different composites [97–99]. Under reducing conditions found on the fuel electrode, NiO converts into Ni. As a metal, it is purely an electronic conductor, which is normally combined with ionic conductors such as YSZ or GDC to form a cermet composite that lengthens the TPB [100]. Porous Ni–YSZ cermet fulfils a great share of the requirements of an ideal electrode material. The following characteristics of Ni–YSZ made it overtake the SOC technology:

- Nickel is as an outstanding electrocatalyst for the reactions occurring in SOC hydrogen electrodes both in SOFC and SOEC modes with high electronic conductivity (~2×10⁴ S·cm⁻¹ at 1000 °C) [101],
- The YSZ acts as a framework/scaffold for the dispersion of Ni grains [102]. It also inhibits the coarsening of Ni due to its lower melting point and quite strong agglomeration via surface diffusion and diffusion in gas phase,
- YSZ extends the TPB as it offers an ionic contribution to the overall conductivity,
- Ni–YSZ cermet is chemically stable even in very low partial pressures of oxygen and at high temperatures,
- The TEC of Ni-YSZ is close to that of YSZ-electrolyte and matches well with other SOFC components [103],
- Ni and YSZ are nearly immiscible, and they do not react with each other even at very high temperatures.

Even though Ni–YSZ is the current state-of-the-art material, it experiences degradation issues during extended use, particularly at high current densities (>1 $\text{A}\cdot\text{cm}^{-2}$). Nickel agglomeration and depletion of the reaction sites are the primary concerns. Ni is also susceptible to coking under certain conditions and can be easily attacked by e.g. sulfur to form electrochemically inactive Ni_xS_y .

Furthermore, the electrochemical performance and stability of the Ni–YSZ cermet strongly depend on the quality of starting material – morphology, composition, and porosity. The conventional method for the preparation of Ni–YSZ electrodes involves ceramic powder processing according to the following steps:

- mixing NiO and YSZ powders with appropriate size distribution and at certain ratio until homogeneous. The particle size of NiO powder is usually ~1-10 μm, while that for YSZ is in the range of 200-300 nm. The volume ratio of Ni to YSZ typically lies between 35:65 and 55:45. A pore former, e.g. PMMA or graphite flakes, is added to the mixture to achieve needed porosity,
- firing at high temperature,
- reduction of NiO-YSZ during SOFC operation (600 °C 1000 °C) which causes round 41% volume reduction and formation of the secondary porosity. A minor bulk dimension change happens after the reduction when vol% of YSZ used for Ni-YSZ formation is larger than that of the NiO [45,104].

Fig. 15 is included to visualize the measured changes in conductivity of the Ni–YSZ composite depending on the initial size of the YSZ particles in the cermet concerning also the loading of Ni phase. As observed, the electrical conductivity of Ni–YSZ cermet is highly sensitive to the particle size and distribution of both Ni and YSZ.

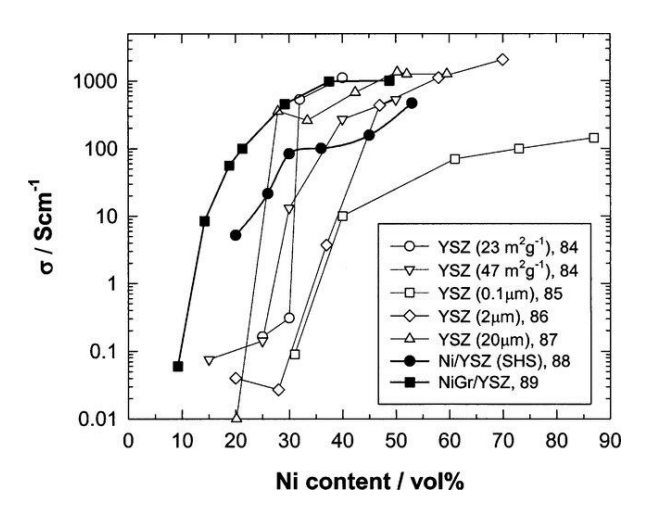


Figure 15. Conductivity of Ni–YSZ cermet as a function of Ni content. The conductivity was measured at $1000\,^{\circ}\text{C}$ in wet H_2 . Numbers are the references cited in [105].

This also affects the threshold at which the percolation paths for electrons form and allow the transition to electronic conduction mechanism. For instance, Huebner et al. [106] found that with small Ni particles (~0.6 μm), a conductivity of ~300 S·cm⁻¹ at 1000 °C can be achieved with 30 vol% of Ni loading. In contrast, larger Ni particles (~16 µm) required 50 vol% Ni to reach a conductivity of S·cm⁻¹ ~100 at the temperature. This indicates that

both the size of the constituent particles as well as Ni:YSZ ratio influences the usability of the cermet material.

To overcome the problems in Ni–YSZ, a lot of research was devoted to the restructuration of the conventional cermet material through the usage of various preparation methods. These studies have explored various aspects, including powder preparation methods [107], NiO–YSZ ratios [108], powder milling techniques [109], and three-dimensional shaping of conventional slurries [110]. As an example, Byeongseok K. *et al.* [111] synthesized a NiO–YSZ composite through a two-step hydrothermal method and utilized it as an anode functional layer. This

composite exhibited significantly greater conductivity compared to the one produced by ball milling, enabling a single cell to achieve a power density of 1.7 W·cm⁻² at 800 °C. At the same time, Song J. H. *et al.* [112] produced NiO–YSZ nanopowders (~100 nm in diameter) through a co-precipitation technique followed by hydrothermal treatment. The cell containing this novel cermet material delivered higher power output compared to cells made using traditional methods. Research by Cho H. J. *et al.* [113] demonstrated that the milling process of the initial NiO and YSZ powders significantly affects the final performance of the SOFC. Using high-energy milling reduced particle sizes much more effectively than conventional ball milling. This resulted in a substantial decrease in polarization resistance and increased single cell power output from approximately 500 mW·cm⁻² to 850 mW·cm⁻² at 800 °C.

Wet chemical synthesis methods typically produce powders that enhance electrode performance, but these processes are usually more complex, time-consuming, and costly [114–116]. As a result, large-scale production of SOCs primarily relies on mechanical processing techniques, with slurries commonly prepared through ball milling. To improve the commercial viability of bottom-up chemical methods, it is important to reduce their complexity and avoid the use of rare or expensive feedstock materials.

2.5.3 Oxygen electrode

In SOCs, an air electrode performs oxygen reduction reaction (ORR) when the cell is in SOFC mode or oxygen evolution reaction (OER) under SOEC polarization. Furthermore, it provides a pathway for the migration of the O²⁻ ions and facilitates the mass transport of the gases into the proximity of electroactive areas. Therefore, the requirements for an air electrode include both high electronic and ionic conductivity, high activity towards OER/ORR, sufficient open porosity for the diffusion of oxygen, low cost, acceptable degradation rates, and thermal expansion coefficient (TEC) matching the electrolyte [117]. In addition, the materials should be stable under oxidizing conditions during both fabrication and operation in SOC.

Specifically, for the Solid Oxide Fuel Cell (SOFC) to operate efficiently, the cathode materials must exhibit the following functionalities:

- Both high electronic conductivity (at least 100 S·cm⁻¹ in air) and oxygen-ion conductivity,
- High electrocatalytic activity for OER/ORR,
- Thermal expansion coefficient matching other cell components (electrolyte and interconnect material),
- Sufficient chemical stability and compatibility with electrolyte and interconnect material,
- Well-developed porosity for fast oxygen diffusion,
- Cost effectiveness [45].

The electrochemical reduction or evolution of O₂ usually demands a lot of energy input to overcome the activation barrier of the process. This implies slow kinetics at lower operating

temperatures, thus, a significant drop in performance. As a result, a lot of research was focused in recent years on new air electrode materials to increase the performance and long-term stability of the SOCs. Similar to hydrogen electrode the reactions occur on TPB, including gas (oxygen), electrode, and electrolyte. This is why the most common group of materials used in the research are Mixed Electronic Ionic Conductors (MIEC). MIEC, as a p-type metal oxide, generates numerous oxygen vacancies that promote the transport of oxygen anions via a vacancy hopping mechanism [118]. It exhibits both electronic and ionic conductivity. By that it enables to extend the TPB to whole surface of the grains of the material, what, as a result, decreases the polarization resistance of the cells [119]. The schematic overview of the difference in the utilization of various materials in the cathodes of SOFCs is presented in Fig. 16.

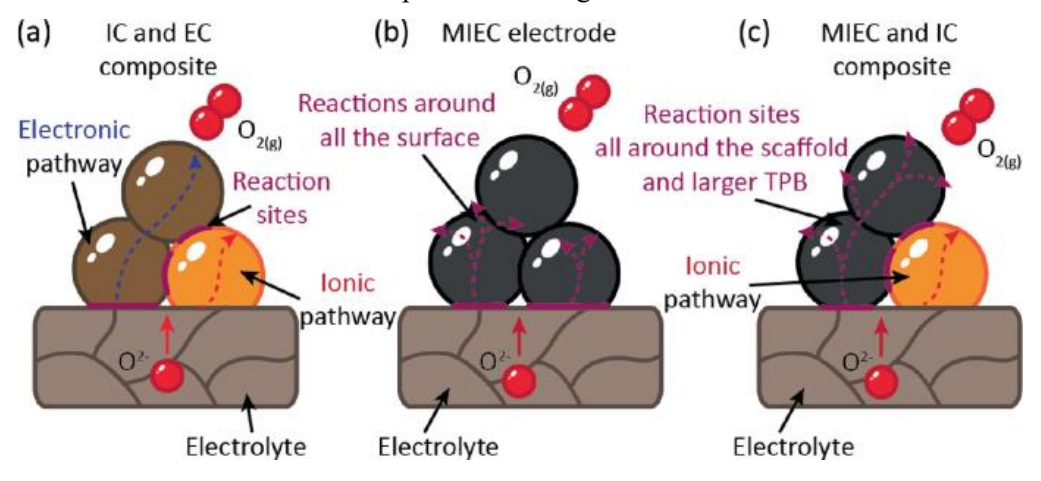


Figure 16. Schematic representation of the operation of the cathode in SOFC depending on the selection of the material [120] IC – ionic conductor, EC – electronic conductor, MIEC – mixed ionic electronic conductor

Perovskites with the general formula $ABO_{3-\delta}$, where A and B are cations with a total charge equal to +6, are among the most used air electrode materials in SOCs, primarily due to their high doping flexibility. In perovskite structure, the A-site is typically occupied by a large cation with 12-fold coordination to oxygen, while the B-site hosts a smaller cation with 6-fold coordination. By partially or fully doping one or both sublattices, key properties such as electronic and/or ionic conductivity, catalytic activity, and thermal expansion can be tailored to meet specific requirements. The A-site is commonly occupied by a combination of rare-earth cations (often La, Sm, Pr) and alkaline-earth metal such as strontium, calcium, or barium. The B-site is composed of one or more transition metal cations, including manganese, cobalt, iron, or nickel. Mixed valence states at the B-site contribute to enhanced catalytic activity in oxygen reactions. Additionally, substituting the A and/or B sites with aliovalent cations (A' and/or B') can further improve conductivity [121].

 $La_xSr_{1-x}CoO_{3-\delta}$ (LSC) is most common perovskite material applied as an oxygen electrode for SOC application and is used on a large scale today. $La_{1-x}Sr_xMnO_{3-\delta}$ (LSM) was used primarily for cathode application, and until today, it is still highly investigated material for SOC. Besides these examples, the most common perovskites used for research and application in SOC

technology for oxygen electrode are (La,Sr)MnO_{3-δ} (LSM), (La,Ca)MnO_{3-δ} (LCM), (La,Sr)(Co,Fe)O_{3-δ} (LSCF), (La,Sr)CoO_{3-δ} (LSC) and La(Ni,Fe)O_{3-δ} (LNF) [48,117,122]. Despite better conductivity or higher catalytic activity, a lot of novel materials were discarded from further integration with SOCs due to instability, mismatch in TEC, high volatility or aggressive reactivity with the electrolyte forming insulating layers like SrZrO₃ or La₂Zr₂O₇ [123]. Composition of air electrodes in SOFC and SOEC is a heavily studied topic, and the reported development of the materials resulted in an increase of maximum flowing current densities as well as stability over the years. This is quite beneficial in terms of commercial viability of SOC technology.

2.6 Degradation in SOC

The harsh operating conditions of SOFCs lead to various degradation processes originating from individual components and their interactions, posing significant challenges to achieving long-term stability. Degradation is typically defined as a decline in performance, with the rate often expressed as voltage loss per 1000 hours, particularly in stacks [124]. Assessing the degradation process in SOFCs is complex, as it requires long-term studies and is influenced by various operational factors such as temperature, fuel impurities, and current density. Despite these problems in testing the lifespan in SOCs, the key issues are commonly mentioned regarding the mechanism of degradation in the air electrode, hydrogen electrode and electrolyte. A summary of the main causes of the degradation in main components is presented below.

Degradation of the materials on the SOC can be affected both by intrinsic and extrinsic factors. Intrinsic factors come from the material itself and arise during the operation of the cell. The major issues included in this group are: coarsening of the electrode structure caused by diffusion and sintering of the ceramic or metallic grains, decomposition of the base material, reactivity with other components of the cell and delamination of electrodes from electrolyte surface. During testing and operation, the electrode material can be subjected to degradation from extrinsic factors, which come into picture when the cells are being tested, especially in real-life systems involving e.g. stainless-steel interconnects [125].

Air electrode undergoes degradation as a result of three main mechanisms:

- poisoning by e.g. Cr, CO₂, S, and H₂O,
- deformation of the microstructure,
- delamination caused by thermal and chemical stress.

One of the most severe degradation mechanisms in Sr-based perovskites making up the air electrode is chromium (Cr) poisoning, which comes from the evaporation of Cr species from unprotected metallic interconnects. Cr poisoning can occur via two main ways. In the first route, volatile Cr compounds interact directly with the cathode surface and segregated ions, leading to

the formation of precipitates that degrade e.g. electrical performance [126]. This process also increases the rate of surface segregation and decomposition of the material. In the second pathway, Cr species deposit at the triple-phase boundary (TPB), forming compounds like Cr₂O₃ that block oxygen reactions and lower O₂ transport across the electrode decreasing the overall current flowing through the system [127].

Another issue recognized as a cause of degradation in e.g. LSCF is sulfur poisoning by the SO_x from the ambient air. It can result in the formation of SrSO₄ precipitates along the grain boundaries at the electrode/electrolyte interface. This again lowers the electrochemical activity for oxygen reduction and evolution in the electrode. A schematic view on the segregation phenomena in the SOC electrodes is depicted in Fig. 17.

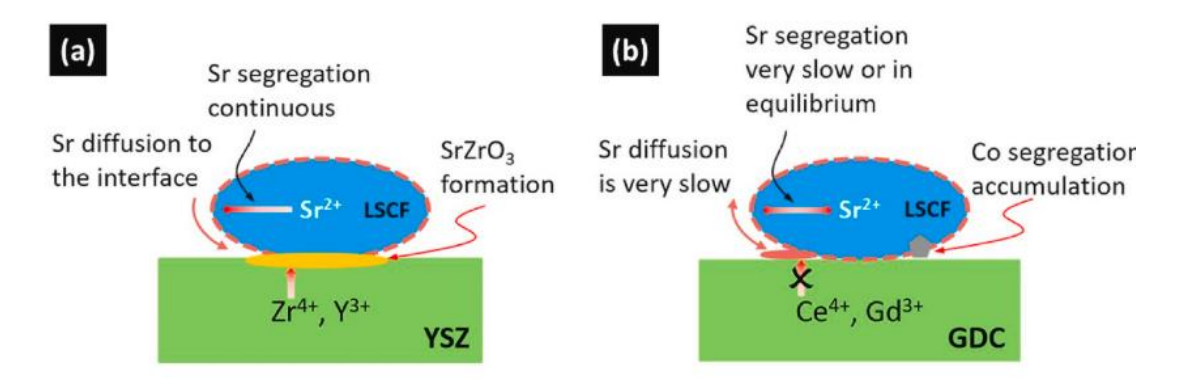


Figure 17. Schematic view on the surface segregation in (a) LSCF/YSZ and (b) LSCF/GDC cell. The red arrow indicates direction of the Sr segregation and diffusion [128].

Morphological change of the air electrode is another degradation mechanism, typically occurring under high overpotential and resulting in altering of the microstructure and phase composition. This phenomenon, known as 'kinetic demixing', often arises when material contains cations with significantly different mobilities, leading to component segregation [129]. For LSC the most common result of this process is segregation of SrO and Co_xO_y species in the electrode affecting the oxygen exchange kinetics. Furthermore, strontium enrichment at the interface can cause the reaction with YSZ, forming insulating phases like SrZrO₃, which lead to an increase in the cell's ohmic resistance [130].

Chemical strain is another degradation mechanism in air electrode material, arising from oxygen non-stoichiometry, which is often a positive aspect increasing the overall ionic conductivity. The formation of oxygen vacancies reduces the overall valence of B-site cations, increasing their ionic radius and causes an expansion of the lattice. This leads to a mismatch in the thermal expansion coefficient between the electrode and the electrolyte. Finally, the internal stress is braking the electrode layer by bending and it delaminates causing the whole cell to fail [130,131].

The major degradation sources of the electrolyte can be listed as follows:

- change of the crystal structure and diffusion of the dopants,
- reactivity with the electrodes,
- mechanical failure, formation of the pinholes.

Under high-temperature and harsh operating conditions, phase changes in the electrolyte layer can negatively impact SOC performance by reducing ionic conductivity and compromising phase stability, ultimately leading to degradation. The most crucial issue, in the widely used YSZ electrolyte, is the phase transformation from cubic to tetragonal zirconia, which is highly dependent on the Y₂O₃ concentration in ZrO₂. By properly controlling the concentration of the dopant it is possible to nearly eliminate this process and the phase transition in currently used YSZ electrolytes is considered a secondary degradation issue [132]. The problem persists in alternative electrolyte materials of much more complex composition e.g. LSGM or BiMEVOX structures.

Moreover, chemical reactions at the interface between the electrolyte and adjacent electrodes constitute a significant degradation mechanism. These interactions can promote the formation of interfacial layers and thermodynamically stable, insulating or poorly conducting secondary phases that impair electrochemical performance. For example, in LSCF/YSZ constructs, high-temperature sintering of the air electrode and high polarization both facilitate the thermodynamically driven segregation of Sr at the interface, leading to the formation of insulating SrZrO₃ phase [130]. This interfacial reaction is detrimental to the electrochemical performance of the SOC. Another degradation mechanism is observed for perovskite-based electrolytes such as LSGM, where the reaction between the electrolyte and the cathode material primarily occurs via cation interdiffusion, rather than through the formation of secondary phases. As a result the electrolyte is losing the ability to effectively conduct ions and the cell stops operating [133].

A minor source of degradation is the mechanical failure of the electrolyte induced by thermal and chemical stresses. At high temperatures the SOCs are almost stress-free, but the cooling down, heating up cycles or interdiffusion and formation of new phases can induce tension in the thin electrolyte layer. This minor stress when accumulated can cause internal cracking or formation of the pinholes, which enable the gases from both electrodes to intermix and lower the OCV. Furthermore, the uncontrolled increase in the utilization factor of sudden change in the flow of the fuel or oxidant can cause an uneven heat distribution. The formation of hot spots and huge thermal gradients is another major cause of the mechanical breakdown of the SOCs [134,135].

The degradation of the anode is mostly caused by:

- change in microstructure,
- carbon deposition or Ni poisoning,
- delamination.

Nickel-based Ni-YSZ anodes in SOCs commonly undergo microstructural degradation processes such as Ni coarsening, migration, and Ni depletion, which are closely interdependent [136]. Among these, Ni coarsening is regarded as the most critical degradation mechanism, predominantly driven by surface and interfacial diffusion, especially under high water vapor concentration and high polarization. The phenomenon is generally attributed to an Ostwald ripening [130]. The possible mechanisms driving this process include the transport of volatile Ni species (e.g. Ni(OH)2) through the gas phase and diffusion of the vacancies caused by the differences in grain size and surface curvature [137]. Ni particle coarsening in the anode is directly correlated with a corresponding decrease in the triple-phase boundary (TPB) length, thus lowering the amount of the sites for chemical reactions to happen. Furthermore, the agglomeration of Ni particles into bigger objects decreases the electrical conductivity of the electrode and ultimately deteriorates the contact between the Ni and YSZ leading to the separation of those two phases from each other [138,139]. This redistribution of the phases eventually causes the cell to deteriorate. Fig. 18. shows the micrographs taken by SEM of the Ni-YSZ electrodes tested for 9000 h at 800 °C by Mogensen M. B. et al. [140]. In A) there is a pristine structure of the cell before testing (Ni in white, YSZ in grey). Then the images in B) and C) differ only with the polarization applied to the cell. In B) picture the cell was operating with no current load, while in C) the cell was working under $-1 \text{ A} \cdot \text{cm}^{-2}$.

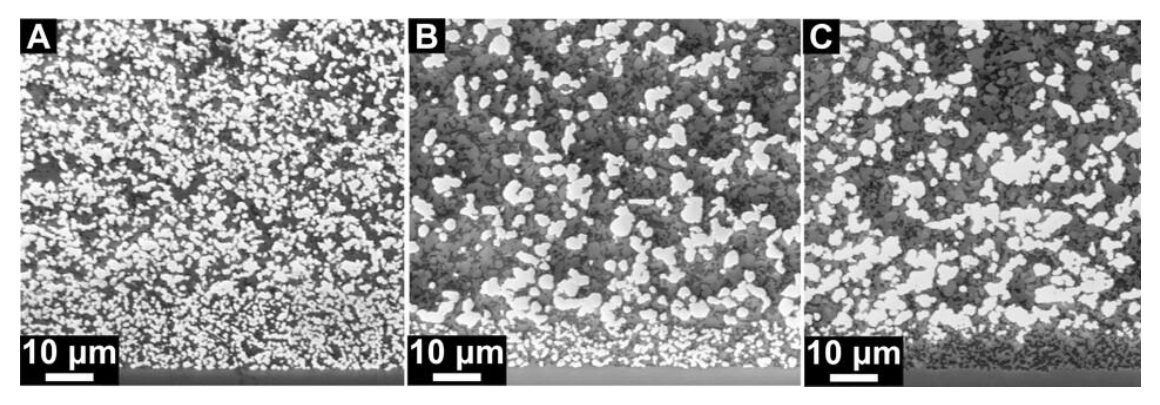


Figure 18. SEM images of the cell cross-sections after 9000 h operation at 800 $^{\circ}$ C. A) pristine, reference cell, B) held under OCV and C) working under $-1 \text{ A} \cdot \text{cm}^{-2}$ current density [140].

It is noteworthy that the region in the proximity of the electrolyte in C) has been nearly depleted of Ni particles, whereas the Ni structure shown in B) remains largely intact after 9000 hours under open circuit voltage (OCV) conditions. This clearly indicates that Ni migration is dependent on the polarization and is responsible for the depletion of the reactive zone of Ni, leading to the deterioration of the cell.

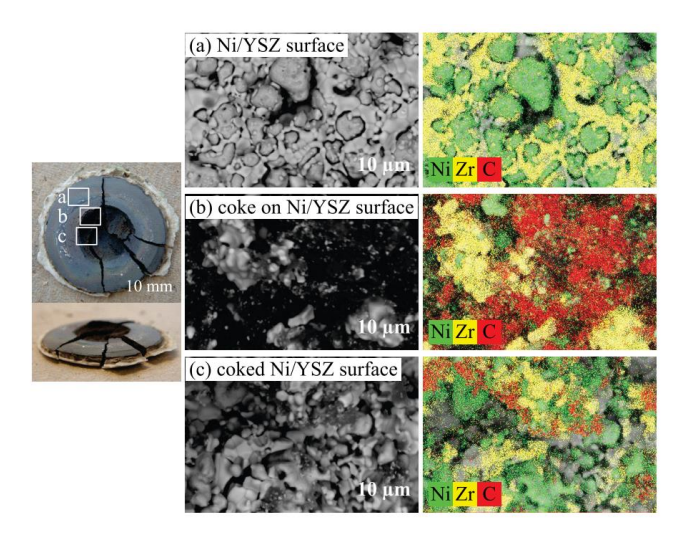


Figure 19. The Ni–YSZ anode optical image and scanning electron microscopy (SEM) image with EDX mapping of the (a) Ni–YSZ surface; (b) coke deposited on the Ni–YSZ surface; and (c) coked spot on the surface after the long-term test in CH₄ [141].

Apart from using pure H₂ to power up the SOFC, it is possible to utilize different fuels such as e.g. hydrocarbons. This is one of the biggest advantages of SOCs as they allow for an internal reforming of the hydrocarbon fuels at high operating temperatures. Unfortunately, when the conditions are not optimal, the Ni–YSZ electrode can be susceptible towards coking. The coking deposits carbon on the surface of mostly Ni grains, obstructing the triple-phase boundaries (TPBs) and blocking gas

channels, what leads to both mechanical and electrochemical degradation. As carbon accumulation intensifies, the resulting pressure can cause the electrode to break. Mirzababaei J. et al. [141] investigated the SOFC under CH₄ feeding. The post-mortem images of the cell are represented in Fig. 19. It was found that severe carbon accumulation resulted in degradation and fracture of pure Ni–YSZ anode without the catalyst layer after 38 h of testing in CH₄. The authors stated, that graphitic carbon contributed to anode degradation through dissolution into the bulk of the Ni–YSZ cermet, leading to volumetric expansion and the disruption of the Ni–Ni conductive network [141,142]. In addition to coking, hydrocarbon-based fuels often contain various compounds with contaminating elements such as sulfur (S), phosphorus (P), arsenic (As), selenium (Se), chlorine (Cl), and antimony (Sb), which can interact adversely with Ni–YSZ, leading to performance degradation and reduced stability. The general mechanism of the degradation lies in the reactivity of those contaminants with Ni metal leading to the formation of inactive ceramics (e.g., NiP, Ni_xS_y, NiCl₂, NiSb etc.), which also cause internal stress in cermet and enhance formation of the microcracks [143,144].

Delamination of the hydrogen electrode is less common when compared to the air electrode. It is hindered thanks to similar TEC of Ni–YSZ and YSZ, but it still plays a secondary role in the degradation of the cells. The delamination is mostly corresponded to the separation of the metallic and ionic phase in the cermet due to the coarsening of the Ni grains [145].

To achieve commercial viability, Solid Oxide Cells must overcome critical challenges related to durability and long-term stability. However, degradation studies remain limited, as most of the current research prioritize reaching high power densities. While performance improvements are important, they will be insufficient without extension of their lifespan through comprehensive degradation analysis.

3.EXPERIMENTAL METHODS

3.1 Basic material characterization methods

3.1.1 Scanning Electron (SEM) and Transmission Electron (TEM) Microscopy

The morphology and chemical composition of the powder samples as well as cross-section images of the cells were analyzed using a Scanning Electron Microscope (SEM, FEI Quanta FEG 250) with an Energy-Dispersive X-ray spectroscope (EDX, EDAX Genesis APEX 2i) and Apollo X SDD detector or Phenom XL (Thermo Fisher Scientific, The Netherlands) with integrated spectroscopy analyzer (Thermo Fisher Scientific, 25 mm² Silicon Drift Detector).

TEM imaging was performed using a JEOL 2100 F (Tokyo, Japan) microscope operating at 200 kV coupled with Energy-Dispersive X-ray Spectroscope (EDS, Oxford Instruments, UK) or JEOL F200 S/TEM with EDS (JEOL dual EDS for F200) and EELS (Gatan Continuum).

3.1.2 X-ray Diffractometry (XRD)

X-ray diffraction patterns of the samples were collected each time using a Bruker D2 PHASER XE-T with a Cu-K α radiation source with the radiation wavelength $\lambda = 0.154$ nm. For the measurement the samples were mounted onto low-background silicon holders, thus minimizing sample related peak broadening. In general, the samples were each time ground to a fine powder and dispersed onto the holder using isopropanol, then left to dry at room temperature and loaded into the X-ray diffractometer. The measurements were performed in the range of 2 Θ (°) equal to 5-90° in continuous movement manner. Rietveld refinement was performed using the HighScore+ software. Appropriate peak shape functions (e.g., pseudo-Voigt) were selected to model the broadening and asymmetry of the diffraction peaks. Goodness of fit (GOF) parameter was used as an indication of the quality of the fit.

3.1.3 X-ray Photoelectron Spectroscopy (XPS)

The X-ray Photoelectron Spectroscopy (XPS) spectra were collected using an Omnicron NanoTechnology X-ray photoelectron spectrometer with a 128-channel collector. XPS measurements were undertaken in ultra-high vacuum conditions, below 1.1×10^{-8} mbar. Photoelectrons were excited by an Mg-K α X-ray source with the anode operating at 15 keV and 300 W. The obtained spectra were deconvoluted using the XPSPEAK41 software. The samples used for the characterization were each time powdered and mounted on the sample holder using carbon tape.

3.1.4 Temperature Programmed Reduction (TPR) and Oxidation (TPO)

Temperature Programmed Reduction (TPR) and Temperature Programmed Oxidation (TPO) tests were carried out in an AutoChem II 2920 (Micromeritics, TCD detector) under 40

mL·min⁻¹ stream of 5% v/v H_2 in Ar and 2% v/v O_2 in Ar, respectively. The tests were each time carried out from 100 to 900 °C with a 10 °C min⁻¹ heating rate to examine the reducibility and substrate integration of fabricated samples. Two reduction cycles were performed each time to deliver more reliable reduction profiles and to determine the tendency of catalyst to undergo degradation. The TPO profiles were collected between the reduction cycles.

In some cases, the measurements were performed using an apparatus constructed by the PhD candidate consisting of a TCD detector (Buck Scientific, USA), a cold trap, and a heated gas transfer line. A fixed amount of sample was loaded into a quartz reactor, with the bed temperature monitored internally. The samples were first degassed at 200 °C for 20 minutes under a 5N He flow. For H₂-TPR, the samples were reduced in a 40 mL·min⁻¹ flow of 6 vol% H₂ in Ar, with the temperature ramped to 900 °C at 10 °C·min⁻¹. Following the TPR, the samples were cooled to room temperature, and the gas stream was switched to a 5 vol% O₂ in He mixture. After a 1-hour equilibration period in the O₂-He stream, O₂-TPO tests were performed using the same temperature program as the TPR. Data was collected at a frequency of 1 Hz using PeakSimple software.

3.1.5 Dilatometry

The thermal expansion coefficient (TEC) was examined using a Netzsch DIL 402 PC dilatometer working in the 100–1500 °C temperature range. All the measurements procedures involved prior preparation of the bulk pellet with the density of >95%, which was further cut using diamond saw into rectangular prism (cuboid) shaped sample. The measurements were performed under a synthetic air stream at a 3 °C min⁻¹ heating-cooling rate.

3.1.6 Thermogravimetry (TG) and Differential Scanning Calorimetry (DSC)

Coupled thermogravimetry (TG) and differential scanning calorimetry (DSC) measurements were performed using Netzsch STA 449 F1 Jupiter apparatus with 403 C Aëolos quadrupole mass spectrometer. The data was collected from room temperature up to 1370 °C at a heating rate of 5 °C min⁻¹ under synthetic air (SynAIR) flow in alumina crucibles.

3.1.7 Archimedes principle density measurement and Mercury Intrusion Porosimetry

The values of total and open porosity of the pellets were evaluated by Archimedes principle of density measurement. Dry samples were weighed and then immersed in the kerosene. Samples were subjected to vacuum treatment at RT until no more bubbling occurred. The soaked samples were reweighed when submersed in the kerosene and after that in ambient air after the removal of excess surficial fluid. The calculations were done according to the standard procedure of Archimedes density and porosity measurements given in [146].

Studies of the pore space via the MICP (Mercury Injection Capillary Pressure) method were performed using a mercury porosimeter (AutoPore IV 9520, Micromeritics). The samples

were first dried at $105\,^{\circ}$ C for 24 h to remove the moisture. The analysis was carried out assuming sample evacuation to $50\,\mu m$ Hg (6.67 Pa) for 2 min and an equilibrium time equal to $10\,s$. The pressure was measured for 120 points in the range of $1.7–60\,000\,psi$ (0.01–413.7 MPa). To calculate the average pore diameter and the total pore area, the Washburn equation based on the behavior of a non-wetting liquid was used. The contact angle was assumed to be 130° .

3.1.8 Nitrogen sorption measurement

Following the BET isotherm model, the specific surface area (SSA) was measured using the N_2 adsorption technique on Quantachrome, NovaTouch LX1 apparatus. The samples were placed in borosilicate 9 mm test tubes and degassed prior to sorption measurement at 300 °C for 3 h in high vacuum. The SSA was evaluated using the BET range of collected isotherms i.e. p/p_0 values within 0.1-0.3.

3.2 Electrical measurement methods

3.2.1 Conductivity measurement using Van der Pauw method (VdP)

The electrical conductivity of the pellets was measured by the Van der Pauw (VdP) method using custom-built cell. The measured pellets were each time polished on both sides to remove any affected area that may form due to the direct contact between the pellet and the alumina substrate during high-temperature sintering. Four platinum reversible electrodes were brush-painted on the corners of the square-shaped pellets and dried at 150 °C for 30 mins. The Pt wires were attached to the previously prepared electrodes using Ag conductive paste and air dried until a solid connection was obtained. The cell was placed in a high-temperature furnace and a stream of the selected gas was set using mass flow controller (MFC). The measurements were performed according to the standard scheme of the VdP method using a Keithley 2400 SourceMeter. An automatic logging system was used for data collection. The YSZ samples were heated in a stream of SynAIR up to 800 °C and measured every 25 °C down to 400 °C with a stabilization time of 30 min at each step. For the NiO-YSZ samples, the pellets were heated under flowing N₂ (Air Liquide, 4N5) protective gas and flash reduced by switching to 3 vol% H₂O humidified H₂ at 800 °C. After conditioning at 800 °C for 1 h, the samples were tested in the same manner as described above. The raw datasets were used to calculate the apparent electrical conductivity (σ) according to Eq. 37:

$$\sigma = \frac{\ln 2}{\pi h} \frac{2}{R_{AB,CD} + R_{CA,DB}} \tag{37}$$

where: σ is the apparent conductivity of the sample, h is the thickness, $R_{X,Y}$ is the measured resistance value, which is determined by switching the current applied to two electrodes and measuring the voltage between the other pair of the terminals. No additional approximations to the conductivity of the porous samples were made to present real values of conductivity. The

long-term tests were performed in humidified H₂ with continuous collection of resistance every 1 min.

3.2.2 Electrochemical Impedance Spectroscopy (EIS)

The impedance spectra were collected using Gamry Interface 1010E potentiostat (Gamry Instruments Inc.) in galvanostatic mode within the frequency range of 100 kHz to 0.1 Hz with 10 points per decade. If not stated otherwise, all impedance measurements were performed under the polarization of 10 mA·cm⁻² in electrolyzer mode with proper stabilization time under polarization prior to applying the sinusoidal AC signal with the current value of 2.5 mA·cm⁻². The measurements at low applied DC current ensured the spectra collection of the cell held in SOEC mode. At the same time, the passed current was small enough so that the measurement mimicked the OCV conditions with marginal changes in gas composition across the cell [147,148]. All spectra were verified using a linear Kramers-Kronig transformation and impedance data sets with errors above ±1 % were eliminated from further processing.

3.2.3 Distribution of Relaxation Times technique (DRT)

The Distribution of Relaxation Times (DRT) technique is an analytical approach used to resolve complex impedance spectra in electrochemical systems. It helps in transformation of impedance data from the frequency domain (EIS) into a time-domain representation. As a result, it yields a continuous distribution of relaxation processes in the form of a DRT profile. This methodology enables a more fundamental interpretation of the underlying electrochemical behavior without relying on equivalent circuit models. By analyzing the placement of the distinctive peaks in the profile, the DRT effectively separates and quantifies overlapping physicochemical processes e.g., charge transfer, mass transport or interfacial adsorption within. This method is especially useful in cases where predefined equivalent circuit models are not able to accurately resolve the complexity of the processes. It is a situation commonly found in energy storage and conversion devices (e.g. fuel cells), corrosion systems, and solid-state ionic conductors.

In this work the distribution of relaxation times (DRT) computing was performed using DRTtools software based on Tikhonov regularization [149]. The impedance data was processed by the discretization method using Gaussian function and a regularization parameter equal to $1 \cdot 10^{-3}$. If deconvoluted, the DRT spectra were fitted into corresponding processes using purely Gaussian curves. The DRT peaks were each time attributed to the corresponding electrochemical processes based on the supporting equivalent circuit model.

3.3 Synchrotron radiation-based measurement methods

Synchrotron radiation is the electromagnetic radiation that is being emitted when the particles, which own a charge, are radially accelerated. The most interesting properly of this type of radiation lies in its brightness and high intensity, that is impossible to reach in conventional X-ray sources. Synchrotron radiation features wide tunability in energy, high polarization level, and ultrafast pulse light emission in the range of picoseconds. This is why synchrotron light-based characterization techniques hold great promise in many areas, especially in physics of condensed matter, chemistry, materials engineering, and medicine. What makes synchrotron light so unique is the possibility to cover the frequencies of entire electromagnetic spectrum. By that, an outstanding amount of techniques for probing materials' properties were introduced ranging from subnanometer, trough nanometer to micro- and centimeter scale [150].

3.3.1 X-ray Absorption Fine Structure Spectroscopy (XAFS)

X-ray absorption fine structure (XAFS) spectroscopy is an interesting tool for studying the local structure around selected elements forming a material at the atomic and molecular level. XAFS is specific to the element thanks to X-ray radiation that can own the energy above and belove the binding energy of a particular core-electronic level of an atom. In the very core of this technique an absorption of the energy E of an X-ray is studied, where an electron with energy E_0 is destroyed and photoelectron is being formed (E- E_0). An isolated atom would have a sharp step at the core-level binding energy and a smooth function of energy after the edge jump [151]. In real materials, where another nearby atom exists, the ejected photoelectron is normally scattered, and the interferences occur. The analysis of the absorption coefficient $\mu(E)$ change can give the information about the electronic surrounding structure of the atoms in the material [150].

X-ray Absorption Spectroscopy (XAFS) measurements were performed at the PIRX (former PEEM/XAS) beamline at the SOLARIS National Synchrotron Radiation Centre, Kraków, Poland [152]. The used synchrotron energy range ensured the collection of the transition metals-L_{2,3} (TrMe-L_{2,3}) and O–K edges of the as-prepared and spent cells. Powdered samples were dispersed onto carbon tape and placed on measurement plates for spectra collection. The measurements were performed using total electron yield (TEY) and/or partial fluorescence yield (PFY) using an SDD window C2 detector from Amptek depending on the self-absorption of the samples under high vacuum conditions. The energy resolution was 200 meV and better, and the beam size (h × v) was 250 μ m × 40 μ m.

Hard X-rays radiation was also utilized to collect *in operando* transition metal K-edge signals at LISA beamline at ESRF (Grenoble, France). The appropriate amount of the powder was calculated using XAFSmass software to obtain the optimum edge jump for high quality data collection. Powdered samples were mixed with ethyl cellulose powder and pelletized. Subsequently, the pellets were mounted in the holder suitable for transmission measurements.

Samples were provided in both oxidized state (marked as OX) and reduced in pure hydrogen at 800 °C (marked as RED). Additional ultrapure reference oxides and mixed compounds were delivered to ESRF and measured at RT. All data was processed and analyzed using PyMca and Athena freeware software.

3.3.2 Scanning Transmission X-ray Microscopy (STXM)

Among various imaging tools, Scanning Transmission X-ray Microscopy (STXM) is a highly advanced technique that allows for the characterization of the chemical phases in the materials with nanometric spatial resolution [153]. STXM involves generation a focused beam of X-ray radiation in synchrotron facility, focusing it on a sample using zone plate diffraction grating, and collecting the signal from transmitted X-rays by the usage of e.g. photodiodes. By the movement of the beam across the sample in point-by-point manner, it provides energy-stacked chemical state information about the studied material. The *in-operando* mode of imaging allows for environmental measurements of the samples at altered conditions e.g., higher temperature, various atmospheres, under magnetic field [154].

The STXM imaging was performed at the DEMETER beamline at SOLARIS National Synchrotron Radiation Centre (Kraków, Poland) on the powdered samples dispersed on a Si₃N₄ membrane or 100 nm lamellae cut out from bulk samples using FIB-SEM. A series of image stacks were collected under flowing helium. The detection of the transmitted radiation was done using a photomultiplier (PM) tube. The collected images were processed using the aXis2000 software. Elemental maps of the selected elements were formed as the difference between the signal collected in the absorption peak and the pre-peak energy representing global distribution of the selected element in the sample.

3.3.3 Near Ambient Pressure X-ray Photoelectron Spectroscopy (NAP-XPS)

X-ray Photoelectron Spectroscopy (XPS) is, so far, one of the best analytical methods for characterizing the composition and electronic structure of the materials, especially in catalyst research. However, in conventional XPS the sample is being measured under ultra-high vacuum conditions (UHV). It creates many problems and often lowers the scientific value of the collected spectra as many compounds can show totally different electronic structure under vacuum. Fortunately, the recent developments enabled the spectrometers to operate at a mbar pressure range, what allows to study materials under the reaction conditions resembling real-life situations. Thanks to that it is possible to describe *in situ* interaction between the catalyst and reactants (intermediates) in real time [155]. Furthermore, it is possible to collect the data in the form of surface map similar to the STXM imaging.

The imaging was performed using the high-pressure cell (HPCell) at Elettra synchrotron (Trieste, Italy) using ESCA microscopy beamline. The images were collected for as-prepared and

in-situ reduced sample (H₂, 400 °C), samples heated in the reactant mixture and stabilized for 1 h, and samples flushed with H₂ at high temperature to observe the desorption. All imaging procedures were conducted at ~0.1 mbar and 500 °C in flowing mixture of 50:50 by vol. H₂:CO₂ with 20 vol.% H₂O vapor or H₂ for the reduction step. The XPS special spectra in HPCell were be collected for O1s, C1s, Ni2p, and TrMe2p (TrMe=transition metal) looking mostly for space distribution of the species and changes in the oxygen spectra.

3.4 Chemical equilibrium simulations

Chemical equilibrium of the reaction is a state where the rates of the reaction in both directions are equal. This state of balance can be achieved whether the reaction starts with only reactants, only products, or a mixture of both. At an equilibrium point the concentrations of the reagents are constant. This state can be achieved only for the systems where the volume of the reaction vessel is enclosed, and no products nor reactants can enter or escape [156]. The composition of the gases in the catalytic system was each time simulated using *Gem* module of the HSC ChemistryTM software under normal pressure of 101.325 kPa and activity coefficients equal to 1 for all substances. All calculations were performed using the Gibbs energy minimization method.

3.5 Non-equilibrium thermodynamic analysis of the reaction state

Equilibrium calculations can be only utilized to estimate the maximum yield of the products when in equilibrium conditions at specific conditions and in an enclosed container. The equilibrium is seldomly reached in packed-bed reactors where a linear or non-linear constant flow of gases is maintained. Furthermore, concentrations of the gases at an outlet of the reactor can be a superposition of multiple reactions. To determine the behavior of each undergoing reaction, a time-dependent thermodynamic analysis using reaction quotients (Q_r) was developed by the author of this thesis and applied in the study [85]. Q_r represents a ratio between an actual non-equilibrium constant and equilibrium constant of a specific reaction. Q_r value aids in evaluating momentary direction in which reactions are likely to proceed. Mathematically Q_r is calculated as given in Eq. 38 as a ratio of actual overall partial pressures p_i of a specie i raised to the power of stoichiometric coefficient x_i (positive for products and negative for reactants) and the equilibrium constant $K_{p,r}$ of considered reaction.

$$Q_{r(t)} = \frac{(\prod_{i} p_{i(t)}^{x_i})_r}{K_{p,r}}$$
(38)

Each reaction is taken into consideration separately to simplify the calculation method while providing sufficient data for the analysis of equilibrium state shifting. Theoretical equilibrium constants K_p were retrieved using HSC ChemistryTM software.

Calculated quotients change during the testing time indicates if the specific reaction goes to the right (for $Q_r < 1$) or to the left (for $Q_r > 1$). If $Q_r = 1$ the reaction has reached the equilibrium state. It is generally agreed that $Q_r \sim 10^{-3}$ stands for the situation where mostly reactants are present in the reaction zone, on the other hand, when $Q_r \sim 10^3$ nearly all components are products. The Q_r values in between state that significant amount of both products and reactants is visible in the stream.

3.6 SOC testing system construction

A measuring vertical testing rig was designed and constructed for SOC studies. A schematic view on the rig is shown in Fig. 20. Main construction elements are made of high purity alumina to minimize the degradation issues caused by e.g. Cr evaporation from stainless steel. In general, for every test procedure the cells were mounted and sealed using a noble metal paste (Ag) and spring-loaded. Two sets precious metal (Au, Pt) wires ensured electrical connection to the electrodes, allowed for applying

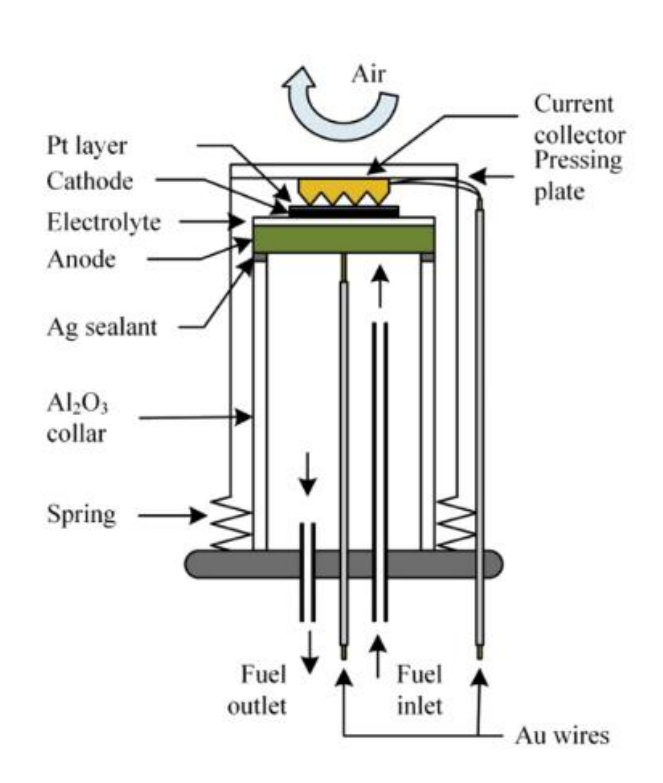


Figure 20. Measurement rig for SOC testing [157].

various voltages to SOC, and perform EIS measurements using Gamry 1010E potentiostat. The air electrode was connected to the wires via gold-plated alumina interconnector and gold mesh. Hydrogen electrode chamber was hermetically enclosed while the air electrode was fed with ambient air supplied through simple convection (open electrode setup). The measuring rig was surrounded by an external high temperature furnace. Precise control of all gas components was achieved using electronic flowmeters. Hydrogen was supplied by H₂ generator. Other gases, with a purity exceeding 99.9%, were obtained from pressure tanks (Air Liquide).

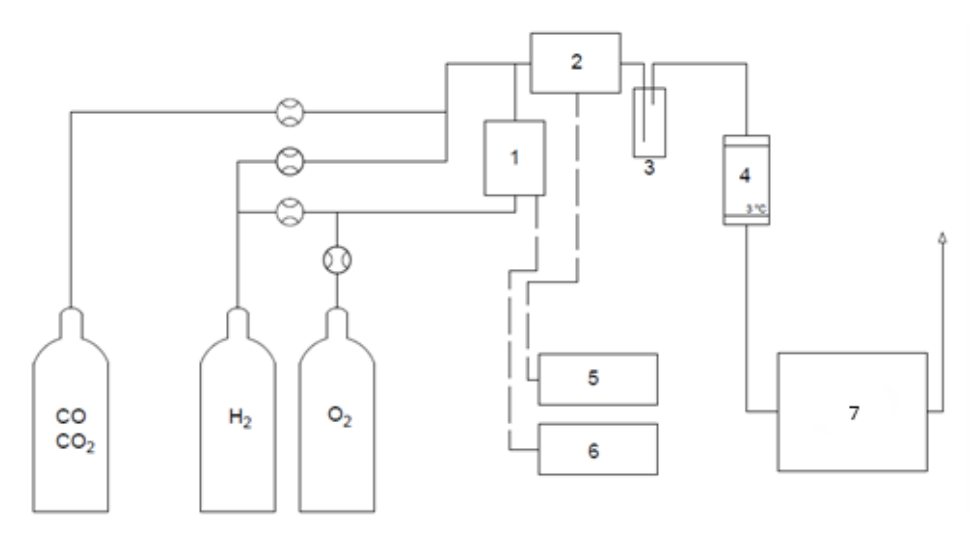


Figure 21. Schematic representation of catalytic activity measurement unit. $1-H_2O$ vapor generator, 2-main SOC chamber or packed-bed reactor, 3-initial condenser, 4- water coldtrap, 5,6- thermostats, 7-FTIR/GCMS

Water vapor was generated by burning a controlled H₂-O₂ mixture within an external reactor. This reactor, containing a platinum (Pt) sponge catalyst, was maintained at 700 °C. The outlet gases were dried using an initial condenser, a cold trap set to 4 °C, and a Nafion dryer tubing before entering the GCMS-FTIR gas concentration measuring unit. The schematic view of the whole setup is presented in Fig. 21. To analyze the processes deeper, knowledge about the composition of reactive gases is required. The gas analysis methods included in this research involved Gas Chromatography with Mass Spectrometry (GCMS) and Fourier Transform Infrared spectroscopy (FTIR) forming a combined system for additional check of the reliability of the collected data.

Gas Chromatograph GCMS-QP2010 SE was delivered by Shimadzu and contained mass spectrometer with EI ionization. The GCMS was equipped with Carboxen GC capillary porous layer open tubular (PLOT) column for separation of the CH₄, CO₂, CO, N₂-O₂ etc. The column was heated to 90 °C and the analysis duration was 5 min. The gaseous samples were injected periodically by the automatic injection valve. The concentrations of the outlet gases were calculated based on the peak intensity of the specific m/z ratio signals using the calibration curves made before the tests. The processing of the spectra was performed using GC Postrun software from Shimpol, Poland.

Fourier Transform Infrared (FTIR) spectroscopy is an absorption technique used to analyze vibrational spectra, which arises from changes in dipole moments during molecular vibrations. FTIR measures the energy absorbed by a sample as it transitions between vibrational energy levels. The spectrum, obtained via a Fourier transform provides high-resolution data. This allows for selective analysis and simultaneous measurement of multiple substances. FTIR is versatile, accommodating solids, liquids, and gases using appropriate sample adapters. In this study, a gas sample heated adapter was mounted into FTIR spectrometer which was supplied with the outlet gases from the cell rig in a free-flow manner. The spectrophotometer (PerkinElmer

Spectrum 100) was equipped with a 10 cm length heated gas cell (60 °C) and ZnSe optical windows. The methodology of concentration calculation based on the integrated area of the whole band peak was established and described in detail in the publication [85] M. Chlipała, P. Blaszczak, S.F. Wang, P. Jasiński, B. Bochentyn, In situ study of a composition of outlet gases from biogas fuelled Solid Oxide Fuel Cell performed by the Fourier Transform Infrared Spectroscopy, Int. J. Hydrogen Energy. 44 (2019)13864–13874. https://doi.org/10.1016/j.ijhydene.2019.03.243. The studies involved the buildup, calibration and setup of the cell working under biogas feeding. Based on the resulting FTIR spectrum (example in Fig. 22D) it was possible to integrate the areas under the specific range of the measured bands. The calibration data was obtained using high purity (5N5) mixtures of the gases and the spectra integration was performed at 3760-3520 cm⁻¹ for CO₂, 2226-2143 cm⁻¹ for CO, and 3250-2650 cm⁻¹ for CH₄, respectively. Based on the change in the area, the calibration curves were established as seen in Fig. 22A-C.

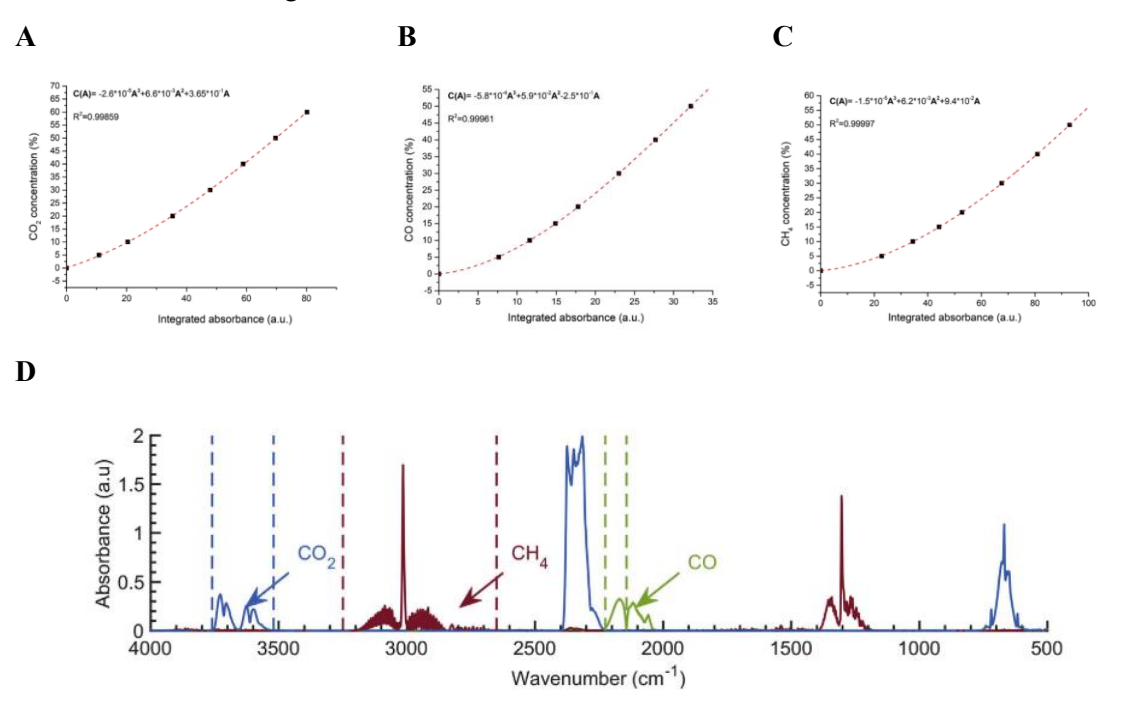


Figure 22. A-C) Calibration curves for CO₂, CO, and CH₄ and D) FTIR spectrum of biogas (Vertical dashed lines mark the wavenumber ranges used for quantitative analysis) [157].

The calculation and batch processing of the FTIR spectra was performed using Spectragryph software provided by Dr Friedrich Menges. The calibration procedure performed on FTIR spectroscope resulted in a polynomial dependence between the concentration of a particular gas and the corresponding integrated absorbance in particular wavenumber ranges. It was impossible to detect the homoatomic H₂, O₂, and N₂ gases in the FTIR spectroscope. The amount of H₂ was determined as the difference between 100% and the sum of the CO₂, CO, and CH₄ concentrations. Simultaneously, the GCMS signal was utilized for a direct measurement of the concentration of H₂ and N₂-O₂ mixture.

3.7. SOC testing cells and selected measurement procedure

The support of the 1-inch button cells used for the measurements was composed of ~300 μm NiO–YSZ (60:40 v/v) composite with the porosity of approximately 30% and ~100 μm NiO–YSZ (60:40 v/v) functional layer of decreased porosity. The electrolyte was ~10 μm thick 8YSZ dense layer with ~5 μm thick CGO barrier layer prepared by co-sintering. The cells were fabricated via slurry casting and tape processing by our partner research team of Prof. Sea-Fue Wang from the National Taipei University of Technology. The air electrode was bimodal and composed of ~30 μm thick LSCF6428 (La_{0.6}Sr_{0.4}Co_{0.2}Fe_{0.8}O₃, Electro-Science Laboratories 4421A, USA) and ~ 10 μm thick LSC64 (La_{0.6}Sr_{0.4}CoO₃, Fiaxell SOFC Technologies, Switzerland) layers that were subsequently screen-printed, dried at 120 °C and co-sintered in situ during the startup of the rig at 800 °C for 4 h. The active surface area of the air electrode was 0.78 cm². LSC porous layer was acting as a current collecting layer [158]. The exemplary SEM fracture image is presented in Fig. 23.

Each time the cells were heated up under constant flow of N₂ up to 850 °C, and then the feeding gas was switched gradually to pure H₂ for 45 min to perform the reduction of the NiO-YSZ composite electrode. The conditions were selected based on the previous experience and assumed optimal for obtaining proper microstructure and

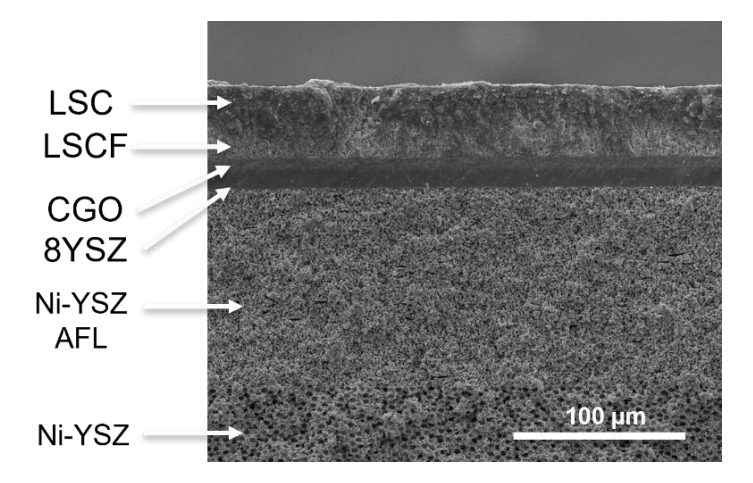


Figure 23. SEM fracture image of the Ni–YSZ supported Solid Oxide Cell.

power density. After prereduction the temperature was lowered typically to 700-750 °C depending on the experiment and the cell was held at that temperature for 12 h for conditioning and equilibration before the test.

For the initial measurement in the SOFC mode a constant stream of 50 ml·min⁻¹ of H₂ was introduced and the cell was subjected to the characterization of the performance. The iV curves were collected and analyzed each time before moving on to the electrolysis tests. The cells were also tested under 0.65 V for a prolonged period of 12 h to verify the stability and proper work of the cell. If any major issues were encountered with the cell efficiency during the SOFC operation further testing was terminated. After initial tests in SOFC mode, the cell was flushed with the mixture of 50:50 v/v H₂-H₂O mixture and equilibrated at 250 mA·cm⁻² for 12 h. After SOEC conditioning, the gas stream was switched to a CO₂/H₂O/H₂ mixture.

For direct SOEC methanation tests experimental procedure began with setting the inlet gas mixture to 20 vol% H_2O vapor with the rest made up of CO_2 and H_2 , which were mixed at a 1:2 ratio (by volume). This mixture was deliberately chosen to be far from equilibrium ($H_2:CO_2\approx 4$) to facilitate a measurable change in CH_4 concentration for each SOEC. The total flow rate was maintained at 28 ml·min⁻¹. After introducing the test gas mixture, the SOEC was initially conditioned at open-circuit voltage (OCV) until a stable voltage was reached. Then, a 1.3 V potential was applied until a stable current was achieved. The exhaust gas composition was analyzed using the FTIR-based measurement system described above [85]. The measurements of the concentrations of gases in the outlet mixture were performed between 700 °C and 500 °C with a 20 °C step and 60 min delay for thermal stabilization and equilibration. Simultaneously, the current through the cell was continuously monitored using a Gamry potentiostat, operating at a constant potential of 1.3 V. Additional tests were conducted under varying potential and gas mixture ratios, while maintaining a constant 20 vol% H_2O . The applied potential varied between 1.1 V and 1.6 V, and the H_2/CO_2 volume ratio at 1.3 V was adjusted between 0.25 and 7.

For the tests of the modified SOC in syngas production the procedure was nearly identical to the previously mentioned one except the water vapor concentration was switched to 25 vol.% of the inlet gas stream and CO_2 - H_2 were mixed in 50:50 v/v ratio. The ratio was chosen as such to better visualize the effect of the modifications on the catalytic and electrocatalytic activity for syngas formation via RWGS. The tests were conducted between 700 and 800 °C. Most of the electrolysis tests were conducted at ~260 mA·cm⁻² what resulted in utilization factor of H_2O (UF_{steam}) equal to 40 %. During the tests iV curves and EIS spectra were collected. The cells were subjected to prolonged studies with 12 h Time-on-Stream (ToS) measurements to validate the stability of the modified cells.

The quality of the prepared cells for efficient coelectrolysis and methane production was described by means of the CO_2 conversion (X_{CO2}), CH_4/CO yields (Y_i) and CH_4 selectivity (S_{CH4}) catalytic coefficients calculated from the measured molar flow values using Eq. 39 – 42. The yields were calculated considering the CO_2 input stream.

$$X_{CO_2}(\%) = \frac{\dot{n}_{CO_2}^{in} - \dot{n}_{CO_2}^{out}}{\dot{n}_{CO_2}^{in}} \times 100 \quad (39) \qquad S_{CH_4}(\%) = \frac{\dot{n}_{CH_4}^{out}}{\dot{n}_{CO_2}^{in} \times \frac{X_{CO_2}}{100}} \times 100 \quad (40)$$

$$Y_{CH_4}(\%) = \frac{\dot{n}_{CH_4}^{out}}{\dot{n}_{CO_2}^{in}} \times 100 \qquad (41) \qquad Y_{CO}(\%) = \frac{\dot{n}_{CO}^{out}}{\dot{n}_{CO_2}^{in}} \times 100 \qquad (42)$$

where: \dot{n}_i^{out} and \dot{n}_i^{in} are the molar flow rates of a specified gas (i) at the outlet and inlet of the reactor, respectively.

3.8 Packed-bed reactor and measurement procedures

Measurement of the catalytic activity of the powdered samples in methanation reaction was performed under atmospheric pressure (free-flow) using a packed-bed bed reactor setup. The main reaction chamber was a 4 mm inner diameter quartz tube sealed from both ends with compression fittings and Teflon ferrules. The reactor was filled each time with 100 mg of catalyst powder mixed properly with nonporous alumina carrier balls (99% Al₂O₃, Ø 1 mm) to ensure a linear and undisturbed flow of gases as well as provide even heat distribution throughout the catalyst bed. The volume of the bed was fixed for each test. Quartz wool was used on both ends of the bed to maintain good dispersion of the gas mixture and ensure that the catalyst remains in the same place. Everything was thermally insulated to minimize the temperature fluctuations. The whole setup involving the steam generation unit, temperature control, condensers, and gas detection system was the same as previously described and presented in Fig. 21. replacing the SOC rig with a packed-bed reactor.

Prior to each measurement, the catalyst was activated using simulated conditions of SOC reduction. It was heat treated under H₂ stream (24 ml·min⁻¹) for 2 h at 800 °C. After cooling down to 700 °C, reactants were added to the feed stream, and the resulting outlet gas composition was analyzed at 25 °C intervals down to 300 °C, allowing for a 60-minute equilibration period at each temperature step. The experimental setup aimed to replicate the conditions present at the working electrode of an SOEC during the coelectrolysis of CO₂ and H₂O. This was achieved by introducing a mixture of water vapor and syngas into the reactor. The inlet gas composition was carefully controlled, with a mixture of 80 vol% syngas (with a CO/H₂ ratio of 1:3) and 20 vol% water vapor. The selection of this specific gas composition was guided by thermodynamic equilibrium calculations for methanation reactions, performed using the HSC ChemistryTM software. The chosen mixture was designed to promote the highest possible methane yield while preventing the formation of carbon deposits during the catalytic tests [159]. This simplified approach allowed for the examination and prediction of the catalytic behavior of each transition metal under the ideal, simulated conditions of an SOEC's working electrode. The humidified syngas was passed through the unit at a total flow rate of 27.4 mLSTP min⁻¹ (16,440 mLSTP g_{cat} $^{1} \cdot h^{-1}$, GHSV = 4443 h^{-1}). The FTIR spectra for the calculation of gas concentration were collected every 5 min in the range of 4000-450 cm⁻¹ with 5 accumulations (4 cm⁻¹ spectral resolution). Prior to each test, a proper reactor check was performed to ensure no leakage. The long-term stability of the selected samples was evaluated through experiments conducted at 700 °C for 24 hours, utilizing the same feeding mixture and experimental setup. After the stability tests, the catalysts were re-tested using the standard catalytic procedure to determine the impact of high-temperature aging. The performance of the catalysts was then quantified based on the following parameters: CO conversion (X_{CO}), CH₄/CO₂ yields (Y_i), and selectivities (S_i). These values were derived from the measured molar flow rates, providing a comprehensive assessment of the catalysts' ability to produce methane. The given parameters were calculated using Eqs. 43 - 47.

$$X_{CO}(\%) = \frac{\dot{n}_{CH_4}^{out} + \dot{n}_{CO_2}^{out}}{\dot{n}_{CH_4}^{out} + \dot{n}_{CO}^{out} + \dot{n}_{CO_2}^{out}} \times 100$$
(43)

$$S_{CH_4}(\%) = \frac{\dot{n}_{CH_4}^{out}}{\dot{n}_{CH_4}^{out} + \dot{n}_{CO_2}^{out}} \times 100 \tag{44}$$

$$S_{CO_2}(\%) = \frac{\dot{n}_{CO_2}^{out}}{\dot{n}_{CH_4}^{out} + \dot{n}_{CO_2}^{out}} \times 100$$
 (45)

$$Y_{CH_4}(\%) = \frac{X_{CO} \times S_{CH_4}}{100} \tag{46}$$

$$Y_{CO_2}(\%) = \frac{X_{CO} \times S_{CO_2}}{100} \tag{47}$$

where \dot{n}_i^{out} is a molar flowrate of a specified gas at the outlet of the reactor.

3.9 Synthesis of materials

Methods for synthesizing nanomaterials can be classified into two distinctive groups as top-down and bottom-up approaches. In top-down route the material is getting transformed from bulk macromaterial into small nanometric particles. This approach includes techniques such as ball milling, thermal evaporation, laser ablation, or sputtering. Although top-down methods are much simpler to use, they are considered less effective in manufacturing extremely small nanoparticles and require a lot of energy input. Those two aspects are the main downsides of this approach [160]. On the other hand, a constructive technique is a name for the bottom-up approach and is a total opposite of top-down techniques. Nanomaterials are formed through the growth and self-assembly of atoms or molecules. In that case it is easy to obtain a well-defined shape, size, and increase the homogeneity of the materials [161,162][161]. The mixing of the substrates at a molecular level can decrease the energy needed for the synthesis of the desired material as normally much lower temperature is needed to obtain products [163]. This approach includes techniques such as chemical vapor deposition (CVD), hydrothermal route, co-precipitation and sol-gel method. Through proper control over the formation of the nanoparticles from the 'building blocks' it is possible to tune the physiochemical properties of the resulting material. In this study a major focus was put on two techniques from the bottom-up family i.e. impregnation method and co-precipitation. Even though throughout this thesis a few examples of the results considering the sol-gel route will be mentioned as a supporting results.

3.9.1 Wet impregnation method

Key characteristics of a high-performance catalyst are a narrow size distribution and high dispersion on the support material. The goal of catalyst synthesis, encompassing preparation and manufacturing, is to tailor the composition and structure of these materials to achieve the desired catalytic properties. In addition, the process should be easy, reproducible, possible to scale up, and low in cost to increase its technological viability [164].

All catalysts were synthesized using the novel wet impregnation method of a nanometric CeO₂ substrate (99.5%, Alfa Aesar, particle diameter: 15-30 nm, SSA: 30-50 m²g⁻¹). Solutions of transition metal nitrates — Ni(NO₃)₂·6H₂O (99.9%, Merck), Co(NO₃)₂·6H₂O (99.9%, Merck), Cu(NO₃)₂·6H₂O (99.9%, Merck), Mn(NO₃)₂·4H₂O (99%, Merck), and Fe(NO₃)₃·9H₂O (99.95%, Merck) — of 0.2 M concentration were prepared using 10 vol% ethanol in deionized (DI) water as a solvent. A β -cyclodextrin (β CD, \geq 97%, Sigma-Aldrich) as a coordinating/capping agent (0.05 mol β CD per 1 mol cations) was then added and stirred at room temperature until clear. These solutions were added to the dry CeO₂ nanopowder to achieve a 10 wt% metal loading (based on the Me⁰ form). The resulting slurry was evaporated with constant stirring at 90 °C until a viscous paste formed. The solid was then dried at 120 °C for 12 hours, ground using a mortar, placed in an alumina crucible, and fired at 400 °C for 4 hours in air to decompose the nitrates and remove organic residue. An additional series of catalysts without the usage of the β CD was prepared for comparison and study of the β CD influence.

A similar approach was used to prepare the modified steam electrodes in SOEC performing coelectrolysis of CO₂-H₂O mixture. The first study was conducted on Co impregnation. The preparation involved a series of steps, beginning with the reduction of the half-cells at 850 °C under an H₂ atmosphere to increase cermet layer porosity. The cells were impregnated with 100 μL of Co-βCD precursor solution (maximum sorption volume of the layer) and placed in a vacuum chamber for 15 minutes to facilitate penetration. The samples were dried and sintered to decompose nitrates and organics at 450 °C for 4 h. The samples were prepared by repeating the impregnation step one, two, and three times, which resulted in different Co⁰ loadings (1.8, 3.6, and 5.4 wt%). A reference sample was also prepared, following the same thermal treatment but without the impregnation process. The cells containing other transition metals (Cu, Mn, Fe) were prepared according to the same procedure and the amount of the metal was fixed to 3.6 wt.% (2 cycles) based on the results obtained from Co-impregnation.

3.9.2 Co-precipitation method for NiO-YSZ and YSZ scaffold synthesis

One of the very popular methods in synthesis of nanomaterials is called co-precipitation. It is commonly used thanks to its simplicity, wide scalability, ability to mix the constituents at atomic scale, and full control over morphology of the particles [165]. The process usually involves

two major steps. The first one is the formation of nanoparticles using coprecipitation reaction, which rely on crushing out the insoluble oxides or hydroxides from the solution by the addition of the precipitating agent. The second step involves drying, removing solvents, and further processing. The coprecipitation method ensures uniform mixing of the components at the atomic scale. This facilitates the formation of the final product with the desired phase and crystallinity at lower temperatures and shorter holding times during the calcination. As a result the nanometric morphology of the precursor particles can be retailed along internal porosity and high surface area [166].

All samples were prepared using novel and simple preparation technique based on precipitation of the metal ions from aqueous solution enriched with a stabilized micellar system for structure templating. Firstly, a proper amount of precursor salts ZrCl₄ (Alfa Aesar, 98%), YCl₃·6H₂O (Alfa Aesar, 99.9%), NiCl₂·6H₂O (Chempur, 98%) was weighed and placed into a beaker depending on the final product to be fabricated (NiO-YSZ cermet or pure YSZ). The Ni-YSZ cermet composition was designed to result in 60:40 v/v ratio of metallic Ni and YSZ after the synthesis and sintering. A micelle-forming system, composed of CTAB (cetyltrimethylammonium bromide, Alfa Aesar, 98%) and Pluronic P123 (PEG-PPG-PEG, Merck, Mn~5800), was then added. The CTAB concentration was set to 25 times its critical micelle concentration (CMC) in DI water at room temperature (~25 mM). Pluronic P123 was added at a concentration of 1 mM. These concentrations were based on screening studies of the micelle system before fabrication of the larger-scale batch. The mixture was diluted with DI water to achieve final metal cation concentrations of 0.1, 0.2, 0.25, 0.3, 0.4, and 0.5 M. The solution was each time heated to 70 °C and stirred until cleared, then cooled to room temperature using an ice bath. A calculated amount of NaOH (POCH, 99.9%) was dissolved in 20 cm³ of DI water and brought to room temperature. The NaOH solution was added in 5 ml increments to YSZ or NiO-YSZ precursor solutions with heavy stirring until a pH of \sim 10 was reached and a gel formed. The mixture was agitated for 1 hour and aged for another 12 hours to ensure completion of the reaction. The gel was then separated by centrifugation, collected after decanting the supernatant, and dried at 80 °C overnight. The resulting xerogels were ground using a planetary mill in ZrO₂ milling jars, yielding precursor powders. After a final drying step at 80 °C, the precursor powders were ready for characterization and further processing.

3.9.3 Preparation of the specimens for conductivity measurements

The pellets for the DC4W conductivity measurement were prepared by uniaxial dry pressing of the precursor powders using 20 mm diameter circular shaped die. Later, the green pellets were sintered at 1400 °C (YSZ) or 1370 °C (NiO–YSZ) for 4 h with a heating-cooling rate of 180 °C·h⁻¹. Conventional NiO–YSZ half-cells were provided by the National Taipei University of Technology. The reference YSZ scaffold from conventional cell build-up was prepared by

etching the Ni metal from the conventional cell. The Ni–YSZ composite was reduced at 800 °C and etched with the mixture of 30 vol% HNO₃ with a few drops of HCl at 80 °C. The etching was performed until there was no evidence of Ni nitrate formation. The etched scaffolds were then heavily washed with a bunch of distilled water and strengthened by firing at 1300 °C for 2 h. This step increased the cohesion of the YSZ grains without altering the porosity.

4. RESULTS AND DISCUSSION

4.1 Influence of nanometric catalysts on methanation and methane reforming

Unlike most catalyst studies, this work focused on the catalysts for direct methanation within SOEC operation conditions. The research explored metal-ceria composites as potential catalyst candidates. Specifically, various transition metals (Ni, Co, Cu, Fe, Mn) were deposited on commercially available CeO₂ (99.5%, Alfa Aesar, particle diameter: 15-30 nm, SSA: 30-50 m²g⁻¹) using wet impregnation assisted by β-cyclodextrin. While comprehensive studies on this material are lacking, based on existing literature, it was hypothesized that this approach would yield smaller metallic nanoparticles (enhancing the active surface area for catalytic reactions), stronger bonds to a highly active CeO₂ support, and extended catalyst durability under operating conditions. The results were widely described in [167] Blaszczak P., Mizera A., Bochentyn B., Wang S.-F., Jasiński P. Preparation of methanation catalysts for high temperature SOEC by βcyclodextrin-assisted impregnation of nano-CeO₂ with transition metal oxides. Int J Hydrogen Energy 2022; 47: 1901–16. 10.1016/j.ijhydene.2021.10.144. Besides those core findings, some additional work was done in the field of catalysis in SOC systems. It involves Cu nanocatalysts supported on various oxides used for Direct Internal Reforming Solid Oxide Fuel Cells (DIR-SOFCs). The cited results will also be included as supporting material in this section. The findings were previously presented in [168] Mizera A., Blaszczak P., Bochentyn B., Lach R., Drożdż E. Cu supported on various oxides as a candidate catalyst for dry methane reforming in DIR-SOFCs systems. Int J Hydrogen Energy 2022; 47: 25647–61. 10.1016/j.ijhydene.2022.06.016.

4.1.1 Phase composition

Before conducting catalytic tests, all synthesized powders were thoroughly characterized to assess the impact of β -cyclodextrin on the final product. The comparative X-ray diffraction (XRD) patterns of the prepared metal/CeO₂ catalysts are illustrated in Fig. 24. The powders were composed of two oxide phases, except for the Fe-impregnated sample. The most prominent peaks were attributed to cubic CeO₂ (Fm-3m), following included database pattern (reference in Fig. 24 bottom). The broadening of the peaks is a result of the nanometric nature of the support material used for the catalyst preparation.

The XRD patterns were overlaid to highlight the differences between catalysts prepared using a conventional method of wet impregnation and the ones prepared utilizing the β CD-assisted technique. Generally, the peaks corresponding to transition metal oxides were of relatively low intensity and significantly broadened. In fact, the mentioned peaks could be easily distinguished only in the CeO₂ samples where the β CD additive was not included. Conversely, the introduction of the β CD capping agent into the precursor solutions led to even broader and

less intense peaks. This suggests that the addition of β CD enhanced metal dispersion across the support surface and resulted in formation of smaller crystallites (nanoparticles) [169,170]. For the Fe-impregnated sample, reflections from iron species were not detected, likely due to the high dispersion of nanoparticles, the formation of an amorphous structure, and/or fluorescence under Cu anode irradiation.

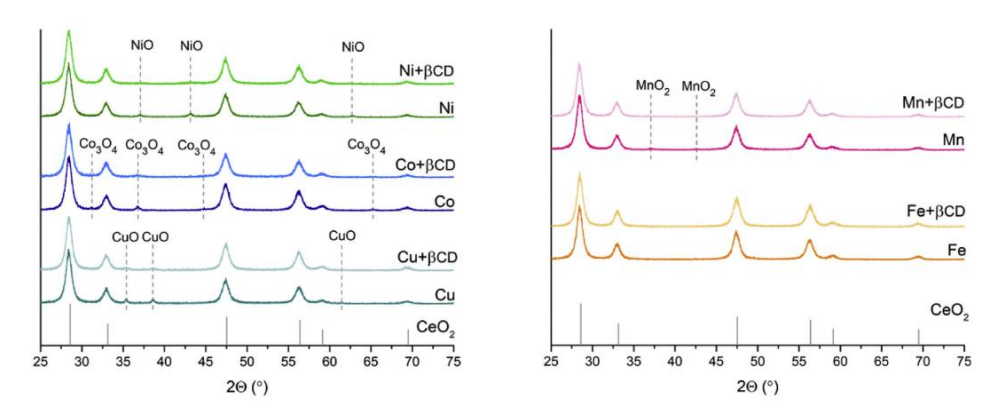


Figure 24. XRD patterns of the impregnated samples with/without β-cyclodextrin additive [167].

To investigate the potential formation of a solid solution between the metal oxides and CeO₂, the lattice constant was determined using the Rietveld refining method. The lattice parameters of the impregnated CeO₂ are detailed in Table 4, along with the corresponding goodness-of-fit (GOF) factors. A minor deviation in the lattice constant of the impregnated nano-CeO₂ was observed compared to 5.408 Å of pure unmodified ceria. The obtained values suggest the possible, although highly surficial, formation of a solid solution between the active metal oxide and the ceria support.

Table 4. Lattice parameters obtained via Rietveld refining.

	CeO ₂	Ni		Со		Cu		Mn		Fe	
		pure	βCD								
Lattice parameter (a=b=c) (Å)	5.408	5.403	5.401	5.405	5.401	5.402	5.401	5.402	5.400	5.405	5.399
GOF	1.68	1.40	1.23	1.24	1.32	1.27	1.22	1.53	1.29	1.21	1.49

The nanoparticles appear to interact with the support material through the corresponding CeO_2 -doped interlayer, as transition metals can minorly dissolve into the ceria lattice. Although minor changes were noted across different impregnated samples, the addition of the βCD capping agent resulted in a more pronounced decrease in the lattice parameter. This effect can primarily be attributed to the enhanced reduction of the Me_xO_y size due to the addition of βCD , as well as the increased presence of the interfacial or interstitial solid solution. The higher dispersion and integration were achieved through interactions between βCD and metal cations, leading to the formation and breakdown of inclusion complexes. Research by M. Najafpour *et al.* [171] on Mncyclodextrin complexes concluded that strong interactions between Mn cations and the oligosaccharide ring facilitated the formation of well-dispersed nanoparticles. Similarly, studies

by H. Liu *et al.* [172] indicated that a small addition of cyclodextrines ensured higher Ni dispersion over the SBA-15 substrate. The peaks observed in mass spectrometry for Ni(NO₃)₂-CD mixtures were pointing out the formation of Ni²⁺CD and NO₃CD complexes. The ability of βCD to surround Ni ions is crucial for preventing the sintering of Ni nanoparticles during the calcination process.

4.1.2 Reducibility and integration of metal with the support

Smaller nanoparticles tend to form stronger interactions with the support material due to their higher surface energy. This synergistic effect arising from reduced particle size and strong coupling at the interface is highly desirable. The use of smaller metal particles ensures a higher density of surface reaction centers, while the formation of a mixed interfacial layer can enhance both the efficiency and stability of the metal-oxide catalyst. On the other hand, the thermal processing of the powders may result in too strong integration of the metallic nanoparticles with the support limiting the accessible catalytic centers on the metal. It is essential to find a silver lining between nanoparticle integration and the availability of a reducible surface. To investigate the catalysts' behavior during the activation process, H₂-TPR measurements were carried out. The TPR profiles are shown on Fig. 25. The first reduction profiles are also included in the graphs (R1 insets).

The TPR profile of the CeO_2 support is a bimodal curve with two distinct peaks, located at 507 °C and 775 °C, labeled as β and γ , respectively. This behavior is typical for ultrafine, nanometric ceria particles with a moderate specific surface area and relatively low internal porosity. The first peak (β), existing at a lower temperature, corresponds to the surface reduction of CeO_2 , which is followed by the second peak (γ) ascribed to the bulk reduction of oxygen in solid [173,174]. The lower temperature of the reduction compared to micrometric ceria powders is attributed to high specific surface area and developed porosity of the nano- CeO_2 powder. Furthermore, the nanocrystallinity of the ceria is changing the valence state of the cations in the bulk material. The concentration of surface oxygen species, amount of oxygen vacancies, and the ratio of Ce^{3+} to Ce^{4+} ions can be significantly higher when reducing the particle size of ceria. For instance, Xu *et al.* [175] observed a substantial decrease in the bulk reduction peak height as the CeO_2 particle size decreased from 30 to 4.4 nm. Concurrently, Zhuo *et al.* [176] reported that the concentration of oxygen vacancies was couple orders of magnitude higher for 4 nm particles of ceria compared to 60 nm.

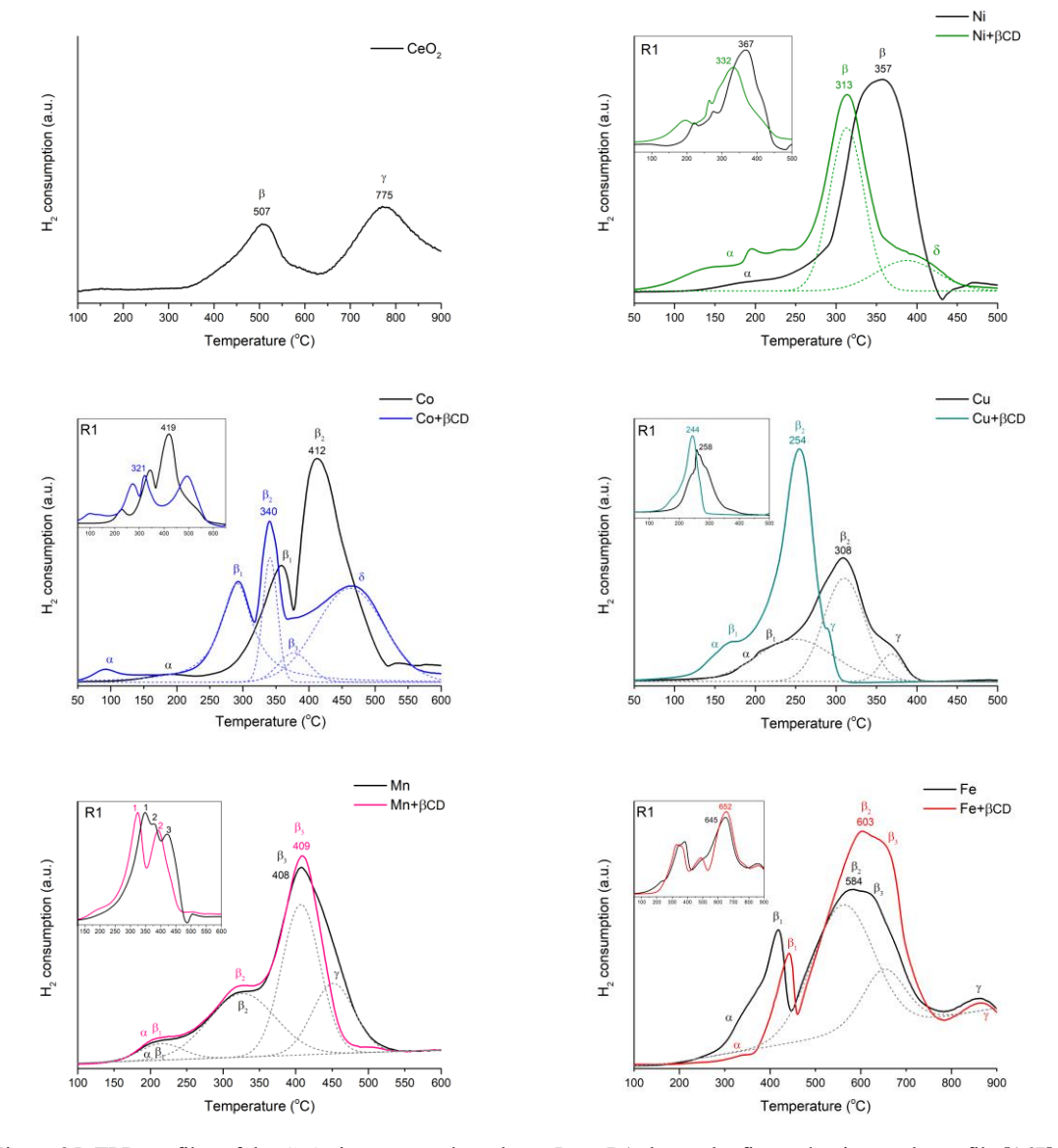


Figure 25. TPR profiles of the CeO₂ impregnated catalysts. Inset R1 shows the first reduction cycle profile [167].

A comparison of the TPR profiles for nickel-, copper-, and cobalt-impregnated CeO_2 samples revealed significant differences in the reducibility of the metal oxide particles synthesized via conventional and βCD -assisted methods. In all three cases, the main reduction peaks of the samples prepared using βCD were shifted to lower temperatures, indicating the formation of smaller and more uniformly dispersed metal oxide nanoparticles on the CeO_2 surface. These temperature shifts were evident in both the first and second reduction cycles, with minimal or no change in the position of the primary reduction peaks, suggesting good cycling stability. For Ni- , Co-, and Cu-based samples, the suppression of peak shifts stands for their high stability under redox cycling and low migration or sintering of the metallic nanoparticles. In contrast, the impact of the βCD additive on Mn- and Fe-impregnated CeO_2 samples was less pronounced. Across all samples, a reduction peak (α) in the low-temperature region ($\sim 200 \, ^{\circ}C$) was observed, commonly attributed to the reduction of surface-adsorbed oxygen species and hydroxyl groups.

The TPR profile of Ni-CeO₂ include a dominant hydrogen consumption peak (β), which was attributed to the reduction of bulk NiO species that are weakly bound to the support surface [177]. In the sample prepared without β -cyclodextrin, this reduction step occurs at approximately 357 °C and constitutes the primary feature of the profile. In contrast, the β CD-assisted Ni-CeO₂ sample exhibits a downward shift in the β peak temperature, along with the emergence of an additional reduction peak at ~400 °C, designated as δ . This δ peak was ascribed to the reduction of finely dispersed Ni species that are strongly anchored to the ceria support via Ni–O–Ce bonds, suggesting the formation of a solid solution or interfacial mixed oxide layer [178,179]. The enhanced intensity of the low temperature α peak, combined with the appearance of the δ feature, provides strong evidence that β CD facilitates improved nickel dispersion and promotes partial incorporation of Ni²⁺ into the ceria lattice.

The TPR profile of the β CD-assisted Co-impregnated CeO₂ sample exhibited significantly greater complexity compared to its conventionally prepared counterpart. The deconvolution ended up in five distinct reduction processes distinguished. The reduction behavior of Co₃O₄ remains a topic of ongoing debate, as its reduction characteristics are highly sensitive to factors such as synthesis method, catalyst composition, and oxide particles' dispersion. It is generally accepted that bulk Co₃O₄ particles with weak interaction with the support undergo a single-step reduction directly to metallic Co⁰. However, for smaller, more dispersed particles interacting strongly with the ceria support, a two-step reduction pathway involving CoO as an intermediate is typically observed [180]. In the β CD-Co/CeO₂ sample, the initial peak (β ₁) was assigned to the reduction of Co³⁺ to Co²⁺ in Co₃O₄ interacting with the CeO₂ support [181]. The subsequent reduction peak, β ₂, appearing at ~340 °C for β CD-Co/CeO₂ and at ~412 °C for conventionally prepared Co/CeO₂, is attributed to the direct reduction of discrete Co₃O₄ particles to Co⁰. This is in line with the assignments made by Luo *et al.* for similar Co₃O₄/CeO₂ systems [182]. For the conventionally prepared catalyst, this process was dominant.

In contrast, two additional reduction features were observed in the β -assisted sample. The β_3 peak likely corresponds to the intermediate reduction of CoO species, while the broad δ peak at approximately 460 °C is attributed to the reduction of Co²⁺ species strongly embedded in the ceria matrix. These species exhibit greater resistance to reduction due to the stabilizing influence of ceria's high oxygen storage capacity (OSC) and the ability of Co cations to accommodate mixed-valence [182,183].

Additionally, the presence of hydrogen spillover was proposed during the reduction process. Once Co₃O₄ species got reduced to metal, these clusters act as active centers for H₂ dissociation. The resulting hydrogen ions facilitates further reduction, particularly of strongly integrated Co²⁺ species and even the underlying support, thereby inducing a self-promoted reduction process and a shift of reduction features toward lower temperatures. The enhanced cobalt dispersion achieved with βCD thus contributed to lower temperature reduction [184,185].

Although the total hydrogen uptake measured through the integration of the reduction peaks for both the βCD-modified and unmodified samples was comparable, further investigations were conducted to assess whether the formation of a solid solution phase between the metal oxide and CeO₂ in the βCD-assisted (Ni/Co)/CeO₂ catalysts led to the incorporation of a significant fraction of Ni or Co ions into the ceria lattice. Such incorporation could potentially decrease the number of reducible, catalytically active metal particles and would be considered negative effect. To explore this, H₂-TPR measurements were carried out using nanocrystalline CeO₂ doped with 20 mol% Ni or Co, synthesized via the reversed microemulsion method. Detailed synthesis protocols and microstructural characterization were reported in [186] Hołówko B., **Blaszczak P.**, Chlipała M., Gazda M., Wang S.-F., Jasiński P., Bochentyn B. *Structural and catalytic properties of ceria layers doped with transition metals for SOFCs fueled by biogas*. Int J Hydrogen Energy 2020; 45: 12982–96. https://doi.org/10.1016/j.ijhydene.2020.02.144.

The TPR profiles and corresponding XRD patterns before and after reduction for Ce_{0.8}Ni_{0.2}O₂ and Ce_{0.8}Co_{0.2}O_{2-σ} are shown in Fig. 26. Each TPR profile could be deconvoluted into two main regions: (I) low-temperature reduction of surface-bound and weakly integrated Me^{x+} species, and (II) high-temperature reduction of Ni²⁺ or Co³⁺ ions strongly incorporated into the CeO₂ lattice through Me–O–Ce interactions. Region II also included the partial reduction of Ce⁴⁺ to Ce³⁺, likely facilitated by hydrogen spillover and the presence of highly dispersed transition metal species. A slight decrease in the overall reduction temperature, particularly for Co-doped CeO₂, was observed.

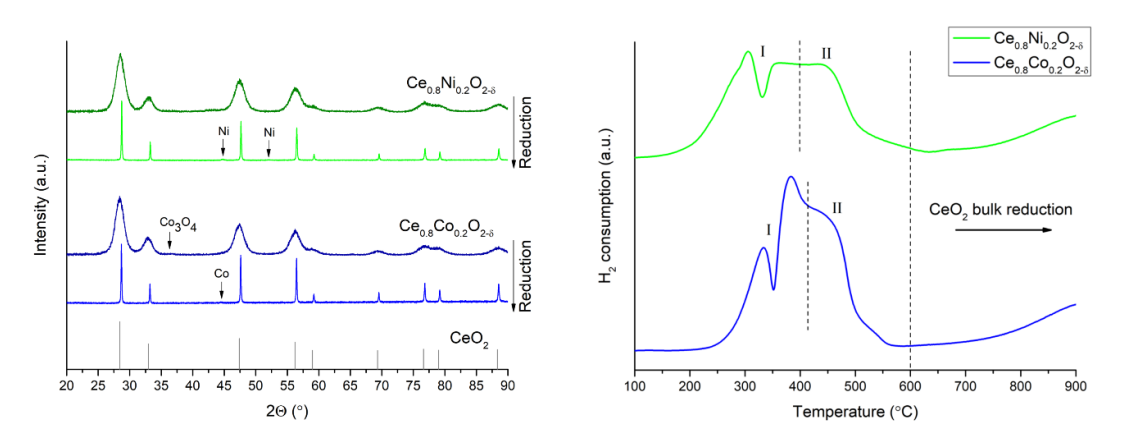


Figure 26. XRD patterns before/after reduction (left) and TPR profiles (right) of Ce_{0.8}Ni_{0.2}O_{2-δ} and Ce_{0.8}Co_{0.2}O_{2-σ} I – surface reduction and II – reduction of Ni and Co ions strongly integrated with the support [167].

The Rietveld refinement of XRD patterns (Fig. 26, left) revealed lattice parameters of 5.408 Å (GOF = 1.57) for $Ce_{0.8}Ni_{0.2}O_{2-\sigma}$ and 5.398 Å (GOF = 1.62) for $Ce_{0.8}Co_{0.2}O_{2-\sigma}$ prior to reduction. After H₂-TPR treatment, both materials exhibited an increase in lattice constants to 5.415 Å and 5.414 Å, respectively. These values closely match the reported unit cell parameter for pure microcrystalline CeO_2 (5.411 Å), supporting the partial substitution of Ni and Co into the fluorite structure and their subsequent reduction to the metallic state. This indicated that even if the

dissolution occurs, the compounds are not thermodynamically stable in reducing atmosphere and the compounds decompose to mixed material upon heat treatment under H_2 .

Coming back to TPR profiles of the catalysts, previous investigations of CuO_x – CeO_2 catalytic systems have demonstrated that the formation of Cu–Ce interfacial interactions enhance the overall redox behavior of the catalyst, as ceria not only acts as a support but also participates actively in redox processes. This synergy results in improved reducibility of both CuO_x and CeO_2 compared to their isolated aggregates [187]. According to the H_2 -TPR analysis of the Cu-impregnated CeO_2 catalyst (Fig. 25), the reduction profile could be deconvoluted into three distinct peaks: β_1 , β_2 , and γ . The β_1 peak, observed at low temperatures, was ascribed to the reduction of finely dispersed CuO_x species. The β_2 peak corresponded to the reduction of Cu^{2+} ions that are strongly integrated within the CeO_2 surface via Cu– $[O_x]$ –Ce interactions. A pronounced γ shoulder peak was detected in the conventionally prepared catalyst (i.e., without the β CD additive) and got assigned to the reduction of big CuO agglomerates [188]. The downward shift in reduction temperature and increased intensity of the β_2 peak in the β CD-assisted sample clearly indicate the beneficial role of β CD usage in enhancing Cu dispersion, decreasing particle size, and promoting metal–support interactions. These modifications are critically important for improving catalytic performance.

The promising results concerning the usage of copper in carbon-containing environments were also obtained in the study of Cu-based catalysts in dry reforming of biogas (65 vol.% CH₄ and 35 vol.% CO₂) for DIR-SOFC [168]. In this study a series of catalysts containing various amounts of Cu were prepared using different supporting oxides, namely Al₂O₃, AlOOH, ZrO₂, CeO₂, and SrTiO₃. The impregnated catalysts were tested for reducibility and support integration via H₂-TPR, and the results are presented in Fig. 27. The reduction analysis of pure CuO. derived from the thermal decomposition of copper (II) nitrate, indicates that its reduction initiates at temperatures approximately 80-100 °C higher than those observed for Cusupported catalysts, while ends around

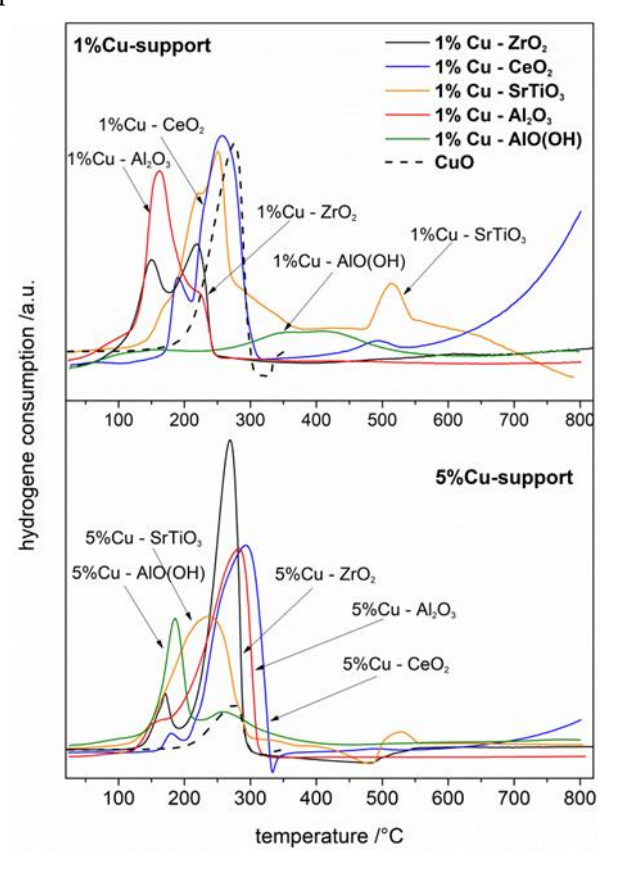


Figure 27. TPR profiles of the catalysts [168]. Reduction profile of copper (II) oxide shown in dashed line.

320 °C, aligning with the reduction profiles of catalytic cermet materials. Upon comparing the reduction profiles of Cu-supported materials with varying copper contents, it is evident that, for most samples, reduction peaks occur within similar temperature ranges. Notably, the Cu/AlOOH samples exhibited distinct profiles, suggesting differences in copper dispersion and interaction with the support. Within the range of approximately 70–350 °C, reduction peaks correspond to the reduction of copper oxide deposited on supports. These profiles are complex, but in most cases bimodal, due to the reduction of copper oxide in the following manner: $CuO \rightarrow Cu_2O \rightarrow Cu$. In two cases, CuO supported on CeO_2 and $SrTiO_3$, the profile exhibits additional reduction peak at higher temperatures (480–560 °C and 420–550 °C), indicating more complex reduction behavior.

The temperature-programmed reduction (TPR) profiles of Cu-supported catalysts revealed that the reduction behavior is influenced by both the copper content and the nature of the support material. The presence of additional reduction peaks at higher temperatures suggests that the interaction between copper and the support material plays a significant role in the reduction process. These findings highlight the importance of considering both the metal loading and the support characteristics when designing catalysts for specific reactions.

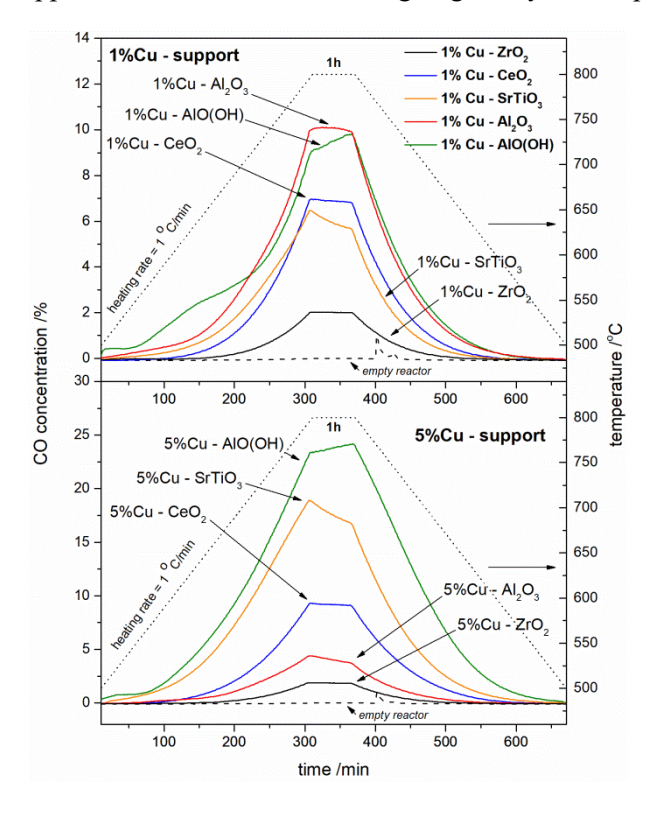


Figure 28. The change of CO concentration during the catalytic tests for 1% Cu and 5% Cu samples in temperature and process time [168].

After initial characterization, deeply described in [168] the samples were subjected to the tests in packed-bed reactor in the heating-cooling range from 500 to 800 °C with 1 h of holding time at 800 °C. All samples were activated at 600 °C for 2 h in hydrogen prior to the measurements. The catalytic tests were carried out in gas mixture simulating biogas fed at flow rate of 30 ml·min⁻¹. The results of the tests concerning the CO concentration in the outlet stream are presented in Fig. 28.

As observed, within both material series, the Cu/ZrO₂ composites exhibited the lowest catalytic activity. In contrast, the Cu/AlOOH samples demonstrated the highest activity among the studied

systems. The Cu/SrTiO₃ and Cu/CeO₂ were in between yet still had considerable catalytic performance for both low and high copper loadings. In case of the Cu/SrTiO₃ system, the elevated activity might be attributed to the high copper dispersion facilitated by the incorporation of copper

into the SrTiO₃ lattice. Interestingly, the performance of the Cu/Al₂O₃ system displayed unexpected behavior: the 1% Cu/Al₂O₃ composite showed catalytic activity comparable to or slightly exceeding that of 1% Cu/AlO(OH). However, in the 5% Cu/Al₂O₃, the activity was significantly reduced. This suggests that lower catalytic efficiency of the 5% Cu/Al₂O₃ material may be due to fewer accessible copper active sites, potentially caused by particle agglomeration or poor dispersion, limiting their interaction with reactant gases. This study revealed that metal loading is as important as the proper selection of the support material. The synergy between the active metallic centers and the oxide can influence not only the activity but stability and alter the reaction products.

The TPR profiles corresponding to the second reduction cycle for both Mn-CeO₂ catalysts exhibited similar features, characteristic of MnO₂ reduction behavior (Fig. 25). The sequential hydrogen consumption peaks — β_1 , β_2 , and β_3 — were assigned to the step reduction of MnO₂ \rightarrow Mn₂O₃, Mn₂O₃ \rightarrow Mn₃O₄, and Mn₃O₄ \rightarrow MnO, respectively [189]. In the conventionally prepared Mn/CeO₂ sample, the presence of larger Mn₃O₄ accumulates contributed to an additional overlapping γ peak, which is indicative of bulk phase reduction. The influence of the β CD additive on MnO₂ reducibility was primarily observed during the first reduction cycle (refer to Mn R1 inset, Fig. 25). The significantly altered TPR profile, exhibiting two distinct peaks, is attributed to direct transitions: (1) Mn⁴⁺ \rightarrow Mn³⁺ and (2) Mn³⁺ \rightarrow Mn²⁺. The bypassing of the Mn₃O₄ intermediate phase is quite common for highly nanostructured MnO₂ with high specific surface area (SSA), where such structural development can facilitate direct, two-step reduction pathway. The positive impact of the β CD additive was in the end too weak to suppress the tendency of MnO to agglomeration and sintering, the phenomena, which lower its cycling, long-term stability and catalytic activity.

The H₂-TPR profiles of Fe-impregnated CeO₂ (Fig. 25) revealed four main reduction stages in addition to the low-temperature peak (α). Both samples exhibited similar reduction behavior, regardless of the presence of β -cyclodextrin (β CD) in the precursor solution. The reduction pathway was consistent with that of Fe₂O₃, as extensively described in the literature [190–192]. The β ₁ peak, observed within the 350–450 °C range, corresponded to the reduction of Fe₂O₃ to Fe₃O₄. The subsequent β ₂ and β ₃ peaks were described as overlapping reduction processes of Fe₂O₃ \rightarrow FeO and FeO \rightarrow Fe⁰ reductions, respectively. The γ peak was associated with the reduction of bulk FeO clusters to metallic iron.

Overall, the H₂-TPR results indicated that the microstructural modifications induced by the β CD additive are most significant when transition metal ions such as Ni, Co, or Cu are impregnated. The observed decrease in nanoparticle size is likely due to the capping effect of β -cyclodextrin, which can encapsulate metal cations within its macrocyclic glucose rings. This encapsulation enhances metal ion dispersion and mitigates agglomeration during burnout. Furthermore, upon combustion, β CD may act as a mild reducing agent, promoting the formation

of nonstoichiometric metal oxides and facilitating their partial incorporation into the surface layers of the slightly reduced CeO₂ support.

4.1.3 Microstructure

Specific surface area (SSA) and microstructural characteristics are fundamental properties of catalysts, impacting their overall performance to a degree comparable with chemical composition. The N₂ adsorption–desorption isotherm of the representative βCD–Ni/CeO₂ sample is shown in Fig. 29, with all other samples exhibiting similar profiles. According to the classification by IUPAC, the observed isotherms correspond to type II, indicative of materials possessing a well-developed mesoporous structure. The isotherms had an H₃-type hysteresis loop, which is characteristic of materials with slit-like pores and non-uniform, open pore structures, indicating good connectivity between intragranular voids. This microstructure is advantageous for facilitating efficient transport of reactant gases [193,194].

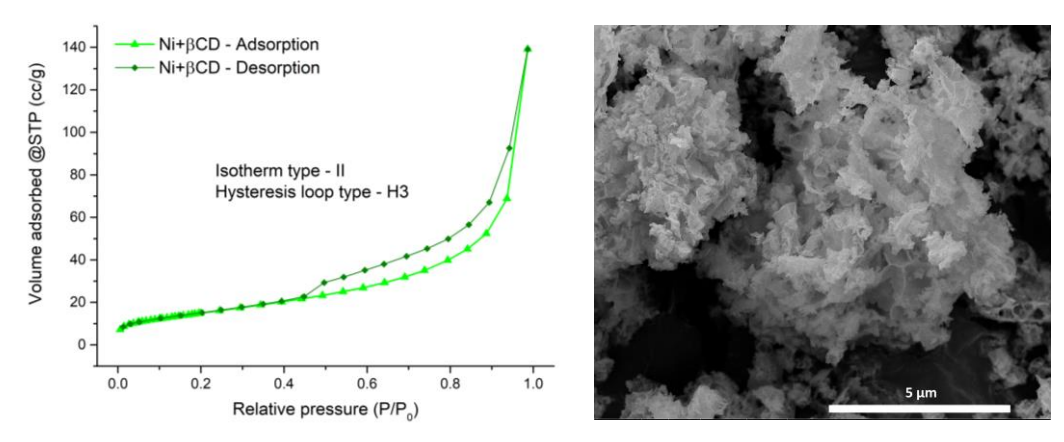


Figure 29. Adsorption-desorption isotherm (left) and SEM image (right) of the βCD-Ni/CeO₂ catalyst [167].

Transmission electron microscopy (TEM) imaging combined with micro-energy dispersive X-ray spectroscopy (μEDS) revealed that the precursor solution with βCD significantly improved nickel dispersion across the ceria support. The images are presented on Fig. 30. These findings are consistent with earlier observations from TPR and XRD analyses. The use of cyclodextrin promoted uniform distribution of Ni²⁺ ions throughout the sponge-like nanostructure of CeO₂. High-resolution TEM (HR-TEM) imaging (Fig. 30B) provided further evidence for the partial formation of a mixed NiO–CeO₂ phase. Bright spots in the image correspond to the (111) lattice planes of cubic CeO₂, with an interplanar spacing of approximately 3.1 Å, in agreement with literature values [195]. Interestingly, in the identified regions, these (111) distances were consistently lower (ranging from 2.9 to 3.1 Å), suggesting lattice distortion potentially caused by the diffusion of minor amount of Ni in ceria. This contraction in d-spacing, along with μEDS data, supports the hypothesis of Ni incorporation into the CeO₂ lattice. Such doping likely occurs at the metal–support interface during synthesis, facilitated by cation interdiffusion [196]. The resulting surficial Ni–O–Ce mixed oxide is considered beneficial for catalytic applications such as CO₂

methanation, due to improved metal-support interaction and redox properties [197]. Comparable structural features were also observed for the Co–CeO₂ catalyst series.

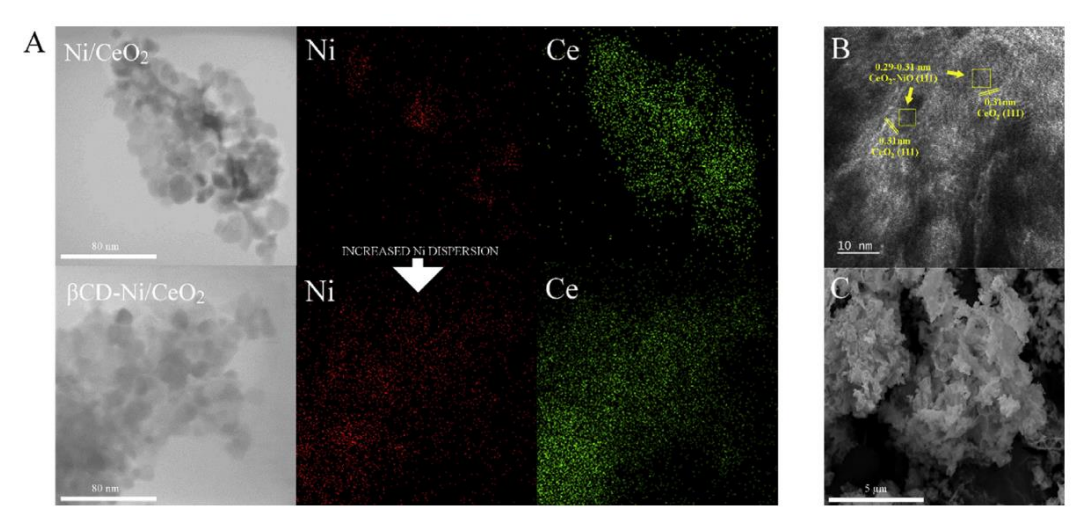


Figure 30. (A) TEM images and elemental maps of Ni and Ce in βCD-Ni/CeO₂ and Ni/CeO₂ catalysts, (B) HR-TEM image of βCD-Ni/CeO₂ and (C) SEM image of βCD-Ni/CeO₂ [167].

The specific surface areas (SSA) of the as-synthesized catalyst powders are summarized in Table 5. All impregnated samples exhibited higher SSA values compared to the unmodified CeO_2 , with measured surface areas ranging from 49.8 to $70 \, \text{m}^2\text{g}^{-1}$ In nearly all cases – except for the Fe-impregnated catalyst – the inclusion of β -cyclodextrin (β CD) during synthesis resulted in a modest increase in SSA, attributed primarily to enhanced metal oxide dispersion

Table 5. Specific surface area (SSA) and total pore volume of the catalysts. Error in SSA value estimated as $\pm 5\%$ according to the manufacturer of the equipment.

	CeO ₂	Ni		Cu		Co		Mn		Fe	
		pure	βCD								
BET surface area (m ² g ⁻¹)	35.5	52.1	55.4	49.8	60.6	57.0	61.1	52.7	54.4	70.0	69.8
Total pore volume (10 ⁻¹ ccg ⁻¹)	1.5	1.9	2.2	1.7	2.0	1.6	1.7	1.6	1.7	1.8	2.1

The most significant effect of β CD was observed in the Cu-impregnated sample, where the SSA increased from 49.8 to $60.6 \,\mathrm{m^2 \cdot g^{-1}}$. This enhancement is likely due to the strong and stable complexation of $\mathrm{Cu^{2+}}$ ions with β CD, further stabilized by nitrate ($\mathrm{NO_3^{-1}}$) counterions. Previous studies have shown that Cu and Co form particularly stable and thermally distinct complexes with β CD, differing from those formed with other transition metal salts and influencing their decomposition behavior [198]. This suggests that, in the case of Cu- and Co-impregnated catalysts, the presence of β CD facilitates the formation of significantly smaller nanoparticles – consistent with the notable temperature shifts observed in their respective H₂-TPR profiles. In contrast, the influence of β CD on SSA was less pronounced in Mn- and Fe-containing catalysts. The Fe/CeO₂ sample exhibited the highest SSA overall, likely due to the formation of highly amorphous Fe₂O₃ phases during low-temperature (400 °C) calcination, which preserved the

nanostructured morphology of the support. Total pore volumes for the catalysts ranged from 0.16 to $0.22 \, \text{cm}^3 \cdot \text{g}^{-1}$, with generally higher values observed in β CD-assisted samples, further supporting improved textural properties induced by the additive.

4.1.4 Catalytic efficiency

The catalytic performance of the prepared samples was evaluated using a fixed-bed reactor system, with FTIR spectroscopy employed to analyze the composition of the exhaust gases. A baseline experiment, conducted with unmodified CeO₂ mixed with alumina as a diluent, exhibited no detectable methane formation. Among all tested catalysts, only the Ni- and Co-impregnated CeO₂ samples demonstrated visible methane amounts at the outlet of the reactor. For the remaining samples, CH₄ concentrations remained below 1%, and thus only the Ni- and Co-based catalysts – with and without β-cyclodextrin – were selected for further investigation. Temperature-dependent CO conversion, CH₄ selectivity, and CH₄/CO₂ yield were quantified and presented in Figures 31 and 32, respectively. The Ni/CeO₂ catalysts outperformed Co-impregnated sample in both CO conversion and methane selectivity, confirming the superior catalytic activity of Ni in CO methanation. The beneficial impact of βCD incorporation was evident, particularly in the case of the Ni-based system. The βCD-Ni/CeO₂ catalyst achieved a CO conversion of 98.5% at 375 °C, in contrast to 71.4% for the Ni-CeO₂. Conventionally prepared catalyst peaked at 84.4% conversion at a significantly higher temperature of 475 °C.

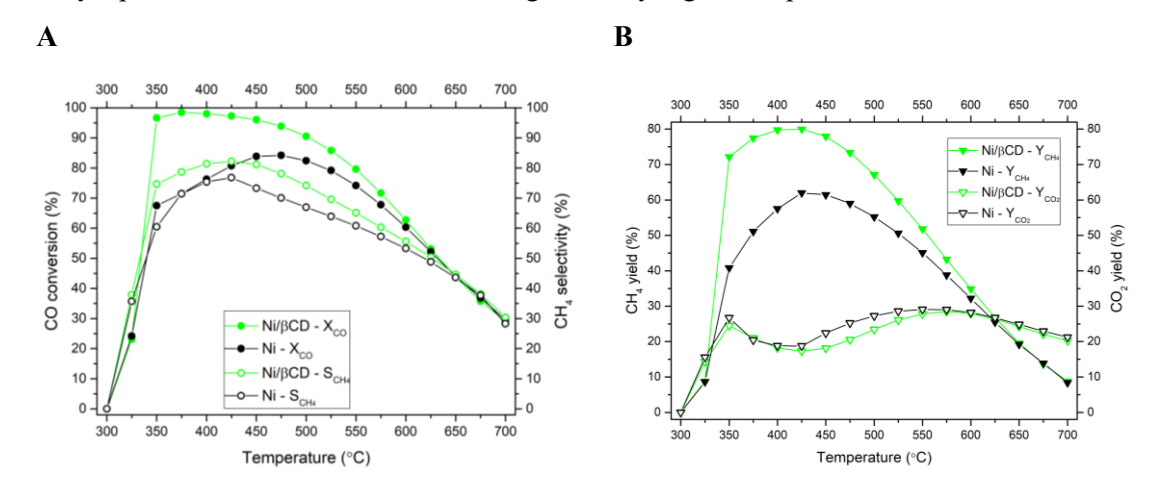


Figure 31. Catalytic performance of the βCD-Ni/CeO₂ and Ni-CeO₂. A) CO conversions (X) and CH₄ selectivity (S), and B) CH₄ and CO₂ yields (Y) [167].

Across the tested temperature range (625–350 °C), the β CD-Ni/CeO₂ catalyst demonstrated consistently higher or comparable CH₄ selectivity and CO conversion relative to the conventional catalyst. In terms of CH₄ yield, the β CD-Ni/CeO₂ catalyst reached 79.9%, compared to only 61.9% for the sample prepared without the additive.

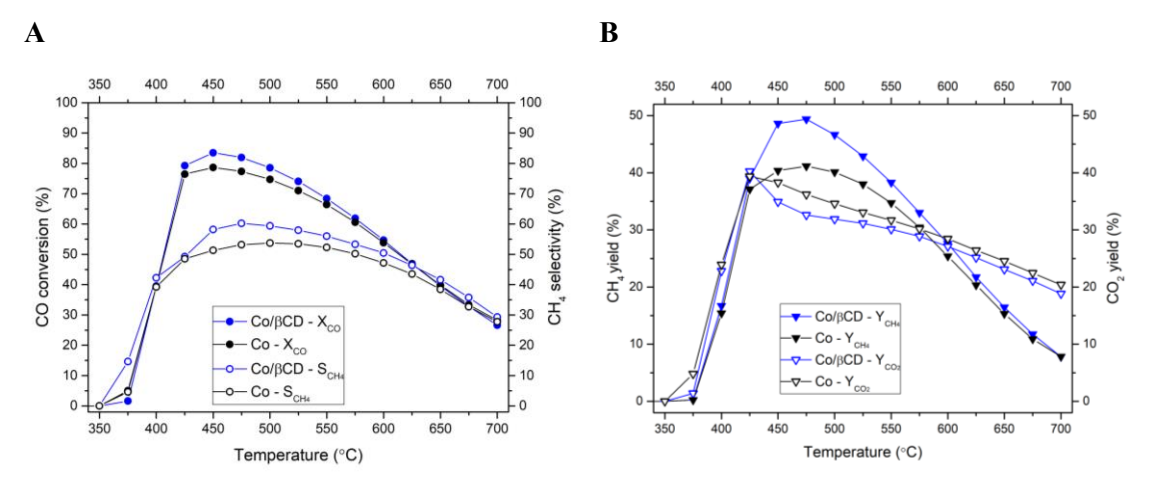


Figure 32. Catalytic performance of the βCD-Co/CeO₂ and Co-CeO₂. A) CO conversions (X) and CH₄ selectivity (S), and B) CH₄ and CO₂ yields (Y) [167].

Simultaneously, CO₂ yield was assessed as an indicator of the undesired Water–Gas Shift (WGS) side reaction, in which CO is consumed to generate nonvaluable CO₂. In the context of a Solid Oxide Electrolysis Cell (SOEC), where CO₂ is intended to be electrochemically reduced to CO, catalytic activity that promotes the reverse reaction – i.e., CO reacting with H₂O – is counterproductive. As shown in Fig. 31, the CO₂ yields for both Ni/CeO₂ catalysts (with and without β-cyclodextrin) were comparable. However, considering the significantly higher CH₄ yield achieved by the βCD-assisted Ni/CeO₂ catalyst, this indicates superior overall efficiency in the methanation reaction under the tested conditions. According to the findings of S. Tada *et al.* [199], Ni nanoparticles supported on CeO₂, when properly pretreated, exhibited high activity for CO₂ reduction to CO, particularly at the metal–support interface. This high catalytic performance is attributed to nickel, helping to overcome the substantial kinetic barrier associated with this eight-electron process and thus enhancing yield within thermodynamic constraints.

Although the precise reaction mechanism remains under active investigation, it is widely accepted that the formation of a well-integrated metal-ceramic interface, combined with highly dispersed, nanoscale Ni particles, plays a critical role in enhancing methanation efficiency [200]. Metallic Ni sites act as active centers for H₂ adsorption and dissociation [201], while the formation of a thin layer of Ni-O-Ce mixed oxide phase promotes the formation of ultra-fine Ni nanoparticles, thereby enhancing hydrogenation kinetics.

For the Co-impregnated series, the influence of β -cyclodextrin was less pronounced than in the Ni-based catalysts, yet still clear. The β CD-Co/CeO₂ catalyst achieved a maximum CO conversion of 83.5% at 450 °C, compared to 78.6% for the conventionally prepared Co/CeO₂ catalyst at the same temperature. As shown in Fig. 32, CH₄ selectivity was consistently higher across the entire temperature range for the β CD-assisted sample, indicating enhanced methanation activity. The usage of β CD during synthesis led to a notable improvement in CH₄ yield, with approximately a 20% increase at the peak conversion point relative to the conventional

counterpart. Concurrently, CO₂ formation was suppressed, as evidenced by the lower CO₂ yield observed for the βCD-Co/CeO₂ catalyst. It is also noteworthy that the maximum methane production for Co-based catalysts occurred at higher temperatures than those required for Ni-based systems, reflecting the differing activation energies and catalytic behaviors of the two metals.

To observe the prolonged stability of the catalysts, the ageing was carried out over a 24hour period under continuous exposure at 700 °C. Following this treatment, the samples were subjected to the same catalytic test protocol to evaluate performance degradation due to potential deactivation mechanisms such as metal particle sintering or metal volatilization. The comparative results, highlighting the catalysts' resistance to deactivation, are presented in Fig. 33. To enhance clarity and focus on the most relevant temperature window for SOEC, the data is shown for a narrowed temperature range. Changes in these catalytic indicators are expressed as Δ % at selected temperatures, providing a quantitative measure of performance decline. The thermodynamic equilibrium values for conversion, yield, and selectivity are included in Fig. 33 as dashed reference lines. The βCD-Ni/CeO₂ catalyst demonstrated the highest CO conversion and CH₄ yield, closely approaching the limitations imposed by thermodynamic equilibrium, particularly at elevated temperatures. In contrast, the Ni/CeO₂ catalyst synthesized without β-cyclodextrin exhibited lower overall efficiency, although both samples showed comparable selectivity toward CH₄ formation. For the Co-impregnated catalysts, the differences between βCD-modified and unmodified samples were less significant but still indicated a minor beneficial effect of βCD addition on performance. Nevertheless, both Co-based catalysts exhibited larger deviations from equilibrium compared to Ni-containing samples, suggesting a lower intrinsic efficiency for cobalt in driving methanation reaction under the tested conditions. Overall, the catalytic results suggest that, at high temperatures, methanation efficiency is primarily governed by thermodynamic constraints rather than kinetic limitations. Both catalysts exhibited minimal degradation during the 24-hour stability test at 700 °C. The use of nanostructured CeO₂ likely contributed to suppressing metal agglomeration. Notably, the catalysts synthesized with the addition of βcyclodextrin obtained enhanced thermal stability. At 600 °C, changes in catalytic performance indicators like CO conversion, CH₄ yield, and CH₄ selectivity were significantly smaller for the βCD-Co/CeO₂ and βCD-Ni/CeO₂ catalysts, indicating superior resistance to performance loss. This stability was particularly evident for the βCD-Co/CeO₂ catalyst in both low and hightemperature range, reflecting strong metal-support interaction, as previously suggested by H₂-TPR analyses. The βCD-Co/CeO₂ sample consistently exhibited smaller declines after ageing, highlighting the substantial role of cyclodextrin in improving both the operational durability and overall catalytic performance.

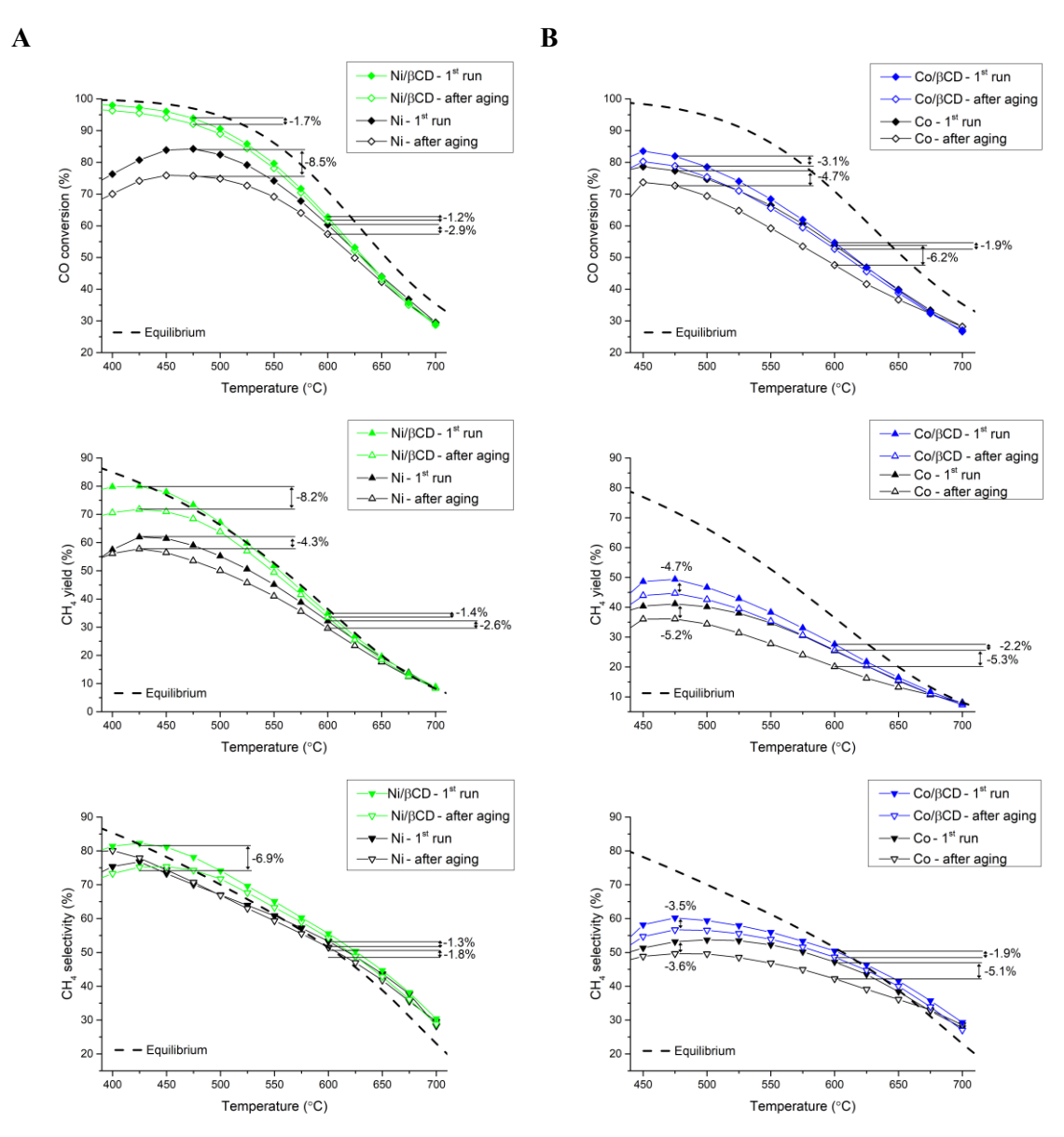


Figure 33. Change in calculated parameters after aging at 700 ℃ for 24 h. A) Ni-impregnated CeO₂, and B) Coimpregnated CeO₂. Dashed line represents thermodynamic equilibrium values [167].

4.1.5 Analysis of reaction quotients of methanation

Fig. 34 presents the reaction quotient values (Q_r) as a function of temperature for the Niand Co-impregnated CeO₂ catalysts. The Q_r values were calculated considering only the CO/CO₂ methanation and water–gas shift (WGS) reactions, as these are the dominant under the experimental conditions.

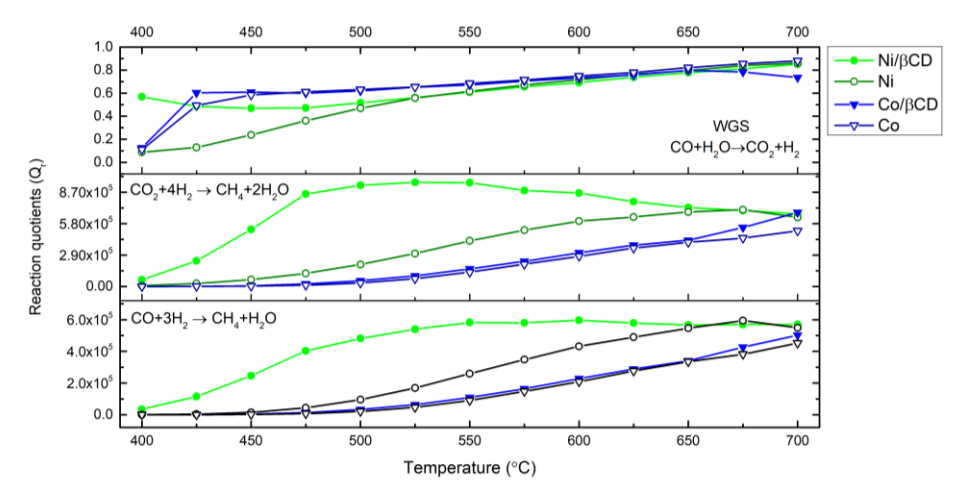


Figure 34. Reaction quotients for CO/CO₂ methanation and WGS reactions [167].

To evaluate the extent of CO and CO₂ methanation, as well as the water–gas shift reaction (WGS), the temperature-dependent nonequilibrium reaction quotient (Q_r) values were calculated for each reaction independently. This approach provided simplified yet insightful trends into the dynamic behavior of the gas-phase composition in the exhaust stream. At temperatures above 550 °C, all catalytic systems demonstrated similar WGS behavior, closely approximating equilibrium conditions ($Q_r \sim 1$). This observation aligns well with the observed decline in CO₂ production rates at higher temperatures. Notably, WGS activity was more pronounced in Co/CeO₂ catalysts, while Ni/CeO₂ exhibited reduced WGS rates at intermediate temperatures (400-600 °C). This was attributed to increased Ni nanoparticle size, a trend consistent with previous literature reports on WGS catalysts [202].

Among all tested samples, the β CD-Ni/CeO₂ catalyst demonstrated superior performance for both CO and CO₂ methanation. This enhanced activity is a direct result of the smaller and highly dispersed Ni nanoparticles. Stable CO methanation performance was evident from 550 °C onward, as indicated by the plateau in Q_r values. CO₂ methanation, although secondary, contributed significantly within the intermediate temperature range (400-600 °C). For Co-based systems, both CO and CO₂ methanation exhibited more sluggish kinetics compared to Ni-based catalysts. Interestingly, the trends in Q_r values were nearly identical for both Co/CeO₂ and β CD-Co/CeO₂ samples, suggesting limited influence of β CD on methanation kinetics. However, the consistent and stable methanation behavior observed in Co-based systems across both CO and CO₂ pathways may prove advantageous in practical SOEC environments, where mixed CO/CO₂ gas feeds are expected. In such conditions, cobalt could offer a more robust alternative to nickel.

Summary of the section

This study explored transition metal-based ceria-supported catalysts for direct methanation in Solid Oxide Electrolysis Cells (SOECs). The catalysts were fabricated using novel β -cyclodextrin (β CD)-assisted wet impregnation of CeO₂ with various transition metals (Ni, Co, Cu, Fe, Mn). The XRD and TEM analyses showed that β CD significantly enhanced metal dispersion, yielding smaller, well-distributed nanoparticles and stronger metal—support interactions. The measurements suggested partial formation of the solid solution and mixed interfacial layers, improving catalyst stability and activity. β CD promoted cation complexation, reduced coalescence of nanoparticles, and improved their stability. The study was supported by the findings from Cu-based catalysts for dry reforming in SOC systems.

H₂-TPR profiles confirmed that βCD-assisted catalysts exhibited lower reduction temperatures, indicating smaller, uniform metal nanoparticles strongly anchored to the CeO₂ support. For Ni–CeO₂, new reduction peaks indicated Ni–O–Ce bond formation and partial Ni incorporation into the lattice, while Co–CeO₂ showed multi-step reduction behavior reflective of enhanced Co–CeO₂ interactions. In Cu–CeO₂, βCD increased the reducibility of well-dispersed CuO_x and suppressed large CuO aggregate formation, enhancing metal–support synergy. In contrast, Mn- and Fe-based systems showed weaker βCD effects. Mn–CeO₂ improved slightly in reducibility but suffered from sintering, and both for Mn and Fe, the reduction pathways remained rather unaffected.

 N_2 adsorption measurements confirmed a well-developed mesoporosity across all catalysts, with β CD promoting higher SSA, except for Fe/CeO₂. The greatest SSA improvement was denoted in Cu/CeO₂. It was a rise from 49.8 for a conventional sample to 60.6 m²·g⁻¹ for proposed preparation route. It was attributed to stable β CD–Cu²⁺ complex formation. Enhanced textural properties align with improved reducibility observed in H₂-TPR analyses.

Catalytic evaluation revealed that only Ni- and Co-impregnated CeO₂ catalysts exhibited significant methanation activity, with Ni-based systems outperforming Co-based one. βCD-Ni/CeO₂ achieved 98.5% CO conversion and 79.9% CH₄ yield at 375 °C. It was far better than conventionally prepared Ni–CeO₂ thanks to highly dispersed Ni nanoparticles and strong metal–support interactions. Co-based catalysts also benefited from βCD, achieving 83.5% CO conversion and ~20% higher CH₄ yield.

Reaction quotient (Q_r) analysis confirmed superior CO and CO_2 methanation efficiency for βCD –Ni/CeO₂, with stable high-temperature performance and reduced water–gas shift activity, what improved selectivity towards methane. Co-based catalysts were characterized by slower kinetics but very stable CO and CO_2 methanation rates, suggesting their robustness for SOEC environment.

Finally, 24-hour stability tests at 700 °C revealed minimal degradation for both catalysts. β CD-modified samples exhibited enhanced thermal stability and resistance to performance loss, especially β CD-Co/CeO₂. The results highlighted the crucial role of β CD in improving both catalytic activity and long-term durability. Overall, β CD-assisted synthesis is a powerful strategy for optimizing metal/CeO₂ catalysts for SOEC and broader SOC applications.

4.2 Modification of SOEC with nanoparticles performing coelectrolysis and methanation

High-temperature H_2O/CO_2 coelectrolysis using Solid Oxide Electrolysis Cells (SOECs) has recently emerged as a promising alternative to conventional syngas (CO + H_2) production methods, such as steam reforming or coal gasification, which are associated with significant greenhouse gas emissions. To overcome the technological issues with the efficiency of the SOECs in performing electrochemical splitting of compounds different than H_2O and facilitating further reactions e.g. methanation, a proper set of catalysts must be introduced into the fuel electrode of the electrolyzer.

Nickel is already present in the fuel electrode and is widely used due to its high catalytic activity, selectivity, and low cost [203–205]. Numerous studies have demonstrated that methanation is most effective at temperatures below 400 °C, which contrasts with the typical high-temperature operating conditions of SOECs [206–208]. Above 450 °C, the coelectrolysis reaction becomes dominant, but reducing the selectivity towards CH₄ [209]. While Ni catalyst degradation is minimal in the low temperature methanation regime, elevated SOEC operating temperatures promote Ni particle agglomeration and carbon deposition, leading to performance deterioration [29,210,211].

Alternative catalysts exhibiting e.g. enhanced resistance to coking during CO₂ electrochemical conversion include noble metals such as platinum (Pt), rhodium (Rh), and ruthenium (Ru) [212,213]. These metals demonstrate excellent catalytic performance; however, their implementation is severely constrained by high material costs. To overcome this limitation, considerable research has focused on the development of bimetallic systems, particularly through the incorporation of a secondary metal into nickel-based catalysts. These systems are designed to synergistically combine the catalytic advantages of both constituents. The formation of bimetallic catalysts leads to significant modifications in electronic structure and geometric configuration, which can influence adsorption energies, alter reaction intermediates, and ultimately, power-up catalytic performance [214]. Among the most widely studied dopants are transition metals such as iron (Fe) and cobalt (Co), both of which exhibit complete solubility in the nickel lattice. This allows for the formation of homogenous Ni–Fe or Ni–Co alloys and intermetallic phases with tunable catalytic behavior [215]. The introduction of a secondary metal into Ni catalysts has been shown to improve thermal stability and resistance to sintering and carbon deposition at elevated operating temperatures [216].

Herein, a series of SOEC modified with the nanoparticles of Co was prepared and widely characterized in coelectrolysis and methanation. Based on those results further study on the influence of the transition metals on the performance of SOEC was determined by the introduction of Cu, Mn, and Fe was conducted. The detailed mechanistic explanation of the enhancement was

also given based on finesse synchrotron radiation-based characterization methods such as STXM or XAS. The research revealed a complexity of the synergistic effects in the modified electrodes.

This section will contain the results obtained and published in [217] **Blaszczak P.**, Zając M., Ducka A., Matlak K., Wolanin B., Wang S.-F., Mandziak A., Bochentyn B., Jasiński P. *Hightemperature Coelectrolysis of CO₂/H₂O and direct methanation over Co-impregnated SOEC. Bimetallic synergy between Co and Ni*. Int J Hydrogen Energy 2022; 47:35017–37. 10.1016/j.ijhydene.2022.08.057. The results will be also accompanied by the preliminary results obtained for the samples impregnated with other transition metals – Mn, Cu, and Fe. The findings will not be considered as a core of this section but rather supplementary data to present further plans and emphasize the scientific possibilities in the topic.

4.2.1 Phase composition and microstructure

The X-ray diffractograms of the as-prepared and subsequently modified fuel electrodes are depicted in Fig. 35. Prior to modification, the NiO/YSZ composite underwent a reduction process, resulting in a phase composition comprising the ionic conductor 8YSZ and metallic Ni. The impregnation procedure, utilizing a novel precursor solution, involved cyclic firing of the electrode at 400 °C to decompose the nitrate and organic additives present in the precursor. This thermal treatment led to the formation of a minor layer of surficial NiO/NiOOH via partial reoxidation of metallic Ni. As a result of the cyclic impregnation steps a successful Co loading equal to 1.8, 3.6, and 5.4 wt.% was achieved.

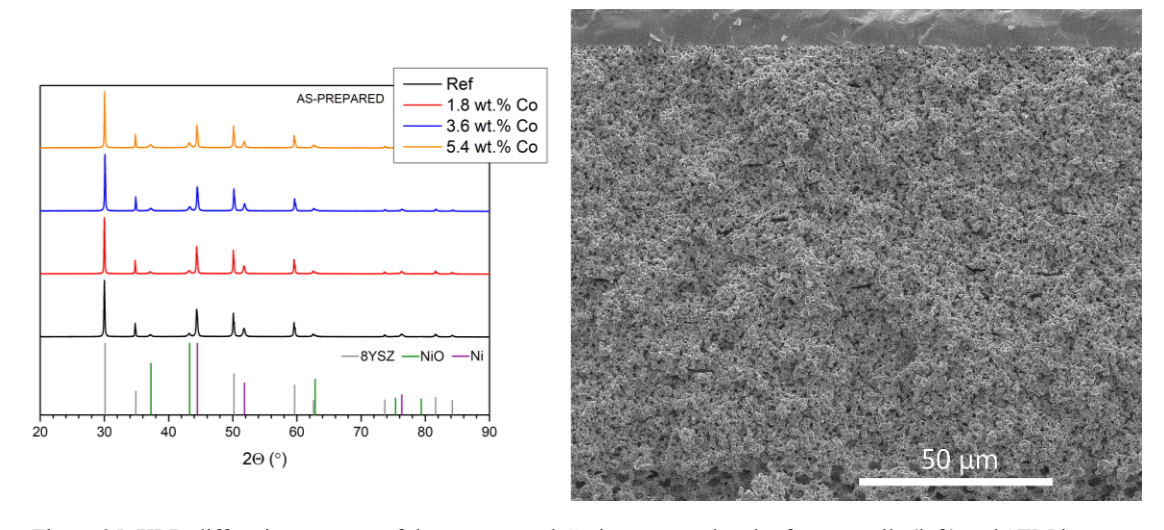


Figure 35. XRD diffraction patterns of the as-prepared Co-impregnated and reference cells (left) and SEM image of the prereduced half-cell (right) [217]

Cobalt ions introduced into the electrode matrix did not cause the emergence of additional distinct phases. This absence of new phases can be attributed to the low concentration of cobalt, which falls below the detection threshold of the XRD apparatus. Furthermore, the cobalt mixed species most likely formed highly nanocrystalline structures, resulting in very broad and less intense diffraction peaks that may have been covered by instrumental noise. Additionally, no significant

shifts were observed in the diffraction peaks, even though the formation of a mixed NiO–Co₃O₄ oxide phase was likely. Cobalt exhibits infinite solubility in metallic Ni. Studies on Ni–Co alloyed nanoparticles and their oxidation suggested that under the synthesis conditions, the formation of a mixed (Ni,Co)O phase with traces of the metastable NiCo₂O₄ spinel is highly probable [218]. Although XRD analyses provided limited information regarding internal phase composition changes, they indicated the partially nanometric nature of the modified electrode.

Scanning electron microscopy (SEM) analysis of the cross-section of the pristine starting cell (Fig. 35 right), revealed that the microstructure of electrode consisted of micrometer-sized grains of 8YSZ and Ni. The NiO–YSZ composite was composed in a way to achieve approximately 35–40% total open porosity in a reduced form. Two distinct levels of porosity were observed: bigger in the outer layer and smaller in the functional layer (FL). The reduction of NiO–YSZ facilitated better penetration of the precursor solution. SEM images of fractured surfaces of both reference and modified electrodes after one, two, and three cycles of impregnation are presented in Fig. 36. These images illustrate the evolution of the microstructure with successive impregnation steps, providing insights into the distribution and interaction of the impregnated phases within the electrode matrix.

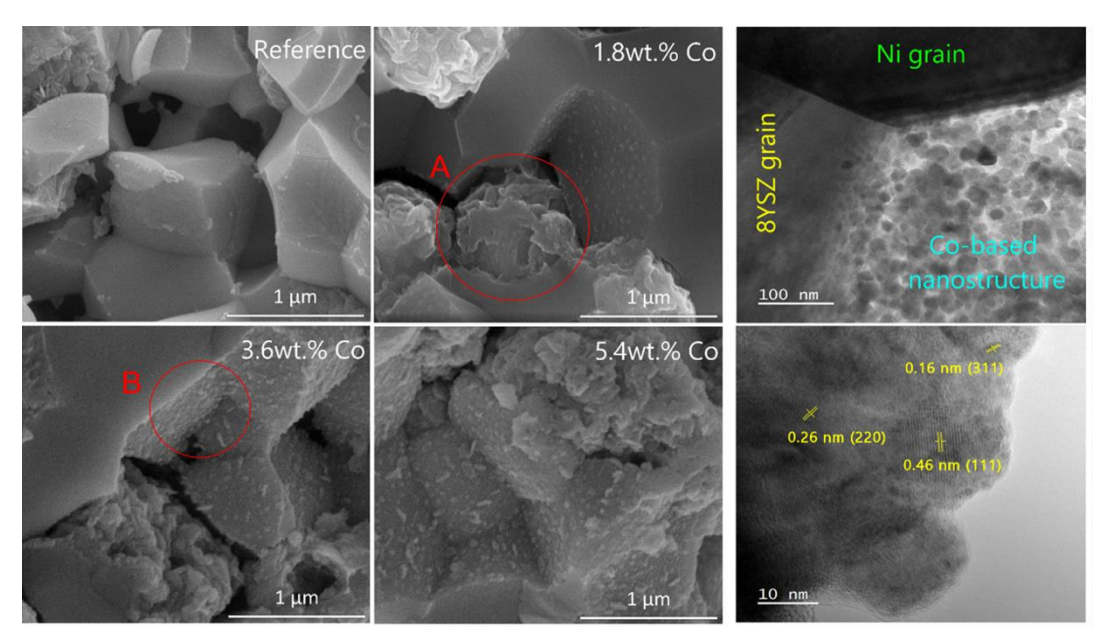


Figure 36. SEM images of the prepared Co-impregnated electrodes and pristine cell (left), TEM image of the 3.6wt.% Co sample at the 8YSZ–Ni–Co interface (right up), and HRTEM of the Co-based nanostructure (right down). A – paper ball-like structure, B – Co/YSZ surface [217].

The microstructure of the electrodes varies significantly depending on the amount of Co introduced during the cycling. SEM observations revealed the formation of two distinct cobalt-containing species in two regions. The first included well-dispersed nanoparticles of cobalt oxides or hydroxides deposited without the reaction on the surface of 8YSZ grains. These nanoparticles (NPs) were uniformly distributed on the YSZ surface. The second type resembled paper ball-like oxide structures, attributed to cobalt species introduced via, most likely, reactive deposition.

These objects formed during thermal treatment in ambient air and were also detected in the reference electrode, although less developed in SSA. EDX point analysis confirmed that these oxide scales are composed primarily of Ni and O, with a minor Co content, indicating the formation of a surface mixed oxide layer on the Ni grains. The morphology and texture of this layer suggest a high surface area, and its complex structure may be indicative of spinel-type phases, which are known to exhibit intricate nanostructured morphologies [219,220]. Spinel materials have been extensively investigated for electrochemical applications due to their exceptional properties and evolving potential for various energy technologies [221,222].

The spatial distribution, size, and morphology of the Co-based nanoparticles on 8YSZ grains varied across the three samples of different Co loading. At higher cobalt concentrations, the discrete nanoparticles began to merge, forming a more continuous coating, along with the appearance of larger aggregates. This trend is especially pronounced in the sample containing 5.4 wt% Co (Fig. 36), where significant growth of Co oxide phases was evident. In terms of reactive deposition of Ni grains, each successive impregnation cycle further modified the morphology of the Co–Ni oxide structures, resulting in larger and more agglomerated clusters.

To gain deeper insight into the internal architecture of the Co-modified electrode samples, a series of TEM analyses were performed on lamellae extracted from the cells (Fig. 36 right). A representative image of the 3.6 wt% Co sample illustrates well the structural evolution following cobalt impregnation. The observations confirmed a bimodal distribution of cobalt species, attributed to both reactive and non-reactive deposition mechanisms. Specifically, Co ions were found to partially dissolve into NiO scale, while simultaneously forming nanoparticles on the surface of 8YSZ grains. Furthermore, a complex microstructure composed of sphere-shaped polycrystalline nanoparticles was observed. High-resolution TEM (HRTEM) imaging was conducted to examine this structure in more detail. The outermost regions of the structure exhibited an amorphous morphology, likely a result of low-temperature sintering conditions and the presence of cyclodextrin during synthesis. Within the interior of this structure, several lattice distances corresponding to defined interplanar spacings were identified. A spacing of 0.46 nm matched well with previously reported (111) plane of the NiCo₂O₄ spinel phase, as described by L. Huang et al. and A. Cetin et al. [223,224]. Additional spacings of 0.26 nm and 0.16 nm were indexed to the (220) planes of NiCo₂O₄ and the (311) planes of Co₃O₄, respectively [225]. Slight difference from ideal interplanar distances was attributed to non-stoichiometric composition of the phase and coexistence of mixed oxyhydroxide phases such as NiCo₂(OH)₆, which includes both NiOOH and CoOOH layers [226]. In addition to the spinel structures, free Co_xO_y nanoparticles were detected near the surface. These findings suggest that Ni ions actively reacted with Co species during the impregnation and firing steps, forming a surface layer composed of finely dispersed spinel-like structures and residual Co_xO_y nanoparticles. Unreacted NiO regions remained near the surface of the initial Ni grains, and this hierarchical structure of the modified electrode was obtained.

A similar set of pristine microstructure characterization was performed on the samples that were impregnated in the same way as the first Co trials. After two impregnation cycles the samples contained 3.6 wt% of Mn, Co, Cu, and Fe. The SEM images of the electrode structures are presented in Fig. 37.

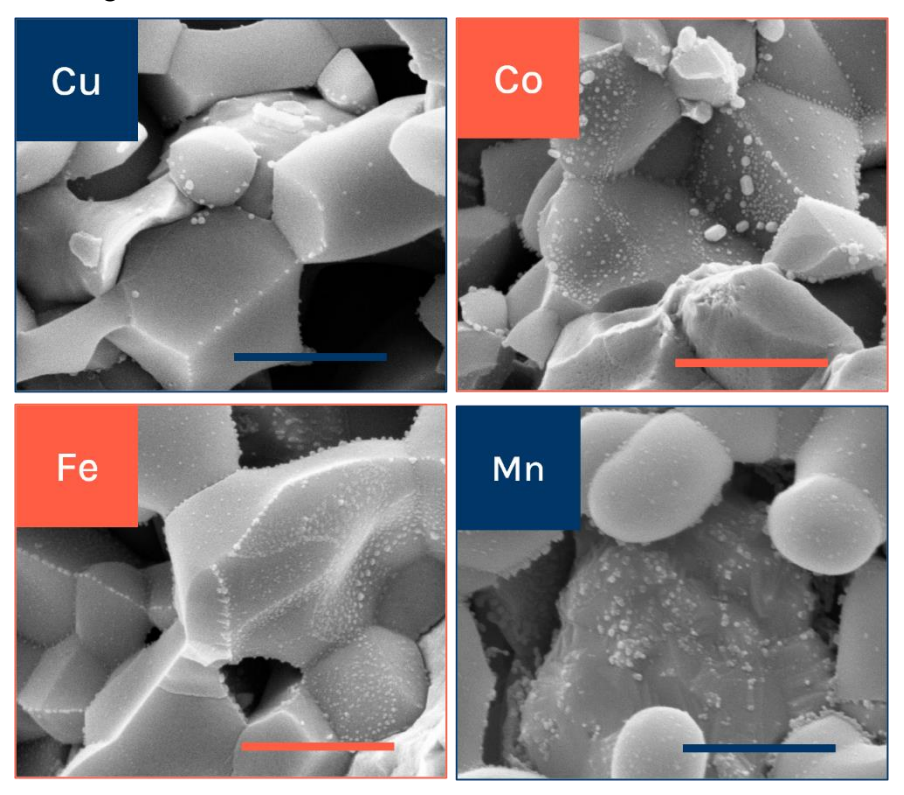


Figure 37. SEM images of the Ni–YSZ electrodes impregnated with transition metals (after reduction at 800 °C. Scale bar is 1 µm [unpublished results].

The images present the structures really similar to the ones obtained in case of Coimpregnation. Despite that, there could be some differences distinguished between the samples.

In Cu-impregnated cermet, the metal particles formed rather islands of metallic copper than welldistributed and homogeneous nanoparticles. The low melting temperature of copper enhanced the
remelting and diffusion of the nanoparticles. This effect is even more pronounced when the Cu
form nanoobjects as the melting temperature can go down to even 450 °C based on the study of
L. Somlyai-Sipos *et al.* [227]. This unfortunate depression of the phase transition temperature
may, in the final environment, lead to the short shelf-life of the SOC. In case of Fe-impregnated
sample the structure resembled Co-containing sample or was even considered of finer
microstructure. This was caused most likely by a higher melting point of Fe than other reducible
metals and the tendency to form the oxide scales of highly developed microstructure and porosity.

In case of Mn-containing sample the microstructure of the Ni grains is significantly less uniform.

This observation led to the hypothesis that Mn ions reacted with Ni grains forming mixed oxide
that did not undergo full reduction under hydrogen. According to general knowledge, the Mn

cations will not be reduced to metallic Mn under the conditions used in this study [228], so the surface of the Ni grains should still contain a copious amount of the oxide phase, most likely MnO. To sum up, the lower the melting point of the metal the lower the homogeneity and dispersity of the nanoparticles. Furthermore, the metals that are not easily reducible will most likely form the oxide species mixed with Ni rather than homogenous alloy or intermetallic.

4.2.2 Study of chemical state changes

To assess the surface composition and determine the chemical states of the constituent elements, X-ray photoelectron spectroscopy (XPS) analyses were conducted on both the freshly prepared and electrodes. Representative XPS spectra for the 3.6 wt% Coimpregnated, as-prepared sample are visible in Fig. 38. The corelevel spectra for Ni2p and Co2p revealed characteristic spin-orbit doublets corresponding to the $2p_{3/2}$ and $2p_{1/2}$ transitions. Each doublet subjected was Lorentzian-Gaussian

deconvolution, yielding bands associated with +2 and +3 valence. For Ni (Fig. 38A), the peaks at binding energies of 853.7 eV and 871.8 eV were attributed

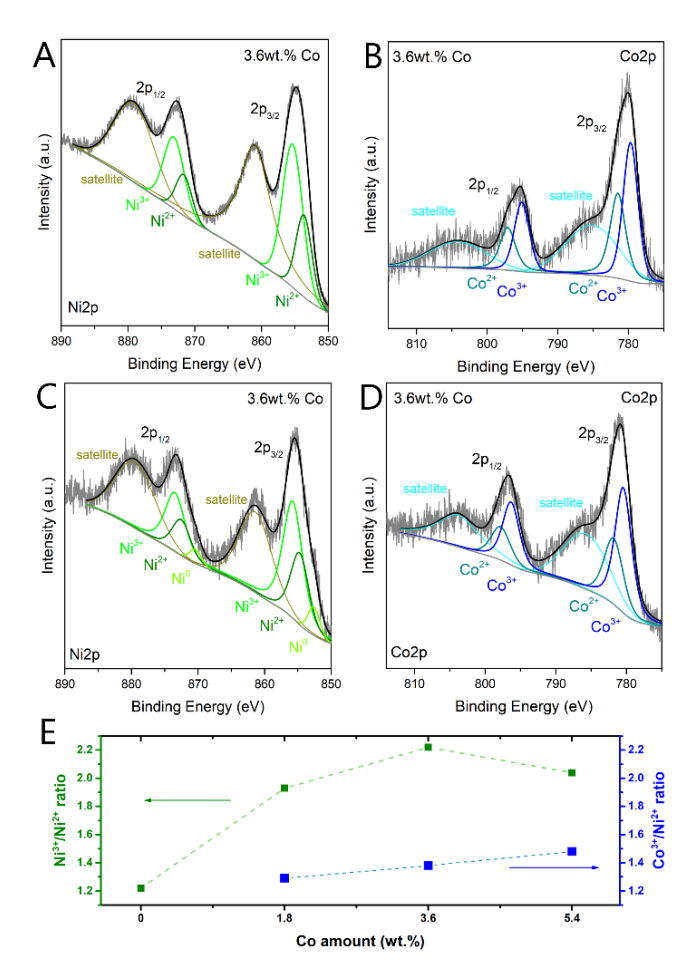


Figure 38. XPS spectra of 3.6wt.% Co SOC. A,C) Ni2p, B,D) Co2p, and E) change of the (Ni,Co)³⁺/(Ni,Co)²⁺ ratios vs. wt.% of Co loading. A,B – pristine samples, and C,D – after SOEC testing [217]

to Ni^{2+} species, while those at 855.4 eV and 873.2 eV correspond to Ni^{3+} . These peak assignments are consistent with previously reported data for $NiCo_2O_4$ -based systems [229,230]. A slight shift in binding energy (~0.4 eV) in the Ni^{2+} peak positions suggested the formation of a new phase (surrounding), likely involving cobalt incorporation [231,232]. The Co2p spectrum (Fig. 38B) further supported the presence of mixed-valence states. Co^{3+} is represented by peaks at 779.6 eV (2p_{3/2}) and 795.2 eV (2p_{1/2}), while Co^{2+} was identified through peaks at 781.4 eV and 797.0 eV. These values align well with literature data, including the studies by X. Tong *et al.* on hierarchical $NiCo_2O_4$ nanostructures and other literature findings [233–235]. At the same time, a systematic

positive shift of 0.3–0.4 eV in the Co2p_{3/2} bands was observed with the increase in Co loading, indicating progressive change within the composite material. The doublets in the XPS spectra enabled precise quantification of the average oxidation state for both nickel and cobalt cations in the surface layer. Specifically, the Ni³+/Ni²+ and Co³+/Co²+ ratios were determined and are plotted in Fig. 38 as a function of cobalt loading. A notable increase in the Ni³+/Ni²+ ratio was observed with increasing Co surface concentration, rising sharply from 1.22 to 2.22. This pronounced shift is indicative of the formation of a mixed Ni–Co oxide phase. It suggests that the introduction of cobalt ions into the NiO_x matrix promotes oxidation of N²+ to Ni³+. Prior studies have demonstrated that cobalt doping in NiO facilitated the formation and stabilization of higher-valence nickel states (e.g., Ni₂O₃), functioning effectively as a p-type dopant [236,237]. However, beyond 3.6 wt% of Co, a slight decrease in the Ni³+ concentration was observed. This phenomenon has also been reported in some studies, where an excess of surface-deposited Co_xO_y was found to act as charge carrier trap, limiting effective electron transfer between Ni and Co centers [237].

Regarding cobalt oxidation state, the Co³⁺/Co²⁺ ratio exhibited only a moderate increase along following impregnation cycles, increasing from 1.29 to 1.48. This trend was further studied by complementary X-ray absorption spectroscopy (XAS) analyses (described later in the text). Importantly, the elevated Ni³⁺ content is known to enhance electrocatalytic activity in processes such as the oxygen evolution reaction (OER) and oxygen reduction reaction (ORR), suggesting that similar benefits may be obtained in this system [238,239].

Post-operational (post-mortem) XPS spectra (Fig. 38C and 38D) revealed the emergence of metallic Ni and NiOOH (CoOOH) phases due to the high amount of Ni³⁺ and Co³⁺ peaks. This behavior was attributed to the presence of water vapor in the gas stream during the cooling of the cell, which promoted the reoxidation processes. The emergence of phases such as NiOOH and CoOOH under these conditions further underscores the high reactivity of the Ni–Co system with H₂O, which may critically influence water adsorption and activation mechanisms during electrolysis [240].

Going further, a Mn-impregnated sample was tested using more sophisticated XPS measurements. The sample was representative of the transition metal-modified Ni–YSZ electrode and underwent characterization using Near Ambient Pressure XPS (NAP-XPS) at ESMI beamline in Elettra synchrotron (Trieste, Italy). The measurements were treated as proof-of-concept as similar tests were not proposed before to the beamline scientists. The methodology of measurement was described in the previous chapter (see 3.3.3). The exemplary results are presented in Fig. 39 in form of elemental distribution maps and XPS spectra collected at two distinctive points of the electrode, namely Ni-rich and Ni-poor spots.

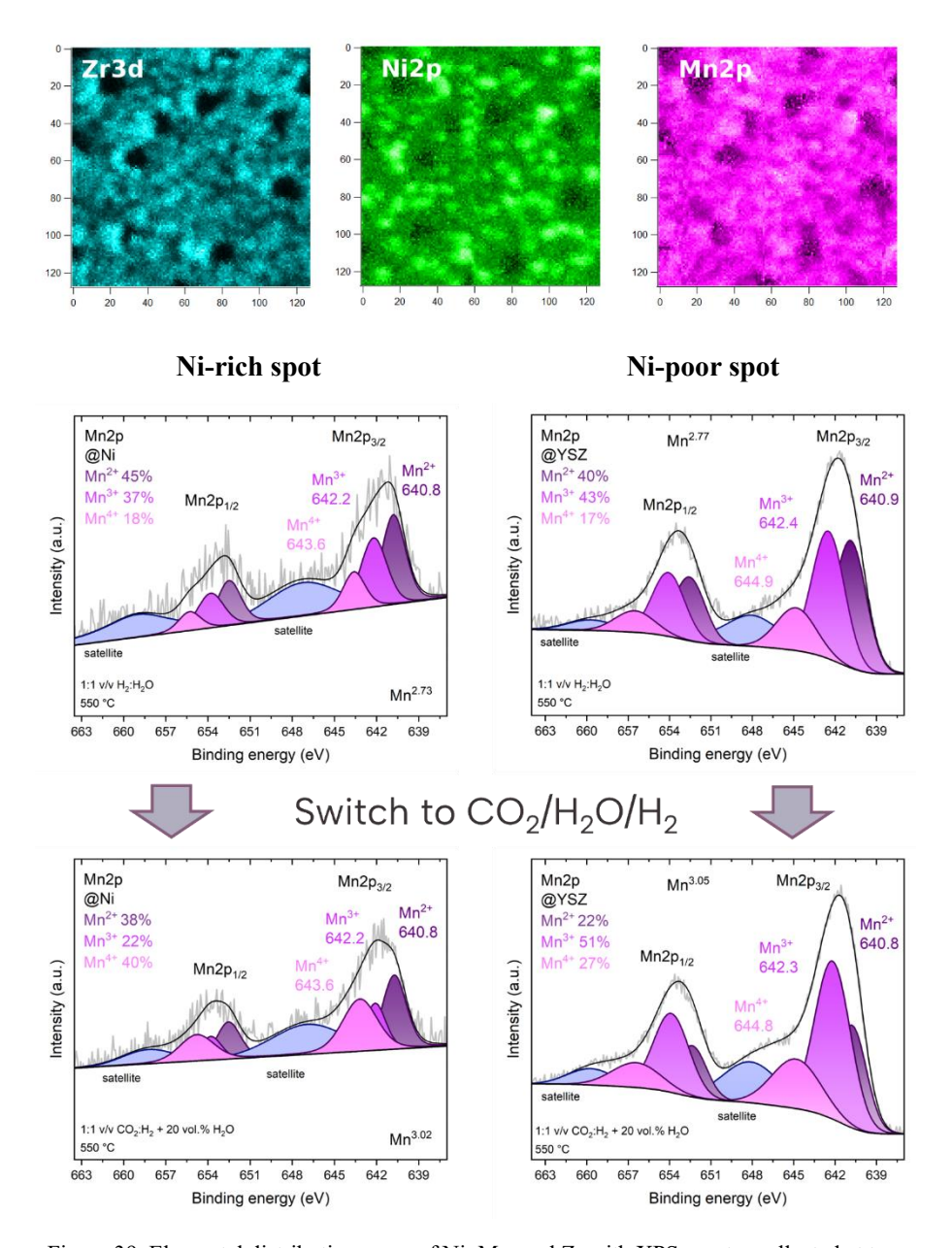


Figure 39. Elemental distribution maps of Ni, Mn, and Zr with XPS spectra collected at two points of the electrode – Ni-rich and Ni-poor spot. The scale is given in μ m [unpublished results]

The maps and spectra were taken at Mn2p, Zr3d, Ni2p, O1s, and C1s. Along a wide survey was collected each time. All the high temperature images and measurements were performed at 500 °C. The second series of measurements weas done under H₂O:CO₂:H₂ (25% vol. H₂O + 1:1 vol. H₂:CO₂) after around 30 min of stabilization. The same set of spectra and maps was collected. It was clearly visible that in the sample, being a composite of Ni and YSZ, a clear distinction between the areas of ionic conductor and Ni metallic phase were revealed during the fixed energy scanning. The dark spots correspond to the micrometric porosity of the SOC electrode. The Mn ions were rather homogeneously distributed over the composite structure with some spots of higher signal intensity, normally ascribed to the YSZ grains covered with Mn_xO_y species. In that case the signal form Mn was stronger due to nonexistence of Ni signal interrupting

the Mn spectra. The distribution of the elements did not change during the heating nor the change of the atmosphere. According to the Mn2p doublets, the overall valence of the manganese ions was found to be mostly located between +2 and +3 oxidation state. The hydrogen atmosphere caused the reduction on Mn ions to +2 state to higher extent. The valence of Mn varied strongly between the Ni-rich and Ni-poor spot. A clear difference in the chemical environment of the manganese ions was observed, where the Mn most likely formed a mixed oxide with Ni. It is clear for the Ni-rich spot that Mn +4 peak has shifted towards lower binding energies what is quite common for Mn-Ni spinel structure. Spinel formation was achieved during the preparation steps carried out under oxygen-containing atmosphere, where Ni got reoxidized and formed mixed oxide of spongy texture. The Mn_xO_y species formed on the surface of the 8YSZ grains did not integrate (reacted) with the support. Based on the spectra, the nanoparticles mostly consisted of MnO/Mn₃O₄ with the minor amount of Mn³⁺ species under H₂ atmosphere. When changed to CO₂ atmosphere the Mn ions got oxidized and Mn³⁺ valence got more pronounced. These results revealed that the interchanging oxidation state of Mn species may be the key to the enhanced catalytic activity of the electrode as it promotes the increase in the number of active redox couples on the surface. Furthermore, this preliminary experiment ensured the viability of this methodology to characterize the samples in semi-in-situ conditions.

4.2.3 Efficiency of SOEC

The electrocatalytic performance of the Co-modified SOEC electrodes for simultaneous H₂O/CO₂ coelectrolysis and methanation was evaluated under operational Solid Oxide Electrolysis Cell (SOEC) conditions. The experiments were conducted using a gas mixture composed of 20 vol% H₂O in CO₂ with H₂ (1:4 by vol.) to suppress reoxidation of the metallic phase and to enhance FTIR sensitivity. The measurements were carried out under both open circuit voltage (OCV) and under a thermoneutral voltage of 1.3 V. The change of CH₄ concentration as a function of temperature for both the unmodified (reference) and cobalt-impregnated electrodes is shown in Fig. 40A and 40B. Surprisingly, despite the significant differences in methane production, the corresponding current densities (Fig. 40C) were only minorly different across the samples, indicating comparable SOEC electrical efficiency regardless of Co incorporation. However, the impact of cobalt modification on methanation activity was substantial.

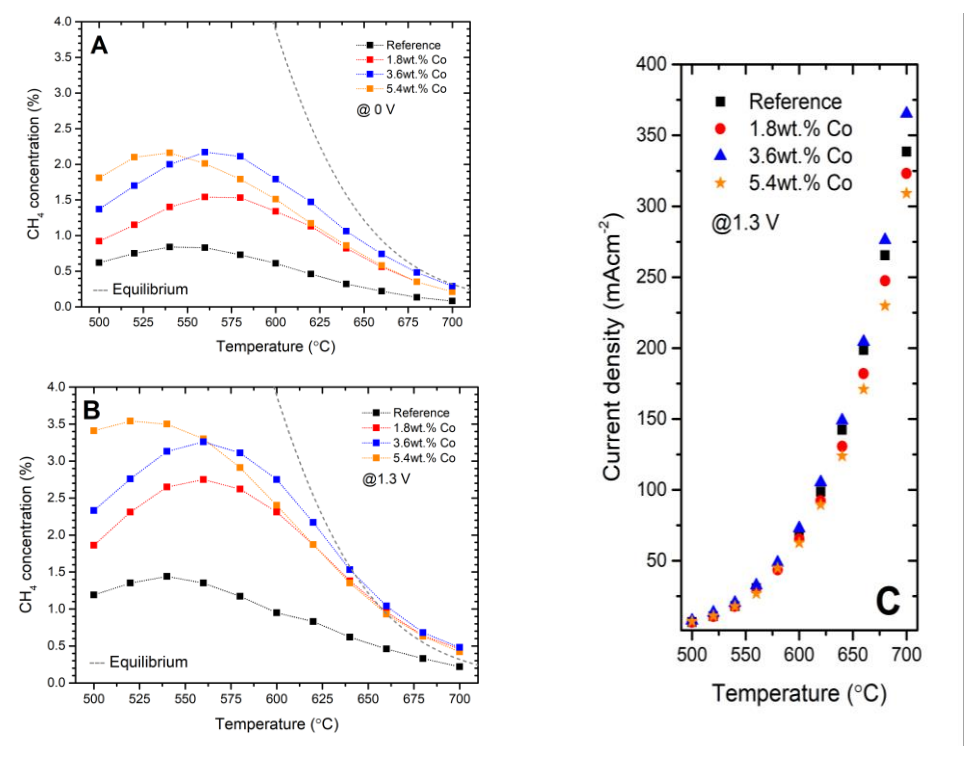


Figure 40. Change of methane concentration in the outlet of SOEC at OCV (A) and 1.3 V (B). Equilibrium marked as a dashed line. (C) Current densities at 1.3 V bias vs. temperature [217].

The CH₄ concentration in the outlet stream increased strongly with the addition of small quantities of Co into the electrode structure. Most notably, the 3.6 wt% Co-modified sample exhibited a peak CH₄ concentration of 2.1% at OCV. It was more than 2.5 times higher than the ~0.8% concentration recorded for the unmodified cell. These findings clearly demonstrate the highly promising catalytic enhancement introduced by Co impregnation, even at low loading levels. For the 1.8 and 3.6 wt% Co-impregnated samples, the CH₄ concentration peak shifted to a higher temperature compared to the reference cell. This shift was attributed to improved efficiency in the electrocatalytic CO₂/H₂O splitting. Overall, these samples exhibited enhanced activity within the temperature range suitable for optimal SOEC operation.

To quantitatively assess the catalytic performance, parameters such as CH₄ yield, CO₂ conversion, CH₄ selectivity, and CO yield were given in Fig. 41. All values were calculated for electrolysis tests at 1.3 V. The CH₄ yield was used to determine the efficiency of methanation. At 1.3 V and ~640 °C, all Co-modified cells achieved thermodynamic equilibrium, unlike the reference cell. This difference is most likely caused by two factors: (i) the modified cells attained higher electrochemical efficiency, and (ii) the methane synthesis kinetics were enhanced as seen through the increase in CO₂ conversion. The CO₂ conversion rate surpassed the simulated thermodynamic equilibrium. Thus, direct CO₂ hydrogenation reaction was facilitated by the novel electrode composition. Overall, the modified SOECs exhibited an outstanding increase in CH₄ yield. The samples with 1.8 and 3.6 wt% Co loading revealed different temperature-related catalytic responses. Addition of Co above 3.6 wt% did not increase methane concentration but

did alter the overall activity profile, making it more similar to that of the unmodified sample. Based on the outcomes of the study, the 3.6 wt% Co-impregnated sample was selected as the most promising candidate. Regarding CH₄ selectivity, the samples followed the trends observed for CH₄ yield. There was clear evidence of an increased methane formation rate. The 5.4 wt% Co-impregnated sample exhibited even higher activity, though a shift in peak to the lower temperature was also observed. In all examined cells, both the conversion of CO₂ and CO yield values significantly exceeded the theoretical thermodynamic equilibrium limits, highlighting the prominent role of electrochemical H₂O/CO₂ splitting. This suggests that the subsequent CH₄ formation is largely decoupled from direct electrochemical reactions at the electrode surface. The extent to which direct CO₂ electrolysis and the Reverse Water-Gas Shift (WGS) reaction contribute to the overall performance of SOEC remains an active area of debate [241].

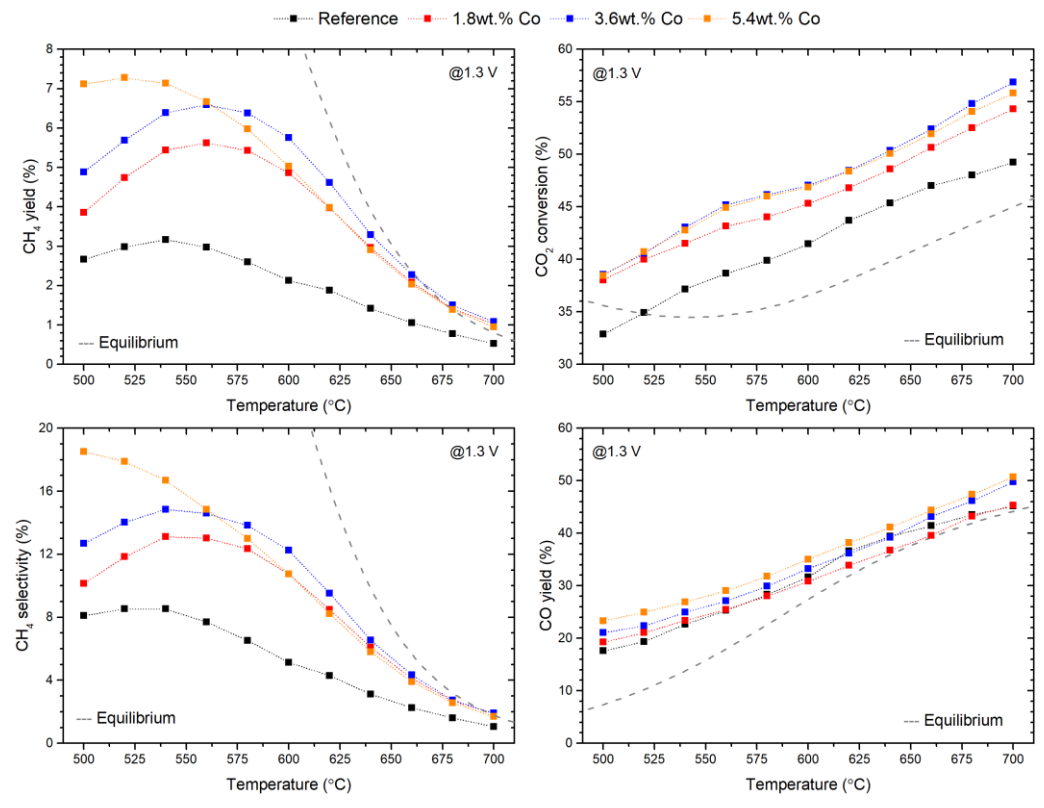


Figure 41. Temperature change of CO₂ conversion (left column) and CH₄ selectivity (right column) for the reference and modified SOEC at 1.3 V. Equilibrium state values are marked as dashed lines [217].

In the light of this study, it was proposed that the impregnated electrode material promotes simultaneous direct electrochemical CO₂ reduction as well as the RWGS reaction kinetics. This statement is supported by the fact that there was only a minor increase in current density, coupled with unchanged CO production levels and a substantial rise in CH₄ output. The enhanced CO₂ electrolysis rate was likely associated with the increased basicity and higher reactivity of cobalt-containing species compared to NiO_x, particularly during their interaction with water. Cobalt tends to oxidize in humid environments and subsequently form cobalt oxyhydroxide species [Co(O)OH], which can react with CO₂ and generate metal carbonates. This increased surface

basicity and CO₂ retention time are expected to (i) enhance the CO₂ electrolysis rate and (ii) improve the likelihood of CO₂ hydrogenation to CH₄ [242,243]. To further understand the underlying processes contributing to the improved performance of Co-impregnated Ni–YSZ SOECs, additional advanced characterization techniques were employed and are discussed in the following sections (sections 4.2.4-4.2.6).

To further investigate the influence of various transition metals, i.e. Mn, Fe, and Cu, on the electrochemical and chemical efficiency of the SOECs during the electrolysis of H₂O/CO₂ a series of modified samples were subjected to similar electrical testing as Co-impregnated samples. The procedure was described in detail in the previous chapter (3.7). The electrochemical performance of the cells in the form of iV curves is presented in Fig. 42.

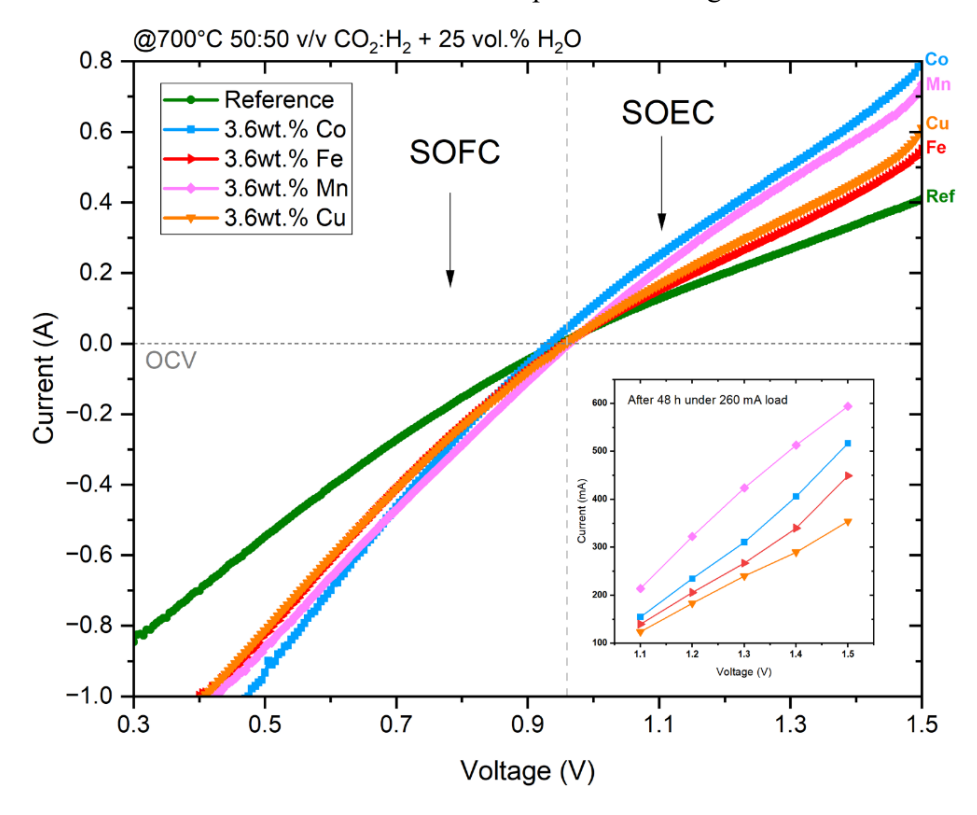


Figure 42. iV curves of the transition metal-impregnated SOECs. The change in electrolysis efficiency after 48 h in the inset [unpublished results]

All modified cells outperformed reference sample both in fuel cell and electrolysis mode, what is visible in Fig. 42. The differences in SOFC mode were rather minor between the impregnated samples. The impregnation steps with secondary metals decreased the overpotentials in hydrogen oxidation reaction and increased power output of the fuel cell. The SOFC mode of operation was of lower importance in this study, thus the rest of the section will be devoted to the operation under coelectrolysis conditions.

The influence of the various metals on the electrical efficiency of the cell became more pronounced in the case of coelectrolysis mode. It is visible in the SOEC region of the iV curve. The activity of the cells increased in the order Fe < Cu < Mn < Co. For Co- and Mn-impregnated

samples the performance was similar if one considers the minor shift in OCV value most likely due to slightly lower ohmic resistance. Furthermore, the SOCs were held in electrolysis mode for 48 h and the same polarization curves were collected. In contrary to the initial performance, the Co-impregnated cell underwent degradation while the Mn-impregnated sample maintained nearly same efficiency. Based on these results, Mn- and Co-modified cells were subjected to more complex characterization through the means of DRT analysis presented in Fig. 43.

Based on the model that was presented in [59] **Blaszczak P.**, Mäkinen P., Mroziński A., Ducka A., Jasiński G., Himanen O., et al. *Uncovering the electrochemical processes and understanding the causes of the degradation via EIS-DRT in large-scale Solid Oxide Fuel Cell*. Appl Energy 2025; 393. 10.1016/j.apenergy.2025.125983. and other findings considering the electrochemical processes occurring in SOECs [244–246] the following processes (P1-P5) were ascribed to the limiting processes in the electrolysis: (P1) – the gas diffusion in both oxygen electrode and hydrogen electrode (0.1 - 10 Hz), (P2) – steam-hydrogen conversion in the hydrogen electrode (10 - 30 Hz), (P3) – oxygen surface exchange and O²⁻ diffusion (30 - 10³ Hz), (P4) – charge transfer and electrochemical reactions (10 - 2·10⁴ Hz), and (P5) – oxygen electrode ionic transport, distorted by the inductance. By the analysis of integrated area and frequency placement of the peaks it is possible to observe the changes in the overpotentials brought to the cell by corresponding processes. Overall, the impedances of the processes bound to the charge transfer in electrochemical reactions (P2 – P4) were strongly reduced for the impregnated samples. It is direct proof that the electrochemical activity got enhanced thanks to the introduction of secondary transition metal.

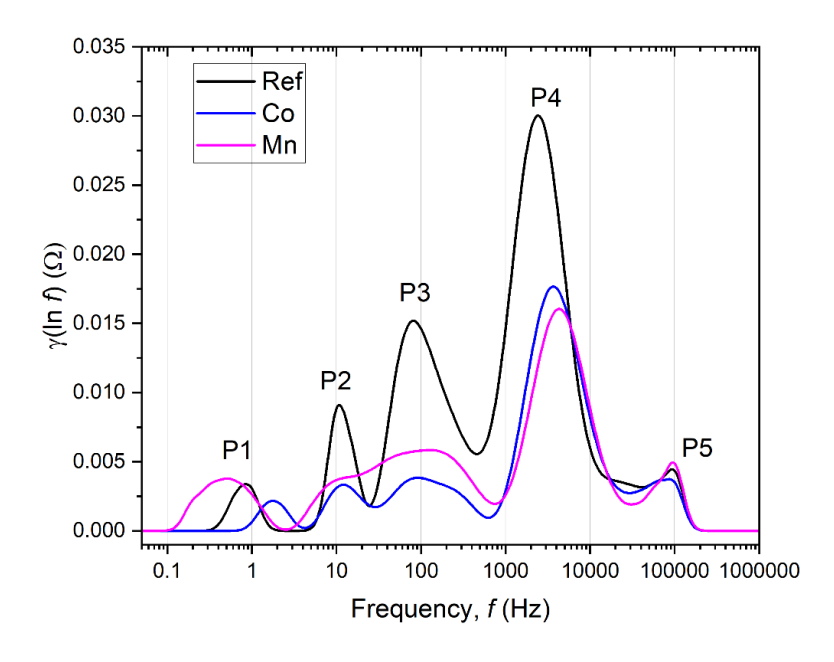


Figure 43. DRT spectra of Mn-/Co-impregnated samples and reference cell [unpublished results].

A significant decrease in the impedance of the intermediate frequency processes resulted in an increase in the SOEC efficiency, leading to the conclusion that impregnation of Ni–YSZ

composite generated synergistic effects between two coexisting metals. The resistance of process P1 is most likely minorly increased due to highly developed internal structure of the electrodes, what can negatively influence the mass transport of water vapor across the porous structure. In contrast, the process P5 ascribed to the oxygen electrode was not influenced by the modifications as those were performed on the fuel side of the cell. The cathodes were identical for all cells.

4.2.4 XAS measurements

To investigate the modifications in material properties induced by the incorporation of Co ions, a comprehensive series of X-ray absorption spectroscopy (XAS) and scanning transmission X-ray microscopy (STXM) measurements were conducted. Energy-resolved scans were performed to collect absorption spectra at the Ni and Co L_{2,3} edges, as well as the O K edge, for both as-prepared and post-operation (spent) samples. Given the predominant Ni content in the base material, Ni L_{2,3} edge spectra exhibited high similarity across all samples, with only subtle indications of Ni³⁺ species formation at the surface after testing [247]. The data will be omitted from further comments as the analysis of the collected spectra could lead to unreliable conclusions. More definitive evidence of electronic structural changes is presented in Fig. 44, showcasing the Co L_{2,3}-edge spectra obtained via both total electron yield (TEY) and partial fluorescence yield (PFY) modes. In TEY mode the signal comes from couple first atomic layers of the material, while in PFY mode the data is collected from hundreds of nm below the surface of the sample.

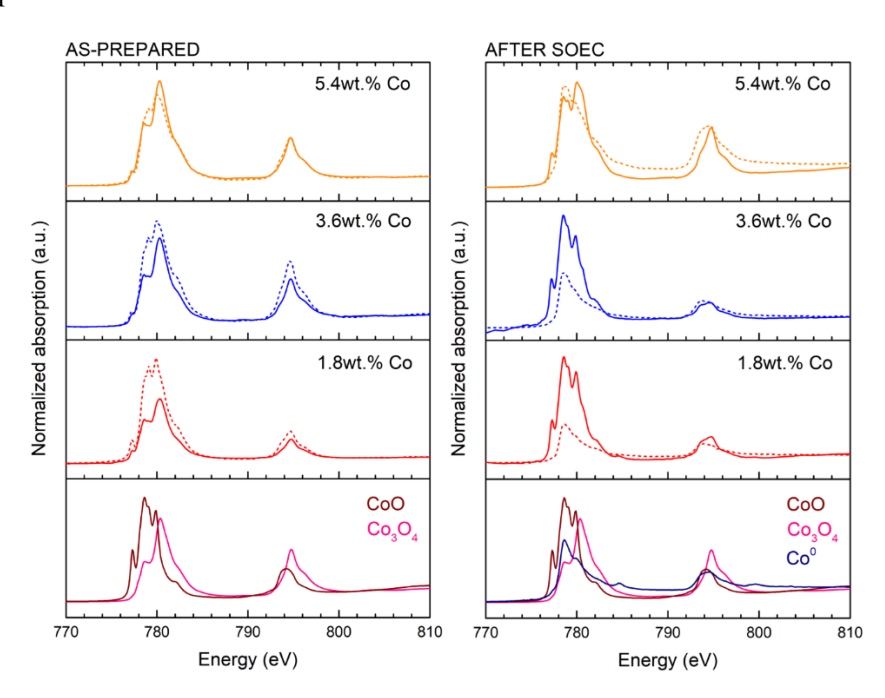


Figure 44. Co-L absorption edge of Co-impregnated SOEC: as-prepared (left) and post mortem (right). TEY signal is a solid line and PFY signal is dashed [217].

The spectra are predominantly influenced by the Co2p core-level spin-orbit coupling, resulting in the characteristic splitting into the L₃ and L₂ white lines. Notable variations in the absorption edge

profiles are evident. TEY signal intensity increased proportionally with the Co content in the material. When compared against the partial fluorescence yield (PFY) data, it was observed that samples with lower Co loading exhibited a higher proportion of cobalt cations incorporated deeper within the oxide scale. However, after successive impregnation cycles, the TEY-to-PFY intensity ratio approached value of 1, indicating a tendency for Co ions to predominantly form Co_xO_y on the surface rather than diffuse into the NiO matrix. This observation follows earlier findings from XPS analysis and TEM imaging. Beyond intensity, subtle modifications in the edge shape were also dependent on Co concentration. Reference spectra for CoO and Co₃O₄ revealed clear distinctions in pre-edge and post-edge features. The 1.8 wt% Co-impregnated sample displayed an enhanced pre-edge intensity and distortions characteristic of CoO, a trend even more pronounced in the PFY signal. Increasing Co concentration resulted in progressive oxidation, with absorption edge shapes increasingly resembling Co₃O₄. Zhang et al. reported similar spectral features corresponding to a Co²⁺/Co³⁺ ratio [248]. Post-SOEC testing spectra revealed reduction of cobalt species during cell startup, with spectral features approximating metallic Co. Subsequent exposure to residual water vapor and non-inert storage conditions led to the formation of a nanometric Co_xO_y oxide layer on the metal surface, with a higher Co₃O₄ content in the 5.4 wt% Co-impregnated sample, suggesting reduced stability and enhanced oxidation susceptibility linked to the greater initial concentration of surficial Co oxides.

Oxygen K-edge absorption spectra were recorded for the as-prepared 3.6 wt% Co sample (Fig. 45), alongside reference spectra for NiO, Co₃O₄, and NiCo₂O₄ to elucidate the composition of the surface layer, as these compounds exhibit closely spaced edge energies. Absorption features from the 8YSZ substrate and carbon tape occurred outside the energy window relevant to Ni/Co-based oxides, avoiding spectral interference. Deconvolution of the O K-edge revealed three overlapping regions consistent with NiCo₂O₄, Co₃O₄, and NiO. A distinct pre-edge peak at approximately 529 eV indicated an increased Ni³⁺ content within the surface layer of the electrode [56]. The Co pre-edge feature further confirmed the presence of Co₃O₄ nanoparticles embedded within the spinel structure and dispersed on the 8YSZ surface.

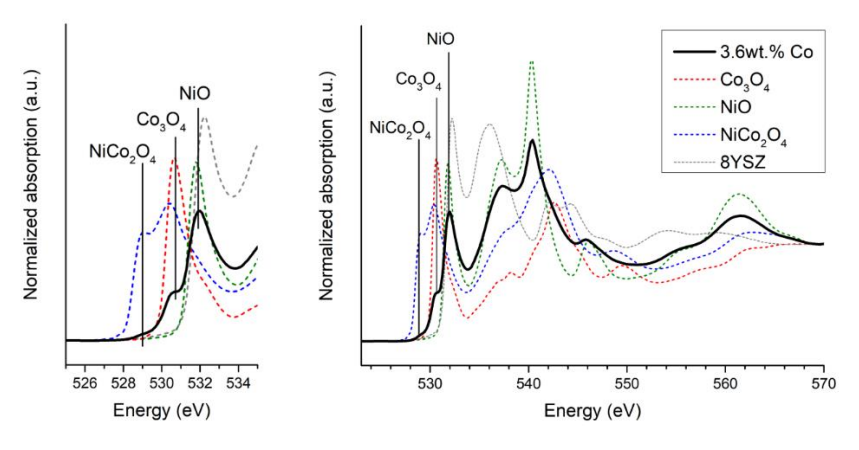


Figure 45. O-K absorption edge of 3.6wt.% Co-impregnated SOEC and reference materials [217]

The existence of NiCo₂O₄ enhanced the density of Ni²⁺/Ni³⁺ and Co²⁺/Co³⁺ redox couples, thus providing a high concentration of active sites for electrochemical reactions. Some research underscores the importance of NiCo₂O₄ spinel as electrocatalysts [249]. It is also widely recognized that a high concentration of Ni³⁺ ions is essential for the electrochemical performance enhancement of the catalyst.

In addition to the presented analysis, Mn and Co spectra of the corresponding impregnated cells are also presented in this dissertation due to promising properties of these samples. The XANES region of Mn K-edge with all the reference materials is shown in Fig. 46 left. As Mn is not easily reducible into Mn⁰ form, a pure signal from metallic Mn itself is rather hardly expected. In the case of oxidized sample, it was found out that the XANES spectrum originates from the presence of Mn₃O₄ and Mn₂O₃, while after the reduction, the oxides were reduced to MnO. What is more, it is probable that a small amount of Mn nanoparticles was formed upon reduction, as the pre-peak feature consistent with this from Mn foil can be found. Another clear evidence for reduction to Mn/MnO is the significant shift of the white line of reduced material to lower energies. The XANES region spectra of Co species were also collected. Based on this, it was possible to draw conclusions about changes in the local environment. It was clear that for the Co-impregnated cell, after reduction, the Co was present mostly in the metallic neighborhood, as the signal is similar to that of the Co foil (Fig. 46 right). At the same time, small amount of oxidized cobalt remained in the sample, which is suggested by remaining small edge feature at 7725 eV, which can be attributed to Co²⁺. At the same time, XAS spectrum for oxidized sample revealed a white line, which position (7727.5 eV) lies between Co₃O₄ (7729 eV) and spinel structure CoNi₂O₄ (7726.7 eV). The XAS spectra of the oxidized cell infiltrated with Co, may be considered as dominated by Co₃O₄ presence with traces characteristic of CoNi₂O₄ spinel, which is consistent with the previous findings.

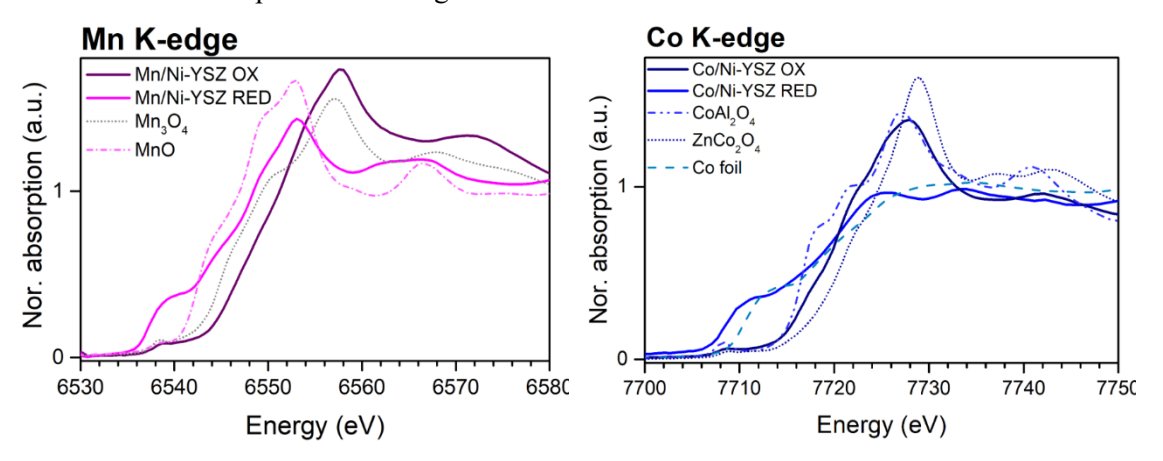


Figure 46. Mn-/Co-K edges of modified SOEC samples along reference materials [unpublished results].

4.2.5 STXM imaging

To more accurately depict the elemental distribution of the components in the electrode (in relation to their electronic structure), a series of STXM images was acquired. A representative set from the as-prepared sample containing 3.6 wt% Co is shown in Fig. 47. This advanced technique for mapping element-specific absorption edges provided new insights beyond those obtained from other imaging. Visible evidence supported earlier conclusions regarding the formation of Co-8YSZ regions and Ni–Co intermixed oxides. A reference scan taken well below the Ni and Co absorption edge energies produced an image resembling the TEM micrographs. Elemental maps were generated by subtracting images taken below and in absorption edges. Upon reaching the Co-L₃ edge energy, Co nanoparticles and NiCo₂O₄-like structures became visible within the imaging area. At higher scanning energies corresponding to the Ni-L₃ edge, a distinct bimodal distribution of Ni was observed. The dark regions corresponded to 8YSZ particles, which were impermeable to the radiation.

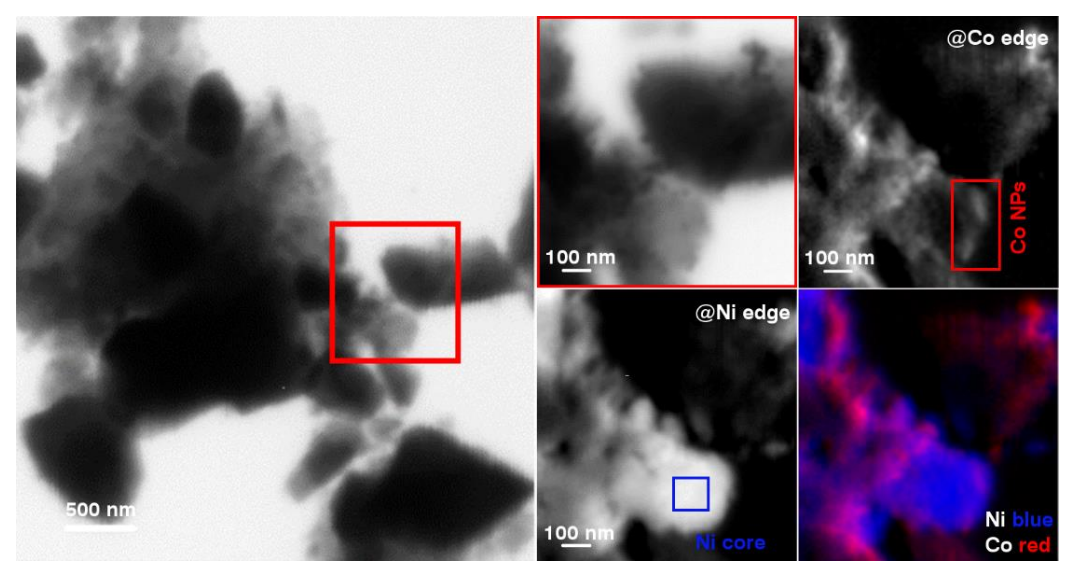


Figure 47. STXM images of the 3.6wt. % Co-impregnated SOEC (as-prepared) and elemental maps of Ni and Co. Ni and Co distribution overlay is presented [217].

Cobalt was found to be homogeneously distributed across the spongy surface of the reoxidized Ni particles, indicating the presence of a NiO–CoO mixed oxide phase. Additionally, nanoparticles of Co_xO_y , barely discernible in TEM and SEM, were identified on the YSZ surface without forming a visible interlayer, as well as spherical inclusions embedded within the Ni–Co oxide matrix. Only the trace number of larger agglomerates was detected, suggesting that impregnation assisted by β -cyclodextrin is a promising approach for achieving uniform modification of SOC cells. Ni mapping revealed distribution of the cations in the electrode. Interestingly, the structure resembled the core-shell particles, where the core consisted mainly of metallic Ni, surrounded by a NiCo₂O₄-like shell and an outer Co-enriched phase containing separated Co_xO_y nanoparticles. This complex layered architecture reflects the diffusion constraints of Co ions.

The differences in the distribution of the cations across the samples, especially for Coand Mn-impregnated materials, were clearly presented in STXM images taken on the lamellae cut out from the modified electrodes. The images with the elemental distribution maps are depicted in Fig. 48.

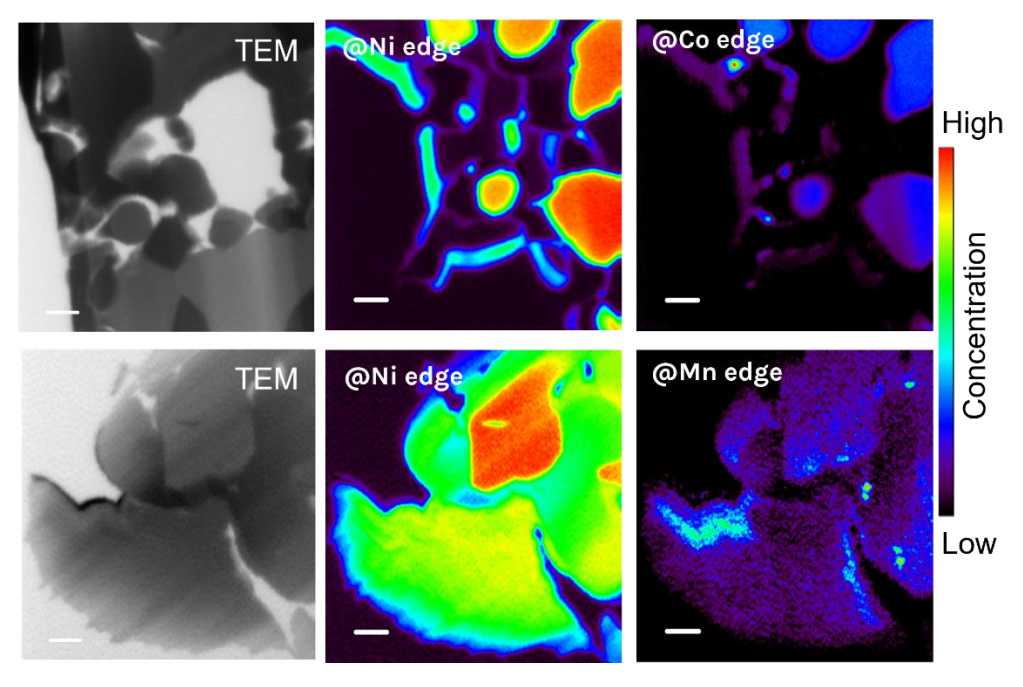


Figure 48. STXM images and elemental maps of Mn-/Co-impregnated SOEC (reduced state).

The mapping at the absorption edges of Mn, Co, and Ni revealed higher concentration of Co located within the regions occupied by Ni grains. This means that Co ions diffused into the metallic Ni and could be detected even in the cross-sections of the grains at quite high concentration. This effect indicated that cobalt is more easily dissolving in the Ni lattice than Mn, where the distribution was more discrete. Mn ions were visible across whole sample, but some higher concentration regions could be determined likely in the proximity of the Ni granule outer layer as well as YSZ grain surface. The imaging using STXM supported the statement given before, as the Mn ions are mostly forming the surface layer and Co ions are getting more dissolved into Ni grains. This could also explain the stability loss of Co-impregnated sample, where the deterioration was most likely caused by the diffusion of Co from the surface to the center of Ni grains. This finally decreased the surficial concentration of active centers for the reactions to take place. STXM is a powerful tool to determine the chemical structure of the samples and give information not only about space distribution, but also about the chemical environment. More studies will be needed to fully understand the synergistic effects of other metals introduced into the structure of Ni–YSZ.

4.2.6 Behavior during reduction and oxidation

To understand the interaction dynamics between cobalt and nickel within the Coimpregnated SOEC during heat up and subsequent reduction under a flowing H₂ atmosphere, a series of H₂-TPR experiments were conducted. The resulting reduction profiles are illustrated in Fig. 49. The reduction of all samples was completed well below 400 °C, indicative of nanostructured and porous objects that substantially decrease the reduction temperature by facilitating hydrogen access and enhancing diffusion kinetics.

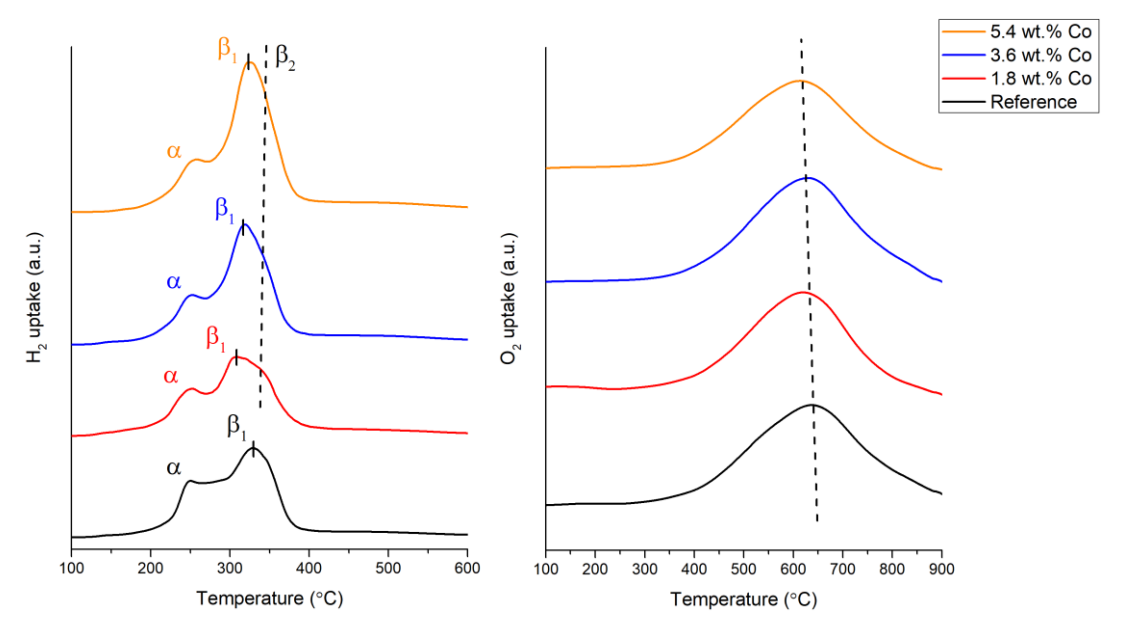


Figure 49. Reduction (left) and oxidation (right) profiles of the reference and Co-impregnated SOEC [217].

Each profile exhibits two distinct regions: a low-temperature peak (α) and a high-temperature peak (β). The α region, characterized by a reduction peak around 250 °C, was attributed to the surficial oxide layers resembling paper balls, which are most likely highly reactive due to their high oxygen mobility and low activation energy for reduction. In accordance with prior literature [248,250], the α peak corresponds to the reduction of adsorbed oxygen species on mixed-metal oxyhydroxides and/or highly dispersed oxide nanoparticles. The presence of a similar α peak in the reference sample suggests a significant concentration of Ni³⁺ ions, likely present as NiOOH. The formation of this oxyhydroxide-rich surface layer is attributed to low-temperature sintering under ambient air, as supported by TEM observations. The β region, primarily observed in the Co-impregnated sample containing 1.8 wt.% Co, exhibited a clear peak splitting. This phenomenon was ascribed to the simultaneous reduction of a NiCo₂O₄ spinel-like phase and Co_xO_y nanoparticles. To deconvolute overlapping reduction events, additional H₂-TPR analyses were conducted on 8YSZ supports individually impregnated with 5 wt.% NiO, Co₃O₄, and NiCo₂O₄, replicating the synthesis pathway used in this study. As presented in Fig. 50, the Co-impregnated YSZ sample exhibited a TPR profile reflecting a convolution of the reduction

behaviors of NiO-YSZ and Co_3O_4 -YSZ systems, with significant resemblance to that of NiCo₂O₄-YSZ.

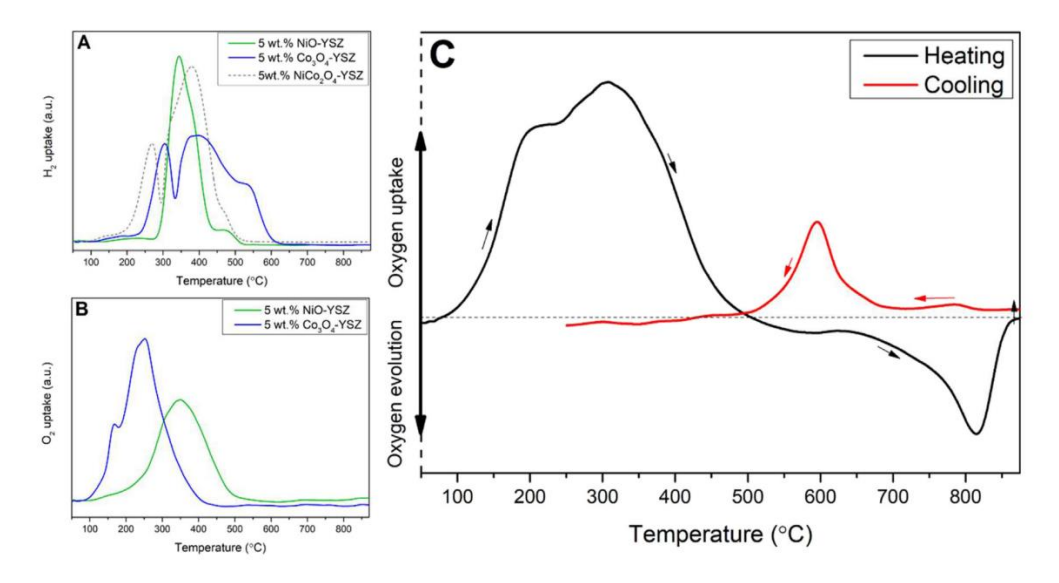


Figure 50. A) Reduction and B) oxidation profiles of NiO–YSZ and Co₃O₄–YSZ, C) Cyclic oxidation profile of the NiCo₂O₄-YSZ sample [217].

The β region was resolved into two processes – β_1 and β_2 . The β_1 subpeak got associated with the reduction of Ni²⁺ species within a Ni–Co spinel framework. Due to the strong electronic interaction and mutual dispersion of Ni and Co within the spinel matrix, the reduction temperature was substantially lowered. According to Y. Yi *et al.* [251], this shift arises from two primary factors: (i) a synergistic redox interaction between Ni³⁺ and Co²⁺, governed by the reversible charge transfer process (Ni³⁺ + Co²⁺ \rightarrow Ni²⁺ + Co³⁺), which promotes the reduction of Ni species, and (ii) enhanced dispersion of the NiO phase and increased mesoporosity of the oxide scale induced by cobalt phase formation. A well visible peak at ~300 °C is characteristic of nanometric NiO reduction to metallic Ni. Simultaneously, the reduction of Co³⁺ to Co²⁺ contributes minorly to the β_1 peak, consistent with previous findings [249].

The β_2 reduction peak, observed near 340 °C, was attributed to the reduction of cobalt species, consistent with the Co₃O₄–YSZ reference profile presented in Fig. 50A. Niu *et al.* [252] reported that for NiCo₂O₄-based catalysts the reduction of Co²⁺ to metallic Co occurs within this temperature range. The modified cell experienced synergistic effects arising from transition metal interaction. Specifically, Co ions facilitated the reduction of Ni cations at lower temperatures, while formed metallic Ni particles promoted the reduction of Co ions to the metallic state, likely via a hydrogen spillover mechanism [253,254]. With increasing Co loading, the β_1 and β_2 peaks increasingly overlap, producing a TPR profile closely resembling that of the NiCo₂O₄–YSZ reference (Fig. 50A). This implied that high Co concentration enhanced the formation of a mixed spinel phase. However, for the sample impregnated with 5.4 wt.% Co, the distinct bimodal reduction peaks diminish, suggesting that the presence of a lower-crystallinity surface layer plays a critical role in sustaining enhanced reducibility.

To further measure the changes in redox behavior, oxidation (O₂-TPO) experiments were conducted (Fig. 49), with additional reference profiles provided in Fig. 50B. Consistent with Gibbs free energy of Ni and Co oxidation and the TPO data, increasing Co content in the electrode correlated with a decreased oxidation temperature, demonstrating enhanced oxygen uptake by the modified samples. Given that SOEC operate under high water vapor partial pressures and considering the established importance of oxyhydroxides as well as Me³⁺/Me²⁺ redox pairs, the increased oxygen bonding capacity and formation of a surficial Ni–Co mixed oxide layer are critical factors influencing cell performance.

A novel, previously undocumented behavior of the NiCo₂O₄–YSZ catalyst was identified during these investigations. While the reduction characteristics aligned with literature reports [255], O₂-TPO revealed that, despite exposure to oxidizing conditions, the material released lattice oxygen at higher temperatures (Fig. 50C). This observation was verified via cyclic heating cooling experiments. Upon heating, the Ni-Co alloy supported on YSZ fully oxidized up to approximately 450 °C. Further heating beyond 600 °C caused the emergence of lattice oxygen into the gas stream (containing 5 vol.% O₂ in He), evidenced by a negative TCD signal. Upon cooling, the process reversed nearby 600 °C, with a corresponding positive TCD peak of similar magnitude, confirming the reversibility of oxygen exchange. Three primary hypotheses of this phenomena were proposed: (1) thermal decomposition of the spinel into separate NiO and CoO phases accompanied by oxygen release; (2) structural modifications (phase change) of the spinel lattice forcing evolution of oxygen; and (3) a shift in the oxygen activity coefficient and bond strength under slightly oxygen-deficient conditions, where partial surface reduction of the spinel at lower pO_2 enables lattice oxygen release kinetics to surpass oxygen uptake kinetics. These findings may hold a potential in explaining the enhanced catalytic activity observed upon Co incorporation. The associated increase in oxygen exchange rate is demanded to significantly improve electrocatalytic performance in water-splitting applications within SOEC systems.

4.2.7 Performance tests and long-term stability

To formulate the relationship between the inlet gas composition and the resultant output of the SOEC, a series of experiments were conducted when changing the H₂:CO₂ ratio and under various applied operating voltages. The experimental results are summarized in Fig. 51A–C. All tests were performed at a representative temperature of 640 °C using the sample impregnated with 3.6 wt.% Co. For voltage-dependent studies, the inlet gas composition was fixed at a 2:1 volumetric ratio of H₂ to CO₂, whereas for investigations of feed composition effects, a thermoneutral voltage of 1.3 V was used. As the cell bias increased, a linear rise in CH₄ concentration was noticed, closely followed by an increase in CO amount (Fig. 51A). This increase was compensated by a proportional decrease in CO₂ concentration, reflecting enhanced conversion efficiency. The current density also exhibited a linear rise along applied voltage,

confirming good cell performance despite the relatively low operating temperature. The observed increase in methane production was attributed to the thermodynamic equilibrium shift induced by higher reactant partial pressures (mostly CO and H₂) driving the methanation reactions.

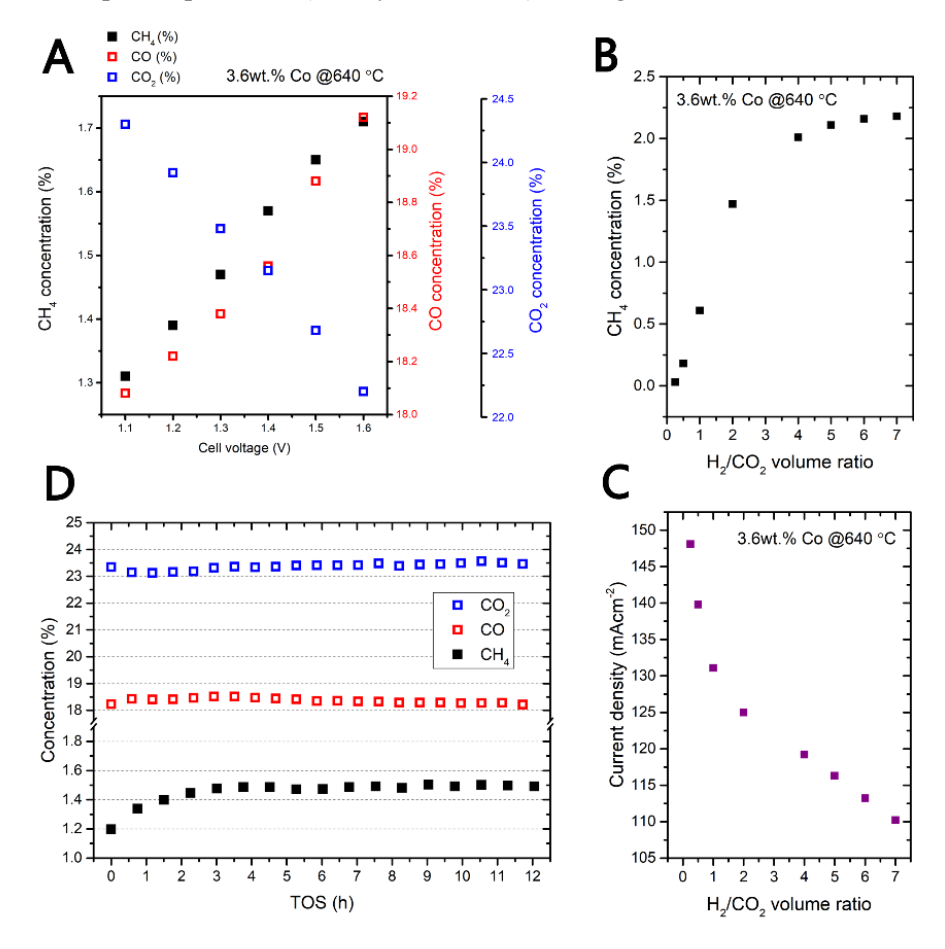


Figure 51. Extended tests of the 3.6wt.% Co-impregnated SOEC. A) change of the outlet gas composition vs. cell voltage, B-C) change of methane concentration and current density vs. H₂:CO₂ inlet mixture ratio, and D) change of gas composition during prolonged measurements in SOEC mode [217].

When varying the H₂/CO₂ volumetric ratio at a fixed potential of 1.3 V, methane production increased progressively until a ratio of 4:1 was reached, beyond which the CH₄ yield plateaued. This saturation could be explained by the full utilization of carbon, limiting further methanation. A detailed electrochemical observation emerged from comparing changes in outlet CH₄ concentration (Fig. 51B) along variations in cell current (Fig. 51C). Increasing the H₂ fraction in the feed stream caused CH₄ levels to approach thermodynamic equilibrium limitations, while the cell current simultaneously declined. This inverse correlation could suggest that a fixed amount of H₂O vapor, combined with a decreasing amount of CO₂ on the inlet, restricted electrolysis efficiency due to reactant starvation. Importantly, these findings may provide indirect evidence that CO₂ can also undergo electrochemical reduction at the electrode surface alongside Reverse Water-Gas Shift (RWGS) reaction. To evaluate the stability of the modified electrodes, an extended 12-hour durability test was conducted. The cell followed the standard startup protocol, after which the feed gas was switched to an H₂/CO₂ mix, and outlet gas concentrations

were collected at 15-minute intervals. The resulting time-on-stream change of the concentrations, presented in Fig. 51D, unequivocally demonstrates that Co impregnation does not lower the intrinsic stability of the pristine cell. Instead, it enhances catalytic activity while maintaining consistent performance throughout the 12-hour period. During the initial hours of electrolysis, a minor decline in activity was observed, primarily due to Ni particle coarsening and sintering. Beyond this phase, CH₄ concentration stabilized, exhibiting negligible variation. Similar behavior was noted for CO and CO₂ concentrations, which oscillated around 18% and 23.5%, respectively (after six hours of operation). These results confirmed that Co improves catalytic activity without inducing negative effects on cell durability.

Additional microstructural characterization was performed on spent cells (after 12h) to assess morphological and compositional changes. SEM and TEM micrographs of the used electrodes are provided in Fig. 52, complemented by µEDS elemental maps for the 3.6 wt.% Co-impregnated sample. Following reduction, Ni and Co mixed oxides were reduced down to metals, resulting in the formation of a bimetallic Ni–Co alloy on the surface of Ni particles. The Ni grains exhibited homogeneity, with no detectable secondary phase segregation. It is consistent with the Ni–Co binary phase diagram, which predicts complete solid solution formation across all compositional ranges due to similar atomic sizes and crystal structures of both metals [256,257].

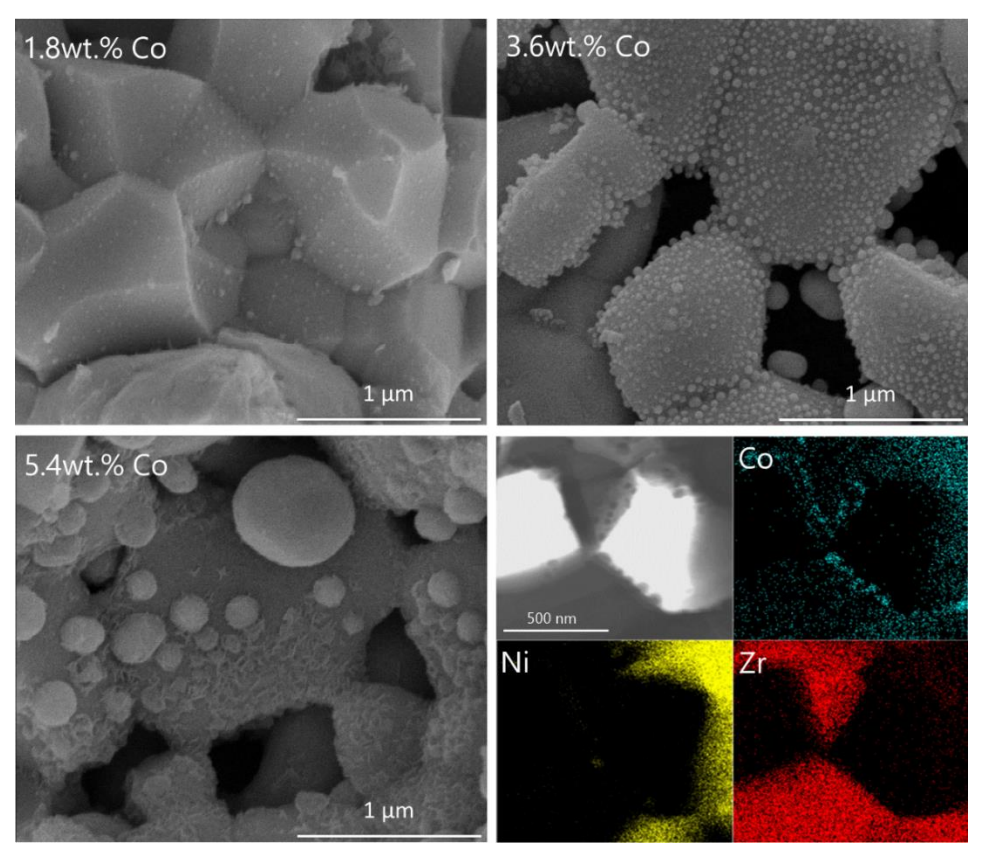


Figure 52. SEM images of spent SOEC and TEM image of 3.6wt.% Co-impregnated electrode with elemental maps [217].

Interestingly, metallic Co formed spherical nanoparticles decorating the 8YSZ grains, indicating negligible solubility of Co within the 8YSZ lattice. This behavior was evident in samples with 1.8 and 3.6 wt.% Co loadings. At the same time, the 5.4 wt.% Co-impregnated sample exhibited significant nanoparticle agglomeration and a higher propensity for oxidation, likely resulting in the formation of secondary cobalt phases visible in Fig. 52 in the form of flake-like agglomerates. These phases presumably originated from cobalt oxides precipitates that were partially reduced and not fully incorporated into the Ni matrix, subsequently reoxidized during the cooling phase, as supported by prior XAS data. The best microstructure was observed in the 3.6 wt.% Co sample, where TEM and elemental mapping revealed a uniform Ni–Co alloy alongside Co nanoparticles firmly attached to the 8YSZ grains. The enhanced electrochemical performance of the cell may be connected primarily to the synergistic coexistence of the Co–YSZ interface, which should increase surface basicity, and the NiCo₂O₄-like phase, which provides abundant active sites and develops the specific surface area, thereby driving catalytic activity improvements.

Summary of the section

This part explored the enhancement of Ni–YSZ fuel electrodes in Solid Oxide Electrolysis Cells (SOECs) through the incorporation of transition metal nanoparticles mainly cobalt, aiming to improve the efficiency and stability of CO₂/H₂O coelectrolysis and direct methanation. While nickel is widely used due to its high catalytic activity and affordability, it suffers from structural degradation under SOEC operating conditions, including sintering, carbon deposition, and particle agglomeration. The addition of Co via low-temperature impregnation addressed these limitations by introducing highly dispersed Co nanoparticles on YSZ and forming nanostructured NiCo₂O₄-like spinel phases on Ni surfaces, as confirmed by advanced microscopy and spectroscopy techniques.

The most significant improvements were observed at 3.6 wt.% Co loading, where Co incorporation increased surface basicity and both Ni³+/Ni²+ and Co³+/Co²+ ratios, leading to improved electrochemical activity. At the same time, it preserved the structural integrity of the electrode. CH₄ production more than doubled compared to unmodified electrodes (2.1% vs. 0.8%) at 1.3 V and 640 °C, with the Co-modified electrodes reaching near-thermodynamic equilibrium for methane synthesis. Additionally, CO₂ conversion and CO production exceeded equilibrium predictions, indicating the contribution of both electrochemical reduction and catalytic reactions, such as the Reverse Water-Gas Shift (RWGS). The tests of coelectrolysis in transition-metal impregnated samples, i.e. Mn, Fe, and Cu revealed positive impact of Mn on the efficiency, besides Co incorporation, in both SOFC and SOEC modes. In contrast, Fe and Cu showed limited benefits.

Durability tests confirmed the robustness of Co-modified electrodes. Over 12 hours of operation, only minor initial activity loss occurred due to Ni sintering, with gas output stabilizing thereafter. Microstructural analysis post-operation showed homogeneous Ni–Co alloy formation without secondary phase segregation, and Co nanoparticles remained well-dispersed on YSZ in optimal Co-loaded samples. However, excessive Co (5.4 wt.%) led to nanoparticle agglomeration, reoxidation, and decreased effectiveness, emphasizing the importance of optimal loading.

Redox behavior studies using H₂-TPR and O₂-TPO revealed that Co incorporation significantly enhances the reducibility and oxygen exchange dynamics of the electrodes. The formation of NiCo₂O₄ spinel phases facilitated reversible redox transitions and introduced a unique reversible lattice oxygen release around 600 °C, a previously unreported mechanism that likely contributes to enhanced catalytic activity. XAS and STXM further revealed a core–shell structure in Co-modified electrodes. Metallic Ni core was surrounded by NiCo₂O₄ and Co_xO_y inclusions. Deeper Co diffusion into Ni grains was observed compared to Mn ions via STXM imaging, what most likely contributed to long-term surface Co depletion and performance decline.

Ultimately, this work underscores the critical role of controlled nanostructuring and bimetallic synergy, particularly in the Ni–Co system, in optimizing SOEC electrode performance by balancing high catalytic activity, redox flexibility, and long-term stability.

4.3 Suppression of degradation in nanostructured fuel electrode

In this part, a novel synthesis approach for 8YSZ (Zr_{0.84}Y_{0.16}O₂) and NiO-YSZ is reported. This method employs a dual soft-hard templating strategy, utilizing a micelle-forming system based on CTAB/Pluronic P123. The fabrication route utilizes the effect of crystallizing NaCl, which results in a wormhole-like microstructure of the pellets after the sintering step. The exact procedure was described in detail in section 3.9.2. Despite the absence of any external poreforming agents, high porosities of approximately 50% were retained after high-temperature treatment. It was attributed to the synergistic effects of both organic templates and the hightemperature meltdown and removal (volatilization) of NaCl. The synthesized materials were comprehensively characterized and benchmarked against conventional state-of-the-art materials typically used in Solid Oxide Cells. The co-precipitation of NiO-YSZ via this synthesis route enabled thorough dispersion of NiO grains, which were strongly integrated with the YSZ matrix. Extended degradation studies demonstrated that the novel composite exhibited a lower degradation rate and enhanced microstructural stability under Solid Oxide Fuel Cell (SOFC) operational conditions. The results described in this chapter were previously presented in [258] Blaszczak P., Ducka A., Wolanin B., Matlak K., Machowski G., Prześniak-Welenc M., Wang S.-F., Bochentyn B., Jasiński P. Fabrication of wormhole-like YSZ and Ni-YSZ by the novel softhard template CTAB/NaCl-assisted route. Suppressing Ni coalescence in SOFC. J Eur Ceram Soc 2023; 43:438–51. 10.1016/j.jeurceramsoc.2022.09.054.

4.3.1 Microstructure and phase composition

The phase composition of the synthesized precursor powders and fired pellets was analyzed using X-ray diffraction (XRD), with the corresponding patterns shown in Fig. 53. The precursor exhibited powders low crystallinity and consisted of multiple phases (Fig. 53, left). The dominant diffraction peaks were attributed to the cubic halite phase (NaCl, space group

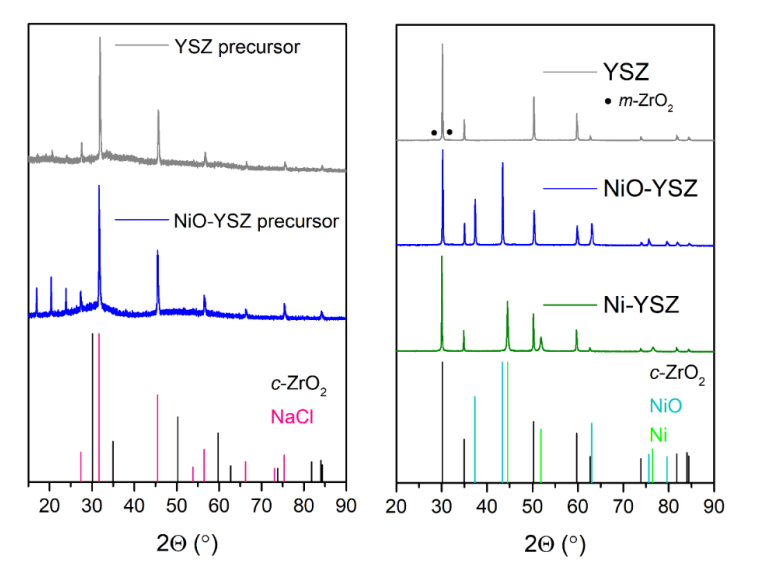


Figure 53. XRD diffractograms of the precursor powders (left) and fired pellets (right) [258].

Fm-3m), which formed during the drying stage of synthesis, indicating a substantial retention of NaCl within the material structure. Additional low-intensity and broad peaks were assigned to mixed oxyhydroxide/hydroxide phases of zirconium, yttrium, and nickel. Only weak and

broadened reflections associated with a ZrO₂-like phase could be distinctly identified. Despite the presence of NaCl, the salt phase did not form well-defined, highly crystalline cubic structures. The XRD data for sintered pellets prepared from 0.3 M CTAB/NaCl-modified YSZ and NiO–YSZ will be discussed in detail in further parts of this dissertation. The '0.3 M CTAB/NaCl-modified' prefix stands for the samples prepared using starting solution of cation concentration equal to 0.3 M with the addition of CTAB/Pluronic P123 and with crystallized NaCl.

The precursor NiO–YSZ xerogel, post-milling, exhibited a spongy and flaky morphology, with no clearly distinguishable crystalline domains. The SEM image of the precursor milled powder is presented in Fig. 54 right. The mild milling process introduced good homogeneity of the powders. Some degree of particle agglomeration was noted, likely due to the high specific surface area and the hygroscopic nature of the material. Nevertheless, the amorphous oxyhydroxide particles appeared well-dispersed and effectively embedded within the NaCl matrix. The structure of pure YSZ precursor powder was similar to the one of NiO–YSZ. Despite that, the 0.3 M CTAB/NaCl NiO–YSZ precursor powder exhibited a greater tendency towards clumping. The gel formed a heterogeneous matrix composed of intermixed Ni- and Zr–Y-based oxyhydroxides, with no distinct phase separation between the Ni and Zr–Y components. Nanoparticles of oxyhydroxides were observed to be embedded within large agglomerates of poorly crystalline NaCl.

The spatial distribution of the Ni–containing subphase was further investigated using synchrotron-based Scanning Transmission X-ray Microscopy (STXM). A set of images was collected at 848 eV (below the Ni absorption edge), 853 eV (at the Ni absorption edge), and 1070 eV (at the Na absorption edge). The two images acquired at two distinctive Ni energies were used to generate a nickel distribution elemental map, shown in Fig. 54 left. The absorption edge aligned closely with that of the NiO phase but appeared slightly shifted to lower energies, with a noticeable pre-edge feature. This suggested a modest increase in the average oxidation state beyond +II, likely due to the formation of NiOOH alongside NiO during the low-temperature synthesis [259].

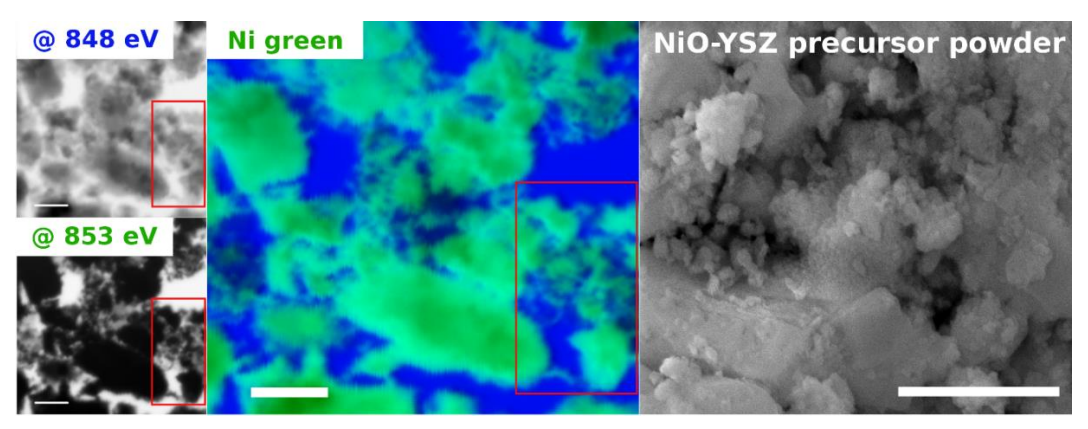


Figure 54. STXM images of the NiO–YSZ precursor powder, Ni elemental map and complementary SEM image. Scale bars are 1 µm [258].

Transmission images taken at the Ni absorption edge revealed a fairly uniform distribution of Ni across the imaged area. In regions where particle sizes approach the critical thickness for beam transmission, the absorption by Ni compounds fully darkens those portions of the image. Conversely, areas with finer precursor particles (highlighted in red in Fig. 54) show selective darkening, indicating clusters with high Ni amount. This points out the presence of submicron Ni-rich precipitates embedded within the surrounding gel. The question was if those highly intermixed species would form the resulting NiO-YSZ composite upon sintering. In practice, the two precipitated phases separated distinctly. This was driven by the significant differences in the thermodynamic parameters governing the precipitation of Ni(OH)₂ from NiCl₂ compared to the Zr(OH)₄–Y(OH)₃ system. Thermochemical calculations using HSC Chemistry software indicated that the neutralization of NiCl₂ with NaOH has a substantially lower enthalpy change (ΔH_{303K} = -47.4 kcal·mol⁻¹) than those of Zr and Y salts (Zr: -163.1 kcal·mol⁻¹; Y: -103.4 kcal·mol⁻¹). Coupled with a higher entropy change (ΔS_{303K}), Ni(OH)₂ precipitates rapidly at 30 °C. It is well ahead of Zr and Y hydroxides e.g. due to thermal limitations, such as release of the heat in the reaction environment during Ni precipitation [260]. As a result, the two components could form two respective phases despite the nanoprecipitate scale. Moreover, Ni exhibits minimal solubility within the YSZ cubic lattice, preventing interdiffusion of NiO and YSZ during sintering. This separation allows for the formation of a highly interwoven yet phase-separated structure during one-pot synthesis. Additional measurements at Na absorption edge confirmed the huge amount of NaCl, which later acted as a high-temperature pore former and flux. Upon leaving the structure it left behind the wormhole structure described below. Unfortunately, the Zr and Y absorption edges could not be measured because they fall outside the energy range accessible at the synchrotron facility.

Following the sintering of precursor powders at 1400 °C and 1370 °C, respectively, crystalline products of pure YSZ and NiO–YSZ were obtained. For the 0.3 M CTAB/NaCl NiO–YSZ sample, sintering at 1400 °C resulted in a fully dense pellet. To preserve the wormhole-like porous structure characteristic of the 0.3 M CTAB/NaCl NiO–YSZ, the sintering temperature was thus lowered to 1370 °C. The XRD analysis indicated that sintering at 1400 °C led to the formation of cubic YSZ phase (*Fm-3m*), with only minor traces of monoclinic ZrO₂ (*P21/c*). The unit cell parameter (a = b = c) for the YSZ phase was determined to be 5.129 Å, consistent with literature values for 8 mol% Y₂O₃-stabilized zirconia (8YSZ) [261], indicating the formation of the desired product. The minor presence of the monoclinic phase may be attributed to local fluctuations in Y dopant concentration or a slightly insufficient sintering temperature. However, the quantity of this secondary phase is so low that its impact on overall ionic conductivity is negligible. The formation of a single-phase cubic YSZ with appropriate stoichiometry confirms the effectiveness of co-precipitation method in the synthesis of both YSZ and NiO–YSZ.

The XRD pattern of the sintered 0.3 M CTAB/NaCl NiO-YSZ sample (Fig. 53, right) clearly shows the presence of two distinct crystalline phases: cubic NiO (Fm-3m) and 8YSZ. Despite that, the unit cell parameter of the 8YSZ phase calculated using Rietveld refining method was slightly reduced (5.125 Å) compared to conventional 8YSZ. According to Linderoth et al. [262], such a decrease in lattice parameter can occur when small amounts of Ni²⁺ incorporate into the YSZ lattice. In another study, Ni-doped YSZ underwent reduction in hydrogen, leading to the exsolution of Ni particles from what initially appeared to be a single-phase material [263]. A similar phenomenon is likely to have occurred in the current study: a limited amount of nanometric NiO may have dissolved into the YSZ lattice during high-temperature sintering step. Although the solubility of NiO in ZrO₂ is extremely low (~2 mol%) and typically not achievable through bulk reactions [264], the presence of yttrium to stabilize the cubic phase increases the solubility limit, though it likely still remains below 5 mol% [265]. In the CTAB/NaCl-assisted synthesis route, the dissolution of NiO into the YSZ lattice was facilitated by nanoscale effects. However, the amount of NiO incorporated into the NiO-YSZ solid solution was still considered minimal. To estimate this incorporation, the equation proposed by Kuzjukevics et al. [265] was applied. This formula is given in Eq. 48 and relates the lattice parameter of NiO-doped YSZ (a_{NiO-} YSZ) to the molar fractions of YO_{1.5} and NiO incorporated into the crystal lattice.

$$a_{NiO-YSZ} = 0.5119 + 0.0001394 m_{YO_{1.5}} - 0.000515 m_{NiO}$$
 (48)

It was estimated that approximately 1 mol% of NiO was dissolved within the 8YSZ lattice following the sintering step, consistent with previous investigations into NiO–YSZ interactions in nanocomposite systems [262]. Despite the relatively low level of dissolution, the partial incorporation of Ni ions into the YSZ lattice was ultimately leading to the formation of minor amount of the Ni nanoparticles in the novel structures presented in this study. This phenomenon will be discussed later in the section. For the 0.3 M CTAB/NaCl Ni–YSZ sample (i.e., NiO–YSZ subjected to reduction at 800 °C for 10 hours in H₂), the XRD analysis revealed the coexistence of two phases: cubic Ni (*Fm-3m*) and cubic 8YSZ. Notably, the diffraction peaks corresponding to the Ni phase were broadened, indicative of nanoscale crystallite formation. The greyish-green coloration of the sintered NiO–YSZ pellets further supported the statement that the CTAB/NaCl synthesis method promotes the formation of submicrometric NiO grains. This novel fabrication approach effectively restricts NiO grain growth, despite the well-known tendency of NiO to sinter and coalesce at elevated temperatures.

Furthermore, SEM images of YSZ pellets synthesized via the novel route are shown in Fig. 55. These images were taken from fractured surfaces of porous samples sintered at 1400 °C. As the concentration of metal cations in the precursor solution increased, distinct changes in microstructure and porosity were observed. Samples prepared from the lowest (0.1 M) and highest (0.5 M) cation concentrations exhibited significantly higher densification compared to intermediate compositions.

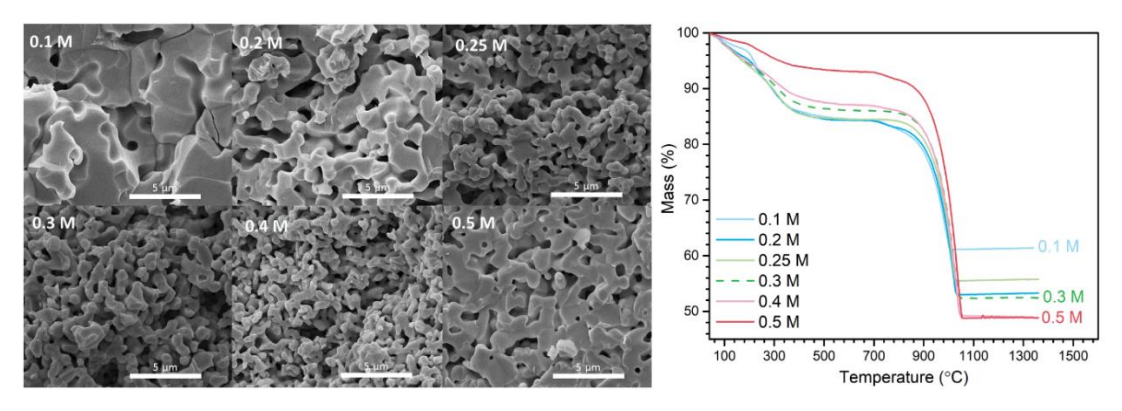


Figure 55. SEM images of YSZ scaffolds sintered at 1400 °C (left) and TGA curves of YSZ precursor powders (right) [258].

For the 0.1 M solution, densification was attributed to the formation of highly dispersed, strongly nanometric particles during precipitation. Additionally, the diluted precursor favored the generation of a loose, separated precipitation, which did not effectively retain the organic phase within the gel structure. Increasing the cation concentration led to a progressive increase in porosity and specific surface area (SSA), reaching a maximum at 0.3–0.4 M, where the most interesting structures were observed. Further increase of the concentration beyond 0.4 M resulted in enhanced densification and total loss of porosity. During synthesis, it was obvious that the precipitates formed large, agglomerated chunks. Relative to the whooping amount of precipitate generated, the fixed quantity of organic additives became insufficient to act as an effective template, thus compromising the formation of a porous network. For intermediate cation concentrations, a noticeable change in microstructure was observed, characterized by a network of small, rounded particles with an average diameter of approximately 400 nm. These particles formed a highly porous scaffold composed of sintered grains interconnected by narrow channels. This distinctive architecture is referred to throughout the text as the 'wormhole-like structure'.

4.3.2 Thermal analysis

Despite the absence of conventional pore formers such as PMMA, graphite, or starch, the structure was porous even after sintering. When considered as a potential SOC anode, this microstructure offers significant advantages by providing a high specific surface area, which facilitates efficient oxygen ion distribution within the Ni–YSZ composite. An additional benefit lies in the minimal use of nontoxic organic additives (CTAB/P123). Although present in low concentrations, they contribute effectively to the formation of a highly porous and homogeneous scaffold. The development of this unique microstructure can be attributed to two key mechanisms. First, the thermal decomposition and removal of the organic surfactants serve to separate YSZ grains, functioning analogously to traditional pore formers. Second, NaCl crystals within the gel structure, up to its melting point, act as a rigid template that mechanically supports the structure and inhibits excessive densification during sintering. Previous studies have shown that washing the gel with deionized water prior to sintering removes the salt and results in dense YSZ pellets,

confirming the essential role of NaCl in forming the wormhole-like porous structure. This approach offers practical and environmental advantages: it eliminates the need for external pore formers and minimizes the release of gaseous byproducts during the burnout process.

To gain a deeper understanding of the processes occurring during sintering, thermogravimetric (TG) and differential scanning calorimetry (DSC) analyses were conducted on the precursor powders. The thermogravimetric data for YSZ precursors with varying cation concentrations are shown in Fig. 55 (right). A significant mass loss was observed between 50 °C and 1000 °C, with the final mass of the residue of approximately 45–60% of the initial mass. The TG curve can be divided into two distinct regions: the first, occurring below 400 °C, and the second between 800 °C and 1050 °C. The initial mass loss is primarily attributed to the evaporation of physically adsorbed water. It is followed by the decomposition and burning of the organics. The latter region of the TG curve is marked by a significant weight loss, initially associated with the melting of NaCl, followed by substantial salt volatilization as the temperature continues to rise. To gain more information about the sintering behavior, thermogravimetric and differential scanning calorimetry (TG/DSC) analyses were carried out on the 0.3 M CTAB/NaCl YSZ and 0.3 M CTAB/NaCl NiO–YSZ pristine powders. The corresponding TG/DSC curves are shown in Fig. 56A.

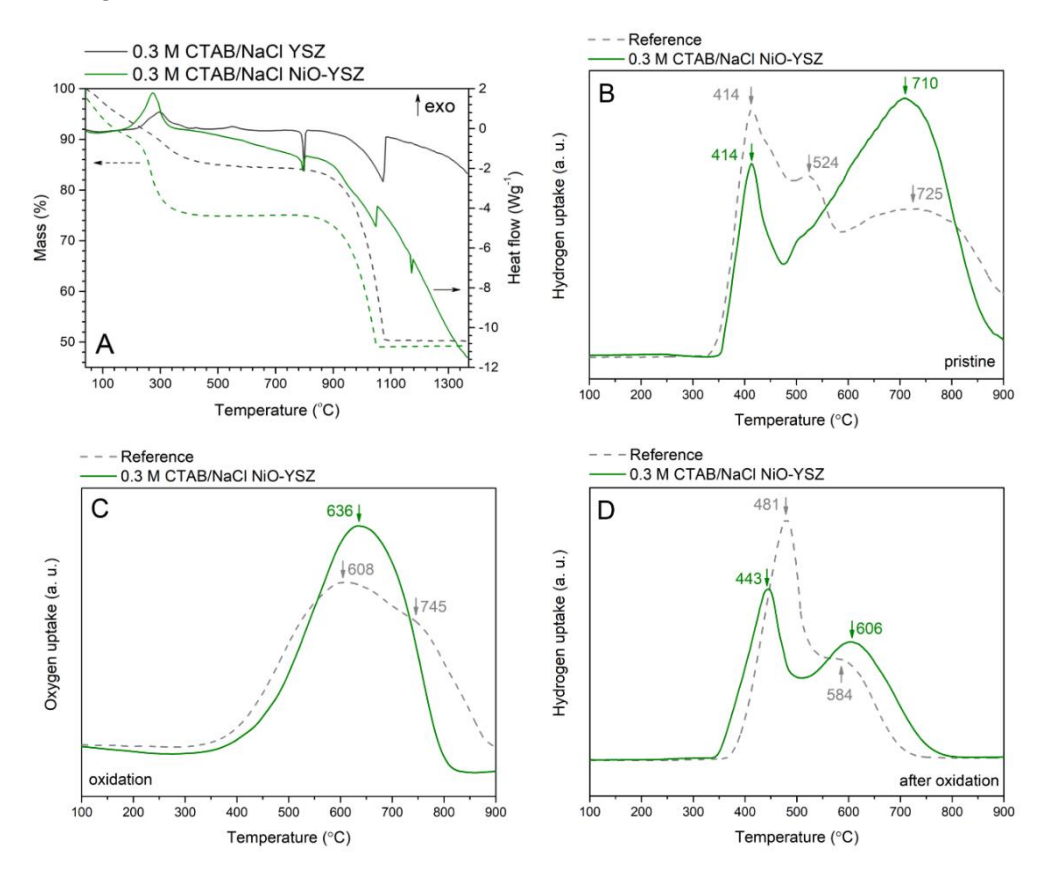


Figure 56. A) TG-DSC curves of YSZ and NiO-YSZ precursors, and B,C,D) reduction-oxidation-reduction curves of 0.3 M CTAB/NaCl NiO-YSZ and conventional cermet material [258].

The initial mass loss is attributed to the evaporation of residual structural water present in the powders. Subsequently, at approximately 273 °C for NiO-YSZ and 293 °C for YSZ, respectively, the decomposition and burnout of CTAB and other organic components occurred, producing a distinct endothermic peak in the DSC signal along with a noticeable reduction in mass. In both precursor systems, NaCl melting occurred at approximately 800 °C, followed by volatilization at 1075 °C for YSZ and 1047 °C for the NiO-YSZ cermet. The volatilization of NaCl was completed by 1080 °C, resulting in a total mass loss of 50% for YSZ and 51% for NiO-YSZ. Sintering began above 1100 °C, as evidenced by the emergence of an endothermic signal and a corresponding decrease in DSC heat flow. An additional endothermic peak observed at approximately 1180 °C in the NiO-YSZ sample was attributed to the melting of trace amounts of Na₂O based on [266]. This feature is absent in the YSZ curve and is believed to result from an excess of Na+ ions introduced during the synthesis of the NiO-YSZ precursor. In fact, no Na-rich phases were detected in the XRD patterns, suggesting that the surplus sodium does not influence either the sintering behavior or the final phase composition of the cermet. The endothermic valley associated with sintering was more pronounced in the cermet sample, which is consistent with the well-established effect of NiO addition on lowering the activation energy required for YSZ densification [267].

4.3.3 Reducibility of the nanocomposites. Integration of Ni and YSZ

To gain a more comprehensive understanding of the metallic phase integration with YSZ, a series of temperature-programmed reduction (TPR) and oxidation (TPO) experiments were conducted. The complete measurement cycle included two consecutive reduction steps separated by an intermediate oxidation step. The results are presented in Fig. 56B, C, and D. The 0.3 M CTAB/NaCl NiO–YSZ sample was compared with a reference anode-supported cell obtained from NTUT. In the first reduction profile (Fig. 56B), both the reference and the 0.3 M CTAB/NaCl NiO–YSZ sample exhibited a reduction peak at approximately 414 °C, which is attributed to the reduction of weakly bound or surface NiO particles [206]. In the reference sample, a distinct reduction peak at 524 °C corresponded to the reduction of the anode functional layer, which is characterized by lower porosity and worse permeability of gases. This behavior was not observed in the 0.3 M CTAB/NaCl NiO–YSZ sample, as the synthesis approach did not produce bimodal porosity. At higher temperatures (~700 °C), both reduction profiles peaked due to the reduction of NiO particles that were strongly integrated with YSZ. What is interesting, the 0.3 M CTAB/NaCl NiO–YSZ powder reduced at a slightly lower temperature with significantly higher consumption of H₂ compared to the reference.

These observations indicated that the CTAB/NaCl-assisted route led to the higher degree of NiO incorporation with the YSZ ionic support. Furthermore, the reduction kinetics were less limited by mass transport effects, most likely due to the smaller NiO size, compared to the high-

energy milling approach used in preparation of the reference sample [268]. The degree of NiO–YSZ interaction depends on the NiO content. At lower loadings, NiO tends to be well-dispersed. However, coarsening becomes more likely as the NiO content increases. In the present case, the formation of much smaller NiO particles was attributed to inhibited aggregation, caused by strong interfacial interactions [268–270]. The initial nanostructure and high dispersion of the hydroxides in the precursor facilitated the development of an extended interface between NiO and the ionic phase, enhancing interdiffusion and anchoring during sintering.

The presence of two distinctive cermet layers in the reference sample was also evident in the TPO profile (Fig. 56C), where two oxidation peaks appeared at 608 °C and 745 °C. The first one was associated with oxidation of the gas-transport (more porous) layer, while the second most likely corresponded to bulk oxidation of densely packed Ni grains in the AFL. In contrast, the 0.3 M CTAB/NaCl Ni–YSZ sample exhibited a single oxidation peak at 636 °C, indicating complete oxidation occurring in a single process.

To further validate the results, a second TPR run was performed, with results shown in Fig. 56D. The growth of Ni/NiO grains in the 0.3 M CTAB/NaCl NiO-YSZ was clearly suppressed. The low-temperature reduction peak (initially at 414 °C) shifted by only 29 °C, compared to a 67 °C shift in the reference sample. It indicated that the formed NiO particles in the CTAB/NaCl NiO-YSZ sample remained smaller, more dispersed, and most likely more stable. Additionally, the absence of a high-temperature reduction peak in the second cycle for both samples confirms that the first reduction fully decomposed the minor amounts of reducible NiO-YSZ phases.

To conclude it may be stated that smaller upward shift of the initial reduction peak, combined with a relatively intense secondary peak at higher temperature, indicates reduced NiO migration and coalescence. The novel synthesis method aided in preservation of Ni–YSZ interfacial anchoring in the cermet.

4.3.4 Porosity and thermal expansion

The porosity of YSZ after the sintering at 1400 °C was assessed using the Archimedes principle density measurements, with results summarized in Fig. 57. The results highlight the distinction between open and total porosity. To ensure statistical reliability and minimize measurement errors, at least three samples per composition were tested. A theoretical density equal to 6.1 g·cm³ was used for yttria-stabilized zirconia. The error was estimated to be the standard deviation of the mean value.

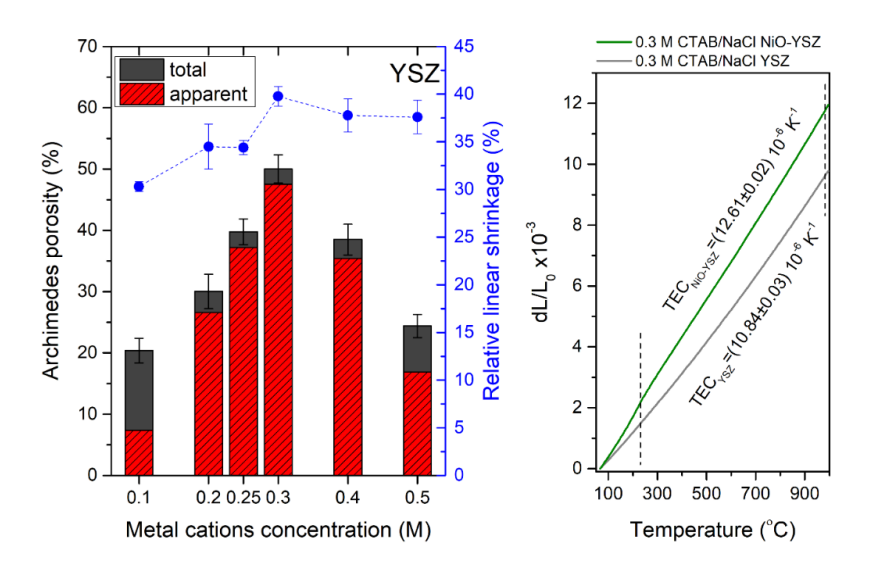


Figure 57. Porosity (bars) and linear shrinkage (dots) of CTAB/NaCl YSZ vs. starting cation concentration (left) and TEC of 0.3 M CTAB/NaCl YSZ and NiO-YSZ (right) [258].

The data revealed that porosity reached its maximum at a metal cation concentration of 0.3 M, which correlates well with the microstructural observations from SEM analysis. For intermediate cation concentrations (0.2–0.4 M), open porosity took a major portion of the total porosity, indicating a well-developed porous network. Conversely, at the lowest (0.1 M) and highest (0.5 M) concentrations, a larger fraction of the porosity was attributed to closed porosity, suggesting increased densification or reduced pore connectivity. The reference Ni–YSZ material with Ni etched exhibited total porosity of $(66.1 \pm 1.2)\%$, with an open porosity of $(64.0 \pm 1.0)\%$.

The porosity of NiO–YSZ fired at 1370 °C was evaluated, revealing a total porosity of $(36.1 \pm 0.4)\%$, with an apparent (open) porosity equal to $(34.0 \pm 1.0)\%$. Following reduction at 800 °C, the total porosity increased to $(50.0 \pm 1.0)\%$, and the open porosity reached $(48.0 \pm 1.0)\%$, comparable to the values retrieved for the 0.3 M YSZ sample. Osinkin D. *et al.* [271] demonstrated that a porosity range of 40–50% in Ni–YSZ anodes offers an optimal balance between mechanical integrity and gas permeability. Traditionally, achieving such porosity levels requires the addition of e.g. 5–15 wt% graphite as a pore-forming agent prior to sintering. In contrast, the CTAB/NaCl-assisted synthesis developed in this study achieves the target porosity without the use of any external pore formers.

In addition to porosity measurements, the relative shrinkage of the samples after high-temperature sintering was calculated, and the results are presented in Figure 57 (left) as blue dots. To minimize the possible error, multiple pellets of the same composition were used for the measurement (3). The relative linear shrinkage ranged from 30–40%, reaching highest value for the 0.3 M CTAB/NaCl YSZ equal to (39.8 ± 1.1) %. In fact, this value increased along increasing porosity of the samples. This indicates a significant loss of additives present in the green pellets during sintering, followed by the diffusion and growth of the YSZ grains. Samples synthesized

via the CTAB/NaCl templating method exhibited higher shrinkage values compared to conventional YSZ materials fabricated using conventional techniques at similar sintering temperatures [272,273]. The novel $0.3 \, \mathrm{M} \, \mathrm{CTAB/NaCl} \, \mathrm{NiO-YSZ}$ cermet demonstrated a relative linear shrinkage of $(37.8 \pm 0.8)\%$. Similar shrinkage values for the YSZ electrolyte and composite electrodes are essential to reduce mechanical stress between the components and in case of this material it can be tuned by properly designing the sintering procedures of the NiO-YSZ and YSZ layers [273]. Consequently, the $0.3 \, \mathrm{M} \, \mathrm{CTAB/NaCl} \, \mathrm{YSZ}$ and NiO-YSZ materials described in this study meet compatibility requirements.

Dilatometry results for the CTAB/P123-assited 0.3 M YSZ and 0.3 M NiO–YSZ are shown in Fig. 57 (right). The TEC was calculated by linear regression (R^2 = 0.999) over the temperature interval indicated by dashed lines. The range was narrowed to exclude the deviation in slope observed in the NiO–YSZ curve near 230 °C, which corresponds to the magnetic transition of NiO from antiferromagnetic to paramagnetic behavior [274]. Mori *et al.* [103] previously reported that even composites containing as little as 10 vol% NiO may exhibit noticeable changes in TEC due to this transition. The determined TEC values were $(10.84 \pm 0.03) \times 10^{-6} \cdot \text{K}^{-1}$ for 0.3 M CTAB/NaCl YSZ and $(12.61 \pm 0.02) \times 10^{-6} \cdot \text{K}^{-1}$ for NiO–YSZ, consistent with reported values for similar materials measured in synthetic air [271].

The specific surface area (SSA) was determined using nitrogen adsorption based on the Brunauer–Emmett–Teller (BET) isotherm model. The resulting adsorption isotherms are shown in Fig. 58 (A,C).

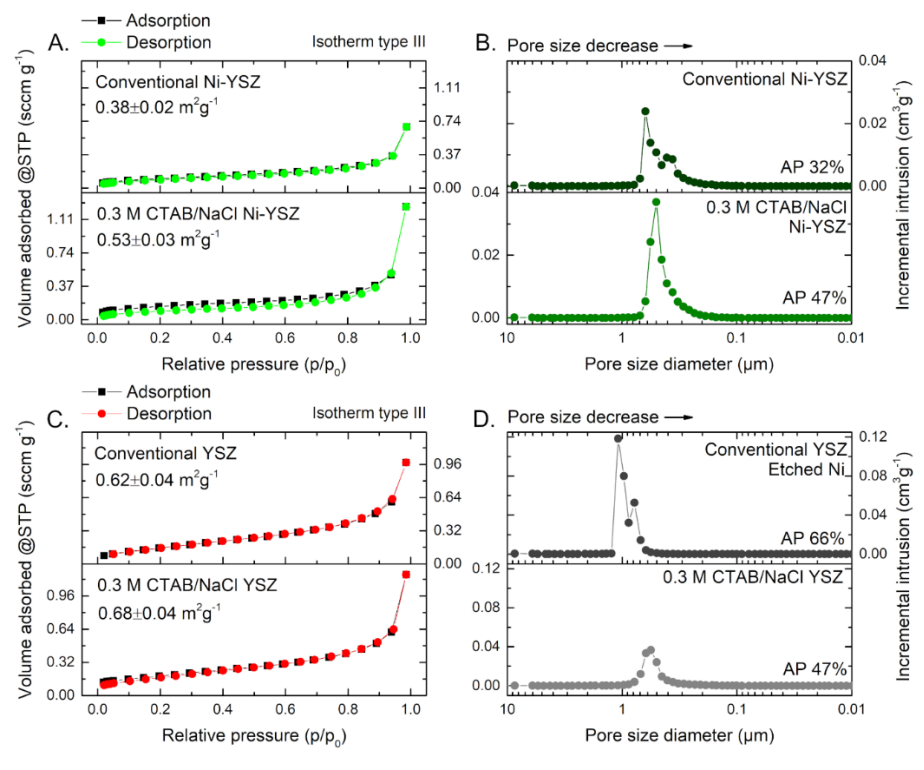


Figure 58. Nitrogen adsorption isotherms (A,C) and pore size distribution (B,D) of 0.3 M CTAB/NaCl YSZ and Ni–YSZ. Reference materials are NiO–YSZ after reduction and YSZ after Ni etching [258].

The nitrogen adsorption isotherms of the cermets and yttria-stabilized zirconia (YSZ) samples, as depicted in Figures 58A and 58C, exhibit a type III isotherm without any hysteresis loop. This behavior suggests the absence of microporosity and a minimal presence of mesopores in these materials. Most of the specific surface area (SSA) arises from macroporosity, which rapidly fills as the relative pressure (p/po) approaches 1, primarily due to capillary condensation processes. Consequently, the structures are fully permeable, with negligible N2-substrate interactions. Comparative analysis indicates that the novel 0.3 M CTAB/NaCl NiO–YSZ and YSZ materials exhibit similar pore size distributions, despite differences in SSA values. The smaller grain sizes of NiO and YSZ in the novel cermet are expected to enhance the triple-phase boundary (TPB) length, potentially improving the electrochemical performance of cells incorporating this material. This statement could not be supported by the BET isotherm SSA measurements. The CTAB/NaCl templating method facilitated the formation of highly porous structures with long, effective pore channels, even when high-temperature sintering is employed to achieve sufficient mechanical strength.

Pore size distribution curves obtained via Mercury intrusion porosimetry (MIP), shown in Figures 58B and 58D, reveal that both the novel Ni–YSZ (reduced NiO–YSZ) and YSZ materials possessed a narrower and more uniform pore size distribution in the 0.3– $0.7~\mu m$ range, with average pore diameters of $0.50~\mu m$ and $0.59~\mu m$, respectively. In contrast, the reference YSZ obtained by the removal of metallic nickel by etching from the Ni–YSZ scaffold exhibited larger pores with an average diameter of $1.08~\mu m$. The reduced reference Ni–YSZ had a similar average pore diameter ($0.53~\mu m$) compared to the novel material. MIP data indicated that the novel $0.3~\mu m$ CTAB/NaCl NiO–YSZ cermet has a higher total pore area compared to the reduced reference cermet. This suggests that the CTAB/NaCl templating method led to the formation of highly porous compounds with uniformly distributed pores. Table 6 summarizes the porosity parameters of the reference samples and novel YSZ/NiO–YSZ materials obtained by MICP.

Table 6. Comparison of the porosity parameters of the reference and novel YSZ and cermet materials obtained by the MICP technique. The measurement uncertainty is 5% as given by the manufacturer of the equipment.

	0.3 M CTAB/NaCl YSZ	Conventional YSZ (etched Ni)	0.3 M CTAB/NaCl Ni–YSZ (after reduction in H ₂)	Conventional Ni–YSZ (after reduction in H ₂)
Total pore area (m ² g ⁻¹)	1.054	1.258	1.049	0.771
Median pore diameter by volume (μm)	0.6022	1.0622	0.5208	0.5782
Median pore diameter by area (μm)	0.5663	1.0059	0.4884	0.4575
Average pore diameter (µm)	0.5965	1.0894	0.5002	0.5287
Apparent porosity (%)	47.19	65.83	46.85	31.95

The results indicated that the CTAB/NaCl templating method yields scaffolds with comparable total pore areas and apparent (open) porosities for both YSZ and NiO-YSZ. The open porosity values derived from MICP align with those obtained using the Archimedes principle density measurement method, though slight discrepancies exist due to the different measurement techniques. While nitrogen adsorption isotherms are commonly used to determine SSA, MICP provides complementary and more reliable information on pore volume and size distribution. However, the two techniques yield different results due to their distinct measurement principles and limitations. Therefore, comparisons between SSA values obtained from these methods should be made cautiously, considering the overlapping pore size ranges accessible to both techniques [275,276].

4.3.5 Electrical conductivity and stability of composite

The conductivity of YSZ and NiO–YSZ samples synthesized via the CTAB/NaCl-assisted method was evaluated using the Van der Pauw (VdP) technique under synthetic air for YSZ and humidified hydrogen (3 vol% H₂O) for NiO–YSZ, respectively. The 0.3 M CTAB/NaCl YSZ sample exhibited purely ionic conductivity, which increased with temperature and peaked in 0.011 S·cm⁻¹ at 800 °C. On the other hand, the 0.3 M CTAB/NaCl NiO–YSZ cermet demonstrated predominantly electronic conductivity, reaching values around 1000 S·cm⁻¹ quite normal for metallic conduction through Ni particles. Despite the influence of porosity, the conductivity values obtained for these novel materials fall within the typical ranges reported in the literature [271,277,278].

Long-term electrical degradation of the novel 0.3 M CTAB/NaCl NiO-YSZ and conventional Ni-YSZ cermets was assessed through continuous conductivity measurements under simulated operational conditions. Both anodes were subjected to a reduction process at 800 °C for 1 hour in a hydrogen atmosphere, followed by conductivity monitoring. The results, depicted in Fig. 59, show both the absolute conductivity value and the percentage loss over time.

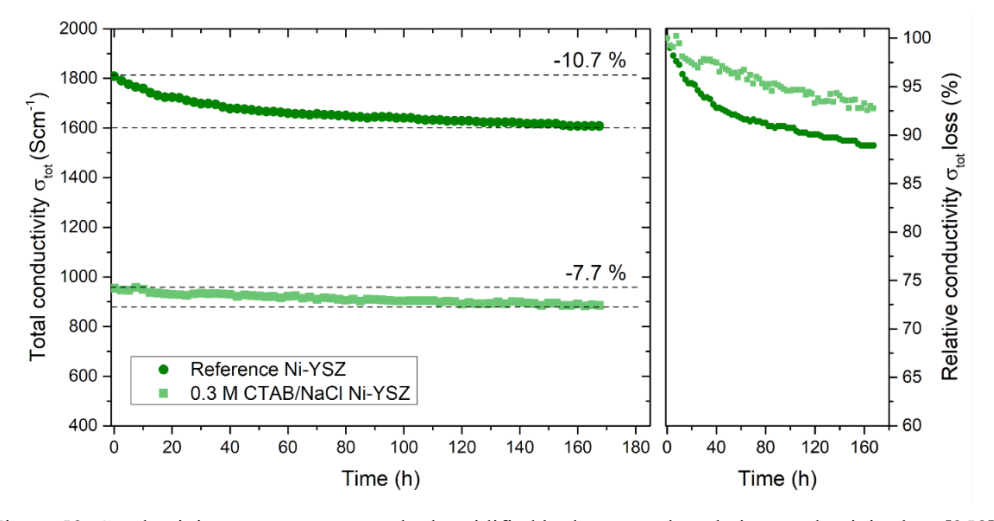


Figure 59. Conductivity measurements under humidified hydrogen and a relative conductivity loss [258].

Despite similar initial thicknesses (~400 µm), the two samples exhibited various microstructural characteristics, influencing their total conductivity. The reference Ni–YSZ sample demonstrated higher conductivity but also a rapid decline within the first 24 hours, which is consistent with general behavior of the cells. This early degradation is typically attributed to the migration and sintering of nickel particles, leading to a reduction in the three-phase boundary (TPB) length and a subsequent decrease in electrochemical activity. In contrast, the 0.3 M CTAB/NaCl NiO–YSZ anode maintained quite stable conductivity over the same period, indicating superior resistance to microstructural changes. This enhanced stability is likely due to the smaller, more uniformly distributed nickel particles resulting from the templating method, which reduces the driving force for sintering. These findings suggest that the CTAB/NaCl templating approach effectively mitigates early-stage degradation in NiO–YSZ cermets, offering a promising strategy for enhancing the long life and stable performance of fuel electrodes.

The YSZ backbone structure significantly influences Ni migration, as the coalescence and breakdown of conduction paths occur immediately after the loss of contact between YSZ and Ni. Enhanced integration at the interface and improved wettability of Ni on the YSZ surface stabilizes the 0.3 M CTAB/NaCl Ni–YSZ composite, effectively suppressing the extensive growth of Ni grains during operation. This stabilization can be tailored during the preparation steps, underscoring the critical role of microstructure in the performance of Solid Oxide Cells (SOCs) [140]. To elucidate the degradation mechanisms through microstructure change, a series of structural analyses were conducted using scanning electron microscopy (SEM) imaging of polished cross-sections of both samples, coupled with energy-dispersive X-ray spectroscopy (EDS) spatial elemental mapping. The results, presented in Figure 60, clearly indicate that the fresh 0.3 M CTAB/NaCl Ni–YSZ exhibited smaller initial grains of both Ni and YSZ compared to the reference sample.

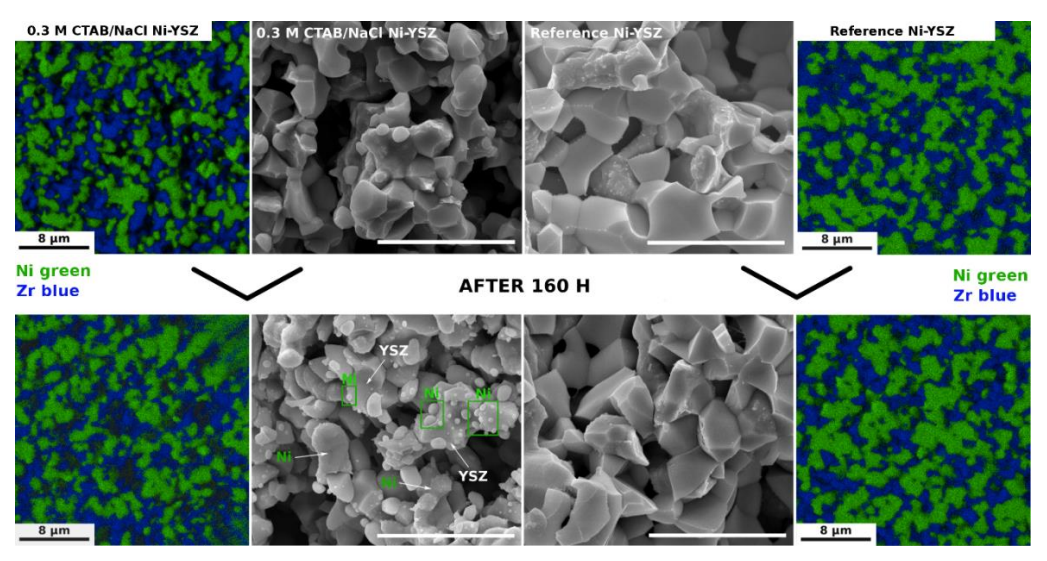


Figure 60. SEM images and elemental maps of 0.3 M CTAB/NaCl Ni–YSZ in reduced state and conventional Ni–YSZ before and after the aging. Scale bar is 8 μm [258].

The Ni grains had a finely dispersed 3D structure within the YSZ scaffold. This microstructure facilitates the development of a robust triple-phase boundary (TPB), which is essential for electrochemical reactions [279]. The microstructure of the novel 0.3 M CTAB/NaCl NiO-YSZ composite demonstrates a significant enhancement over conventional cermet structures, particularly in terms of nickel (Ni) migration and long-term stability. The CTAB/NaClassisted synthesis method results in smaller, more homogeneously distributed Ni and YSZ grains, which are crucial for maintaining good ionic and electronic conduction pathways. No formation of isolated Ni or YSZ regions was easily encountered, which can lead to performance loss in Solid Oxide Cells (SOCs). Post-mortem analyses after 160 hours of aging under humidified hydrogen revealed that the CTAB/NaCl NiO-YSZ composite underwent minimal Ni coarsening compared to the conventional reference cermet material (based on EDS mapping). While both materials maintain a homogeneous phase distribution, the reference sample shows significant Ni agglomeration and a reduction in pore channels, leading to a loss of conduction pathways. In contrast, the CTAB/NaCl NiO-YSZ maintained its microstructure, with rounded Ni grains and preserved intergranular connections, indicating superior structural stability. Furthermore, the 0.3 M CTAB/NaCl NiO-YSZ composite experienced phase decomposition following extended reduction similar as in TPR measurements. This was evidenced by the formation of submicronsized spherical Ni agglomerates on the surfaces of YSZ grains (see Fig. 60, center bottom). Over time, this phenomenon could prove advantageous for practical cell operation, as these metallic Ni particles may serve as active sites for the reactions. To validate this hypothesis, future work will include a series of symmetrical and full-cell electrochemical measurements.

Summary of the section

A novel soft–hard templating method using CTAB/Pluronic P123 and crystallizing NaCl was developed to synthesize highly porous 8YSZ and NiO–YSZ composites for Solid Oxide Cells (SOCs). This approach produced unique wormhole-like porous structures (with ~50% porosity) without the need for the use of external pore formers. The formation of pores was driven by synergistic effects of organic templating and NaCl volatilization. XRD and synchrotron STXM analyses confirmed uniform Ni dispersion in precursor gels, while thermochemical studies revealed controlled phase separation that prevented NiO and YSZ interdiffusion. Post-sintering, crystalline cubic 8YSZ and NiO phases formed with slight lattice contraction indicating ~1 mol% NiO incorporation into 8YSZ. Upon reduction, nanometric Ni grains were obtained while suppressed grain growth was observed. Optimal microstructures (for 0.3–0.4 M cation initial concentration) yielded <1 μm YSZ grains interconnected by narrow channels. The deviation from this concentration range led to densification or poor porosity.

Thermal analysis confirmed ~50% mass loss due to organic burnout and NaCl volatilization, with sintering onset above 1100 °C. TPR/TPO studies demonstrated improved redox behavior such as lower reduction temperatures, more uniform porosity, and a single oxidation peak in CTAB/NaCl NiO-YSZ, what indicated strong Ni dispersion and excellent gas transport trough the electrode. A second TPR cycle confirmed minimal Ni grain growth, highlighting superior stability and Ni-YSZ interfacial anchoring compared to reference materials.

Porosity studies validated the possibility to precisely control the porosity. Maximum open porosity (\sim 50% after reduction) correlated well with optimal open pores network, meeting the ideal 40–50% range for SOC fuel electrodes. TEC values equal to \sim 10.8×10⁻⁶ K⁻¹ for YSZ and \sim 12.6×10⁻⁶ K⁻¹ for NiO–YSZ were fully compatible with the expansion of other components of the cell. Nitrogen adsorption confirmed dominance of macropores for efficient gas transport, while MIP revealed narrow, uniform pore sizes (\sim 0.5–0.6 μ m). The cermet material fabricated using this novel synthesis route also exhibited higher active surface compared to conventional composite.

Electrical performance testing revealed purely ionic conductivity for YSZ (0.011 S·cm⁻¹ at 800 °C) and high electronic conductivity (~1000 S·cm⁻¹) for the Ni–YSZ reduced cermet. Long-term tests showed superior stability of conductivity readings for the CTAB/NaCl NiO–YSZ compared to conventional Ni–YSZ, which exhibited more rapid degradation due to stronger Ni migration and metal grain coarsening. The novel structures stayed finer and more uniform in microstructure, what was confirmed via SEM–EDS, maintaining porosity and conductive paths after 160 h.

Overall, the CTAB/NaCl templating approach enabled scalable fabrication of SOC fuel electrodes with optimized porosity, mechanical robustness, and long-term performance. Future work will explore electrochemical behavior in full cells and fine-tune NiO-YSZ ratios to further mitigate degradation and harness the stabilizing effects of this wormhole-like structure.

5. SUMMARY OF THE RESEACH

Growing awareness of climate change and its associated risks has accelerated the shift from fossil fuels to renewable energy sources. The increasing need of electricity for heating, cooling, and transportation poses significant challenges to current power generation and distribution systems, pointing out also the urgent need to reduce greenhouse gas emissions. EU policies enforced a steady rise in renewable energy consumption over the last decade, with hydropower, wind, solar photovoltaics, and biofuels becoming key contributors. Despite major improvements, the intermittent nature of renewables causes fluctuations in the energy supply, creating periods of surplus and shortage that complicate power management.

Smart grids, which are flexible and self-sustaining systems designed to balance supply and demand in real-time, offer a promising solution to these issues. A key component of this approach might be the use of hydrogen as a clean energy carrier. Hydrogen can be produced from excess renewable electricity via electrolysis and stored for future use, helping to stabilize energy supply. Solid Oxide Cells (SOCs), capable of functioning as both fuel cells and electrolyzers with high efficiency are facing challenges such as degradation issues, high costs, and material accessibility concerns.

Recent advances in nanotechnology and catalyst development, especially with bimetallic nanoparticles made from transition metals like nickel and cobalt, are enhancing SOC performance by improving catalytic activity, durability, and resistance to e.g. carbon buildup. These nanocatalysts benefit from synergistic interactions between metals that optimize reactions kinetics and enhance stability. However, many bimetallic combinations remain underexplored, and further research is needed to understand the phenomena occurring during the work of such a catalytic system. Ongoing studies of nanostructured materials and catalysts are crucial for advancing SOC technology, supporting efficient and sustainable renewable energy integration, and promoting a low-carbon future.

The main aim of this study was to present several novel advances in the design and synthesis of catalysts and electrodes for Solid Oxide Cells (SOCs), focusing on enhancing catalytic activity, stability of performance, and durability under high-temperature conditions without the need to use noble metals. One of key innovations was the introduction of β -cyclodextrin (β CD)-assisted wet impregnation to fabricate ceria-supported transition metal catalysts (Ni, Co, Cu, Fe, Mn) for direct methanation, that could be further utilized in SOC systems. Structural analyses (XRD, TEM) demonstrated that β CD significantly improved metal dispersion, yielding smaller, well-distributed nanoparticles with strong metal—support interaction. This led to the formation of an interfacial layer, which enhanced catalyst stability and activity by reducing nanoparticle agglomeration thanks to cation complexation. H₂-TPR results confirmed lower reduction temperatures for the catalysts prepared using β CD, indicating smaller and more

uniform metal nanoparticles strongly anchored to CeO₂. Ni–CeO₂ exhibited new reduction peaks linked to Ni-O-Ce bonding and partial Ni lattice incorporation, while Co-CeO2 showed multistep reduction reflecting stronger metal-support interactions. Cu-CeO2 reached improved reducibility and suppressed CuO aggregation, enhancing metal-support synergy, whereas Mn and Fe catalysts were less affected by BCD additive. N2 adsorption tests revealed increased mesoporosity and active surface area, especially notable in Cu/CeO2 due to formation of stable βCD-Cu²⁺ complexes. Catalytic tests showed that Ni- and Co-impregnated CeO₂ catalysts delivered significant methane yields, with βCD-Ni/CeO₂ achieving 98.5% CO conversion and 79.9% CH₄ yield at 375 °C, outperforming conventionally prepared catalysts. Reaction quotient analysis confirmed superior methanation efficiency and selectivity, while 24-hour stability tests at 700 °C demonstrated minimal degradation and enhanced thermal stability, particularly for βCD-Co/CeO₂. These findings established βCD-assisted synthesis as a powerful strategy to optimize catalysts for SOCs and related applications. Furthermore, the results of this study corroborated the first hypothesis of this dissertation, demonstrating that nanoparticles with robust metal-support interactions can be synthesized using simple wet chemistry methods, yielding stable and high-performance catalysts.

In parallel, the study explored Ni-YSZ fuel electrodes enhanced by cobalt nanoparticle incorporation via the proposed impregnation route to improve CO₂/H₂O coelectrolysis efficiency and direct methanation. Introduction of highly dispersed Co nanoparticles and nanostructured NiCo₂O₄-like spinel phases on Ni surfaces, confirmed by advanced microscopy and spectroscopy, was found to be beneficial for the efficiency of both processes. Optimal Co loading (3.6 wt.%) increased surface basicity and oxidation state ratios (Ni³⁺/Ni²⁺, Co³⁺/Co²⁺), boosting electrochemical activity while maintaining electrode integrity. This modification more than doubled CH₄ production, with CO₂ conversion and CO production exceeding thermodynamic equilibrium, indicating synergistic electrochemical and catalytic effects. Similar, Mn impregnation enhanced efficiency, while Fe and Cu brought no major benefits when tested in working cell. Durability tests over 12 hours confirmed the robustness of Co-modified electrodes, showing minor initial activity loss and stable work. Microstructural analysis revealed Ni-Co alloy formation without visible phase segregation. However, excessive Co loading (5.4 wt.%) caused agglomeration and reduced performance, highlighting the need to find optimized composition of the catalytic system. Redox studies (H2-TPR, O2-TPO) revealed Co-enhanced reducibility and oxygen exchange dynamics, with NiCo₂O₄-like spinel phases enabling reversible lattice oxygen release around 600 °C. This interesting oxygen evolution mechanism most likely contributed to catalytic enhancement. XAS and STXM uncovered formation of core-shell structure with metallic Ni surrounded by NiCo₂O₄ and Co_xO_y, as well as greater Co diffusion into Ni grains compared to Mn, linked to long-term surface depletion and probable cause of performance decline. The results presented in this study demonstrated that the electrochemical and chemical

efficiency of SOC devices can be enhanced through the synergistic effects between two transition metals, thereby supporting the second hypothesis outlined in this dissertation.

Finally, during the study a novel soft-hard templating method was developed, combining CTAB/Pluronic P123 system and crystallizing NaCl to fabricate highly porous (~50% open porosity) 8YSZ and NiO-YSZ composites without external pore formers. This method produced wormhole-like porous structures with uniform Ni dispersion and allowed for controlled phase separation preventing NiO-YSZ interdiffusion. The nanometric Ni grains with suppressed grain growth were obtained. Optimized cation concentration yielded submicron grains interconnected by narrow channels, crucial for gas transport and electrode performance. Thermal and redox analyses showed improved stability and enhanced Ni dispersion compared to conventional material. Porosity and pore size distribution were precisely controlled, meeting ideal ranges for SOC fuel electrodes. The composite exhibited high ionic (YSZ) and electronic (Ni-YSZ) conductivity with superior long-term stability, maintaining fine microstructure and conductive paths after 160 hours of testing. This scalable CTAB/NaCl templating approach offers a robust platform for fabricating SOC electrodes with optimized porosity, mechanical strength, and electrochemical performance. In light of these results, the final hypothesis, which suggested that nanostructuring the fuel electrode enhances metal-oxide interactions and improves the lifespan of SOC devices, has been confirmed.

As a final remark, this study treated the development of novel catalytic materials using simple and scalable methods, resulting in a significant improvement in the performance of Solid Oxide Cells (SOCs). What is more, the underlying mechanisms behind this enhancement were also thoroughly examined and formulated, offering a detailed insight into the catalytic processes occurring within the cells. In my opinion the presented results supported well and confirmed all the hypotheses that were stated at the beginning of this dissertation. Future work will be devoted to the optimization of the bimetallic catalysts to further achieve the stable and efficient systems able to operate for at least 1,000 hours without detrimental loss in performance. I deeply believe that by fine tuning the composition of the metals and through reengineering of the microstructure it is possible to increase the value of SOC technology in the race towards cleaner environment.

List of scientific publications of candidate

- 1) **Blaszczak P.**, Ducka A., Wolanin B., Matlak K., Machowski G., Prześniak-Welenc M., Wang S.-F., Bochentyn B., & Jasiński P. (2023). *Fabrication of wormhole-like YSZ and Ni–YSZ by the novel soft-hard template CTAB/NaCl-assisted route. Suppressing Ni coalescence in SOFC.* Journal of the European Ceramic Society, 43(2), 438–451.
- 2) **Blaszczak P.**, Łapiński M., Wang S.-F., Jasiński P., & Bochentyn B. (2020). *Exsolution of Ni nanoparticles on the surface of cerium and nickel co-doped lanthanum strontium titanate as a new anodic layer for DIR-SOFC. Anti-coking potential and H₂S poisoning resistance of the prepared material. International Journal of Hydrogen Energy, 45(53), 29186–29200.*
- Blaszczak P., Mizera A., Bochentyn B., Wang S.-F., & Jasiński P. (2022). Preparation of methanation catalysts for high temperature SOEC by β-cyclodextrin-assisted impregnation of nano-CeO₂ with transition metal oxides. International Journal of Hydrogen Energy, 47(3), 1901–1916.
- 4) **Blaszczak P.**, Zając M., Ducka A., Matlak K., Wolanin B., Wang S.-F., Mandziak A., Bochentyn B., & Jasiński P. (2022). *High temperature Coelectrolysis of CO₂/H₂O and direct methanation over Co-impregnated SOEC. Bimetallic synergy between Co and Ni.* International Journal of Hydrogen Energy, 47(82), 35017–35037.
- 5) **Blaszczak P.**, Mäkinen P., Mroziński A., Ducka A., Jasiński G., Himanen O., Jasiński P., (2025) *Uncovering the electrochemical processes and understanding the causes of the degradation via EIS-DRT in large-scale Solid Oxide Fuel Cell*. Appl Energy, 393, 125983
- 6) Bochentyn B., **Blaszczak P.**, Gazda M., Fuerte A., Wang S.-F., & Jasiński P. (2020). *Investigation of praseodymium and samarium codoped ceria as an anode catalyst for DIR-SOFC fueled by biogas*. International Journal of Hydrogen Energy, 45(53), 29131–29142.
- 7) Chlipała, M. **Blaszczak P.**, Wang S.-F., Jasiński P., & Bochentyn B. (2019). *In situ study of a composition of outlet gases from biogas fuelled Solid Oxide Fuel Cell performed by the Fourier Transform Infrared Spectroscopy*. International Journal of Hydrogen Energy, 44(26), 13864–13874.
- 8) Drewniak A., Koszelow D., **Blaszczak P.**, Górnicka K., Jurak K., Javed H., Sabato A. G., Jasiński P., Molin S., & Smeacetto F. (2021). *Glass-ceramic sealants and steel interconnects: Accelerated interfacial stability and reactivity tests at high temperature*. Materials & Design, 212, 110259.
- 9) Hołówko B., **Blaszczak P**., Chlipała M., Gazda M., Wang S.-F., Jasiński P., & Bochentyn B. (2020). *Structural and catalytic properties of ceria layers doped with transitionmetals for SOFCs fueled by biogas*. International Journal of Hydrogen Energy, 45(23), 12982–12996.

- 10) Lankauf K., Górnicka K., **Błaszczak P**., Karczewski J., Ryl J., Cempura G., Zając M., Bik M., Sitarz M., Jasiński P. (2023). *Tuning of eg electron occupancy of MnCo₂O₄ spinel for oxygen evolution reaction by partial substitution of Co by Fe at octahedral sites*. International Journal of Hydrogen Energy, 48(24), 8854–8866.
- 11) Lankauf K., Lemieszek B., Górnicka K., **Blaszczak P.**, Zając M., Jasiński P., & Molin S. (2024). *Enhanced electrochemical performance of MnCo_{1.5}Fe_{0.5}O₄ spinel for oxygen evolution reaction through heat treatment*. Energy & Fuels, 38(2), 1330–1336.
- 12) Lankauf K., Mroziński A., **Błaszczak P**., Górnicka K., Ignaczak J., Łapiński M., Karczewski J., Cempura G., Jasiński P., & Molin S. (2021). *The effect of Fe on chemical stability and oxygen evolution performance of high surface area* $SrTi_{x-1}Fe_xO_{3-\delta}$ *mixed ionic-electronic conductors in alkaline media*. International Journal of Hydrogen Energy, 46(56), 28575–28590.
- 13) Lemieszek B., Ignaczak J., Lankauf K., **Blaszczak P**., Bik M., Zając M., Sitarz M., Jasiński P., & Molin S. (2024). *CuMn*_{1.7}*Fe*_{0.3}*O*₄–*RE*₂*O*₃ (*RE*= *Y*, *Gd*) bilayers as protective interconnect coatings for Solid Oxide Cells. Journal of the European Ceramic Society, 44(15), 116743.
- 14) Lemieszek B., Ilickas M., Jamroz J., Tamulevičienė A., Karczewski J., **Blaszczak P.**, Maximenko, A., Abakevičienė B., Małys M., Tamulevičius S., (2024). *Enhanced electrochemical performance of partially amorphous La*_{0.6}Sr_{0.4}CoO_{3-δ} oxygen electrode materials for low-temperature Solid Oxide Cells operating at 400 °C. Applied Surface Science, 670, 160620.
- 15) Mizera A., **Blaszczak P.**, Bochentyn B., Lach R., & Drożdż E. (2022). *Cu supported on various oxides as a candidate catalyst for dry methane reforming in DIR-SOFCs systems*. International Journal of Hydrogen Energy, 47(61), 25647–25661.
- 16) Mroziński A., Molin S., **Blaszczak P.**, Miruszewski T., Górnicka K., Karczewski J., & Jasiński P. (2023). *Impact of strontium nonstoichiometry of* $Sr_xTi_{0.3}Fe_{0.7}O_{3-\delta}$ *on structural, electrical, and electrochemical properties for potential oxygen electrode of intermediate temperature Solid Oxide Cells.* International Journal of Hydrogen Energy, 48(90), 35250–35266.
- 17) Pawłowska S., Lankauf K., **Błaszczak P.**, Karczewski J., Górnicka K., Cempura G., Jasiński P., & Molin S. (2023). *Tailoring a low-energy ball milled MnCo₂O₄ spinel catalyst to boost oxygen evolution reaction performance*. Applied Surface Science, 619, 156720.
- 18) Ducka A., **Blaszczak P.**, Zając M., Mizera A., d'Acapito F., Bochentyn B. (2024). *Limited dissolution of transition metals in the nanocrystalline cerium (IV) oxide*. Ceramics International, 50, 50921-50933.
- 19) Ducka A., **Blaszczak P.**, Zając M., Maximenko A., Gazda M., Bochentyn, B. (2025). *Investigation of the phase transition to the Ruddlesden–Popper phase in La- or Nb-doped* $Sr_2Fe_{1.5}Mo_{0.5}O_{6-\delta}$ double perovskites and the impact of lanthanum or niobium doping. Nanoscale, 17, 12371-12384.

Literature

- [1] Puertas R, Marti L. Renewable energy production capacity and consumption in Europe. Sci Total Environ 2022; 853:158592. https://doi.org/10.1016/j.scitotenv.2022.158592.
- [2] Igliński B, Kiełkowska U, Mazurek K, Drużyński S, Pietrzak MB, Kumar G, et al. Renewable energy transition in Europe in the context of renewable energy transition processes in the world. A review. Heliyon 2024; 10:1–25. https://doi.org/10.1016/j.heliyon.2024.e40997.
- [3] Mulder FM. Implications of diurnal and seasonal variations in renewable energy generation for large scale energy storage 2016; 033105:1–14.
- [4] Xu H, Mercedes Maroto-Valer M, Ni M, Cao J, Xuan J. Modeling of a combined CH₄-assisted solid oxide co-electrolysis and Fischer-Tropsch synthesis system for low-carbon fuel production. Energy Procedia 2019; 158:1666–71. https://doi.org/10.1016/j.egypro.2019.01.388.
- [5] Nielen S van. Techno-economic Assessment of Solid Oxide Fuel Cells and Fuel-assisted Electrolysis Cells in Future Energy Systems 2016.
- [6] Lorena M, Lochinvar M. A review of the development of Smart Grid technologies. Renew Sustain Energy Rev 2016; 59:710–25. https://doi.org/10.1016/j.rser.2016.01.011.
- [7] Khan B, Getachew H, Alhelou HH. Components of the smart-grid system. INC 2021. https://doi.org/10.1016/B978-0-12-816816-5.00017-6.
- [8] Maruf H, Asif M, Dey SK, Mansur A Al, Shihavuddin ASM. Adaptation for sustainable implementation of Smart Grid in developing countries like Bangladesh. Energy Reports 2020; 6:2520–30. https://doi.org/10.1016/j.egyr.2020.09.010.
- [9] Chateau J, Miho A, Borowiecki M. Economic effects of the EU's "Fit for 55" climate mitigation policies: A computable general equilibrium analysis 2023.
- [10] Lin R-H, Zhao Y-Y, Wu B-D. Toward a hydrogen society: Hydrogen and smart grid integration. Int J Hydrogen Energy 2020; 45:20164–75. https://doi.org/https://doi.org/10.1016/j.ijhydene.2020.01.047.
- [11] Zheng L, Wang J, Yu Y, Li G, Zhou M, Xia Q, et al. On the Consistency of Renewable-to-Hydrogen Pricing. CSEE J Power Energy Syst 2022; 8:392–402. https://doi.org/10.17775/CSEEJPES.2021.05630.
- [12] Wu X, Li H, Wang X, Zhao W. Cooperative Operation for Wind Turbines and Hydrogen Fueling Stations with On-Site Hydrogen Production. IEEE Trans Sustain Energy 2020; 11:2775–89. https://doi.org/10.1109/TSTE.2020.2975609.
- [13] El-Taweel NA, Khani H, Farag HEZ. Hydrogen Storage Optimal Scheduling for Fuel Supply and Capacity-Based Demand Response Program under Dynamic Hydrogen Pricing. IEEE Trans Smart Grid 2019; 10:4531–42. https://doi.org/10.1109/TSG.2018.2863247.
- [14] Han J, Wang J, He Z, An Q, Song Y, Mujeeb A, et al. Hydrogen-powered smart grid resilience. Energy Convers Econ 2023; 4:89–104. https://doi.org/10.1049/enc2.12083.
- [15] Tran HT, Balchanos M, Domerçant JC, Mavris DN. A framework for the quantitative assessment of performance-based system resilience. Reliab Eng Syst Saf 2017; 158:73–84. https://doi.org/10.1016/j.ress.2016.10.014.
- [16] Li C, Xi Y, Lu Y, Liu N, Chen L, Ju L, et al. Resilient outage recovery of a distribution system: co-optimizing mobile power sources with network structure. Prot Control Mod

- Power Syst 2022;7. https://doi.org/10.1186/s41601-022-00256-9.
- [17] Brouzgou A, Demin A, Tsiakaras P. Advances in Medium and High Temperature Solid Oxide Fuel Cell Technology 2017; 574.
- [18] Kim J, Park H, Jang J, Song H, Lee BH, Lee D, et al. Integrated Energy Conversion and Storage Device for Stable Fast Charging Power Systems. ECS J Solid State Sci Technol 2020; 9:125003. https://doi.org/10.1149/2162-8777/abcc49.
- [19] Hayashi K, Yokoo M, Yoshida Y, Arai H. Solid Oxide Fuel Cell Stack with High Electrical Efficiency. NTT Tech Rev 2009;7.
- [20] Arshad MS, Yangkou Mbianda X, Ali I, Wanbing G, Kamal T, Kauhaniemi K, et al. Advances and Perspectives on Solid Oxide Fuel Cells: From Nanotechnology to Power Electronics Devices. Energy Technol 2023; 11. https://doi.org/10.1002/ente.202300452.
- [21] Patel NK, Bishop SR, Utter RG, Das D, Pecht M. Failure modes, mechanisms, effects, and criticality analysis of ceramic anodes of solid oxide fuel cells. Electron 2018; 7. https://doi.org/10.3390/electronics7110323.
- [22] Mahdi HI, Muraza O. An exciting opportunity for zeolite adsorbent design in separation of C₄ olefins through adsorptive separation. Sep Purif Technol 2019; 221:126–51. https://doi.org/10.1016/j.seppur.2018.12.004.
- [23] Mahdi HI, Ramlee NN, da Silva Duarte JL, Cheng YS, Selvasembian R, Amir F, et al. A comprehensive review on nanocatalysts and nanobiocatalysts for biodiesel production in Indonesia, Malaysia, Brazil and USA. Chemosphere 2023; 319. https://doi.org/10.1016/j.chemosphere.2023.138003.
- [24] Agarwal N, Solanki VS, Pare B, Singh N, Jonnalagadda SB. Current trends in nanocatalysis for green chemistry and its applications- a mini-review. Curr Opin Green Sustain Chem 2023; 41:100788. https://doi.org/10.1016/j.cogsc.2023.100788.
- [25] Ballarini AD, Virgens CF, Rangel MC, De Miguel SR, Grau JM. Characterization and behaviour of Pt catalysts supported on basic materials in dry reforming of methane. Brazilian J Chem Eng 2019; 36:275–84. https://doi.org/10.1590/0104-6632.20190361s20170158.
- [26] Garbarino G, Bellotti D, Finocchio E, Magistri L, Busca G. Methanation of carbon dioxide on Ru/Al₂O₃: Catalytic activity and infrared study. Catal Today 2016; 277:21–8. https://doi.org/10.1016/j.cattod.2015.12.010.
- [27] Wang H, Pei Y, Qiao M, Zong B. Advances in methanation catalysis. Catalysis 2017; 29:1–28. https://doi.org/10.1039/9781788010634-00001.
- [28] Li H, Ren J, Qin X, Qin Z, Lin J, Li Z. Ni/SBA-15 catalysts for CO methanation: effects of V, Ce, and Zr promoters. RSC Adv 2015; 5:96504–17. https://doi.org/10.1039/c5ra15990c.
- [29] Liu Q, Zhong Z, Gu F, Wang X, Lu X, Li H, et al. CO methanation on ordered mesoporous Ni-Cr-Al catalysts: Effects of the catalyst structure and Cr promoter on the catalytic properties. J Catal 2016; 337:221–32. https://doi.org/10.1016/j.jcat.2016.01.023.
- [30] Yin C, Wang Y. Effect of sulfidation process on catalytic performance over unsupported Ni-Mo-W hydrotreating catalysts. Korean J Chem Eng 2017; 34:1004–12. https://doi.org/10.1007/s11814-017-0016-2.
- [31] Liu L, Corma A. Metal Catalysts for Heterogeneous Catalysis: From Single Atoms to Nanoclusters and Nanoparticles. Chem Rev 2018; 118:4981–5079. https://doi.org/10.1021/acs.chemrev.7b00776.

- [32] Liu H, Xu S, Zhou G, Huang G, Huang S, Xiong K. CO₂ hydrogenation to methane over Co/KIT-6 catalyst: Effect of reduction temperature. Chem Eng J 2018; 351:65–73. https://doi.org/10.1016/j.cej.2018.06.087.
- [33] Zhu Y, Dai J, Zhou W, Zhong Y, Wang H, Shao Z. Synergistically enhanced hydrogen evolution electrocatalysis by in situ exsolution of metallic nanoparticles on perovskites. J Mater Chem A 2018; 6:13582–7. https://doi.org/10.1039/c8ta02347f.
- [34] Miao B, Ma SSK, Wang X, Su H, Chan SH. Catalysis mechanisms of CO₂ and CO methanation. Catal Sci Technol 2016; 6:4048–58. https://doi.org/10.1039/c6cy00478d.
- [35] Zhao X, Wei L, Cheng S, Julson J. Review of heterogeneous catalysts for catalytically upgrading vegetable oils into hydrocarbon biofuels. Catalysts 2017; 7. https://doi.org/10.3390/catal7030083.
- [36] Nowicka E, Sankar M. Designing Pd-based supported bimetallic catalysts for environmental applications. J Zhejiang Univ Sci A 2018; 19:5–20. https://doi.org/10.1631/jzus.A1700257.
- [37] Tomishige K, Li D, Tamura M, Nakagawa Y. Nickel-iron alloy catalysts for reforming of hydrocarbons: Preparation, structure, and catalytic properties. Catal Sci Technol 2017; 7:3952–79. https://doi.org/10.1039/c7cy01300k.
- [38] Mironova EY, Ermilova MM, Orekhova N V., Basov NL, Yaroslavtsev AB. Hydrogen Production by Ethanol Steam Reforming in the Presence of Pd-, Pt-, Ru-, and Ni-Containing Nanodiamonds in Conventional and Membrane Reactors. Membr Technol 2019; 1:246–53. https://doi.org/10.1134/S251775161904005X.
- [39] Shakil Hussain SM, Kamal MS, Hossain MK. Recent Developments in Nanostructured Palladium and Other Metal Catalysts for Organic Transformation. J Nanomater 2019. https://doi.org/10.1155/2019/1562130.
- [40] Soyal-Baltacioğlu F, Aksoylu AE, Önsan ZI. Steam reforming of ethanol over Pt-Ni Catalysts. Catal Today 2008; 138:183–6. https://doi.org/10.1016/j.cattod.2008.05.035.
- [41] Resini C, Concepción Herrera Delgado M, Presto S, Alemany LJ, Riani P, Marazza R, et al. Yttria-stabilized zirconia (YSZ) supported Ni-Co alloys (precursor of SOFC anodes) as catalysts for the steam reforming of ethanol. Int J Hydrogen Energy 2008; 33:3728–35. https://doi.org/10.1016/j.ijhydene.2008.04.044.
- [42] Garbarino G, Cavattoni T, Riani P, Brescia R, Canepa F, Busca G. On the Role of Support in Metallic Heterogeneous Catalysis: A Study of Unsupported Nickel–Cobalt Alloy Nanoparticles in Ethanol Steam Reforming. Catal Letters 2019; 149:929–41. https://doi.org/10.1007/s10562-019-02688-9.
- [43] Wang M, Yang J, Chi B, Pu J, Li J. High performance Ni exsolved and Cu added La_{0.8}Ce_{0.2}Mn_{0.6}Ni_{0.4}O₃-based perovskites for ethanol steam reforming. Int J Hydrogen Energy 2020; 45:16458–68. https://doi.org/10.1016/j.ijhydene.2020.04.108.
- [44] Kim KM, Kwak BS, Park NK, Lee TJ, Lee ST, Kang M. Effective hydrogen production from propane steam reforming over bimetallic co-doped NiFe/Al₂O₃ catalyst. J Ind Eng Chem 2017; 46:324–36. https://doi.org/10.1016/j.jiec.2016.10.046.
- [45] Maric R. Solid Oxide Fuel Cells: From Fundamental Principles to Complete Systems (1st ed.). CRC Press; 2020. https://doi.org/https://doi.org/10.1201/9780429100000.
- [46] Talukdar A, Chakrovorty A, Sarmah P, Paramasivam P, Kumar V, Yadav SK, et al. A Review on Solid Oxide Fuel Cell Technology: An Efficient Energy Conversion System. Int J Energy Res 2024; 2024:6443247. https://doi.org/https://doi.org/10.1155/2024/6443247.

- [47] Duan C, Huang J, Sullivan N, O'Hayre R. Proton-conducting oxides for energy conversion and storage. Appl Phys Rev 2020; 7:11314. https://doi.org/10.1063/1.5135319.
- [48] He S, Zou Y, Chen K, Jiang SP. A critical review of key materials and issues in solid oxide cells. Interdiscip Mater 2023; 2:111–36. https://doi.org/https://doi.org/10.1002/idm2.12068.
- [49] Kim D, Lee TK, Han S, Jung Y, Lee DG, Choi M, et al. Advances and challenges in developing protonic ceramic cells. Mater Today Energy 2023; 36:101365. https://doi.org/https://doi.org/10.1016/j.mtener.2023.101365.
- [50] Wu Z, Zhu P, Huang Y, Yao J, Yang F, Zhang Z, et al. A Comprehensive Review of Modeling of Solid Oxide Fuel Cells: From Large Systems to Fine Electrodes. Chem Rev 2025. https://doi.org/10.1021/acs.chemrev.4c00614.
- [51] Fu Q, Li Z, Wei W, Liu F, Xu X, Liu Z. Performance enhancement of planar solid oxide fuel cell using a novel interconnector design. Int J Hydrogen Energy 2021; 46:21634–56. https://doi.org/https://doi.org/10.1016/j.ijhydene.2021.04.001.
- [52] Chen R, Gao Y, Gao J, Zhang H, Motola M, Hanif MB, et al. From concept to commercialization: A review of tubular solid oxide fuel cell technology. J Energy Chem 2024; 97:79–109. https://doi.org/https://doi.org/10.1016/j.jechem.2024.05.026.
- [53] Cimen FM, Kumuk B, Ilbas M. Simulation of hydrogen and coal gas fueled flat-tubular solid oxide fuel cell (FT-SOFC). Int J Hydrogen Energy 2022; 47:3429–36. https://doi.org/https://doi.org/10.1016/j.ijhydene.2021.07.231.
- [54] Huang H, Han Z, Lu S, Kong W, Wu J, Wang X. The analysis of structure parameters of MOLB type solid oxide fuel cell. Int J Hydrogen Energy 2020; 45:20351–9. https://doi.org/https://doi.org/10.1016/j.ijhydene.2019.10.251.
- [55] O'Hayre R, Cha SW, Colella W, Prinz FB. Fuel Cell Fundamentals. Wiley; 2016.
- [56] Collins-Martinez VH, Cazares-Marroquin JF, Salinas-Gutierrez JM, Pantoja-Espinoza JC, Lopez-Ortiz A, Melendez-Zaragoza MJ. The thermodynamic evaluation and process simulation of the chemical looping steam methane reforming of mixed iron oxides. RSC Adv 2020; 11:684–99. https://doi.org/10.1039/d0ra08610j.
- [57] Haile SM. Fuel cell materials and components. The Golden Jubilee Issue—Selected topics in Materials Science and Engineering: Past, Present and Future. Acta Mater 2003; 51:5981–6000. https://doi.org/https://doi.org/10.1016/j.actamat.2003.08.004.
- [58] Alns A, Sleiti AK. Combined heat and power system based on Solid Oxide Fuel Cells for low energy commercial buildings in Qatar. Sustain Energy Technol Assessments 2021; 48:101615. https://doi.org/https://doi.org/10.1016/j.seta.2021.101615.
- [59] Błaszczak P, Mäkinen P, Mroziński A, Ducka A, Jasiński G, Himanen O, et al. Uncovering the electrochemical processes and understanding the causes of the degradation via EIS-DRT in large-scale solid oxide fuel cell. Appl Energy 2025; 393. https://doi.org/10.1016/j.apenergy.2025.125983.
- [60] Li Z, Zheng Z, Xu L, Lu X. A review of the applications of fuel cells in microgrids: opportunities and challenges. BMC Energy 2019; 1:1–23. https://doi.org/10.1186/s42500-019-0008-3.
- [61] Laguna-Bercero MA, Wang Y, Zhou X-D, Zhu L. Fundamentals of Solid Oxide Electrolysis Cells (SOEC) BT High Temperature Electrolysis. Springer International Publishing; 2023, p. 5–34. https://doi.org/10.1007/978-3-031-22508-6 2.
- [62] Bianchi FR, Bosio B. Operating Principles, Performance and Technology Readiness Level

- of Reversible Solid Oxide Cells. Sustainability 2021; 13. https://doi.org/10.3390/su13094777.
- [63] Lamagna M, Groppi D, Nastasi B. Reversible solid oxide cells applications to the building sector. Int J Hydrogen Energy 2023; 48:27033–58. https://doi.org/https://doi.org/10.1016/j.ijhydene.2023.03.387.
- [64] Pan J, Yang Y, Lei J, Huang X. Thermodynamic analysis of an integrated reversible solid oxide fuel cell system. Energy Convers Manag X 2023; 20:100484. https://doi.org/https://doi.org/10.1016/j.ecmx.2023.100484.
- [65] Naumovich Y, Jagielski S, Kupecki J, Motylinski K, Martsinchyk K, Niemczyk A, et al. Carbon dioxide capture by direct methanation in co-electrolysis using solid oxide cell. Sustain Mater Technol 2024; 40:00944. https://doi.org/https://doi.org/10.1016/j.susmat.2024.00944.
- [66] Gupta S, Riegraf M, Costa R, Heddrich MP, Friedrich KA. Solid Oxide Electrolysis Cell-Based Syngas Production and Tailoring: A Comparative Assessment of Coelectrolysis, Separate Steam, CO₂ Electrolysis, and Steam Electrolysis. Ind Eng Chem Res 2024; 63:8705–12. https://doi.org/10.1021/acs.iecr.3c03674.
- [67] Chen T, Guan W, Ma C, Chen Z, Xie Y, Xiao J, et al. Highly efficient direct carbon solid oxide fuel cells operated with camellia oleifera biomass. Electrochim Acta 2022; 423:140594. https://doi.org/https://doi.org/10.1016/j.electacta.2022.140594.
- [68] Stoots CM, O'Brien JE, Herring JS, Hartvigsen JJ. Syngas production via high-temperature coelectrolysis of steam and carbon dioxide. J Fuel Cell Sci Technol 2009; 6:0110141–01101412. https://doi.org/10.1115/1.2971061.
- [69] Wang Y, Liu T, Fang S, Xiao G, Wang H, Chen F. A novel clean and effective syngas production system based on partial oxidation of methane assisted solid oxide coelectrolysis process. J Power Sources 2015; 277:261–7. https://doi.org/10.1016/j.jpowsour.2014.11.092.
- [70] Wang Y, Liu T, Lei L, Chen F. High temperature solid oxide H₂O/CO₂ co-electrolysis for syngas production. Fuel Process Technol 2017; 161:248–58. https://doi.org/10.1016/j.fuproc.2016.08.009.
- [71] Ioannidou E, Neophytides S, Niakolas DK. Experimental Clarification of the RWGS Reaction Effect in H₂O/CO₂ SOEC Co-Electrolysis Conditions. Catal 2019; 9:151. https://doi.org/10.3390/CATAL9020151.
- [72] Zhan Z, Kobsiriphat W, Wilson JR, Pillai M, Kim I, Barnett SA. Syngas production by coelectrolysis of CO₂/H₂O: The basis for a renewable energy cycle. Energy and Fuels 2009; 23:3089–96. https://doi.org/10.1021/ef900111f.
- [73] Riedel M, Heddrich MP, Friedrich KA. Experimental Analysis of the Co-Electrolysis Operation under Pressurized Conditions with a 10 Layer SOC Stack. J Electrochem Soc 2020; 167:024504. https://doi.org/10.1149/1945-7111/ab6820.
- [74] Yue X, Irvine JTS. (La,Sr)(Cr,Mn)O₃/GDC cathode for high temperature steam electrolysis and steam-carbon dioxide co-electrolysis. Solid State Ionics 2012; 225:131–5. https://doi.org/10.1016/J.SSI.2012.06.015.
- [75] Ni M. Modeling of a solid oxide electrolysis cell for carbon dioxide electrolysis. Chem Eng J 2010; 164:246–54. https://doi.org/10.1016/j.cej.2010.08.032.
- [76] Mahmood A, Bano S, Yu JH, Lee KH. Effect of operating conditions on the performance of solid electrolyte membrane reactor for steam and CO₂ electrolysis. J Memb Sci 2015; 473:8–15. https://doi.org/10.1016/J.MEMSCI.2014.09.002.

- [77] Ebbesen SD, Graves C, Mogensen M. Production of Synthetic Fuels by Co-Electrolysis of Steam and Carbon Dioxide. 2009; 6:646–60. https://doi.org/10.1080/15435070903372577.
- [78] Kim-Lohsoontorn P, Bae J. Electrochemical performance of solid oxide electrolysis cell electrodes under high-temperature coelectrolysis of steam and carbon dioxide. J Power Sources 2011; 196:7161–8. https://doi.org/10.1016/J.JPOWSOUR.2010.09.018.
- [79] Stoots C, O'Brien J, Hartvigsen J. Results of recent high temperature coelectrolysis studies at the Idaho National Laboratory. Int J Hydrogen Energy 2009; 34:4208–15. https://doi.org/10.1016/J.IJHYDENE.2008.08.029.
- [80] Zhan Z, Zhao L. Electrochemical reduction of CO₂ in solid oxide electrolysis cells. J Power Sources 2010; 195:7250–4. https://doi.org/10.1016/J.JPOWSOUR.2010.05.037.
- [81] Nechache A, Hody S. Alternative and innovative solid oxide electrolysis cell materials: A short review. Renew Sustain Energy Rev 2021; 149. https://doi.org/10.1016/j.rser.2021.111322.
- [82] Ebbesen SD, Mogensen M. Electrolysis of carbon dioxide in Solid Oxide Electrolysis Cells. J Power Sources 2009; 193:349–58. https://doi.org/10.1016/j.jpowsour.2009.02.093.
- [83] Clark JH, Farmer TJ, Herrero-Davila L, Sherwood J. Circular economy design considerations for research and process development in the chemical sciences. Green Chem 2016; 18:3914–34. https://doi.org/10.1039/c6gc00501b.
- [84] Sharma S, Basu S, Shetti NP, Aminabhavi TM. Waste-to-energy nexus for circular economy and environmental protection: Recent trends in hydrogen energy. Sci Total Environ 2020; 713:136633. https://doi.org/10.1016/j.scitotenv.2020.136633.
- [85] Chlipała M, Błaszczak P, Wang SF, Jasiński P, Bochentyn B. In situ study of a composition of outlet gases from biogas fuelled Solid Oxide Fuel Cell performed by the Fourier Transform Infrared Spectroscopy. Int J Hydrogen Energy 2019; 44:13864–74. https://doi.org/10.1016/j.ijhydene.2019.03.243.
- [86] Chen L, Chen F, Xia C. Direct synthesis of methane from CO₂-H₂O co-electrolysis in tubular solid oxide electrolysis cells. Energy Environ Sci 2014; 7:4018–22. https://doi.org/10.1039/c4ee02786h.
- [87] Bell DA, Towler BF, Fan M. Chapter 13 Substitute Natural Gas and Fischer-Tropsch Synthesis. William Andrew Publishing; 2011, https://doi.org/https://doi.org/10.1016/B978-0-8155-2049-8.10013-0.
- [88] Atkinson A, Barnett S, Gorte RJ, Irvine JTS, McEvoy AJ, Mogensen M, et al. Advanced anodes for high-temperature fuel cells. Nat Mater 2004; 3:17–27. https://doi.org/10.1038/nmat1040.
- [89] Tarancón A. Strategies for Lowering Solid Oxide Fuel Cells Operating Temperature. Energies 2009; 2:1130–50. https://doi.org/10.3390/en20401130.
- [90] Guth U. Kröger-Vinks Notation of Point Defects. Encyclopedia of Applied Electrochemistry. New York, NY: Springer New York 2014, https://doi.org/10.1007/978-1-4419-6996-5 310.
- [91] Kawamoto H. Research and Development Trends in Solid Oxide Fuel Cell Materials. Sci Technol Trends 2008; 52–70.
- [92] Brune A, Lajavardi M, Fisler D, Wagner JB. The electrical conductivity of yttria-stabilized zirconia prepared by precipitation from inorganic aqueous solutions. Solid State Ionics

- 1998; 106:89-101. https://doi.org/10.1016/s0167-2738(97)00486-4.
- [93] Fu Q, Tietz F, Sebold D, Tao S, Irvine JTS. An efficient ceramic-based anode for solid oxide fuel cells. J Power Sources 2007; 171:663–9. https://doi.org/10.1016/j.jpowsour.2007.06.159.
- [94] Weber A, Ivers-Tiffée E. Materials and concepts for solid oxide fuel cells (SOFCs) in stationary and mobile applications. J Power Sources 2004; 127:273–83. https://doi.org/https://doi.org/10.1016/j.jpowsour.2003.09.024.
- [95] Szymczewska D, Karczewski J, Chrzan A, Jasinski P. CGO as a barrier layer between LSCF electrodes and YSZ electrolyte fabricated by spray pyrolysis for solid oxide fuel cells. Solid State Ionics 2017; 302:113–7. https://doi.org/https://doi.org/10.1016/j.ssi.2016.11.008.
- [96] Liu Y, Shao Z, Mori T, Jiang SP. Development of nickel based cermet anode materials in solid oxide fuel cells Now and future. Mater Reports Energy 2021; 1:100003. https://doi.org/https://doi.org/10.1016/j.matre.2020.11.002.
- [97] Shaikh SPS, Muchtar A, Somalu MR. A review on the selection of anode materials for solid-oxide fuel cells. Renew Sustain Energy Rev 2015; 51:1–8. https://doi.org/10.1016/j.rser.2015.05.069.
- [98] Goodenough JB, Huang YH. Alternative anode materials for solid oxide fuel cells. J Power Sources 2007; 173:1–10. https://doi.org/10.1016/j.jpowsour.2007.08.011.
- [99] Sasaki K, Nojiri Y, Shiratori Y, Taniguchi S. Fuel Cells (SOFC): Alternative approaches, fuel alternative (Electroytes, Electrodes, Fuels). Encyclopedia of Sustainability Science and Technology. New York, NY: Springer New York 2012. https://doi.org/10.1007/978-1-4419-0851-3 138.
- [100] Lee C-H, Lee C-H, Lee H-Y, Oh SM. Microstructure and anodic properties of Ni/YSZ cermets in solid oxide fuel cells. Solid State Ionics 1997; 98:39–48. https://doi.org/https://doi.org/10.1016/S0167-2738(97)00100-8.
- [101] Haupt S, Edler F, Bartel M, Pernau HF. Van der Pauw device used to investigate the thermoelectric power factor. Rev Sci Instrum 2020; 91. https://doi.org/10.1063/5.0019005.
- [102] Jiang SP. Resistance Measurement in Solid Oxide Fuel Cells. J Electrochem Soc 2001; 148:887–97. https://doi.org/10.1149/1.1383776.
- [103] Mori M, Yamamoto T, Itoh H, Inaba H, Tagawa H. Thermal Expansion of Nickel-Zirconia Anodes in Solid Oxide Fuel Cells during Fabrication and Operation. J Electrochem Soc 1998; 145:1374.
- [104] Shri Prakash B, Senthil Kumar S, Aruna ST. Properties and development of Ni/YSZ as an anode material in solid oxide fuel cell: A review. Renew Sustain Energy Rev 2014; 36:149–79. https://doi.org/https://doi.org/10.1016/j.rser.2014.04.043.
- [105] Zimmerman M, Peterson NA, Zimmerman MA. Beyond the Individual: Toward a Nomological Network of Organizational Empowerment. 2016;34. https://doi.org/10.1023/B.
- [106] W. Huebner, H. U. Anderson, D. M. Reed, S. R. Sehlin XD. SOFC-IV. Electrochem Soc Proc Ser Pennington, NJ 1995; 696.
- [107] Liang M, Yu B, Wen M, Chen J, Xu J, Zhai Y. Preparation of NiO–YSZ composite powder by a combustion method and its application for cathode of SOEC. Int J Hydrogen Energy 2010; 35:2852–7. https://doi.org/https://doi.org/10.1016/j.ijhydene.2009.05.006.

- [108] Kishimoto M, Miyawaki K, Iwai H, Saito M, Yoshida H. Effect of composition ratio of Ni-YSZ anode on distribution of effective three-phase boundary and power generation performance. Fuel Cells 2013; 13:476–86. https://doi.org/10.1002/fuce.201200174.
- [109] Lee S, Kang KH, Hong HS, Yun YS, Woo SK. Performance of Ni/YSZ cermet cathode prepared by mechanical alloying for high temperature electrolysis of water vapor (steam): Effect of anode and cathode thicknesses on the efficiency of hydrogen production. Zeitschrift Fuer Met Res Adv Tech 2008; 99:114–9. https://doi.org/10.3139/146.101613.
- [110] Pesce A, Hornés A, Núñez M, Morata A, Torrell M, Tarancón A. 3D printing the next generation of enhanced solid oxide fuel and electrolysis cells. J Mater Chem A 2020; 8:16926–32. https://doi.org/10.1039/d0ta02803g.
- [111] Kim B, Cho K, Choi J, Shin D. Preparation of NiO-YSZ Composite Powder Through 2-Step Hydrothermal Synthesis and Its Application to Solid Oxide Fuel Cell Anode Functional Layer. J Nanosci Nanotechnol 2015; 15. https://doi.org/10.1166/jnn.2015.8400.
- [112] Song JH, Park MY, Park HW, Lim HT. Single-step preparation of nano-homogeneous NiO/YSZ composite anode for solid oxide fuel cells. Nano-Micro Lett 2013; 5:111–6. https://doi.org/10.5101/nml.v5i2.p111-116.
- [113] Cho HJ, Choi GM. Effect of milling methods on performance of Ni-Y₂O₃-stabilized ZrO₂ anode for solid oxide fuel cell. J Power Sources 2008; 176:96–101. https://doi.org/10.1016/j.jpowsour.2007.09.118.
- [114] Li S, Guo R, Li J, Chen Y, Liu W. Synthesis of NiO–ZrO₂ powders for solid oxide fuel cells. Ceram Int 2003; 29:883–6. https://doi.org/https://doi.org/10.1016/S0272-8842(03)00031-2.
- [115] Martins RF, Brant MC, Domingues RZ, Paniago RM, Sapag K, Matencio T. Synthesis and characterization of NiO-YSZ for SOFCs. Mater Res Bull 2009; 44:451–6. https://doi.org/10.1016/j.materresbull.2008.04.017.
- [116] Imperial JFL, Cervera RB. Synthesis and Characterization of Porous NiO/YSZ Electrode Materials Using Different Pore Formers. Mater Sci Forum 2018; 917:83–7. https://doi.org/10.4028/www.scientific.net/MSF.917.83.
- [117] Khan MS, Xu X, Knibbe R, Zhu Z. Air electrodes and related degradation mechanisms in solid oxide electrolysis and reversible solid oxide cells. Renew Sustain Energy Rev 2021; 143. https://doi.org/10.1016/j.rser.2021.110918.
- [118] Javed MA, Muneer M, Abbas G, Shakir I, Batool R, Iqbal M, et al. Structural and electrochemical characterization of low-cost Li_xCu_{1-x}Co_yFe_{1-y}O_{3-δ} cathode material for intermediate temperature solid oxide fuel cell. Ceram Int 2020; 46:10348–55. https://doi.org/10.1016/j.ceramint.2020.01.031.
- [119] Tahir NNM, Baharuddin NA, Samat AA, Osman N, Somalu MR. A review on cathode materials for conventional and proton-conducting solid oxide fuel cells. J Alloys Compd 2022; 894:162458. https://doi.org/10.1016/j.jallcom.2021.162458.
- [120] Tarancón A, Torrell M, Baiutti F, Bernadet L, Anelli S, Kostretsova N, et al. Emerging Trends in Solid Oxide Electrolysis Cells High Temperature Electrolysis. Springer International Publishing 2023. https://doi.org/10.1007/978-3-031-22508-6_11.
- [121] Kilner JA, Burriel M. Materials for Intermediate-Temperature Solid-Oxide Fuel Cells. Annu Rev Mater Res 2014; 44:365–93. https://doi.org/https://doi.org/10.1146/annurev-matsci-070813-113426.
- [122] Yusoff WNAW, Baharuddin NA, Somalu MR, Muchtar A, Samat AA. A Short Review on

- Selection of Electrodes Materials for Symmetrical Solid Oxide Fuel Cell. IOP Conf Ser Mater Sci Eng 2020; 957. https://doi.org/10.1088/1757-899X/957/1/012049.
- [123] Peng J, Zhao D, Xu Y, Wu X, Li X. Comprehensive Analysis of Solid Oxide Fuel Cell Performance Degradation Mechanism, Prediction, and Optimization Studies. Energies 2023; 16. https://doi.org/10.3390/en16020788.
- [124] Slodczyk A, Torrell M, Hornés A, Morata A, Kendall K, Tarancón A. Understanding longitudinal degradation mechanisms of large-area micro-tubular solid oxide fuel cells. Electrochim Acta 2018; 265:232–43. https://doi.org/https://doi.org/10.1016/j.electacta.2018.01.184.
- [125] Mahato N, Banerjee A, Gupta A, Omar S, Balani K. Progress in material selection for solid oxide fuel cell technology: A review. Prog Mater Sci 2015; 72:141–337. https://doi.org/10.1016/j.pmatsci.2015.01.001.
- [126] Zhou L, Mason JH, Li W, Liu X. Comprehensive review of chromium deposition and poisoning of solid oxide fuel cells (SOFCs) cathode materials. Renew Sustain Energy Rev 2020; 134:110320. https://doi.org/10.1016/j.rser.2020.110320.
- [127] Yokokawa H, Suzuki M, Yoda M, Suto T, Tomida K, Hiwatashi K, et al. Achievements of NEDO Durability Projects on SOFC Stacks in the Light of Physicochemical Mechanisms. Fuel Cells 2019; 19:311–39. https://doi.org/10.1002/fuce.201800187.
- [128] Sun Y, He S, Saunders M, Chen K, Shao Z, Jiang SP. A comparative study of surface segregation and interface of La_{0.6}Sr_{0.4}Co_{0.2}Fe_{0.8}O_{3-δ} electrode on GDC and YSZ electrolytes of solid oxide fuel cells. Int J Hydrogen Energy 2021; 46:2606–16. https://doi.org/https://doi.org/10.1016/j.ijhydene.2020.10.113.
- [129] Kendall K, Kendall M. High-temperature solid oxide fuel cells for the 21st century: fundamentals, design and applications. Elsevier 2015.
- [130] Zarabi Golkhatmi S, Asghar MI, Lund PD. A review on solid oxide fuel cell durability: Latest progress, mechanisms, and study tools. Renew Sustain Energy Rev 2022; 161:112339. https://doi.org/10.1016/j.rser.2022.112339.
- [131] Park K, Yu S, Bae J, Kim H, Ko Y. Fast performance degradation of SOFC caused by cathode delamination in long-term testing. Int J Hydrogen Energy 2010; 35:8670–7. https://doi.org/https://doi.org/10.1016/j.ijhydene.2010.05.005.
- [132] Butz B, Kruse P, Störmer H, Gerthsen D, Müller A, Weber A, et al. Correlation between microstructure and degradation in conductivity for cubic Y₂O₃-doped ZrO₂. Solid State Ionics 2006; 177:3275–84. https://doi.org/https://doi.org/10.1016/j.ssi.2006.09.003.
- [133] Liu L, Kim G-Y, Chandra A. Modeling of thermal stresses and lifetime prediction of planar solid oxide fuel cell under thermal cycling conditions. J Power Sources 2010; 195:2310–8. https://doi.org/https://doi.org/10.1016/j.jpowsour.2009.10.064.
- [134] Gao P, Bolon A, Taneja M, Xie Z, Orlovskaya N, Radovic M. Thermal expansion and elastic moduli of electrolyte materials for high and intermediate temperature solid oxide fuel cell. Solid State Ionics 2017; 300:1–9. https://doi.org/https://doi.org/10.1016/j.ssi.2016.11.015.
- [135] Kim Y-D, Yang J, Lee J-I, Saqib M, Shin J-S, Park K, et al. Degradation studies of ceriabased solid oxide fuel cells at intermediate temperature under various load conditions. J Power Sources 2020; 452:227758. https://doi.org/https://doi.org/10.1016/j.jpowsour.2020.227758.
- [136] Khan MZ, Mehran MT, Song R-H, Lee J-W, Lee S-B, Lim T-H. A simplified approach to predict performance degradation of a solid oxide fuel cell anode. J Power Sources 2018;

- 391:94–105. https://doi.org/https://doi.org/10.1016/j.jpowsour.2018.04.080.
- [137] Holzer L, Iwanschitz B, Hocker T, Münch B, Prestat M, Wiedenmann D, et al. Microstructure degradation of cermet anodes for solid oxide fuel cells: Quantification of nickel grain growth in dry and in humid atmospheres. J Power Sources 2011; 196:1279–94. https://doi.org/10.1016/j.jpowsour.2010.08.017.
- [138] Jiao Z, Shikazono N, Kasagi N. Study on degradation of solid oxide fuel cell anode by using pure nickel electrode. J Power Sources 2011; 196:8366–76. https://doi.org/https://doi.org/10.1016/j.jpowsour.2011.06.069.
- [139] Holzer L, Münch B, Iwanschitz B, Cantoni M, Hocker T, Graule T. Quantitative relationships between composition, particle size, triple phase boundary length and surface area in nickel-cermet anodes for Solid Oxide Fuel Cells. J Power Sources 2011; 196:7076–89. https://doi.org/https://doi.org/10.1016/j.jpowsour.2010.08.006.
- [140] Mogensen MB, Hauch A, Sun X, Chen M, Tao Y, Ebbesen SD, et al. Relation Between Ni Particle Shape Change and Ni Migration in Ni–YSZ Electrodes a Hypothesis. Fuel Cells 2017; 17:434–41. https://doi.org/10.1002/fuce.201600222.
- [141] Mirzababaei J, Chuang SSC. La_{0.6}Sr_{0.4}Co_{0.2}Fe_{0.8}O₃ perovskite: A stable anode catalyst for direct methane solid oxide fuel cells. Catalysts 2014; 4:146–61. https://doi.org/10.3390/catal4020146.
- [142] Koh J-H, Yoo Y-S, Park J-W, Lim HC. Carbon deposition and cell performance of Ni-YSZ anode support SOFC with methane fuel. Solid State Ionics 2002; 149:157–66. https://doi.org/https://doi.org/10.1016/S0167-2738(02)00243-6.
- [143] Liu W, Sun X, Pederson LR, Marina OA, Khaleel MA. Effect of nickel-phosphorus interactions on structural integrity of anode-supported solid oxide fuel cells. J Power Sources 2010; 195:7140–5. https://doi.org/https://doi.org/10.1016/j.jpowsour.2010.06.015.
- [144] Cheng Z, Wang JH, Choi Y, Yang L, Lin MC, Liu M. From Ni-YSZ to sulfur-tolerant anode materials for SOFCs: Electrochemical behavior, in situ characterization, modeling, and future perspectives. Energy Environ Sci 2011; 4:4380–409. https://doi.org/10.1039/c1ee01758f.
- [145] Lu X, Heenan TMM, Bailey JJ, Li T, Li K, Brett DJL, et al. Correlation between triple phase boundary and the microstructure of Solid Oxide Fuel Cell anodes: The role of composition, porosity and Ni densification. J Power Sources 2017; 365:210–9. https://doi.org/https://doi.org/10.1016/j.jpowsour.2017.08.095.
- [146] de Terris T, Andreau O, Peyre P, Adamski F, Koutiri I, Gorny C, et al. Optimization and comparison of porosity rate measurement methods of Selective Laser Melted metallic parts. Addit Manuf 2019; 28:802–13. https://doi.org/10.1016/j.addma.2019.05.035.
- [147] Leonide A, Apel Y, Ivers-Tiffee E. SOFC Modeling and Parameter Identification by Means of Impedance Spectroscopy. ECS Trans 2009; 19:81–109. https://doi.org/10.1149/1.3247567.
- [148] Lyu Z, Li H, Han M, Sun Z, Sun K. Performance degradation analysis of solid oxide fuel cells using dynamic electrochemical impedance spectroscopy. J Power Sources 2022; 538:231569. https://doi.org/10.1016/j.jpowsour.2022.231569.
- [149] Wan TH, Saccoccio M, Chen C, Ciucci F. Influence of the Discretization Methods on the Distribution of Relaxation Times Deconvolution: Implementing Radial Basis Functions with DRTtools. Electrochim Acta 2015; 184:483–99. https://doi.org/10.1016/j.electacta.2015.09.097.

- [150] Chunhai F, Zhentang Z. Synchrotron Radiation in Materials Science. vol. 1. Wiley-VCH; 2018.
- [151] Tsutakawa SE, Van Wynsberghe AW, Freudenthal BD, Weinacht CP, Gakhar L, Washington MT, et al. Solution X-ray scattering combined with computational modeling reveals multiple conformations of covalently bound ubiquitin on PCNA. Proc Natl Acad Sci U S A 2011; 108:17672–7. https://doi.org/10.1073/pnas.1110480108.
- [152] Zając M, Giela T, Freindl K, Kollbek K, Korecki J, Madej E, et al. The first experimental results from the 04BM (PEEM/XAS) beamline at Solaris. Nucl Instruments Methods Phys Res Sect B Beam Interact with Mater Atoms 2021; 492:43–8. https://doi.org/https://doi.org/10.1016/j.nimb.2020.12.024.
- [153] Warwick T, Franck K, Kortright JB, Meigs G, Moronne M, Myneni S, et al. A scanning transmission X-ray microscope for materials science spectromicroscopy at the advanced light source. Rev Sci Instrum 1998; 69:2964–73. https://doi.org/10.1063/1.1149041.
- [154] Kim J, Lee D, Nam C, Chung J, Koo B, Kim N, et al. Energy material analysis via insitu/operando scanning transmission x-ray microscopy: A review. J Electron Spectros Relat Phenomena 2023; 266:147337. https://doi.org/10.1016/j.elspec.2023.147337.
- [155] Zhong L, Chen D, Zafeiratos S. A mini review of in situ near-ambient pressure XPS studies on non-noble, late transition metal catalysts. Catal Sci Technol 2019; 9:3851–67. https://doi.org/10.1039/c9cy00632j.
- [156] Soustelle M. Physico-Chemical Transformations and Equilibria. Chem. Equilibria, 2015. https://doi.org/https://doi.org/10.1002/9781119178545.ch1.
- [157] Chlipała M, Błaszczak P, Wang S-F, Jasiński P, Bochentyn B. In situ study of a composition of outlet gases from biogas fuelled Solid Oxide Fuel Cell performed by the Fourier Transform Infrared Spectroscopy. Int J Hydrogen Energy 2019; 44:13864–74.
- [158] Kamecki B, Cempura G, Jasiński P, Wang SF, Molin S. Tuning Electrochemical Performance by Microstructural Optimization of the Nanocrystalline Functional Oxygen Electrode Layer for Solid Oxide Cells. ACS Appl Mater Interfaces 2022; 14:57449–59. https://doi.org/10.1021/acsami.2c18951.
- [159] Hussain I, Jalil AA, Mamat CR, Siang TJ, Rahman AFA, Azami MS, et al. New insights on the effect of the H₂/CO ratio for enhancement of CO methanation over metal-free fibrous silica ZSM-5: Thermodynamic and mechanistic studies. Energy Convers Manag 2019; 199:112056. https://doi.org/10.1016/j.enconman.2019.112056.
- [160] Abid N, Khan AM, Shujait S, Chaudhary K, Ikram M, Imran M, et al. Synthesis of nanomaterials using various top-down and bottom-up approaches, influencing factors, advantages, and disadvantages: A review. Adv Colloid Interface Sci 2022; 300:102597. https://doi.org/10.1016/j.cis.2021.102597.
- [161] Ealias AM, Saravanakumar MP. A review on the classification, characterisation, synthesis of nanoparticles and their application. IOP Conf Ser Mater Sci Eng 2017; 263. https://doi.org/10.1088/1757-899X/263/3/032019.
- [162] Kolahalam LA, Kasi Viswanath I V., Diwakar BS, Govindh B, Reddy V, Murthy YLN. Review on nanomaterials: Synthesis and applications. Mater Today Proc 2019; 18:2182–90. https://doi.org/10.1016/j.matpr.2019.07.371.
- [163] Vaseghi Z, Nematollahzadeh A. Nanomaterials. Green Synth. Nanomater. Bioenergy Appl 2020,. https://doi.org/https://doi.org/10.1002/9781119576785.ch2.
- [164] Zhang C, Oliaee SN, Hwang SY, Kong X, Peng Z. A Generic Wet Impregnation Method for Preparing Substrate-Supported Platinum Group Metal and Alloy Nanoparticles with

- Controlled Particle Morphology. Nano Lett 2016; 16:164–9. https://doi.org/10.1021/acs.nanolett.5b04518.
- [165] Dong H, Wang A, Koenig GM. Role of coprecipitation and calcination of precursors on phase homogeneity and electrochemical properties of battery active materials. Powder Technol 2018; 335:137–46. https://doi.org/10.1016/j.powtec.2018.05.020.
- [166] Dong H, Koenig GM. A review on synthesis and engineering of crystal precursors produced: Via coprecipitation for multicomponent lithium-ion battery cathode materials. CrystEngComm 2020; 22:1514–30. https://doi.org/10.1039/c9ce00679f.
- [167] Błaszczak P, Mizera A, Bochentyn B, Wang S-F, Jasiński P. Preparation of methanation catalysts for high temperature SOEC by β-cyclodextrin-assisted impregnation of nano-CeO₂ with transition metal oxides. Int J Hydrogen Energy 2021. https://doi.org/10.1016/j.ijhydene.2021.10.144.
- [168] Mizera A, Błaszczak P, Bochentyn B, Lach R, Drożdż E. Cu supported on various oxides as a candidate catalyst for dry methane reforming in DIR-SOFCs systems. Int J Hydrogen Energy 2022; 47:25647–61. https://doi.org/10.1016/j.ijhydene.2022.06.016.
- [169] Jean-Marie A, Griboval-Constant A, Khodakov AY, Monflier E, Diehl F. β-Cyclodextrin for design of alumina supported cobalt catalysts efficient in Fischer-Tropsch synthesis. Chem Commun 2011; 47:10767–9. https://doi.org/10.1039/c1cc13800f.
- [170] Liu H, Li Y, Wu H, Liu J, He D. Effects of α- and γ-cyclodextrin-modified impregnation method on physicochemical properties of Ni/SBA-15 and its catalytic performance in CO₂ reforming of methane. Chinese J Catal 2015; 36:283–9. https://doi.org/https://doi.org/10.1016/S1872-2067(14)60242-4.
- [171] Najafpour MM, Kaboudin B, Mostafalu R, Shahbazy M, Safdari R, Kompany-Zareh M. A proposed mechanism to form nanosized Mn oxides from the decomposition of β-cyclodextrin-Mn complex: Toward nanosized water-splitting catalysts with special morphology. Int J Hydrogen Energy 2017; 42:11187–98. https://doi.org/https://doi.org/10.1016/j.ijhydene.2017.03.005.
- [172] Liu H, Li Y, Wu H, Miyake T, He D. CO₂ reforming of methane over Ni/SBA-15 prepared with β-cyclodextrin Role of β-cyclodextrin in Ni dispersion and performance. Int J Hydrogen Energy 2013; 38:15200–9. https://doi.org/https://doi.org/10.1016/j.ijhydene.2013.09.095.
- [173] Maciel CG, Silva T de F, Hirooka MI, Belgacem MN, Assaf JM. Effect of nature of ceria support in CuO/CeO₂ catalyst for PROX-CO reaction. Fuel 2012; 97:245–52. https://doi.org/https://doi.org/10.1016/j.fuel.2012.02.004.
- [174] Giordano F, Trovarelli A, de Leitenburg C, Giona M. A Model for the Temperature-Programmed Reduction of Low and High Surface Area Ceria. J Catal 2000; 193:273–82. https://doi.org/https://doi.org/10.1006/jcat.2000.2900.
- [175] Xu J, Harmer J, Li G, Chapman T, Collier P, Longworth S, et al. Size dependent oxygen buffering capacity of ceria nanocrystals. Chem Commun 2010; 46:1887–9. https://doi.org/10.1039/b923780a.
- [176] Zhou X-D, Huebner W. Size-induced lattice relaxation in CeO₂ nanoparticles. Appl Phys Lett 2001; 79:3512–4. https://doi.org/10.1063/1.1419235.
- [177] Tang C, Sun B, Sun J, Hong X, Deng Y, Gao F, et al. Solid state preparation of NiO-CeO₂ catalyst for NO reduction. Catal Today 2017; 281:575–82. https://doi.org/https://doi.org/10.1016/j.cattod.2016.05.026.
- [178] Jehng J-M, Chen C-M. Amination of Polyethylene Glycol to Polyetheramine over the

- Supported Nickel Catalysts. Catal Letters 2001; 77:147–54. https://doi.org/10.1023/A:1012782927451.
- [179] Zou W, Ge C, Lu M, Wu S, Wang Y, Sun J, et al. Engineering the NiO/CeO₂ interface to enhance the catalytic performance for CO oxidation. RSC Adv 2015; 5:98335–43. https://doi.org/10.1039/C5RA20466F.
- [180] Spadaro L, Arena F, Granados ML, Ojeda M, Fierro JLG, Frusteri F. Metal–support interactions and reactivity of Co/CeO₂ catalysts in the Fischer–Tropsch synthesis reaction. J Catal 2005; 234:451–62. https://doi.org/https://doi.org/10.1016/j.jcat.2005.07.006.
- [181] Martínez-Arias A, Fernández-García M, Gálvez O, Coronado JM, Anderson JA, Conesa JC, et al. Comparative Study on Redox Properties and Catalytic Behavior for CO Oxidation of CuO/CeO₂ and CuO/ZrCeO₄ Catalysts. J Catal 2000; 195:207–16. https://doi.org/https://doi.org/10.1006/jcat.2000.2981.
- [182] Luo J-Y, Meng M, Li X, Li X-G, Zha Y-Q, Hu T-D, et al. Mesoporous Co₃O₄—CeO₂ and Pd/Co₃O₄—CeO₂ catalysts: Synthesis, characterization and mechanistic study of their catalytic properties for low-temperature CO oxidation. J Catal 2008; 254:310–24. https://doi.org/https://doi.org/10.1016/j.jcat.2008.01.007.
- [183] Sohn H, Celik G, Gunduz S, Dogu D, Zhang S, Shan J, et al. Oxygen Mobility in Pre-Reduced Nano- and Macro-Ceria with Co Loading: An AP-XPS, In-Situ DRIFTS and TPR Study. Catal Letters 2017; 147:2863–76. https://doi.org/10.1007/s10562-017-2176-4.
- [184] Greluk M, Rotko M, Turczyniak-Surdacka S. Enhanced catalytic performance of La₂O₃ promoted Co/CeO₂ and Ni/CeO₂ catalysts for effective hydrogen production by ethanol steam reforming. Renew Energy 2020; 155:378–95. https://doi.org/https://doi.org/10.1016/j.renene.2020.03.117.
- [185] Nabaho D, (Hans) Niemantsverdriet JW, Claeys M, van Steen E. Hydrogen spillover in the Fischer–Tropsch synthesis: An analysis of platinum as a promoter for cobalt–alumina catalysts. Catal Today 2016; 261:17–27. https://doi.org/https://doi.org/10.1016/j.cattod.2015.08.050.
- [186] Hołówko B, Błaszczak P, Chlipała M, Gazda M, Wang SF, Jasiński P, et al. Structural and catalytic properties of ceria layers doped with transition metals for SOFCs fueled by biogas. Int J Hydrogen Energy 2020; 45:12982–96. https://doi.org/10.1016/j.ijhydene.2020.02.144.
- [187] Martínez-Arias A, Fernández-García M, Soria J, Conesa JC. Spectroscopic Study of a Cu/CeO₂ Catalyst Subjected to Redox Treatments in Carbon Monoxide and Oxygen. J Catal 1999; 182:367–77. https://doi.org/https://doi.org/10.1006/jcat.1998.2361.
- [188] Luo M-F, Song Y-P, Lu J-Q, Wang X-Y, Pu Z-Y. Identification of CuO Species in High Surface Area CuO-CeO₂ Catalysts and Their Catalytic Activities for CO Oxidation. J Phys Chem C 2007; 111:12686–92. https://doi.org/10.1021/jp0733217.
- [189] Zhan S, Zhu D, Qiu M, Yu H, Li Y. Highly efficient removal of NO with ordered mesoporous manganese oxide at low temperature. RSC Adv 2015; 5:29353–61. https://doi.org/10.1039/C4RA17300G.
- [190] Fakeeha AH, Barama S, Ibrahim AA, Al-Otaibi R-L, Barama A, Abasaeed AE, et al. In Situ Regeneration of Alumina-Supported Cobalt—Iron Catalysts for Hydrogen Production by Catalytic Methane Decomposition. Catalysts 2018; 8. https://doi.org/10.3390/catal8110567.
- [191] Portnyagin AS, Golikov AP, Drozd VA, Avramenko VA. An alternative approach to kinetic analysis of temperature-programmed reaction data. RSC Adv 2018; 8:3286–95. https://doi.org/10.1039/C7RA09848K.

- [192] Tiernan MJ, Barnes PA, Parkes GMB. Reduction of Iron Oxide Catalysts: The Investigation of Kinetic Parameters Using Rate Perturbation and Linear Heating Thermoanalytical Techniques. J Phys Chem B 2001; 105:220–8. https://doi.org/10.1021/jp003189+.
- [193] Yang Shuang, Chen Guojun, Lv Chengfu, Li Chao, Yin Na, Yang Fei, et al. Evolution of nanopore structure in lacustrine organic-rich shales during thermal maturation from hydrous pyrolysis, Minhe Basin, Northwest China. Energy Explor Exploit 2017; 36:265–81. https://doi.org/10.1177/0144598717723647.
- [194] Brunauer S, Deming LS, Deming WE, Teller E. On a Theory of the van der Waals Adsorption of Gases. J Am Chem Soc 1940; 62:1723–32. https://doi.org/10.1021/ja01864a025.
- [195] Bharathi RN, Sankar S. Investigation of Transport Properties of Pr Doped Cerium Oxide Nanoparticles as a Solid Electrolyte for IT-SOFC Applications. J Inorg Organomet Polym Mater 2018; 28:1829–38. https://doi.org/10.1007/s10904-018-0880-1.
- [196] Ponnar M, Pushpanathan K, Santhi R, Ravichandran S. Enhanced supercapacitor performance and ferromagnetic behavior of Ni-doped CeO₂ quantum dots. J Mater Sci Mater Electron 2020; 31:12661–77. https://doi.org/10.1007/s10854-020-03816-7.
- [197] Shen L, Xu J, Zhu M, Han Y-F. Essential Role of the Support for Nickel-Based CO₂ Methanation Catalysts. ACS Catal 2020; 10:14581–91. https://doi.org/10.1021/acscatal.0c03471.
- [198] Rossi LI, Kinen CO, Rossi RH de. Important role of native β-cyclodextrin in the stabilization of transition metal salts. Comptes Rendus Chim 2017; 20:1053–61. https://doi.org/10.1016/j.crci.2017.09.007.
- [199] Tada S, Shimizu T, Kameyama H, Haneda T, Kikuchi R. Ni/CeO₂ catalysts with high CO₂ methanation activity and high CH₄ selectivity at low temperatures. Int J Hydrogen Energy 2012; 37:5527–31. https://doi.org/https://doi.org/10.1016/j.ijhydene.2011.12.122.
- [200] Tu J, Wu H, Qian Q, Han S, Chu M, Jia S, et al. Low temperature methanation of CO₂ over an amorphous cobalt-based catalyst. Chem Sci 2021; 12:3937–43. https://doi.org/10.1039/D0SC06414A.
- [201] Xu Y, Wu Y, Li J, Wei S, Gao X, Wang P. Combustion-impregnation preparation of Ni/SiO₂ catalyst with improved low-temperature activity for CO₂ methanation. Int J Hydrogen Energy 2021; 46:20919–29. https://doi.org/10.1016/j.ijhydene.2021.03.201.
- [202] Senanayake SD, Evans J, Agnoli S, Barrio L, Chen T-L, Hrbek J, et al. Water—Gas Shift and CO Methanation Reactions over Ni—CeO₂ (111) Catalysts. Top Catal 2011; 54:34—41. https://doi.org/10.1007/s11244-011-9645-6.
- [203] Le Saché E, Pastor-Pérez L, Haycock BJ, Villora-Picó JJ, Sepúlveda-Escribano A, Reina TR. Switchable Catalysts for Chemical CO₂ Recycling: A Step Forward in the Methanation and Reverse Water-Gas Shift Reactions. ACS Sustain Chem Eng 2020; 8:4614–22. https://doi.org/10.1021/acssuschemeng.0c00551.
- [204] Alrafei B, Polaert I, Ledoux A, Azzolina-Jury F. Remarkably stable and efficient Ni and Ni-Co catalysts for CO₂ methanation. Catal Today 2020; 346:23–33. https://doi.org/10.1016/j.cattod.2019.03.026.
- [205] Hatta AH, Jalil AA, Hassan NS, Hamid MYS, Rahman AFA, Teh LP, et al. A review on recent bimetallic catalyst development for synthetic natural gas production via CO methanation. Int J Hydrogen Energy 2021. https://doi.org/10.1016/j.ijhydene.2021.10.213.

- [206] Gao J, Wang Y, Ping Y, Hu D, Xu G, Gu F, et al. A thermodynamic analysis of methanation reactions of carbon oxides for the production of synthetic natural gas. RSC Adv 2012; 2:2358–68. https://doi.org/10.1039/C2RA00632D.
- [207] Younas M, Leong, Kong L, Bashir MJK, Nadeem H, Shehzad A, et al. Recent Advancements, Fundamental Challenges, and Opportunities in Catalytic Methanation of CO₂ 2016. https://doi.org/10.1021/acs.energyfuels.6b01723.
- [208] Lee WJ, Li C, Prajitno H, Yoo J, Patel J, Yang Y, et al. Recent trend in thermal catalytic low temperature CO₂ methanation: A critical review. Catal Today 2021;368:2–19. https://doi.org/10.1016/j.cattod.2020.02.017.
- [209] Nizio M, Albarazi A, Cavadias S, Amouroux J, Galvez ME, Da Costa P. Hybrid plasma-catalytic methanation of CO₂ at low temperature over ceria zirconia supported Ni catalysts. Int J Hydrogen Energy 2016; 41:11584–92. https://doi.org/10.1016/J.IJHYDENE.2016.02.020.
- [210] Czekaj I, Loviat F, Raimondi F, Wambach J, Biollaz S, Wokaun A. Characterization of surface processes at the Ni-based catalyst during the methanation of biomass-derived synthesis gas: X-ray photoelectron spectroscopy (XPS). Appl Catal A Gen 2007; 329:68–78. https://doi.org/10.1016/J.APCATA.2007.06.027.
- [211] Tao M, Meng X, Lv Y, Bian Z, Xin Z. Effect of impregnation solvent on Ni dispersion and catalytic properties of Ni/SBA-15 for CO methanation reaction. Fuel 2016; 165:289–97. https://doi.org/10.1016/J.FUEL.2015.10.023.
- [212] Falbo L, Visconti CG, Lietti L, Szanyi J. The effect of CO on CO₂ methanation over Ru/Al₂O₃ catalysts: a combined steady-state reactivity and transient DRIFT spectroscopy study. Appl Catal B Environ 2019; 256:117791. https://doi.org/10.1016/J.APCATB.2019.117791.
- [213] Rönsch S, Schneider J, Matthischke S, Schlüter M, Götz M, Lefebvre J, et al. Review on methanation From fundamentals to current projects. Fuel 2016; 166:276–96. https://doi.org/10.1016/J.FUEL.2015.10.111.
- [214] Liu P, Zhao B, Li S, Shi H, Ma M, Lu J, et al. Influence of the Microstructure of Ni-Co Bimetallic Catalyst on CO Methanation. Ind Eng Chem Res 2020; 59:1845–54. https://doi.org/10.1021/acs.iecr.9b05951.
- [215] Tsiotsias AI, Charisiou ND, Yentekakis I V., Goula MA. Bimetallic Ni-based catalysts for CO₂ methanation: A review. Nanomaterials 2021; 11:1–34. https://doi.org/10.3390/nano11010028.
- [216] De S, Zhang J, Luque R, Yan N. Ni-based bimetallic heterogeneous catalysts for energy and environmental applications. Energy Environ Sci 2016; 9:3314–47. https://doi.org/10.1039/C6EE02002J.
- [217] Błaszczak P, Zając M, Ducka A, Matlak K, Wolanin B, Wang SF, et al. High-temperature Co-electrolysis of CO₂/H₂O and direct methanation over Co-impregnated SOEC. Bimetallic synergy between Co and Ni. Int J Hydrogen Energy 2022; 47:35017–37. https://doi.org/10.1016/j.ijhydene.2022.08.057.
- [218] Han L, Meng Q, Wang D, Zhu Y, Wang J, Du X, et al. Interrogation of bimetallic particle oxidation in three dimensions at the nanoscale. Nat Commun 2016; 7:1–9. https://doi.org/10.1038/ncomms13335.
- [219] Gonçalves JM, Silva MNT, Naik KK, Martins PR, Rocha DP, Nossol E, et al. Multifunctional spinel MnCo₂O₄ based materials for energy storage and conversion: a review on emerging trends, recent developments and future perspectives. J Mater Chem A 2021; 9:3095–124. https://doi.org/10.1039/d0ta11129e.

- [220] Zhao X, Mao L, Cheng Q, Li J, Liao F, Yang G, et al. Two-dimensional Spinel Structured Co-based Materials for High Performance Supercapacitors: A Critical Review. Chem Eng J 2020; 387:124081. https://doi.org/10.1016/j.cej.2020.124081.
- [221] Pawłowska S, Lankauf K, Błaszczak P, Karczewski J, Górnicka K, Cempura G, et al. Tailoring a low-energy ball milled MnCo₂O₄ spinel catalyst to boost oxygen evolution reaction performance. Appl Surf Sci 2023; 619:156720.
- [222] Niu J, Liu H, Zhang Y, Wang X, Han J, Yue Z, et al. NiCo₂O₄ spinel for efficient toluene oxidation: The effect of crystal plane and solvent. Chemosphere 2020; 259:127427. https://doi.org/10.1016/j.chemosphere.2020.127427.
- [223] Wang H, Wang H, Huang J, Zhou X, Wu Q, Luo Z, et al. Hierarchical Mesoporous/Macroporous Co-Doped NiO Nanosheet Arrays as Free-Standing Electrode Materials for Rechargeable Li-O₂ Batteries. ACS Appl Mater Interfaces 2019; 11:44556–65. https://doi.org/10.1021/acsami.9b13329.
- [224] Cetin A, Esenturk EN. Hierarchical nanowire and nanoplate-assembled NiCo₂O₄–NiO biphasic microspheres as effective electrocatalysts for oxygen evolution reaction. Mater Today Chem 2019; 14:100215. https://doi.org/10.1016/j.mtchem.2019.100215.
- [225] Dai X, Dai Y, Lu J, Pu L, Wang W, Jin J, et al. Cobalt oxide nanocomposites modified by NiCo-layered double hydroxide nanosheets as advanced electrodes for supercapacitors. Ionics (Kiel) 2020; 26:2501–11. https://doi.org/10.1007/s11581-019-03333-6.
- [226] Lai C, Wang Y, Fu L, Song H, Liu B, Guo Z, et al. Aqueous flexible all-solid-state NiCo-Zn batteries with high capacity based on advanced ion-buffering reservoirs of NiCo₂O₄. Adv Compos Hybrid Mater 2022; 5. https://doi.org/10.1007/s42114-021-00375-1.
- [227] Somlyai-Sipos L, Janovszky D, Sycheva A, Baumli P. Investigation of the Melting Point Depression of Copper Nanoparticles. IOP Conf Ser Mater Sci Eng 2020; 903:6–13. https://doi.org/10.1088/1757-899X/903/1/012002.
- [228] Dashevskii VY, Yusfin YS, Aleksandrov AA, Leont'ev LI, Podgorodetskii GS, Gubanov VI. Improving manganese utilization in the production of manganese ferroalloys. Steel Transl 2013; 43:424–8. https://doi.org/10.3103/S0967091213070036.
- [229] Li Y, Yang W, Liu X, Che S, Tu Z, Hou L, et al. Dual interface engineering of NiO/NiCo₂O₄/CoO heterojunction within graphene networks for high-performance lithium storage. Electrochim Acta 2021; 389:138536. https://doi.org/10.1016/j.electacta.2021.138536.
- [230] C. Greskovich. The kinetics of NiCr₂O₄ formation and diffusion of Cr³⁺ ions in NiO. 1940; 279–81.
- [231] Jiang W-J, Gu L, Li L, Zhang Y, Zhang X, Zhang L-J, et al. Understanding the High Activity of Fe–N–C Electrocatalysts in Oxygen Reduction: Fe/Fe₃C Nanoparticles Boost the Activity of Fe–N_x. J Am Chem Soc 2016; 138:3570–8. https://doi.org/10.1021/jacs.6b00757.
- [232] Guan C, Liu X, Ren W, Li X, Cheng C, Wang J. Rational Design of Metal-Organic Framework Derived Hollow NiCo₂O₄ Arrays for Flexible Supercapacitor and Electrocatalysis. Adv Energy Mater 2017; 7:1–8. https://doi.org/10.1002/aenm.201602391.
- [233] Tong X, Pang N, Qu Y, Yan C, Xiong D, Xu S, et al. 3D urchin-like NiCo₂O₄ coated with carbon nanospheres prepared on flexible graphite felt for efficient bifunctional electrocatalytic water splitting. J Mater Sci 2021; 56:9961–73. https://doi.org/10.1007/s10853-021-05892-4.

- [234] Xiao X, Zhang X, Zhang Z, You J, Liu S, Wang Y. Macro-/meso-porous NiCo₂O₄ synthesized by template-free solution combustion to enhance the performance of a nonenzymatic amperometric glucose sensor. Microchim Acta 2020; 187. https://doi.org/10.1007/s00604-019-4063-8.
- [235] Yu Y, Chen C, Liu Y, Yu H, Li S, Xue Y, et al. Hierarchical Ni/Ni(OH)₂-NiCo₂O₄ Supported on Ni Foam as Efficient Bifunctional Electrocatalysts for Water Splitting. J Phys Chem C 2022; 126:5493–501. https://doi.org/10.1021/acs.jpcc.1c07688.
- [236] Kaneko R, Chowdhury TH, Wu G, Kayesh ME, Kazaoui S, Sugawa K, et al. Cobalt-doped nickel oxide nanoparticles as efficient hole transport materials for low-temperature processed perovskite solar cells. Sol Energy 2019; 181:243–50. https://doi.org/10.1016/j.solener.2019.01.097.
- [237] Tippo P, Thongsuwan W, Wiranwetchayan O, Kumpika T, Kantarak E, Singjai P. Influence of Co concentration on properties of NiO film by sparking under uniform magnetic field. Sci Rep 2020; 10:1–12. https://doi.org/10.1038/s41598-020-72883-x.
- [238] Flores CLI, Balela MDL. Electrocatalytic oxygen evolution reaction of hierarchical micro/nanostructured mixed transition cobalt oxide in alkaline medium. J Solid State Electrochem 2020; 24:891–904. https://doi.org/10.1007/s10008-020-04530-4.
- [239] Béjar J, Álvarez-Contreras L, Ledesma-García J, Arjona N, Arriaga LG. Electrocatalytic evaluation of Co₃O₄ and NiCo₂O₄ rosettes-like hierarchical spinel as bifunctional materials for oxygen evolution (OER) and reduction (ORR) reactions in alkaline media. J Electroanal Chem 2019; 847:113190. https://doi.org/10.1016/j.jelechem.2019.113190.
- [240] Zhou LN, Yu L, Liu C, Li YJ. Electrocatalytic activity sites for the oxygen evolution reaction on binary cobalt and nickel phosphides. RSC Adv 2020; 10:39909–15. https://doi.org/10.1039/d0ra07284b.
- [241] Zheng Y, Wang J, Yu B, Zhang W, Chen J, Qiao J, et al. A review of high temperature coelectrolysis of H₂O and CO₂ to produce sustainable fuels using solid oxide electrolysis cells (SOECs): Advanced materials and technology. Chem Soc Rev 2017; 46:1427–63. https://doi.org/10.1039/c6cs00403b.
- [242] Liu Q, Bian B, Fan J, Yang J. Cobalt doped Ni based ordered mesoporous catalysts for CO₂ methanation with enhanced catalytic performance. Int J Hydrogen Energy 2018; 43:4893–901. https://doi.org/10.1016/j.ijhydene.2018.01.132.
- [243] Varun Y, Sreedhar I, Singh SA. Highly stable M/NiO–MgO (M = Co, Cu and Fe) catalysts towards CO₂ methanation. Int J Hydrogen Energy 2020; 45:28716–31. https://doi.org/10.1016/j.ijhydene.2020.07.212.
- [244] Shao Q, Jin D, Lu Y, Yu Y, Luo L, Sun X, et al. Performance evolution analysis of solid oxide electrolysis cells operating at high current densities. Int J Hydrogen Energy 2024; 57:709–16. https://doi.org/https://doi.org/10.1016/j.ijhydene.2024.01.096.
- [245] Sumi H. Co-electrolysis SOEC and internal reforming SOFC for achieving a carbon-neutral society. RSC Sustain 2024; 2:1568–79. https://doi.org/10.1039/d4su00095a.
- [246] Endo N, Fukumoto T, Ushijima R, Natsukoshi K, Tachikawa Y, Matsuda J, et al. DRT Analysis of Solid Oxide Electrolysis Cells: Polarization Resistance of Fuel Electrodes. ECS Meet Abstr 2021; MA2021-03:258–258. https://doi.org/10.1149/ma2021-031258mtgabs.
- [247] Cho DY, Song SJ, Kim UK, Kim KM, Lee HK, Hwang CS. Spectroscopic investigation of the hole states in Ni-deficient NiO films. J Mater Chem C 2013; 1:4334–8. https://doi.org/10.1039/c3tc30687a.

- [248] Zhang B, Zheng X, Voznyy O, Comin R, Bajdich M, García-Melchor M, et al. Homogeneously dispersed multimetal oxygen-evolving catalysts. Science 2016; 352:333–7. https://doi.org/10.1126/science.aaf1525.
- [249] Chang TC, Lu YT, Lee CH, Gupta JK, Hardwick LJ, Hu CC, et al. The Effect of Degrees of Inversion on the Electronic Structure of Spinel NiCo₂O₄: A Density Functional Theory Study. ACS Omega 2021; 6:9692–9. https://doi.org/10.1021/acsomega.1c00295.
- [250] Chang CF, Hu Z, Wu H, Burnus T, Hollmann N, Benomar M, et al. Spin blockade, orbital occupation, and charge ordering in La_{1.5}Sr_{0.5}CoO₄. Phys Rev Lett 2009; 102:0–5. https://doi.org/10.1103/PhysRevLett.102.116401.
- [251] Gutiérrez A, Domínguez-Cañizares G, Krause S, Díaz-Fernández D, Soriano L. Thermal induced depletion of cationic vacancies in NiO thin films evidenced by X-ray absorption spectroscopy at the O1s threshold. J Vac Sci Technol A 2020; 38:033209. https://doi.org/10.1116/6.0000080.
- [252] Niu J, Liu H, Zhang Y, Wang X, Han J, Yue Z, et al. NiCo₂O₄ spinel for efficient toluene oxidation: The effect of crystal plane and solvent. Chemosphere 2020; 259:127427. https://doi.org/10.1016/j.chemosphere.2020.127427.
- [253] Chang HW, Dong CL, Lu YR, Huang YC, Chen CL, Chen JL, et al. Ex-situ soft X-ray absorption spectroscopic investigation of NiCo₂O₄ annealed in different gases for hydrogen generation by electrolysis of urea. Int J Hydrogen Energy 2019; 44:15771–8. https://doi.org/10.1016/j.ijhydene.2018.10.108.
- [254] Cui M, Ding X, Huang X, Shen Z, Lee TL, Oropeza FE, et al. Ni³⁺-Induced Hole States Enhance the Oxygen Evolution Reaction Activity of Ni_xCo_{3-x}O₄ Electrocatalysts. Chem Mater 2019; 31:7618–25. https://doi.org/10.1021/acs.chemmater.9b02453.
- [255] Cai X, Sun W, Xu C, Cao L, Yang J. Highly selective catalytic reduction of NO via SO₂/H₂O-tolerant spinel catalysts at low temperature. Environ Sci Pollut Res 2016; 23:18609–20. https://doi.org/10.1007/s11356-016-7061-y.
- [256] Duch M, Esteve J, Goacutemez E, Peacuterez-Castillejos R, Valleacutes E. Electrodeposited Co-Ni alloys for MEMS. J Micromechanics Microengineering 2002; 12:400–5. https://doi.org/10.1088/0960-1317/12/4/309.
- [257] Karimzadeh A, Aliofkhazraei M, Walsh FC. A review of electrodeposited Ni-Co alloy and composite coatings: Microstructure, properties and applications. Surf Coatings Technol 2019; 372:463–98. https://doi.org/https://doi.org/10.1016/j.surfcoat.2019.04.079.
- [258] Błaszczak P, Ducka A, Wolanin B, Matlak K, Machowski G, Prześniak-Welenc M, et al. Fabrication of wormhole-like YSZ and Ni-YSZ by the novel soft-hard template CTAB/NaCl-assisted route. Suppressing Ni coalescence in SOFC. J Eur Ceram Soc 2023; 43:438–51. https://doi.org/10.1016/j.jeurceramsoc.2022.09.054.
- [259] Frauscher M, Besser C, Allmaier G, Dörr N. Elucidation of oxidation and degradation products of oxygen containing fuel components by combined use of a stable isotopic tracer and mass spectrometry. Anal Chim Acta 2017; 993:47–54. https://doi.org/10.1016/j.aca.2017.09.009.
- [260] Moulik SP, Naskar B, Rakshit AK. Current status of enthalpy-entropy compensation phenomenon. Curr Sci 2019; 117:1286–91. https://doi.org/10.18520/cs/v117/i8/1286-1291.
- [261] Götsch T, Wallisch W, Stöger-Pollach M, Klötzer B, Penner S. From zirconia to yttria: Sampling the YSZ phase diagram using sputter-deposited thin films. AIP Adv 2016;6. https://doi.org/10.1063/1.4942818.

- [262] Linderoth S, Bonanos N. Effects of Dissolution and Exsolution of Ni in YSZ. Mater Electrochem Energy Convers Storage 2002. https://doi.org/10.1002/9781118370858.ch16.
- [263] Joo S, Lim C, Kwon O, Zhang L, Zhou J, Wang J-Q, et al. The first observation of Ni nanoparticle exsolution from YSZ and its application for dry reforming of methane. Mater Reports Energy 2021; 1:100021. https://doi.org/10.1016/j.matre.2021.100021.
- [264] Park YM, Choi GM. Mixed Ionic and Electronic Conduction in YSZ-NiO Composite. J Electrochem Soc 1999; 146:883–9. https://doi.org/10.1149/1.1391696.
- [265] Kuzjukevics A, Linderoth S. Interaction of NiO with yttria-stabilized zirconia. Solid State Ionics 1997; 93:255–61. https://doi.org/10.1016/s0167-2738(96)00529-2.
- [266] Lide DR. CRC Handbook of Chemistry and Physics, 84th edition. CRC Press 2003;84. https://doi.org/10.1136/oem.53.7.504.
- [267] Batista RM, Muccillo ENS. Densification and grain growth of 8YSZ containing NiO. Ceram Int 2011; 37:1047–53. https://doi.org/10.1016/j.ceramint.2010.11.031.
- [268] Mori H, Wen C, Otomo J, Eguchi K, Takahashi H. Investigation of the interaction between NiO and yttria-stabilized zirconia (YSZ) in the NiO/YSZ composite by temperature-programmed reduction technique 2003; 245:79–85. https://doi.org/10.1016/S0926-860X(02)00634-8.
- [269] Hu X, Yang J, Sun W, Wang N, An S, Wang Q, et al. Y-Zr-O solid solution supported Nibased catalysts for hydrogen production via auto-thermal reforming of acetic acid. Appl Catal B Environ 2020; 278:119264. https://doi.org/10.1016/j.apcatb.2020.119264.
- [270] Lopera AA, Chavarriaga EA, Perez-Taborda JA, Amaya SL, Echavarría A, García C. Effect of the Fuel in the Synthesis of NiO–YSZ by Solution Combustion Synthesis with Potential Application in Catalysis of Hydrogen. Int J Self-Propagating High-Temperature Synth 2022; 31:74–9. https://doi.org/10.3103/s1061386222020042.
- [271] Osinkin DA, Bronin DI, Beresnev SM, Bogdanovich NM, Zhuravlev VD, Vdovin GK, et al. Thermal expansion, gas permeability, and conductivity of Ni-YSZ anodes produced by different techniques. J Solid State Electrochem 2014; 18:149–56. https://doi.org/10.1007/s10008-013-2239-4.
- [272] Jing D, Li H, Liping XU, Lei Z, Guangwei W. Preparation of YSZ solid electrolyte by slip casting and its properties. RARE Met 2009; 28:372. https://doi.org/10.1007/s12598-009-0074-7.
- [273] Panthi D, Hedayat N, Du Y. Densification behavior of yttria-stabilized zirconia powders for solid oxide fuel cell electrolytes. J Adv Ceram 2018; 7:325–35. https://doi.org/10.1007/s40145-018-0282-4.
- [274] Balagurov AM, Bobrikov IA, Sumnikov S V, Yushankhai VY, Mironova-Ulmane N. Magnetostructural Phase Transitions in NiO and MnO: Neutron Diffraction Data. JETP Lett 2016;104:84–90. https://doi.org/10.1134/S0021364016140071.
- [275] Rouquerol J, Baron G V., Denoyel R, Giesche H, Groen J, Klobes P, et al. The characterization of macroporous solids: An overview of the methodology. Microporous Mesoporous Mater 2012; 154:2–6. https://doi.org/10.1016/J.MICROMESO.2011.09.031.
- [276] Rouquerol J, Baron G, Denoyel R, Giesche H, Groen J, Klobes P, et al. Liquid intrusion and alternative methods for the characterization of macroporous materials (IUPAC technical report). Pure Appl Chem 2012; 84:107–36. https://doi.org/10.1351/PAC-REP-10-11-19.

- [277] Arifin N, Button T, Steinberger-Wilckens R. Carbon-Tolerant Ni/ScCeSZ via Aqueous Tape Casting for IT-SOFCs. ECS Trans 2017; 78:1417–25. https://doi.org/10.1149/07801.1417ecst.
- [278] Shen CT, Lee KR, Hsieh YP, Lee SW, Chang JK, Jang SC, et al. Effects of TiO₂ and SDC addition on the properties of YSZ electrolyte. Int J Hydrogen Energy 2019; 44:29426–31. https://doi.org/10.1016/j.ijhydene.2019.07.051.
- [279] da Silva FS, de Souza TM. Novel materials for solid oxide fuel cell technologies: A literature review. Int J Hydrogen Energy 2017; 42:26020–36. https://doi.org/10.1016/j.ijhydene.2017.08.105.

List of figures

Figure 1. Conceptual view on smart grids [1].	13
Figure 2. Comparison of the efficiency of SOFC and other energy generators [19]	15
Figure 3. Ishikawa diagram describing degradation issues in SOCs [21].	16
Figure 4. Schematic presentation of steam reforming over Ni-Fe catalytic alloys. Syner	rgistic
effect in (b) Ni-rich Ni-Fe alloy [37]	19
Figure 5. Schematic representation of the working principle in (A) O-SOC and (B) H-SOC	[48].
	23
Figure 6. Representation of different SOFC structures. (a) planar structure; (b) tubular structure	ıcture;
(c) flat tubular structure; (d) MOLB-type structure [50]	25
Figure 7. Representation of the Nernst resistance and the potential changes vs. water p	partial
pressure in fuel feed stream [59].	28
Figure 8. Voltage losses on polarization curves of an operating SOC in (A) SOFC mode [60]	0] and
(B) SOEC mode [61]. V _{rev} – reversible potential	29
Figure 9. Thermal balance regions in SOC (adiabatic conditions). V_{th} – thermoneutral volume V_{th}	oltage,
$V_{eq}-$ steady state voltage. Image adopted from [62].	31
Figure 10. Energy demand of the H ₂ O and CO ₂ electrolysis reactions depicting the total e	nergy
needed with an indication of the electricity demand and the heat demand [73]	33
Figure 11. The design and working principles of Solid Oxide Electrolysis Cell (SOEC) [82]34
Figure 12. Schematic view of the circular economy concept [83].	34
Figure 13. A) Illustration of the setup for direct methane synthesis from coelectrolysis in a to	ubular
cell and B) electrical and chemical performance of the unit operated at 1.3 V [86]	36
Figure 14. Comparison of various electrolyte materials used in SOC [89]. BIMEVOX - Bi_4V	V_2O_{11}
$CGO - Ce_{1-x}Gd_{x}O_{2-\delta}, \ LSGM - La_{0.9}Sr_{0.1}Ga_{0.8}Mg_{0.2}O_{3-\delta}, \ LAMOX - La_{2}Mo_{2}O_{9}, \ YSZ - Zr_{1-x}Y_{0.2}Ga_{0.8}Mg_{0.2}O_{0.2}Ga_{0.8}Mg_{0.2}O_{0.2}Ga_{0.8}Ga_$	$_{x}O_{2}37$
Figure 15. Conductivity of Ni-YSZ cermet as a function of Ni content. The conductivity	y was
measured at 1000 °C in wet H ₂ . Numbers are the references cited in [105].	40
Figure 16. Schematic representation of the operation of the cathode in SOFC depending of	on the
selection of the material [120] IC $-$ ionic conductor, EC $-$ electronic conductor, MIEC $-$ 1	mixed
ionic electronic conductor	42
Figure 17. Schematic view on the surface segregation in (a) LSCF/YSZ and (b) LSCF/GDO	C cell.
The red arrow indicates direction of the Sr segregation and diffusion [128].	44
Figure 18. SEM images of the cell cross-sections after 9000 h operation at 800 °C. A) pro-	istine,
reference cell, B) held under OCV and C) working under $-1~{\rm A\cdot cm^{-2}}$ current density [140].	46
Figure 19. The Ni-YSZ anode optical image and scanning electron microscopy (SEM)	image
with EDX mapping of the (a) Ni-YSZ surface; (b) coke deposited on the Ni-YSZ surface	e; and
(c) coked spot on the surface after the long-term test in CH ₄ [141].	47

Figure 20. Measurement rig for SOC testing [157].
Figure 21. Schematic representation of catalytic activity measurement unit. 1 - H ₂ O vapo
$generator, 2-main\ SOC\ chamber\ or\ packed-bed\ reactor, 3-initial\ condenser, 4-water\ coldtrapped and the sum of the$
5,6 – thermostats, 7 – FTIR/GCMS
Figure 22. A-C) Calibration curves for CO ₂ , CO, and CH ₄ and D) FTIR spectrum of biogast
(Vertical dashed lines mark the wavenumber ranges used for quantitative analysis) [157] 57
Figure 23. SEM fracture image of the Ni-YSZ supported Solid Oxide Cell
Figure 24. XRD patterns of the impregnated samples with/without β-cyclodextrin additive [167]
Figure 25. TPR profiles of the CeO ₂ impregnated catalysts. Inset R1 shows the first reduction
cycle profile [167]
Figure 26. XRD patterns before/after reduction (left) and TPR profiles (right) of Ce _{0.8} Ni _{0.2} O _{2-δ} and
$Ce_{0.8}Co_{0.2}O_{2-\sigma}$ I – surface reduction and II – reduction of Ni and Co ions strongly
integrated with the support [167]
Figure 27. TPR profiles of the catalysts [168]. Reduction profile of copper (II) oxide shown in
dashed line
Figure 28. The change of CO concentration during the catalytic tests for 1% Cu and 5% Cu
samples in temperature and process time [168].
Figure 29. Adsorption-desorption isotherm (left) and SEM image (right) of the βCD-Ni/CeO
catalyst [167]
Figure 30. (A) TEM images and elemental maps of Ni and Ce in βCD-Ni/CeO ₂ and Ni/CeO
catalysts, (B) HR-TEM image of β CD-Ni/CeO $_2$ and (C) SEM image of β CD-Ni/CeO $_2$ [167] 75
Figure 31. Catalytic performance of the βCD-Ni/CeO ₂ and Ni-CeO ₂ . A) CO conversions (X) and
CH ₄ selectivity (S), and B) CH ₄ and CO ₂ yields (Y) [167]
Figure 32. Catalytic performance of the βCD-Co/CeO ₂ and Co-CeO ₂ . A) CO conversions (X) and
CH ₄ selectivity (S), and B) CH ₄ and CO ₂ yields (Y) [167]
Figure 33. Change in calculated parameters after aging at 700 ℃ for 24 h. A) Ni-impregnated
CeO ₂ , and B) Co-impregnated CeO ₂ . Dashed line represents thermodynamic equilibrium values
[167]
Figure 34. Reaction quotients for CO/CO ₂ methanation and WGS reactions [167]
Figure 35. XRD diffraction patterns of the as-prepared Co-impregnated and reference cells (left
and SEM image of the prereduced half-cell (right) [217]
Figure 36. SEM images of the prepared Co-impregnated electrodes and pristine cell (left), TEM
image of the 3.6wt.% Co sample at the 8YSZ-Ni-Co interface (right up), and HRTEM of the Co
based nanostructure (right down). A – paper ball-like structure, B – Co/YSZ surface [217] 85
Figure 37. SEM images of the Ni-YSZ electrodes impregnated with transition metals (after
reduction at 800 °C. Scale bar is 1 µm [unpublished results]

Figure 54. STXM images of the NiO-YSZ precursor powder, Ni elemental map and
complementary SEM image. Scale bars are 1 µm [258]
Figure 55. SEM images of YSZ scaffolds sintered at 1400 °C (left) and TGA curves of YSZ
precursor powders (right) [258]
Figure 56. A) TG-DSC curves of YSZ and NiO-YSZ precursors, and B,C,D) reduction-oxidation-
reduction curves of 0.3 M CTAB/NaCl NiO-YSZ and conventional cermet material [258] 114
Figure 57. Porosity (bars) and linear shrinkage (dots) of CTAB/NaCl YSZ vs. starting cation
concentration (left) and TEC of 0.3 M CTAB/NaCl YSZ and NiO-YSZ (right) [258] 117
Figure 58. Nitrogen adsorption isotherms (A,C) and pore size distribution (B,D) of 0.3 M
CTAB/NaCl YSZ and Ni-YSZ. Reference materials are NiO-YSZ after reduction and YSZ after
Ni etching [258]
Figure 59. Conductivity measurements under humidified hydrogen and a relative conductivity
loss [258]
Figure 60. SEM images and elemental maps of 0.3 M CTAB/NaCl Ni-YSZ in reduced state and
conventional Ni-YSZ before and after the aging. Scale bar is 8 µm [258]

List of tables

Table 1. Comparison of the nanocatalysis with homo- and heterogeneous catalysis. Advantages
and disadvantages
Table 2. Reaction enthalpy, reaction entropy and Gibbs free energy for H ₂ oxidation reaction
(water in liquid phase, minus sign for SOFC, plus sign for SOEC) [55]
Table 3. Reaction enthalpy, reaction entropy and Gibbs free energy for H ₂ oxidation reaction
(water in gas phase, minus sign for SOFC, plus sign for SOEC) [55]
Table 4. Lattice parameters obtained via Rietveld refining
Table 5. Specific surface area (SSA) and total pore volume of the catalysts. Error in SSA value
estimated as $\pm 5\%$ according to the manufacturer of the equipment
Table 6. Comparison of the porosity parameters of the reference and novel YSZ and cermet
materials obtained by the MICP technique. The measurement uncertainty is 5% as given by the
manufacturer of the equipment